

A thesis entitled

# **Acoustic Shock Wave Emissions from Laser Induced Breakdown of Materials**

Submitted to

**University of Hyderabad**

Towards partial fulfillment for the degree of

**Doctor of Philosophy**

in

**Physics**

By

**Manikanta Elle (10ACPP06)**



Under the supervision of

**Dr. P. Prem Kiran**

Advanced Centre for Research in High Energy Materials (ACRHEM)

School of Physics, University of Hyderabad

Hyderabad – 500046, India

**July- 2018**

**Dedicated**

**to**

**My Father, Mother**

**and**

**Babai, Chinnamma**

## **Declaration**

I, **Manikanta Elle**, hereby declare that the work presented in this thesis entitled **“Acoustic Shock Wave Emissions from Laser Induced Breakdown of Materials”** has been carried out by me under the supervision of **Dr. P. Prem Kiran**, Associate Professor in School of Physics, Associate faculty in ACRHEM, University of Hyderabad, Hyderabad, India, as per the Ph.D. ordinances of the University, which is also free from plagiarism. I declare, to the best of my knowledge, that no part of this thesis has been submitted for the award of a research degree of any other University. I hereby agree that my thesis can be deposited in Shodhganga / NFLIBNET.

A report on plagiarism statistics from the University Librarian is enclosed.

**(Manikanta Elle)**

**Reg. No: 10ACPP06**

**Dr. P. Prem Kiran**

Thesis Supervisor,

ACRHEM,

School of Physics,

University of Hyderabad.

**Dr. P. Prem Kiran**  
Associate Professor  
Tel.: +91-40-23138842  
Fax: +91-40-23012800  
E-mail: [prem@uohyd.ac.in](mailto:prem@uohyd.ac.in)  
[premkiranuoh@gmail.com](mailto:premkiranuoh@gmail.com)



ACRHEM, School of Physics  
University of Hyderabad,  
Prof. C. R. Rao Road,  
Gachibowli,  
Hyderabad – 500 046,  
Telangana, India.

---

## Certificate

This is is to certify that the thesis entitled **“Acoustic Shock Wave Emissions from Laser Induced Breakdown of Materials”** being submitted to the University of Hyderabad by **Manikanta Elle** (Reg. No. 10ACPP06), for the award of the degree of Doctor of Philosophy in Physics, is a record of *bonafide* work carried out by him under my supervision and is free of plagiarism.

The matter embodied in this report has not been submitted to any other University or Institution for the award of any degree or diploma.

Dr. P. Prem Kiran  
(Supervisor)

Director  
ACRHEM

Dean  
School of Physics

## Acknowledgements

First and foremost, my deepest gratitude to my supervisor Dr. P. Prem Kiran, for his guidance and support through ups and down during this research. He always keeping me focused and giving me sound advice whenever necessary in all aspects.

I was fortunate to be a part of the ACRHEM, SoP. It was a pleasure to thank present director, Dr. Anil Kumar Aggarwal, and the former directors, Dr. K. Venkateshwara Rao, Prof. S. P. Tewari, of ACRHEM for their constant support in all aspects that helped me in successful completion of the work. I am also thankful to the Dean, School of Physics (SoP), UoH, for the academic support.

A special thanks to my doctoral committee members Prof. Anil Kumar Chaudhary and Dr. G. Manoj Kumar.

I would like to thank the centre ACRHEM for giving the opportunity to carry the research work and DRDO for its financial support without which it would have been very hard to finish the work.

Special thanks to all the teaching staff of ACRHEM, SoP for providing the classes during my course work which really helped me to understand the physics. I would also like to thank all the non-teaching staff of ACRHEM and SoP.

I would like to thank my senior Dr. Ch. Leela for having many fruitful discussions, which helped me to clarify many doubts encountered in understanding the experimental observations. I would also like to thank my seniors Sreedhar, Ashwin, Venkatesh, Syed Hamad, Sita, Debasis Swain and Appalakondaiah for support.

I am lucky to have a good number of friends and I always enjoyed working with them. Without these fellows cooperation, it would have been very difficult to finish the thesis on time. I thank all my friends Sai Shiva, Nagendra, Rakesh, Vinoth, Venkateshwarlu, Nagaraju, Phani Sri, Yellaih, Sree Harsha, Konda Srinivasa Rao, Narsimha Rao, Anubham, Tarun, Yedukondalu, Anusha, Nageswara Rao, Pardu, for their support all the way from the early research work.

I would also like to thank my juniors Kalam, Mounika, Rajendhar, Byram Chandu, Ganesh, Mahendar, Pratap, Moses, John, Samuel and Bhrathi for their support. Many fruitful discussions with them helped me to understand the subject properly and led me to finish the work on time.

I would also like to thank my friends KNVV Satyanarayana, Anil, K Sreenu, Pushparao, Rajendra, Bujji babu, Ravi, Suresh, Paul, Subbarao, Pravitha, Prameela and Anusha.

Special thanks to all the teaching staff of ACRHEM, SoP for providing the classes during my course work which really helped me to understand the physics. I would also like to thank all the non-teaching staff of ACRHEM and SoP.

I am very lucky to have a loving and caring family. Their constant encouragement and blessings all the time had made me to achieve this degree. Their patience, hard work and the moral support had taught me how to survive in this world.

# Contents

List of figures.....	i-viii
List of tables.....	xi-x
<b>CHAPTER 1: Introduction.....</b>	<b>1</b>
1.1 Laser induced breakdown of matter with short laser pulses.....	1
1.1.1 Cascade breakdown.....	1
1.1.2 Multiphoton absorption.....	2
1.2 Radiations from LIB of medium.....	2
1.3 Origin of Laser generated acoustics emissions.....	4
1.4 Organization of thesis.....	7
1.4.1 Chapter 2: Experimental details.....	7
1.4.2 Chapter 3: ASW emissions from ns and ps-LIB of atmospheric air: propagation of ASWs in surrounding atmosphere.....	8
1.4.3 Chapter 4: ASW emissions from LIB of various materials.....	8
1.4.4 Chapter 5: ASWs from high energy materials (HEMs).....	9
1.4.5 Chapter 6: ASW emissions from interaction zone of two counter propagating laser generated shock waves in air.....	9
1.4.6 Chapter 7: Conclusions and future scope.....	10
1.5 References.....	10
<b>CHAPTER 2: Experimental details.....</b>	<b>13</b>
2.1 Technical details and specifications of nano second and pico second lasers.....	13
2.2 Micro phone specifications and working principle.....	14
2.3 Experimental schematics.....	16
2.3.1 Breakdown of target samples in the presence of various gases and in ambient air.....	17
2.3.2 Analysis of ASWs in Time domain.....	18
2.3.3 Analysis of ASWs in Frequency domain.....	22
2.4 Effect of sampling rate on ASW signals.....	23
2.5 References.....	26

**CHAPTER 3: ASW emissions from ns and ps-LIB of atmospheric air:  
Propagation of ASWs in surrounding atmosphere.....29**

3.1 Introduction.....29

3.2 Radial distribution of acoustic shock waves.....30

3.3 Angular distribution of ASWs.....32

3.4 Energy dependence of ASWs.....33

    3.4.1 nano second laser induced breakdown (ns-LIB) of Air.....33

    3.4.2 pico second laser induced breakdown (ps-LIB) of Air.....38

3.5 Effect of input intensity on the acoustic parameters.....40

3.6 Frequency analysis.....47

3.7 Summary.....48

3.8 References.....50

**CHAPTER 4: ASW emissions from LIB of various materials.....53**

4.1 Nano second LIB.....53

    4.1.1 Metals and alloys.....57

    4.1.2 Alloys.....65

    4.1.3 Dielectrics.....66

    4.1.4 Insulators.....68

    4.1.5 Cu powders.....71

    4.1.6 Comparison among various materials.....76

    4.1.7 Frequency analysis.....77

4.2 Pico second LIB.....83

    4.2.1 Conductors.....85

    4.2.2 Comparison of ASW parameters of conductors.....89

    4.2.3 Dielectrics.....90

    4.2.4 Insulators.....91

    4.2.5 Compacted Cu powders.....92

    4.2.6 Comparison among various materials.....94

    4.2.7 Frequency analysis.....95

4.3 Repetitive ablation.....99

4.4	Conclusions.....	102
4.5	References.....	103
<b>CHAPTER 5: Acoustic shock waves from high-energy materials.....</b>		<b>107</b>
5.1	Introduction.....	107
5.2	ns-LIB of AN, DNT, TNT, NTO and Air: .....	109
5.2.1	Reproducibility.....	111
5.3	ns-LIB of 4-Nitro Imidazole, Lead nitrate, Bismuth Nitrate.....	116
5.3.1	ns- LIB of Argon, Nitrogen and Ambient air.....	117
5.3.2	Effect of background gases on LIB.....	119
5.4	ps LIB of RDX, CL-20, NaN <sub>3</sub> and TNT.....	122
5.5	ns-vs ps- LIB of TNT.....	126
5.6	Conclusions.....	127
5.7	References.....	128
<b>CHAPTER 6: ASW emissions from interaction zone of two counter propagating laser generated shock waves in air.....</b>		<b>129</b>
6.1	Introduction.....	129
6.2	Experimental details.....	130
6.2.1	Optimization of microphone position w.r.t plasma.....	133
6.3	Case of Equal impedances.....	135
6.3.1	Comparisons between single and dual plasma.....	135
6.3.2	Total energy 100 mJ (S1+2).....	137
6.3.3	Total energy is 50mJ (S1+2).....	139
6.4	Un-equal impedances (un-equal densities).....	142
6.4.1	Ratio of S1: S2= 1: 1.5.....	142
6.4.2	Ratio of S1: S2 = 1:4.....	147
6.5	Conclusions.....	150
6.6	References.....	151
<b>CHAPTER 7: Conclusions and future scope.....</b>		<b>153</b>
7.1	Future plan.....	155



## List of figures

Fig. 1.1. Steps involved in laser matter interaction to generate Acoustic Shock Waves.....	3
Fig. 1.2. Process of generation of shock waves from the laser produced plasma.....	4
Fig. 2.1. Microphone setup (a), exploded view of mic, pre amplifier, connector (b), and power supply (c).....	15
Fig. 2.2. Calibration spectrum of 1/8" microphone. Inset shows the time domain representation of 1 kHz sound signal. X- Axis is frequency in kHz and Y-axis is power spectral density (PSD).....	15
Fig. 2.3. Arrival times of ASWs at various distances of microphone from plasma, at 40 mJ of energy for ns laser pulses.....	16
Fig. 2.4. Experimental schematic for the detection of ASW measurements from the ns- and ps-LIB of air. Two different lasers were used for two different pulse widths of 7 ns and 30 ps. The microphone is positioned at a distance of 8 cm from the plasma (it can be variable). Target holder is fixed to motion controller to expose laser radiation.....	17
Fig. 2.5. LIB of target samples in the presence of Argon and Nitrogen gaseous environment. Samples are mounted on target holders. Gas tube is included in set up.....	18
Fig. 2.6. Entire time domain ASW signal from the ns-LIB of air at a microphone distance of 8 cm. (a) Reflected components from objects around the plasma are presented along with the main acoustic pulse, where $t = 0$ represents the photo diode signal, when the laser energy is 20 mJ (b) ASW signal from the ns-LIB of atmospheric air at 90 mJ input laser energy per pulse at a microphone distance of 8 cm from the plasma.....	19
Fig. 2.7. Time domain representation of ASW signal, emitted from the ps LIB of Brass sample at 18 mJ of laser energy per pulse.....	19
Fig. 2.8. Peak pressures with error bars of ASWs for each laser shot of ns-LIB of air were plotted at various incident laser energies of 10, 25, 55 and 90 mJ.....	21
Fig. 2.9. (a) Spectrum of ns-LIB of air. Two peaks were fitted to two Lorentzian peaks. The fitting parameters are noted down to understand more about ASWs. Y-axis is power spectral density. (b) Spectrum from ps-LIB of air fitted to only one peak.....	22
Fig. 2.10. Time domain signals and spectrums of manual hitting of target samples of aluminium (Al), copper (Cu), stain les steel (SS).....	23
Fig. 2.11. For a fixed laser energy, ASW signals were collected at timescale of 100, 500 $\mu$ s and 1 milli sec, (a) time domain representation of data points, temporal resolution is more for 100 $\mu$ sec than the 500 $\mu$ sec and 1 msec. (b) Frequency representation of data. Sampling rates are 125, 25 and 12.5 Mega samples/sec for 100, 500 $\mu$ sec and 1 msec respectively. Frequency resolution is more for 1 msec than the 500, 100 $\mu$ sec.....	25
Fig. 3.1. ASW pressures produced by ns LIB of air, at 20 mJ, 40 mJ pulse energies under, (a) f/10 focal geometry and (b) f/19 focal geometry.....	31

Fig. 3.2. Distribution of ASW pressures around plasma for both ns and ps LIB of air at three different radii of 3, 5, 8 cm and time scales for 10mJ of incident laser energy.....	32
Fig. 3.3. Frequency response of ASWs from ns LIB of air, around the plasma at various angles of microphone w.r.t incident laser direction, (a) 10 mJ, (b) 25 mJ, (c)40mJ of incident laser energy.....	33
Fig. 3.4. ASW signals from ns-LIB of air at 10, 25, 40, 55, 70 and 90 mJ of laser energies per pulse, X-axis is time duration of the pulse, Y-axis is peak to peak pressure. Here the source-receiver distance is 8 cm.....	34
Fig. 3.5. During ns-LIB, Plasma plume dimension (from CCD imaging) and ASW pulse width vs laser energy at same experimental condition.....	35
Fig. 3.6. Frequency spectrum of ASWs from ns-LIB of air, (a) at various incident laser energies, X-axis is frequency and Y-axis is Power Spectral Density (PSD), (b) shift in central frequency (peak 1) w.r.t laser energy.....	36
Fig. 3.7. For ns LIB of air, the FWHM and area under the curve of spectrum for both peak 1 (low frequency) and peak 2 (high frequency) (b). These are changing along with the incident laser energy.....	37
Fig. 3.8. ASW signals from ps-LIB of atmospheric air at 3, 6, 12, 18, 24 and 30 mJ of incident laser energies, X-axis is time duration of the pulse, Y-axis is pressure.....	38
Fig. 3.9. Frequency spectrum of ASWs from ps-LIB of air, at different incident laser energies when microphone is at 8 cm distance from plasma, here X-axis is frequency and Y-axis is Power Spectral Density (PSD) (a), Incident laser energy versus FWHM and area.....	39
Fig. 3.10. Arrival time and acoustic pulse widths of ASW w.r.t incident laser energy. (a) ns LIB, f/19 and (b) ps LIB, f/14 focal geometry.....	42
Fig. 3.11. ASW pressure variations and linear fits vs incident laser energy for different focal geometries. (a) ns LIB, (b) ps LIB of ambient air.....	43
Fig. 3.12. Acoustic signal energy vs Laser energy at f/10, f/19, f/25, f/38 focal numbers, from ns LIB of air, lines are guided to the eye.....	46
Fig. 3.13. Ratio of $E_{ac}$ and $E_{in}$ , (a) ns LIB, (b) ps LIB at various laser energies and focal numbers.....	47
Fig. 3.14. Central peak frequencies for various laser energies for both (a) ns LIB peak-1, (b) ns LIB peak-2 and (c) ps LIB of air.....	48
Fig.3.15.ns-and ps- LIB generated ASWs, (a) temporal representation, (b) spectral representation.....	49
Fig. 4.1. Nano second laser pulses and target sample interaction [Taken from Karl-Heinz Leitz et al.]. During laser matter interaction, the associated phenomena are also presented.....	55
Fig.4.2.Schematic of LIB of materials. The position of microphone, target, sample holder (mounted on a translation stage), ASWs are shown.....	57

Fig. 4.3. Typical time domain ASW signal from ns LIB of Aluminium target at 100 mJ of laser energy per pulse. Plasma- microphone distance is 7.5 cm. X-axis is time and Y-axis is pressure.....	58
Fig. 4.4. Peak pressures and arrival times of ASWs emitted from ablation of Aluminium sample at 20, 60, 80 and 100 mJ energies.....	59
Fig. 4.5. Peak heights of -ve and +ve portions of ASW signal at 20, 60, 80 and 100 mJ of incident laser energies for the Al target sample. X- Axis is incident laser energy, Y-axis is Peak height (pressure). The slope of -ve and +ve peak heights are 2.7 and $1.0 \times 10^{-2}$ respectively as shown by solid lines.....	60
Fig. 4.6. Peak widths of both positive (+ve) and negative (-ve) portions of ns-LIB of Al generated ASW. X- Axis is incident laser energy, Y-axis is Peak width. The slopes of -ve and +ve peaks are -0.08 and $8.9 \times 10^{-2}$ . The slope of -ve peak is almost flat, very close to zero compare with the +ve peak.....	61
Fig. 4.7. Area under both positive (+ve) and negative (-ve) portions of time domain ASW signal, which is radiated from the ns-LIB of Al target sample. X- Axis is laser energy, Y- axis is Area under the curve. The slopes of area under the -ve and +ve peaks are 10.2 and $14.9 \times 10^{-2}$ respectively. Both are having increasing slopes.....	62
Fig. 4.8. Peak pressures from ns-LIB of Al, Cu, Brass and SS 316LN at a fixed energy of 20 mJ at 7.5 cm distance of microphone from plasma. Samples are dimensions of 5 cm $\times$ 5 cm, with samples.....	63
Fig. 4.9. Peak-peak pressures of ASWs emitted from the ns-LIB of Brass and SS 304 solid target samples at 10, 25, 40, 55, 70 and 100 mJ of laser energies per pulse. The slopes of Brass and SS304 peak pressures are 4.1, $2.9 * 10^{-2}$ respectively. Both materials are having increasing slopes.....	66
Fig. 4.10. Time domain signals of ns-LIB of Mica generated ASWs at various laser energies of 10, 25, 40, 55, 70 and 100 mJ.....	67
Fig. 4.11. Peak pressures and acoustic shock wave pulse width w.r.t incident laser energy for MICA target sample. The linear fit for data is indicated with a line. The slopes are 0.038, 0.15.....	67
Fig. 4.12. Laser energy vs peak pressure and acoustic pulse width for LIB of PVC sample. The slopes are 0.045, 0.19 for peak pressure and acoustic pulse width respectively. Data is fitted to linear equation.....	68
Fig.4.13.SEM images of copper powders and their corresponding particle size distribution fits.....	71
Fig. 4.14. SEM images of copper samples heat treated at 6000C.....	72
Fig. 4.15. Incident laser energy vs peak pressures for 2, 15, 40 and 420 micron size particles. At three packing densities of 60, 70 and 80 %, peak pressures are plotted for 10, 25, 40, 55 and 70 mJ laser energies. The pressures are increased w.r.t incident laser energy.....	74

Fig. 4.16. Packing density vs peak pressures for 2 micron size particles at 10, 40 and 70 mJ of laser energies.....	74
Fig. 4.17. Packing density vs peak pressures for 420 micron size particles at 10, 40 and 70 mJ of laser energies.....	75
Fig. 4.18. Packing density vs ratio of +ve peak width and -ve peak height for 2, 420 $\mu$ particle sizes for the laser energies of 40, 55, 70 mJ. At each packing density, the 420 $\mu$ particle size having higher value of ratio than the 2 $\mu$ except 80 % packing density and laser energy of 70 mJ. Units of ratio is ( $\mu$ sec/kPa), error is absolute value.....	75
Fig. 4.19. The time domain signals of ASWs emitted from the ns-LIB of Brass, Teflon, Mica, PVC at 10 and 40 mJ of incident laser energies.....	77
Fig. 4.20. Spectral distribution of ASW emitted from the ns LIB of Brass target at various laser energies. X- Frequency, Y-laser energy and Z- power spectral density (PSD).....	78
Fig. 4.21. (a) Lorentzian fitting for spectral peaks of ns LIB of Brass spectrums. X- Axis is frequency, Y-axis is power spectral density (PSD), (b) central frequencies of peak 1, 2, 3 with respect to incident laser energy.....	79
Fig. 4.22. Lorentz fitted peak1 and 2 frequencies due to ns LIB of material samples with their PSD values are plotted for all the samples at a fixed energy of 25 mJ. Each colour sphere is a data point. (a) Peak 1, (b) peak 2 frequencies vs their corresponding PSDs.....	81
Fig. 4.23. Frequency spectrums of ASWs emitted from the ns-LIB of Cu powder pallet of 2 $\mu$ particle size. At various laser energies of 10, 25, 40, 55 and 70 mJ at a fixed packing density 60% and 2 micron particle size.....	82
Fig. 4.24. The frequency responses of ASWs from 60, 70, 80 % dense copper pallets at 40, 55, 70 mJ of laser energies for a 2 micron size particles. Amplitude of PSD is maximum for 80% dense cu pallets than the 60, 70% dense.....	83
Fig. 4.25. Interaction of ultrashort pulse with material [taken from Karl-Heinz Leitz et al.....	84
Fig. 4.26. Pressures and arrival times for Al and Cu samples, at various input energies of 6,12,18,24 and 30 mJ. The slopes of peak pressures for Al, Cu samples are 0.068, 0.065 respectively. The slopes of arrival times for Al, Cu samples are -0.24, -0.20 respectively.....	85
Fig. 4.27. Peak to peak pressures and arrival times for Brass and SS 304 at 6, 12 and 24 mJ of laser energies. The slopes of peak pressures for Brass, SS304 samples are 0.072, 0.075 respectively. The slopes of arrival times for Brass, SS304 samples are -0.26, -0.22 respectively.....	86
Fig. 4.28. For Al sample, (a) comparison of ASW signals, (b) +ve and -ve peak heights w.r.t incident laser energy. The slopes of +ve and -ve peak heights are 0.012 and 0.056 respectively.....	87
Fig. 4.29. (a) The ASW signals from Al target at various incident laser energies of 6,12,18,24 and 30 mJ. Highlighted circles and boxes indicates the changes in signals due to variation in laser ablation. (b) The slopes of +ve and -ve peak widths are 0.53 and 0.03 respectively.....	88

Fig. 4.30. (a) Peak to peak pressures and arrival times of ASWs at 6, 12 and 24 mJ of energies for dielectric samples. (b) The slopes of peak pressures for glass, Mica, ZrSnTiO <sub>4</sub> samples are 0.069, 0.069, 0.069 respectively. The slopes of arrival times for glass, Mica, ZrSnTiO <sub>4</sub> samples are -0.22, -0.27, -0.24 respectively.....	90
Fig. 4.31. (a) Pressures, (b) arrival times for PVC, Teflon at all laser energies of 6, 12, 18, 24, and 30 mJ. The slopes of peak pressures for PVC, Teflon samples are 0.081, 0.084 respectively. The slopes of arrival times for PVC, Teflon samples are -0.27, -0.26 respectively.....	91
Fig. 4.32. Laser energy vs peak pressures and their linear fits for packing densities of 60, 70, 80% for the particle sizes of 2 and 425 micron. Peak pressure are proportional to the incident laser energy.....	93
Fig. 4.33. Laser energy vs peak pressures for particle sizes of 2, 425 $\mu\text{m}$ at each packing density of 60, 70, and 80 %. At each packing density, interaction of laser pulse with each particle size is different.....	93
Fig. 4.34. Packing density vs ratio of +ve peak width and –ve peak height for 2, 425 $\mu$ particle sizes for the laser energies of 15, 27 mJ. At each packing density, the 425 $\mu$ particle size having higher value of ratio than the 2 $\mu$ . Units of ratio is ( $\mu\text{sec/kPa}$ ), error is absolute value.....	94
Fig. 4.35. ASW signals from ps LIB of various samples at (a) 6 mJ, (b) 18 mJ of incident laser energies.....	95
Fig. 4.36. Acoustic spectrum of ps-LIB of Al target sample at 24mJ of laser energy. Frequencies are fitted to Lorentzian function with three different frequencies (peak1 to 3), actual spectrum is super imposed on the peak sum of fitting, and it shows the fitting is good.....	96
Fig. 4.37. Peak 1 frequency vs incident laser energy, for ps LIB of Al target sample. Central fitted peak frequency decreases as the laser energy increases from 6 to 30 mJ.....	96
Fig. 4.38. Peak 1 and peak 2 frequencies of ps – LIB of various samples at 24 mJ of laser energy.....	97
Fig. 4.39. Peak 1 and peak 2 frequencies of ps – LIB of various samples at 12 mJ of laser energy.....	98
Fig. 4.40. Time domain signals (a) and its corresponding acoustic spectrums (b) of 32, 64 and 128 averaged ASW signals at laser energy of 60 mJ.....	100
Fig. 4.41. (a) Peak-to- peak pressures and (b) FWHM of –ve peak of emitted ASW from the LIB of Aluminium sample for consequent laser shots of 32, 64 and 128 on same spot at 60, 80 and 100 mJ energies.....	100
Fig. 4.42. Comparison of ASW peak pressures between the fresh spot area ablation and the ablation due to different number of shots on same spot area at 60, 80, 100 mJ of energies.....	102
Fig. 5.1. Classification of explosives [9].....	109

- Fig. 5.2. ASW signals from LIB of TNT sample, for 20 consecutive laser pulses at 25 mJ of laser energy. Inset shows the image of negative peak (lower) of all 20 ASW signals. X-axis is time, Y-axis is pressure. The maximum deviation in X-axis is  $\approx 0.6 \mu\text{s}$ , Y-axis is 0.2 kPa.....111
- Fig. 5.3. (a) Actual spectrum and fitted peaks (five) of single ASW signal. (b) Spectral peak frequencies of twenty successive ns laser shots on TNT target sample, shown with different colours. Lorentz fitted peak frequencies of twenty laser shots data is presented. Here the laser energy is used is 25 mJ per pulse.....112
- Fig. 5.4. Lorentz fitted acoustic spectral central peak frequencies vs their PSD (power spectral density) at 25 mJ laser energy for ns LIB of AN, DNT, TNT, NTO and Air. (a) Peak 1 frequencies, (b) peak 2 frequencies, here frequency is on X-axis, PSD is on Y-axis.....115
- Fig. 5.5. Lorentz fitted acoustic spectral central peak frequencies vs their PSD (power spectral density) at 40 mJ laser energy for AN, DNT, TNT, NTO and Air. (a) Peak 1 frequencies, (b) peak 2 frequencies, here frequency is on X-axis, PSD is on Y-axis.....115
- Fig. 5.6. Experimental schematic of laser interaction with HEMs in the presence of Nitrogen, Argon gases and Air (a), the actual arrangements of air, argon and plasma above the target sample. Here laser is incidenting on the sample from the top, which is normal to the target sample as shown in (b).....116
- Fig. 5.7. ASW parameters of acoustic signals emitted from the breakdown of only Ar, N<sub>2</sub>, Air gases at 32 mJ of laser energy.....118
- Fig. 5.8. The central peak frequencies and their PSDs for ns LIB of ambient AIR, Argon and Nitrogen at an energy of 32 mJ per pulse.....119
- Fig. 5.9. The variation in peak pressures of 4-N-Imidazole, Bismuth and Lead nitrate samples in Argon and Air environment at a fixed laser energy of 50 mJ.....120
- Fig. 5.10. The Lorentz fitted central peak frequencies and their PSDs (power spectral density) for the materials of Bismuth nitrate, Lead nitrate and 4-Nitro Imidazole at 50 mJ of laser energy. Here the LIB of material environment is ambient air.....121
- Fig. 5.11. The Lorentz fitted central peak frequencies and their PSDs (power spectral density) for the materials of Bismuth nitrate, Lead nitrate and 4-Nitro Imidazole at 50 mJ of laser energy. Here the LIB of material environment is Argon.....121
- Fig. 5.12. Peak pressures for RDX, TNT, CL20 and Sodium Azide (NaN<sub>3</sub>) for 6, 12 mJ laser energies.....124
- Fig. 5.13. Spectrum of ps-LIB of CL-20. The spectrums at two laser energies of 6, 12 mJ. The spectral response is same for both energies. PSD value is high for 12 mJ spectral peak than the 6 mJ.....125
- Fig. 5.14. Peak frequencies (Lorentz fitted) vs PSD values presented in spectrums of ps LIB of RDX, TNT, CL-20 and Sodium azide (NaN<sub>3</sub>) samples, at a fixed energy of 6 mJ....125

- Fig. 5.15. Peak frequencies (Lorentz fitted) vs PSD values presented in spectrums of ps LIB of RDX, TNT, CL-20 and Sodium azide ( $\text{NaN}_3$ ) samples, at a fixed energy of 12 mJ. Each data point is a different colour sphere.....126
- Fig. 5.16. Time domain signals, of ns and ps -LIB of TNT sample at 25 mJ and 12 mJ of laser energies respectively.....126
- Fig. 5.17. Lorentz fitted spectral peak frequencies for both ns, ps LIB of TNT sample.....127
- Fig. 6.1. Experimental schematic of counter propagation of two shock waves. BS is beam splitter, L1 and L2 are two Plano convex lenses of focal length 78 mm. Separation distance between two plasmas is  $d$ , it is variable. Microphone is fixed at a distance of 8 cm from the laser propagation axis. Interaction zone, where two plasmas meet each other....131
- Fig. 6.2. Shadwographic images of dual plasma, formed due to counter propagation of two ns laser beams. Experiments are done with three beam splitters of 40: 60, 20:80 and 50:50 and at time scales of 4, 8, 16 and 30  $\mu$  secs. First row is 40:60 BS (left plasma formed due to 21 mJ of laser energy whereas right one formed with 42 mJ). Interaction zone is clearly highlighted in first row second image, this image is taken at 8 micro sec from the laser pulse. Second row is 20:80 and third row is 50:50 BS.....132
- Fig. 6.3. (a) Microphone position vs the peak pressure for a single source (S2 plasma) at laser energy of 25 mJ ( $S_1+S_2= 50$  mJ). Microphone scan starts from  $z= -10$  mm to  $+10$  mm. (b) Source (S2) is exactly at  $z=-1$  mm position of microphone (indicated with red line), so peak pressure is maximum at this point.....133
- Fig. 6.4. (a) Position of microphone from the interaction zone point of two shock waves, (b) normalized peak pressures from the dual plasma (two plasmas are present and separated by 2 mm distance) at various positions of microphone. Peak pressure is maximum at  $z=0$  microphone position for 50:50 BS and laser energy of  $S_1+S_2$  is 50 mJ. ....134
- Fig. 6.5. ASW time domain signals from LIB of air at laser energies of 50 and 25+25 mJ for a separation distance of 14 mm. Peak pressures of single and dual plasma are 4.75 and 6.59 kPa, respectively. Dual plasma generates the more acoustic pressures than the single plasma under fixed laser energy. Inset shows the plasma plume image integrated over 32 ms. CCD images are at 2 mm separation distance. ....136
- Fig. 6.6. ASW signals from LIB of air at laser energies of 100 and 50 mJ+50 mJ for a separation distance of 25 mm. Peak pressures of single and dual plasma are 6.8 and 10 kPa respectively. Dual plasma generates more acoustic pressures than the single plasma under fixed laser energy. Inset shows the plasma plume image integrated over 32 milli sec. CCD images are at 2 mm separation distance. ....137
- Fig. 6.7. Separation distance vs peak pressures from dual plasma for 50:50 beam splitter. Linear fits with two slopes are mentioned in above graph. From 0-19 mm and 20-28 mm the slopes of linear fits are 0.2 and 0.01 respectively. In set shows that the shadowgraphic image of interaction of counter propagating two shock waves at 2, 5, 10 mm separation distances. Images are presented here are taken at 30  $\mu$ sec time from the plasma initiation.....138

Fig. 6.8. Separation distance vs arrival time of ASW from the dual plasma for 50: 50 beam splitter. Here total energy is 100 mJ. ....	139
Fig. 6.9. Separation distance vs acoustic peak pressures for 50:50 beam splitter, at total energy of 50 mJ. ASW peak pressure behaviour is fitted to three lines of slopes 0.14, -0.06, -0.55.....	140
Fig. 6.10. Separation distance vs arrival time of ASWs from dual plasma. Here total energy is 50 mJ.....	141
Fig. 6.11. Spectral response of ASWs for 50:50 beam splitter and individual laser energies of 50, 25 mJ. Two individual plasmas are having same spectral peak. The separation distance is 2 mm for dual plasma in this case. ....	142
Fig. 6.12. Time domain signals of ASWs emitted from the single plasma (S1 and S2) and dual plasma (S1+2). Laser energies of 24, 41 mJ used to form first plasma (S1) and second plasma (S2) respectively. Arrival times are indicated with coloured lines on signals. Here the separation distance between two plasmas is 2 mm.....	143
Fig. 6.13. Separation distance between two plasmas vs acoustic shock wave peak pressure. The slope is positive. The slopes are different for different distances. For the separation distances of 1 to 5 mm, 6 to11 mm and 12 to 15mm the slopes (m) are 0.16, 0.33, and 0.1 respectively. In set shows that the shadowgraphic image of interaction of counter propagating two shock waves at 2, 5, 10, 12 mm separation distances. Images are presented here are taken at 30 $\mu$ sec time from the plasma initiation.....	144
Fig. 6.14. Separation distance vs arrival time and velocity of ASWs, from the dual plasma, for the beam splitter of 40:60 (1:1.5). Three linear fits for arrival times, with slopes of 0.33, 0.002 (saturation), 0.2 for 1-4mm, 4-7mm, 7-15mm respectively. Here the total laser energy is 65 mJ and divided into 24 and 41 mJ. ASW velocity is decreasing with separation distance.....	145
Fig. 6.15. The acoustic spectra for ASWs emitted from single plasma and dual plasma. The peak frequencies are 52, 40, 34 kHz for S1, S2, S1+2 respectively.....	146
Fig. 6.16. Separation distance vs peak pressures for the interaction of plasma sources with 1:4 impedances. Individual laser energies of 24.5, 101.7 mJ forms the two plasmas of S1, S2.....	148
Fig. 6.17. Separation distance vs arrival time and velocity of ASW emitted from dual plasma for the 20:80 (1:4) beam splitter. Rise in arrival time linear fit shows the two slopes of 0.19, 0.48. Linear fit to the velocity shows the two slopes of -0.32, -0.78. Slopes are indicated with letter 'm'.....	149
Fig. 6.18. Spectra for the ASWs, emitted from single and dual plasma. The separation between the sources is 2 mm. The peak frequencies of spectra are 48, 24, 24 kHz for S1, S2, S1+2 respectively.....	149

## List of tables

Table 2 1. Technical specifications of lasers we have used.....	13
Table 2 2. ASW pressures with errors for various laser energies of ns LIB of air at 80mm focal length of lens.....	21
Table 2 3. Relation between time scale, number of data points, sampling rate and frequency scales.....	26
Table 3 1. The ASW parameters from ns-LIB of atmospheric air at different input laser energies.....	34
Table 3 2. ASW parameters from ps-LIB of air at various laser energies.....	39
Table 3 3. Theoretically estimated spot size, intensity and number of air molecules in focal volume for different focusing conditions.....	41
Table 3 4. Ns LIB generated ASWs parameters at a fixed laser energy of 25 mJ, for various focal geometries.....	44
Table 3 5. Ps LIB generated ASW parameters at 25 mJ of incident laser energy.....	45
Table 3 6. Residual energy of ps laser pulses after focal point at different laser energies at a given ps input laser pulse energies.....	46
Table 4 1. Physical properties of materials from literature.....	56
Table 4 2. ASW parameters of Al, Cu, Brass and SS316LN samples at a fixed energy of 20mJ.....	64
Table 4 3. Area under the -ve and +ve portions of ASW signal for both Brass and SS at various laser energies.....	65
Table 4 4. ASW parameters from LIB of dielectrics at 25 mJ of laser energy.....	68
Table 4 5. ASW parameters from LIB of insulators at 10 mJ of laser energy.....	69
Table 4 6. ASW parameters from ns- LIB of insulators at 25 mJ of laser energy.....	69
Table 4 7. ASW parameters from LIB of insulators at 100 mJ of laser energy.....	70
Table 4 8. Pressure and temperature used to prepare the compacts.....	73
Table 4 9. At 10, 25 mJ laser energies, the ratio of +ve peak width and -ve peak height for the packing densities of 60, 70, 80%.....	76
Table 4 10. +ve peak lengths of ASWs emitted from ns-LIB of Brass, Teflon, Mica and PVC samples at 10 and 40 mJ of laser energies are presented in this table.....	77
Table 4 11. At 25 mJ laser energy, the Lorentz fitted central frequency, spectral width and their ratios for all the samples.....	81
Table 4 12. ASW parameters of Al, Cu, Brass and SS316LN samples at a fixed energy of 30 mJ.....	89
Table 4 13. ASW parameters from LIB of dielectrics at 12 mJ of laser energy.....	91

Table 4 14. ASW parameters of ps LIB of Alumina at 6, 12 mJ of laser energies.....	92
Table 4 15. Area under -ve and +ve portions of PVC and Teflon samples, at various laser energies.....	92
Table 4 16. +ve peak lengths of ASWs emitted from ps-LIB of Al, SS, PVC and Glass samples at 6 and 18 mJ of laser energies are presented in this table.....	95
Table 4 17. The Lorentz fitted central frequency, FWHM and its ratios for all the samples for ps LIB of various samples at 24 mJ laser energy.....	98
Table 4 18. At 12 mJ laser energy, the Lorentz fitted central frequency, peak width and its ratios for all the samples for ps LIB of various samples.....	99
Table 5 1. Molecular formula, structures and number of Nitro groups of the HEMs used.....	110
Table 5 2. Density, Melting point, Boiling point, number of nitrogen, oxygens etc., properties of samples are given here.....	113
Table 5 3. ASW parameters of ns-LIB of Air, DNT, TNT, AN and NTO at 25 mJ laser energy, microphone distance is 8 cm from the plasma.....	114
Table 5 4. Measurements of ASWs which are emitted from the ns LIB of air, nitrogen and argon gases at 32 mJ of laser energy. Here plasma to microphone distance is 9 cm. Here the target is gas itself. Density and thermal conductivities of Ar, N <sub>2</sub> and Air.....	117
Table 5 5. Structure, molecular formula, and number of Nitro groups of TNT, RDX, CL-20 and Sodium Azide.....	122
Table 5 6. ASW parameters of ps-LIB of RDX, CL-20, TNT and Sodium Azide at 6 and 12 mJ of laser energy.....	123
Table 6 1. Arrival times information of single and dual plasma at 2 and 22 mm separation distances. Here the total energy is 100 mJ.....	134
Table 6 2. The ASW parameters of independent S1, S2 sources and S1+2 with a separation of 2 mm. The laser energies supplied to two sources is 50 mJ and 100 mJ respectively..	139
Table 6 3. The ASW parameters of independent S1, S2 sources and S1+2 with a separation of 2 mm. The laser energies supplied are 24 and 41 mJ respectively.....	143
Table 6 4. Lorentz fitted frequency peaks parameters for the ASWs generated from the dual plasma which are distributed in the ratio of S1:S2 = 1: 1.5.....	146
Table 6 5. The ASW parameters of independent S1, S2 sources and S1+2 (dual plasma present) with a separation of 2 mm. The laser energies supplied to S1 and S2 are 24.5±2.1 and 101.7±1.5 mJ respectively. The microphone is kept at a distance of 80 mm.....	147
Table 6 6. Lorentz fitted frequency peaks parameters for the ASWs generated from the ration of S1: S2 = 1: 4.....	150

# CHAPTER 1 : Introduction

---

## Abstract:

This chapter elaborates on the different processes involved in the laser matter interaction with a focus on laser produced plasmas. As plasma constitutes highly ionised matter, optical, thermal and mechanical radiations are emitted. The work in this thesis studies the mechanisms involved in producing mechanical radiation such as acoustic emissions from the plasma. There are several methods to understand the laser produced acoustic emissions. Laser induced breakdown and explosive vaporization are two important methods which are emphasized. This study of laser induced acoustic shockwaves can be used as a scaled lab surrogate for understanding blast waves from explosives in the field.

## 1.1 Laser induced breakdown of matter with short laser pulses

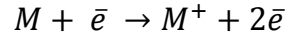
When a high intensity laser pulse interacts with matter, the steps leading up to the formation of an acoustic shockwave are: absorption, heating and ionisation followed by plasma production [1]. Plasma, is a state of matter constituted by electrons, neutrals, and ionized species like atomic and molecular clusters. A brief outlined view is given in fig. 1.1. The detailed explanation about the phenomena involved in these process is given below. Generally plasmas are produced in the lab using two techniques, gas discharge and photo ionisation [1]. This work focusses on plasma generated by photo ionisation. Matter can be ionized by using a focused laser pulse by two different processes, [2-4] cascading electron breakdown and multiphoton ionization.

### 1.1.1 Cascade breakdown

Cascade breakdown happens when two necessary conditions are fulfilled:

1. There are initial electrons in the focal volume.
2. The electrons acquire an energy greater than the ionisation energy of the material (band gap).

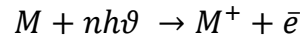
Electrons gain kinetic energy by absorption of laser radiation (inverse bremsstrahlung). These energetic electrons collide with neutrals leading to their ionization. If the acquired energy by an electron is higher than the ionization potential, then the electron may ionize an atom by impact. As an end result of this collision we are left with two extra free electrons, which starts the process again leading to the cascade effect.



This above reaction will lead to cascade breakdown, electron concentration will increase exponentially with time.

### 1.1.2 Multiphoton absorption

Absorption of laser radiation by an atom or molecule causes its ionization [3] (ejection of an electron from the valence band).



Where M is the neutral atom, n is the number of photons,  $\bar{e}$  is the free electron.  $I_0$  is the ionization potential of atom. When the number of incident photons (n) absorbed exceeds as an integer part of  $(\frac{I_0}{h\nu} + 1)$  to cause ionization, it is called multi photon ionization. This process is self-sufficient.

The probability ( $\omega$ ) of an atom absorbing n photons is proportional to the n<sup>th</sup> power of incident laser flux density.

$$\omega \propto F^n$$

At sufficient laser intensities, the electrons at the focus excite the atoms, then rapid ionization takes place by absorbing few photons.

## 1.2 Radiations from LIB of medium

When an intense, short-pulsed laser is focused in a medium, due to the associated high electric field, the medium ionizes, [5] resulting in the production of free electrons, which further gain energy from the incident laser electric field and lead to further ionization resulting in an avalanche breakdown of the medium. This catastrophic ionization raises the temperature of the medium to a few thousand degrees, within short time scales of few hundred picoseconds to several nanoseconds. This plasma appears as a spark. This process [6] is depicted in fig. 2.

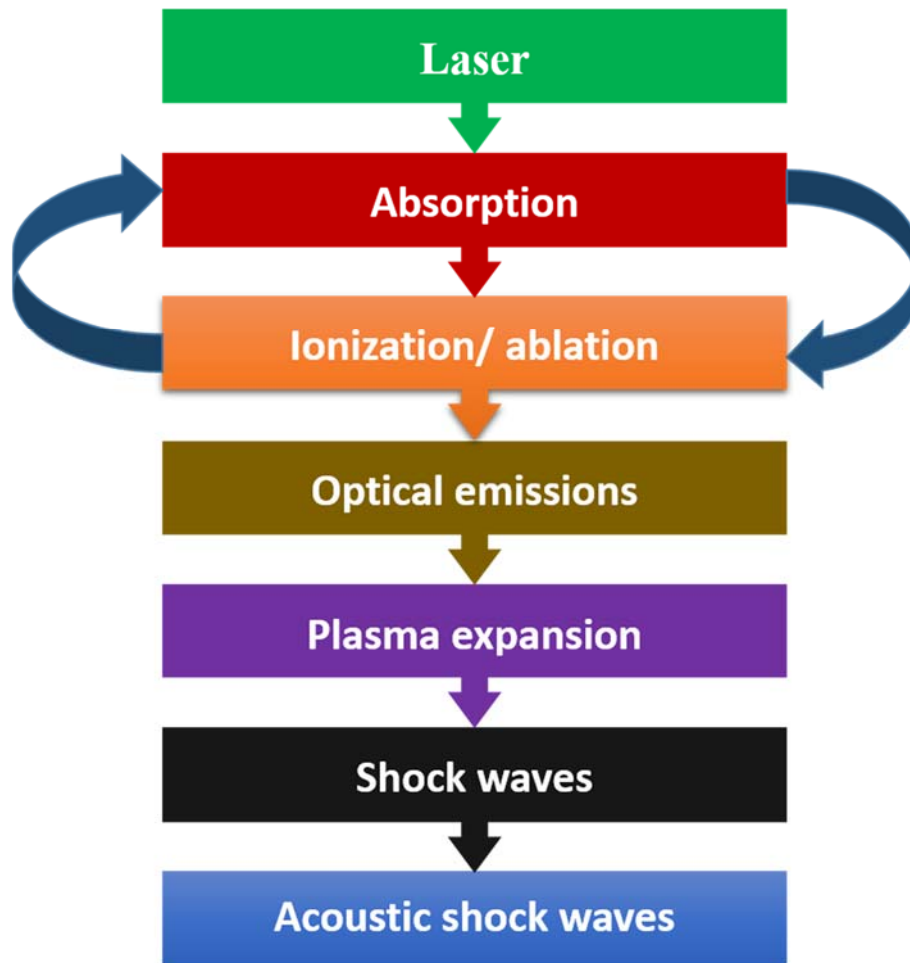


**Fig. 1.1.** Steps involved in laser matter interaction to generate Acoustic Shock Waves.

The ionized material while regaining an equilibrium state, emits the energy in various forms, like: emission in the UV-Visible frequencies, microwave radiation, RF radiation [7, 8] and acoustic radiation (mechanical waves) [9-12]. Plasma itself is a source of hard and soft X-rays dependent on the incident laser energy. Within the plasma, the interaction of charged particles with neutral atoms and molecules will be dominant. These charge-neutral interactions give rise to emissions in the RF [8] and microwave range of frequencies. Therefore, the RF emissions take place as long as there is interaction between the charged particles and the neutrals in the system. Ion-acoustic instabilities in LIB lead to RF and microwave emissions [13] and the UV-Visible emissions are due to the recombination of the ionized species.

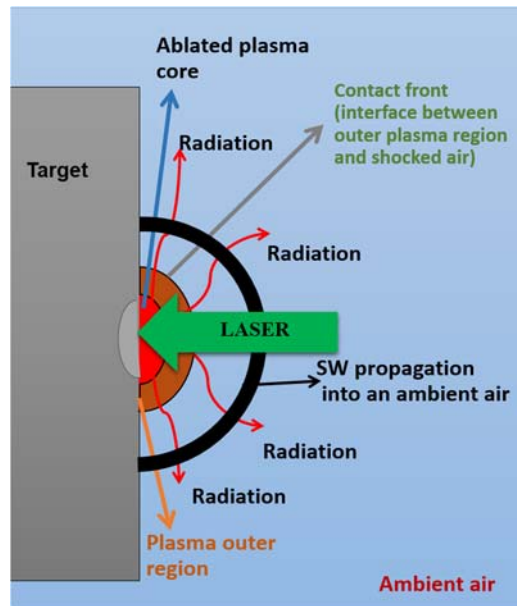


**Fig. 1.2.** process of generation of shock waves from the laser produced plasma [6].

The plasma formation results in gradients of density, pressure and temperature with respect to the surrounding atmosphere. These gradients causes the sudden release of energy into surrounding atmosphere as a shock wave [14, 15], as shown in fig. 2. This shock wave has a high pressure front which travels with supersonic velocity initially and then decays with propagation distance. The shock wave propagates into the material as well as into the surrounding atmosphere. These SWs decay into acoustic shock waves as it propagates into the surrounding atmosphere. These waves are very closely resemble Blast waves or detonation waves [16]. Here our consideration is the ASWs in atmosphere not inside of the target sample.

### 1.3 Origin of Laser generated acoustics emissions

There are five important interaction mechanisms [17] which can be the origin for the production of acoustic wave emissions: dielectric breakdown, explosive vaporization or material ablation, thermo-elastic process, electrostriction, and the radiation pressure. These phenomena are function of incident laser parameters such as pulse width, intensity and optical and thermal parameters of the medium. Each of this process is elaborated below.

#### 1. The dielectric breakdown

It only occurs at laser intensities above  $\sim 10^{10}$  W cm<sup>-2</sup>, which can quite easily be obtained at focal plane of a pulsed laser. This effect has been investigated

experimentally and theoretically in detail for gases, liquids, and solids. The plasma production related to the dielectric breakdown produces a shock wave which propagates initially at supersonic speed in the medium [2]. The dielectric breakdown dominates the longer laser pulse – material interaction.

## 2. Explosive vaporization

This will happen at laser energy densities higher than the breakdown threshold. In the case of liquids or material ablation on solids, it is responsible for the acoustic wave generation, if the laser energy density (within the absorbing volume) exceeds the breakdown threshold of sample. The material ablation on solids is associated with plasma formation. The ejection of material from the surface involves a recoil momentum which propagates into the bulk sample as an acoustic transient. Laser ablation is a process of material removal [18]. The laser pulse, will rapidly break the chemical bonds for photochemical ablation or evaporate the material for photothermal ablation in a small confined illuminated volume. This will lead to a rapid rise in the local particle number density, which results in a rapid rise in the pressure on the materials surface. The high pressure is released as a shock wave [19, 20] and ejects material at high speeds from the irradiated zone. This process usually accompanies plasma generation. The shock wave emitted into the air will decay into acoustic waves by air friction. The acoustic waves generated by laser ablation are both in the sonic and ultrasonic frequency regions.

The temporal shape of the acoustic signal is due to the rapid thermal expansion of a thin layer of air (thermal piston signal) adjacent to the irradiated spot [19]. As fluence is increased above a threshold, shock waves are generated due to material ejection from the sample surface. Since the initial shock waves travel faster than the thermal piston signal, the early part of the ablative piston signal arrives at the detector (Pinducer) earlier than the thermal piston signal.

## 3. Thermo-elastic process

The process is mainly dependent on the laser absorption by the medium and is based on the transient heating of a restricted volume by the absorbed laser energy. The induced temperature gradient produces, as a result of thermal expansion, a strain in the material. This causes an acoustic wave which propagates away from the heated zone.

The thermo-elastic process, i.e., heating without phase change, dominates the excitation of sound in absorbing matter at laser energies below the vaporization threshold. Although the conversion efficiency is rather low, typically  $< 10^{-4}$  for liquids, this process has found interesting applications in opto- or photoacoustic spectroscopy as a sensitive method for the measurement of small absorptions in solids, liquids, and gases. These thermal-acoustic waves are broadband and weaker than ablation mechanism [18].

#### 4. **Electrostriction**

It is due to the electric polarizability of molecules within the sample which causes them to move into or out of regions of higher light intensity depending on positive or negative polarizability. These motions produce a density gradient and, consequently, a sound wave similar to that caused by the thermo-elastic process is generated. Electrostriction as a sound generation mechanism is only important in very weakly absorbing media where it may limit the photoacoustic detection sensitivity. So, for strongly absorbing materials this mechanism is not applicable (for metals, semiconductors, insulators, their absorption of excimer laser (248 nm) is normally strong). However, it has been demonstrated theoretically and experimentally that by using suitable time-gated detection of the acoustic signal, strong suppression of the electrostrictive component is possible.

#### 5. **Radiation pressure**

It is negligible when compared with the other sound generating mechanisms. For the case of total absorption of the laser radiation at the sample surface, the amplitude of the radiation pressure is given by  $P_{\text{rad}} = I/c$ , where  $I$  is the laser intensity and  $c$  the light velocity in vacuum. For a laser intensity of  $10^6 \text{ Wcm}^{-2}$  one obtains  $P_{\text{rad}} = 0.3 \text{ mbar}$  compared, to a few bars in the case of thermo-elastic sound generation under identical conditions. Since, the pulse duration of the laser is very short, the pressure induced on the surface makes the surface vibrate and generate acoustic waves. However, the acoustic waves generated are very weak and is in the range of ultrasonic frequencies (within the target) that can be detected by a piezoelectric sensor.

Three further mechanisms have been omitted in this list since they play a role only under specific circumstances. These are (a) photochemical effects where, e.g., molecules AB are formed from the initial species A and B under the action of laser radiation ( $A + B = AB$ ); (b) molecular dissociation where the opposite takes place (i.e.,  $AB = A + B$ ); and (c) bubble formation.

The energies we have used to study the laser matter interaction are above the breakdown thresholds of target materials so, our main focus is on dielectric breakdown and explosive vaporization. Remaining processes such as photo chemical effects, molecular dissociation and bubble formation are not so dominant at the laser energies, pulse durations used in our studies, hence not mentioned in detail.

### **Applications**

The acoustic detection of laser matter interaction is used in many research areas, such as to find ablation efficiency, amount of material ablated, chemical decomposition, stand-off detection of chemicals, plasma studies, underground land mine detection, measuring the resonant frequencies of metal tubes, laser shock peening efficiency, etc.

## **1.4 Organization of thesis**

### **1.4.1 Chapter 2: Experimental details**

In this chapter, we discuss the technical details of the lasers, acoustic detectors and the data acquisition system (oscilloscope) used in Laser Induced Breakdown (LIB) experiment. The working principle and the calibration of the microphone used for the detection of pressure wave is presented. Effect of sampling rate and the bandwidth of the oscilloscope on ASW measurements is presented. The difference in acoustic signals (transient) generated by mechanical excitation of metal plates (with a metal object) and that generated by LIB is presented in both temporal and spectral domain. The experimental schematic used for LIB of gases (chapter# 3) and solid targets (chapter#5) as well as the spatial acoustic scan of a laser plasma due to interaction of counter propagating laser beams (chapter#6) are presented. Measurements of ASW signal done in time and frequency domain as well as the reproducibility of ASWs at various laser energies under similar conditions is presented.

### **1.4.2 Chapter 3: ASW emissions from ns and ps-LIB of atmospheric air: propagation of ASWs in surrounding atmosphere**

Evolution of Acoustic shock waves (ASW) and their properties in the frequency range of 30-120 kHz generated during Laser Induced Breakdown (LIB) of ambient atmospheric air, using of 7ns and 30ps pulse duration are presented. The specific frequency range and peak amplitude are observed to be different for ns- and ps- LIB. The ASW frequencies for ps-LIB lies between 90 to 120 kHz with one dominant peak whereas for ns-LIB, two dominant peaks with frequencies in the 30-70 kHz and 80-120 kHz range are observed. The radial and angular distribution of ASW is presented. These frequencies are observed to be laser pulse intensity dependent. With increasing energy of ns laser pulses, acoustic frequencies move towards the audible frequency range. The variation in the acoustic parameters: Peak-to-peak pressures, signal energy, frequency and acoustic pulse widths as a function of laser energy for two different pulse durations is presented and compared. The acoustic emissions are observed to be high for ns-LIB than the ps-LIB, indicating higher conversion efficiency of optical energy into mechanical energy.

Dependence of ASW on laser intensity is studied. The intensity is varied by changing focal geometry of ns and ps pulses. The ASW pressures are observed to follow the dynamic interplay between the plasma density and recombination of plasma species. The conversion of laser energy to acoustic energy increases from loose to tight focusing conditions. The central frequencies have moved towards the lower side with increasing laser intensities for both ns-LIB (76 to 48 kHz) and ps-LIB (111.2 to 92.1 kHz). The angular distribution of acoustic emissions were observed to follow the laser induced plasma spark in both ns- and ps-LIB.

### **1.4.3 Chapter 4: ASW emissions from LIB of various materials**

In this chapter, laser pulses of both ns and ps are focused on target materials of metals, dielectrics, insulators and compacted copper micro powders to generate LIB. Under various experimental conditions we have presented the time domain and frequency domain analysis of the acoustic signals. The evolution of ASW parameters as a function of laser energy is presented for each material. The ASW response of one material changed at with respect to incident laser energy. The resulting ASW pressures are proportional to the crater dimensions. The ASW signal is divided into two parts and studied well to understand the laser-matter interaction.

We have tried to establish a relation between ASW strength and density fluctuations caused by ionized species in surrounding atmosphere. Comparisons made between the fresh spot area of sample interaction (each laser pulse falls on virgin area of sample) and shot on shot method (selective number of laser shots are incident on same spot area). Lorentz fitted frequency peaks are plotted for various samples.

#### **1.4.4 Chapter 5: ASWs from high energy materials (HEMs)**

The properties of ASWs from the ns-LIB of High energy materials are presented in this chapter. ns-LIB of the Ammonium Nitrate (AN), Di Nitro Toluene (DNT), Tri Nitro Toluene (TNT), 3-Nitro-1,2,4-triazol-5-one (NTO) samples and ambient Air studied at two laser energies of 25, 40 mJ. ASW reproducibility is presented in both time and frequency domain. Huge peak to peak pressure difference between target samples and the air breakdown is observed. Spectral peak frequencies of DNT have highest amplitude than the remaining samples at 25 mJ of laser energy. Acoustic parameters from the breakdown in air, nitrogen (N<sub>2</sub>) and argon (Ar) as ambient gases were performed. The increment in ASW parameters are observed from the ns LIB in Argon gas ambient than N<sub>2</sub> and air. ASWs from ns-LIB of 4 – Nitro imidazole, Bismuth nitrate (Bi(NO<sub>3</sub>)<sub>2</sub>) and Lead nitrate (Pb(NO<sub>3</sub>)<sub>2</sub>), in the presence of air and Ar background gasses were presented. By changing the background ambient gas, we can control the associated ASW properties. ps-LIB of RDX, CL-20, TNT and NaN<sub>3</sub> are also presented at two different laser energies. Variation in acoustic parameters are presented at a fixed laser energy, it indicated the effect of sample properties on ASW emissions. The peak frequencies are well separated from one sample to another sample.

#### **1.4.5 Chapter 6: ASW emissions from interaction zone of two counter propagating laser generated shock waves in air**

The acoustic emissions due to interaction of two counter propagating laser induced ablative shock waves is presented in this chapter. These two laser plasma induced shock waves were formed by two counter propagating ns laser beams derived from a common laser source. The laser energies of two incident laser beams were varied with respect to each other. The distance between two plasma sources is changed by moving the focusing lenses towards and away from each other. The acoustic features at various separation distances between the two plasma sources were presented. The interaction between two shock sources (plasmas) is observed to effect the peak-to-peak pressure of resulting acoustic shock wave. The characteristics of

interacting shock waves studied through the acoustic diagnostics are observed to give an insight into distribution of plasma into surrounding atmosphere.

### 1.4.6 Chapter 7: Conclusions and future scope

The summary of all the chapters and future scope of this work is presented in this chapter.

## 1.5 References:

1. J. A. Bittencourt, *Fundamentals of Plasma Physics* (Springer New York, 2004).
2. C. DeMichelis, "Laser induced gas breakdown: A bibliographical review," *Quantum Electronics, IEEE Journal of* **5**, 188-202 (1969).
3. C. G. Morgan, "Some aspects of laser-produced plasmas," *Plasma Physics and Controlled Fusion* **26**, 1367 (1984).
4. L. Evans and C. Morgan, "Lens Aberration Effects in Optical-Frequency Breakdown of Gases," *Physical Review Letters* **22**, 1099-1102 (1969).
5. P. Mulser, R. Sigel, and S. Witkowski, "*Plasma production by laser*," *Physics Reports* **6**, 187-239 (1973).
6. S. S. shiva, "Numerical Investigations of ns Laser Induced Shock Waves from Aluminum and Air," (University of Hyderabad, Hyderabad, india, 2016).
7. J. S. Pearlman and G. H. Dahlbacka, "Emission of rf radiation from laser-produced plasmas," *Journal of Applied Physics* **49**, 457-459 (1978).
8. L. Vinoth Kumar, E. Manikanta, C. Leela, and P. Prem Kiran, "Spectral selective radio frequency emissions from laser induced breakdown of target materials," *Applied Physics Letters* **105**, 064102 (2014).
9. Q. Qin and K. Attenborough, "Characteristics and application of laser-generated acoustic shock waves in air," *Applied Acoustics* **65**, 325-340 (2004).
10. J. P. Chen, X. W. Ni, J. Lu, and B. M. Bian, "Initial formation process of laser-induced plasma shock wave in air," *Optics Communications* **176**, 437-440 (2000).
11. S. Conesa, S. Palanco, and J. J. Laserna, "Acoustic and optical emission during laser-induced plasma formation," *Spectrochimica Acta Part B: Atomic Spectroscopy* **59**, 1395-1401 (2004).
12. J. Diaci and J. Možina, "On-line Optodynamic Monitoring of Laser Materials Processing," (1996).
13. G. Gerdin, M. J. Tanis, and F. Venneri, "Observation of microwave emission from a plasma focus at frequencies well below the mean plasma frequency," *Plasma Physics and Controlled Fusion* **28**, 527 (1986).
14. Y. R. Shen, *The Principles of Nonlinear Optics* (Wiley, 1984).
15. Y. B. Zel'dovich and Y. P. Raizer, *Physics of Shock Waves and High-Temperature Hydrodynamic Phenomena* (Dover Publications, 2002).
16. L. J. C. Radziemski, D. A. , *Laser-induced plasmas and applications* (Marcel Dekker Inc, Marcel Dekker Inc, 1989).
17. M. W. Sigrist, "Laser generation of acoustic waves in liquids and gases," *Journal of Applied Physics* **60**, R83 (1986).
18. Y. F. Lu, M. H. Hong, S. J. Chua, B. S. Teo, and T. S. Low, "Audible acoustic wave emission in excimer laser interaction with materials," *Journal of Applied Physics* **79**, 2186-2186 (1996).

19. W. P. Leung and A. C. Tam, "Noncontact monitoring of laser ablation using a miniature piezoelectric probe to detect photoacoustic pulses in air," *Applied Physics Letters* **60**, 23-25 (1992).
20. G. Koren, "Observation of shock waves and cooling waves in the laser ablation of Kapton films in air," *Applied Physics Letters* **51**, 569-571 (1987).

This page is intentionally left blank

## CHAPTER 2 : Experimental details

### Abstract:

In this chapter, we have discussed all the technical details of lasers, acoustic detectors and data acquisition system (oscilloscope). Working principles of microphone for the detection of pressure waves has discussed. Calibration of microphone is also presented. Effect of sampling rate (time scales) and bandwidth of oscilloscope on ASW measurements is presented. Manual (hand) hitting of metal plates with align key produces acoustic transients, these were presented in both temporal and spectrally. Experimental schematics for LIB of gases, material targets presented and acoustic scan of plasma and interaction counter propagating of two shock waves were presented. Measurements on ASW signal is done in time and frequency domain. Reproducibility of ASWs at various incident laser energies under similar focusing conditions is observed.

### 2.1 Technical details and specifications of nano second and pico second lasers

Here we explained the experimental details for all the experiments carried out in the thesis. Two different lasers were used to generate two different pulse widths of 7 ns (INNOLAS, Spitlight-1200) and 30 ps (EKSPLA, PL 2351 series, PLD084).

**Table 2-1.** Technical specifications of lasers used.

	Nano second (ns)	Pico second (ps)
<b>Pulse width</b>	7 ns	30 ps
<b>Wave length</b>	1064, 532 nm	1064, 532 nm
<b>Repetition rate</b>	Max 10 Hz	Max 10 Hz
<b>Model number</b>	INNOLAS, Spitlight-1200	EKSPLA, PL 2351 series, PLD0841

The laser energy is varied between 10-100 mJ per pulse in the ns regime while, in the ps regime it is varied between 3-30 mJ. Experiments were performed in lab at ambient atmospheric conditions ( $T \approx 300$  K,  $P \approx 1$  atm). Breakdown of air, Argon and Nitrogen gases are studied. Few explosive target samples were exposed to ns laser pulses in the presence of ambient Air, Argon and Nitrogen environment.

## 2.2 Micro phone specifications and working principle:

The sensing system that was used for the measurement of ASWs consisted of a calibrated microphone which has a frequency response over 20 Hz to 140 kHz (GRAS 40DP, sensitivity of 1mV/Pa) and a dynamic range of 174 dB (re 20  $\mu$ Pa). Microphone is directly connected to pre amplifier, which amplifies the signal (indirectly it is an impedance converter) then it (microphone along with preamplifier) is connected to power supply (G.R.A.S, 12AR) input through a cable. The output from the power supply directly connect to the oscilloscope, the setup of microphone connections, shown in fig. 2.1.

The pressure difference between plasma and surrounding atmosphere will vibrate the diaphragm of microphone, producing corresponding analog electric signal consisting of positive and negative half periods with different amplitudes. The difference between these two amplitudes is peak-to-peak pressure of the ASW. The type of microphone we have used here is condenser microphone and it is an Omni directional, it takes signals from all directions. Its working principle is same as capacitor, its capacitance changes as the separation distance between two parallel plate's changes, shown in equation (i).

$$C = \frac{\epsilon_0 A}{d} \text{ ————— (i)}$$

$$V = \frac{Q}{C} \text{ ————— (ii)}$$

In microphone there is a diaphragm (thin membrane) and back plate, these two are like a two parallel plates. The applied sound pressure will vibrate (compressions and rarefactions) the diaphragm, so change in separation distance ( $d$ ) occurs. It results change in capacitance. Change in capacitance produces voltage fluctuations (equation (ii)), these voltage fluctuations are nothing but electrical analogue signals for acoustic signals [1, 2].



**Fig. 2.1.** Microphone setup (a), exploded view of mic, pre amplifier, connector (b), and power supply (c).

A Pocket-sized, battery operated calibrator (MODEL: G.R.A.S 42 AB) has used to calibrate the microphone. It produces a constant nominal sound pressure level of 114 dB re. 20  $\mu$ Pa (equivalent to 10 Pa) at 1 kHz. Calibration graph is shown in fig. 2.2.

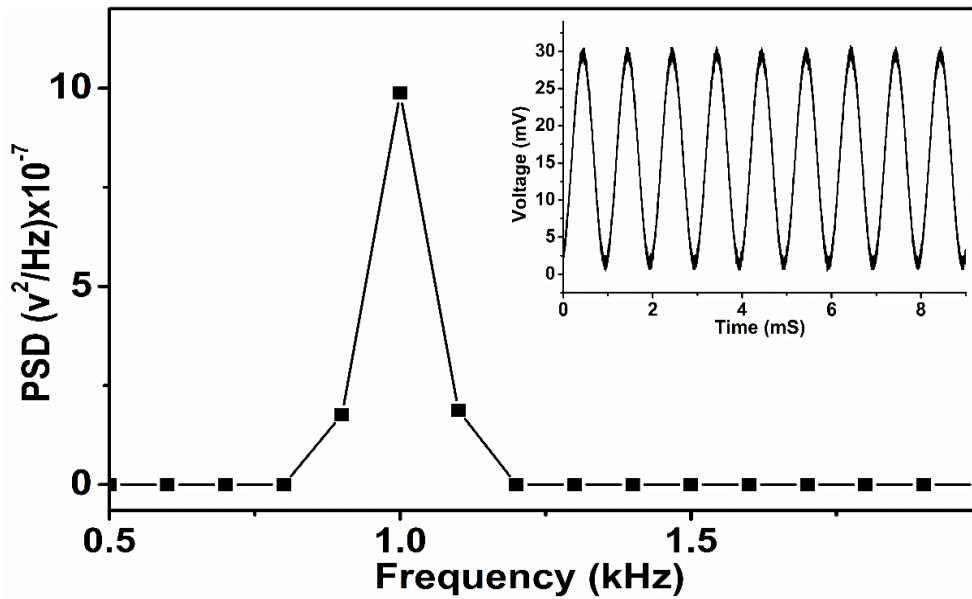


**Fig. 2.2.** Calibration spectrum of 1/8" microphone. Inset shows the time domain representation of 1 kHz sound signal. X- Axis is frequency in kHz and Y-axis is power spectral density (PSD).

Before initiate experiment calibration of microphone is necessary. The single frequency of sound signal captured by microphone. Fast Fourier Transform (FFT) of this sound signal gives frequency in spectrum. The calibrator generated signal has only one peak frequency of 1 kHz. The response of microphone, as the microphone distance varies is presented in fig. 2.3.

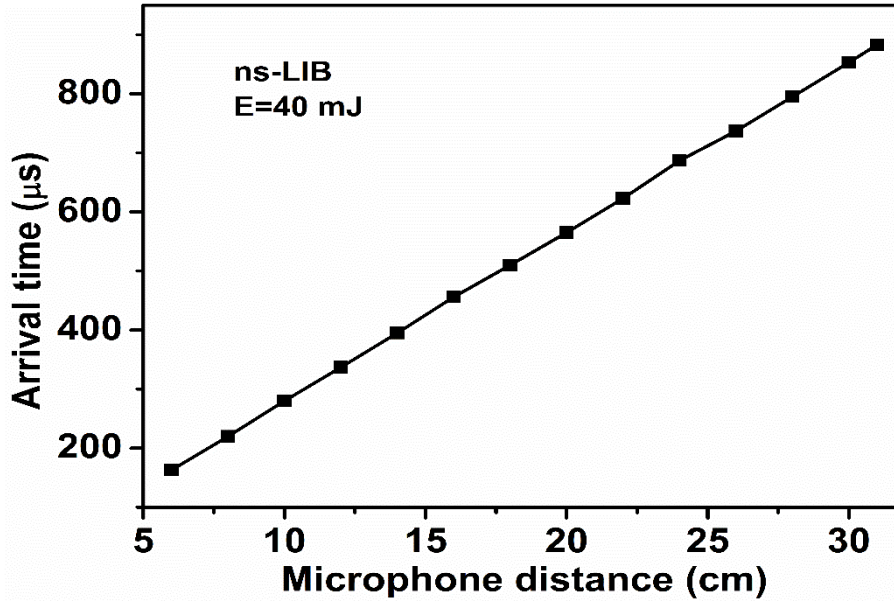


**Fig. 2.3.** Arrival times of ASWs at various distances of microphone from plasma, at 40 mJ of energy for ns laser pulses.

The linear variation of arrival time of ASW with microphone distance confirms the linear response of the detector.

### 2.3 Experimental schematics:

The laser pulses were focused through the Plano convex lens (converging lens) into the air, the breakdown takes place at focal point. The diverged light from the focal point (plasma) will be blocked by the beam dump, shown in figure 2.4. A small part of the incident laser beam is fed back to the oscilloscope (YOKAGAWA DL 9240) through a photo diode. Acoustic measurements were triggered by the photo diode signal. A beam dump is placed in the line of incident laser direction to stop the further scattering of the diverged laser beam. The output of the microphone is connected to the oscilloscope. Signal monitoring and data acquisition was done with the oscilloscope, shown in fig. 2.4. Our aim is to reach the real fields, so no closed container (cells) and anechoic chamber has been used. This is the major difference between photo acoustics and this work. We focused laser pulses in air or in gas medium to obtain breakdown and did a basic analysis. We extended this work to material samples. Targets were mounted with a holder and it is placed on a three-dimensional electronic translational stage (ESP CONTROLLER), which moves the target holder from one point (area) to the next point (area) with a few micrometers span.

The target is kept at a focal point for breakdown, as shown in fig. 2.4. The microphone is normal to the incident laser direction for gaseous breakdown, whereas for target samples the emitted shock

waves are hemi spherical so, microphone is positioned in angled with respect to plasma and incident laser direction, shown clearly in fig. 2.4.

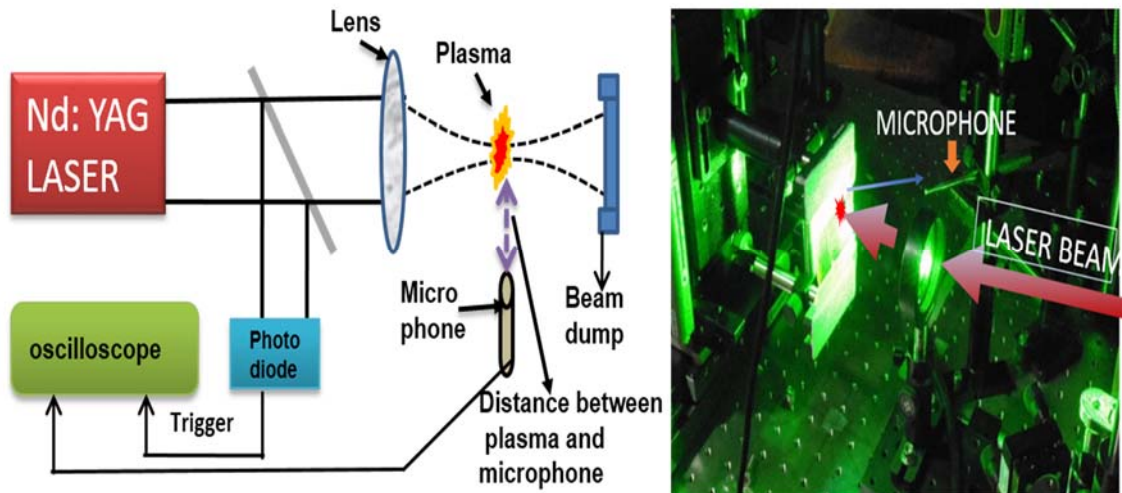


**Fig. 2.4.** Experimental schematic for the detection of ASW measurements from the ns- and ps-LIB of air. Two different lasers were used for two different pulse widths of 7 ns and 30 ps. The microphone is positioned at a distance of 8 cm from the plasma (it can be variable). Target holder is fixed to motion controller to expose laser radiation.

### 2.3.1 Breakdown of target samples in the presence of various gases and in ambient air:

To study the ASWs from LIB breakdown of various gases, simply punch the gases at focal point by using a tube which is connected to gas cylinder, as shown in figure 2.5. The density of argon (Ar) is higher than the nitrogen (N<sub>2</sub>) and air. Change in acoustic parameters were observed for nitrogen, argon and ambient air environments. The results are clearly presented in chapter 5.

Sample is (no gas chamber has used) mounted to target holder, then the gas is allowed towards the focal point. It means that, focal point is surrounded by gas and sample breakdown happen in the presence of applied gas only. The air above the sample was pushed by pressurised Ar and it allows breakdown of sample only. Here no ambient air breakdown takes place at the sample breakdown point. This schematic is used generally in laser induced breakdown studies (LIBS) study for elemental analysis. Microphone is adjusted in angle w.r.t target sample and laser direction, shown in fig 2.5.

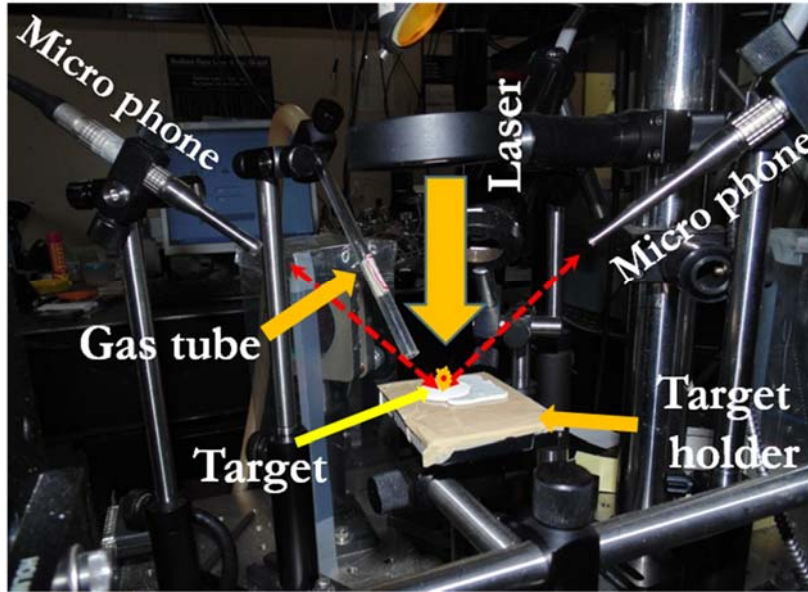


**Fig. 2.5.** LIB of target samples in the presence of Argon and Nitrogen gaseous environment. Samples are mounted on target holders. Gas tube is included in set up.

### 2.3.2 Analysis of ASWs in Time domain:

The ASW pressures generated from the LIB of medium are dynamic. The atmospheric pressure is a static pressure ( $10^5$  Pa) and consider it as a zero in ASW measurement. When there is no acoustic source, the signal is flat and adjusted to zero of Y-axis, it is an atmospheric pressure. In fig. 2.6, the X-axis and Y-axis indicates the time and voltage of a signal respectively. The pressures of ASWs were calculated by using sensitivity of microphone and the corresponding peak to peak voltage value of particular signal. So, Y-axis indicates the pressure. Along with main (impulse in nature) acoustic signal, there will be presence of reflected components from surrounding objects around the plasma, shown in fig. 2.6.

Here we consider only first peak, remaining peaks are neglected because these are reflected components [3]. In time domain analysis peak-to-peak pressure ( $P_k$ ), arrival time ( $A_t$ ), acoustic pulse width ( $W_t$ ), decay time ( $D_t$ ) and signal energy ( $E_s$ ) are important parameters which give details about source (plasma) and its associate effects. The ASW measurements are pictorially explained clearly indicated in fig. 2.6 (b). Photo diode signal is represented by  $t=0$ , this is the point where data acquisition begins.

The arrival time ( $A_t$ ) of ASW is the time taken by the wave to reach the detector from plasma. The decay time ( $D_t$ ) shows the rate at which ASW peak pressure reaches the ambient pressure. Acoustic pulse width ( $W_t$ ) indicates the existence time of ASW from the plasma.

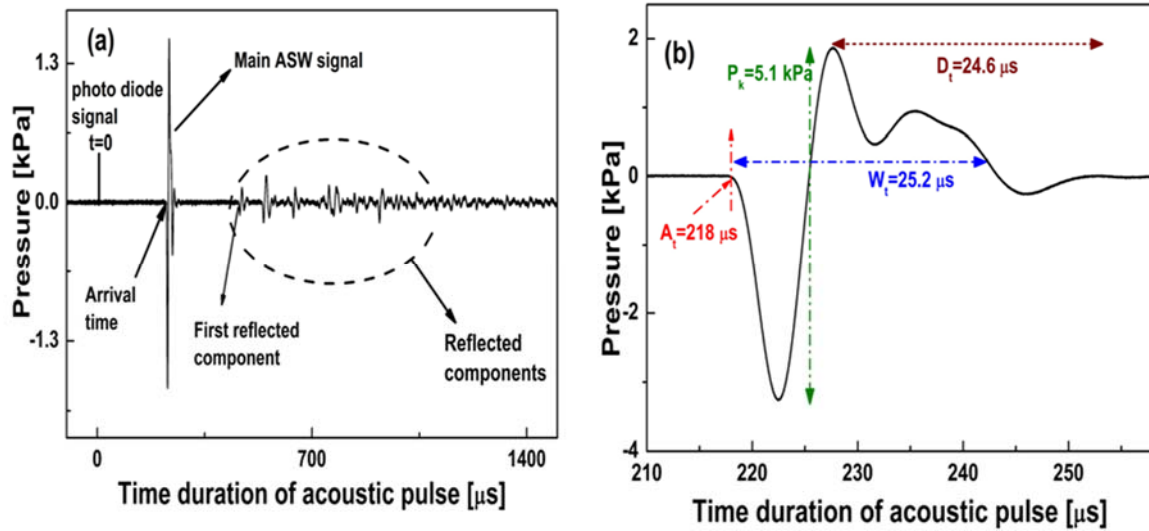


**Fig. 2.6.** Entire time domain ASW signal from the ns-LIB of air at a microphone distance of 8 cm. (a) Reflected components from objects around the plasma are presented along with the main acoustic pulse, where  $t = 0$  represents the photo diode signal, when the laser energy is 20 mJ (b) ASW signal from the ns-LIB of atmospheric air at 90 mJ input laser energy per pulse at a microphone distance of 8 cm from the plasma.

We are trying to extract more information from the ASW in both time and frequency domain. The study of the ASW signal in time domain provides considerable information quantitatively[4]. Majority of the information lies in the first signal. So we focused here on the first part of the signal, as shown in fig. 2.6.

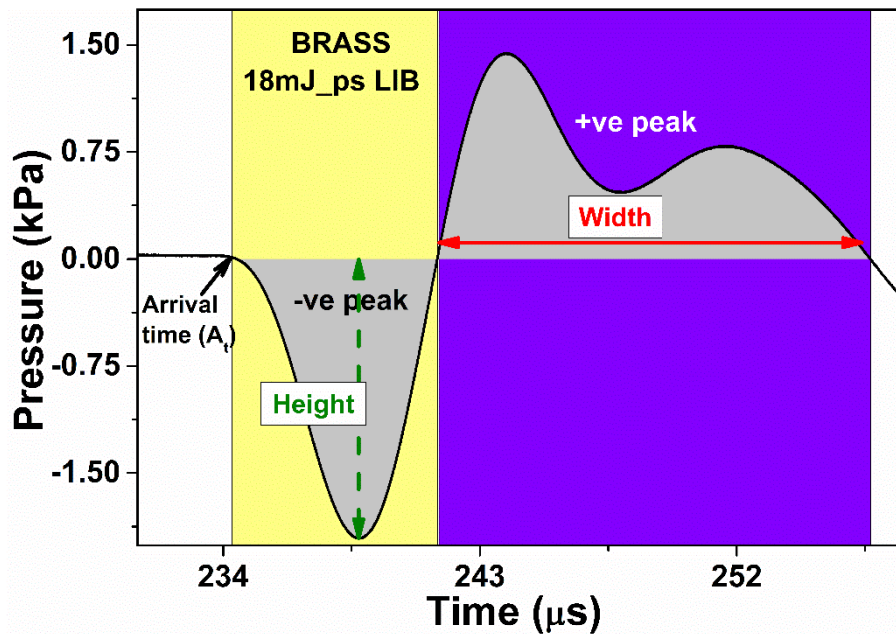


**Fig. 2.7.** Time domain representation of ASW signal, emitted from the ps LIB of Brass sample at 18 mJ of laser energy per pulse.

To understand more, signal has divided into two regions, the one below the zero line (atmospheric pressure) is negative portion (trough) and the other one, which is above of zero line is positive portion (crest), shown in fig. 2.7. The change in these two portions or regions of ASW represents the behavior of laser-matter interaction. Negative peak height (here after it is represented by -ve) represents shock intensity and width of positive peak (here after it is represented by +ve) indicates the density fluctuations. This terminology is used for convenience. These two parameters are shown clearly in fig. 2.7, where ASW signal is emitted from ps-LIB of brass sample at 18 mJ of input laser energy.

After ablation, particles ejected from crater exists till micro seconds. If we use high repetition rates, the ejected particles may interact with the consequent laser pulses [5, 6]. But in our case, rep rate is 10 Hz (with 100 msec time gap between two consequent pulses), hence there is no interaction of ablated particles with subsequent laser pulses. Now we will see how these parameters will change as a function of sample and incident laser energy.

The mechanical wave with high pressures and velocity carries its own energy. The kinetic energy transported by the ASW in the specified time interval [7] can be extracted from the acoustic signal energy ( $E_s$ ) arising from plasma,

$$E_s = \int_{t_1}^{t_2} f^2(t) dt \quad (1)$$

where  $t_1$  and  $t_2$  define the time window of integration,  $E_s$  is a measure of the signal energy [8] and  $f(t)$  is the temporal evaluation of acoustic signal.

The minimum distance of microphone from plasma and the maximum input laser energy were optimized to avoid signal saturation. To increase the signal to noise ratio, average of 32 acoustic data sets of incident laser pulses has taken. A good care has taken to avoid unnecessary reflected components in time domain signal. These precautions helps to understand more about laser-matter interaction and to optimize experimental conditions.

Signal reproducibility is the key aspect for proposing a first-hand application. To prove the homogeneity in the signal, standard deviations are measured for 20 times repeated experimental data for different energies which has used in the experiment. The obtained values of average ASW pressures with error bars (standard deviation) are shown in the below table 2-2.

**Table 2-2.** ASW pressures with errors for various laser energies of ns LIB of air at 80mm focal length of lens.

Laser energy (mJ)	Peak pressure (kPa) with error
10	$2.61 \pm 0.012$
25	$3.21 \pm 0.002$
40	$3.89 \pm 0.008$
55	$4.35 \pm 0.004$
70	$4.91 \pm 0.003$
90	$5.12 \pm 0.004$

The obtained ASW pressures have high precision, as standard deviation are varying in second order. At 10 mJ of laser energy, the pressures are within the range of 2.55 to 2.70 kPa, as shown in fig. 2.8. Higher laser energies generated ASWs with high peak pressures. These pressures are on a straight line for all incident energies. The repeatability of ASW pressures are high at all laser energies.

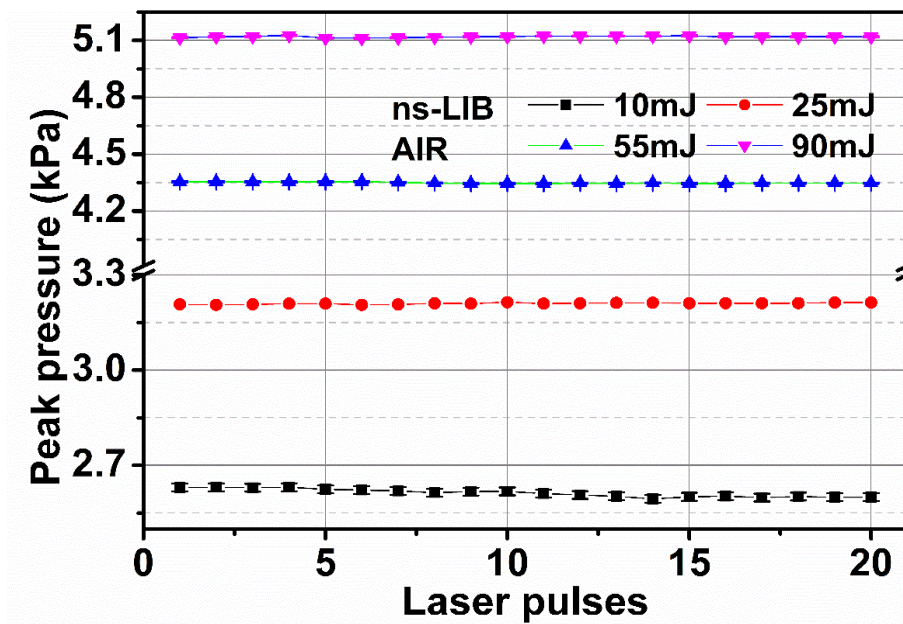


**Fig. 2.8.** Peak pressures with error bars of ASWs for each laser shot of ns-LIB of air were plotted at various incident laser energies of 10, 25, 55 and 90 mJ.

### 2.3.3 Analysis of ASWs in Frequency domain:

Apart from time domain information, evolution of frequency information and spectral density of ASWs is also essential. The frequency components associated with the time domain signals are obtained by applying Fast Fourier transformation (FFT). Frequency spectrum of the acoustic signal shows, the presence of several frequency components associated with the acoustic waves [4, 7, 9].

$$F(\omega) = \int_{t_1}^{t_2} f(t) \exp(-i\omega t) dt \quad \text{----- (2)}$$

Here  $f(t)$  is time domain acoustic signal,  $\omega$  is the frequency. Power spectral density (PSD),  $S(\omega)$  is given by

$$S(\omega) = |F(\omega)|^2 \quad \text{-----(3)}$$

The central peak frequency, full width half-maximum (FWHM) [10] and area under the curve are extracted by fitting the ASW frequency spectrum to Lorentzian function and plotted against incident laser energy, shown in fig 2.9. These time and frequency domain parameters give qualitative and quantitative information of ionized medium [8, 11, 12].

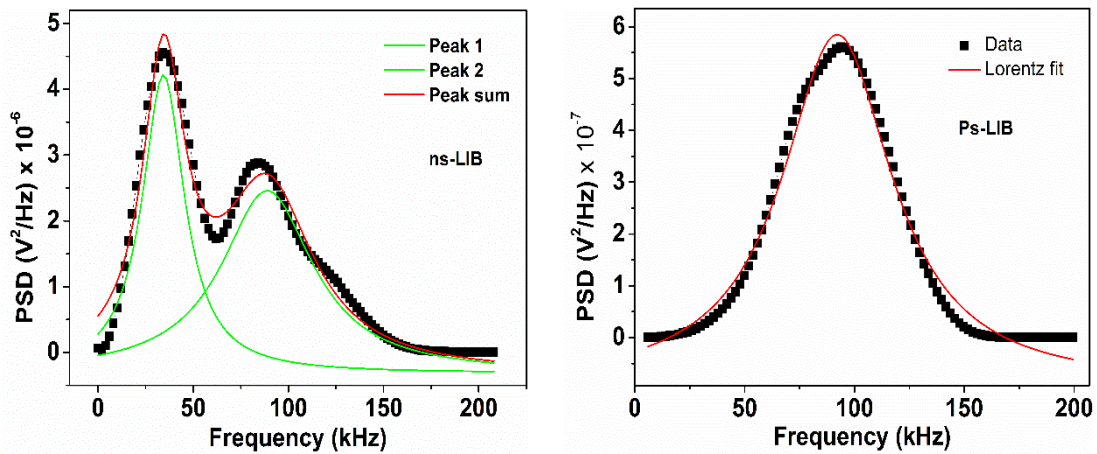


**Fig. 2.9.** (a) Spectrum of ns-LIB of air. Two peaks were fitted to two Lorentzian peaks. The fitting parameters are noted down to understand more about ASWs. Y-axis is power spectral density. (b) Spectrum from ps-LIB of air fitted to only one peak.

The number of peaks and spectral parameters are function of incident laser energy, laser pulse width and target properties. These spectral features provides the information about the plasma. Various focal geometries have used for both ns and ps-LIB. In focusing geometry of ' $f/\#10$ ', where  $f$  is the focal length of lens used and ' $\#10$ ' denotes the ratio of focal length of the lens and incident laser beam diameter.

The frequencies produced by LIB of air are in the range of ultrasonic frequency, shown in fig. 2.9. When the laser pulse irradiated on target surface, it generates the ultrasonic frequencies inside the material target [13, 14]. These frequencies can use in NDT of materials in various industry sectors. Interaction of laser pulses with target sample generates the impulses inside the target and in its surrounding atmosphere.

The rapid hitting of metal plate with other metal object also creates the sound bursts, shown in fig. 2.9 (a). The corresponding spectra of these sound bursts are also presented along with their time domain signals, show in fig. 2.9 (b). And these sound impulses are having sharp frequencies in audible range. These peak frequencies are different for three samples. These impulses (acoustic transients) created from LIB are different from the impulses created by manual hitting of same sample with an (align key) object.

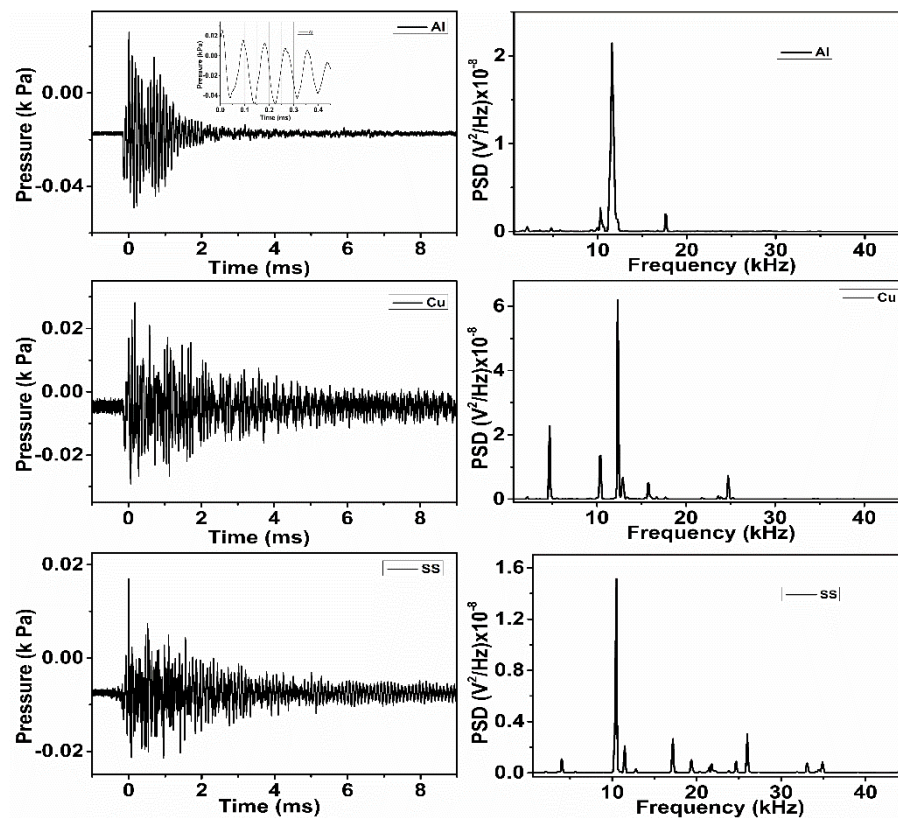


**Fig. 2.10.** Time domain signals and spectra of manual hitting of target samples of aluminium (Al), copper (Cu), stainless steel (SS304).

## 2.4 Effect of sampling rate on ASW signals:

To take acoustic measurements we have to choose proper sampling rate and bandwidth. From Nyquist theorem, the sampling rate should be at least twice the signal (ASW) frequency

to avoid the aliasing effects. The good sampling of signal is that, sampling rate is equal to the twice the measured wave frequency. For example, 44 kHz sampling rate is good to measure the 22 kHz signal. Higher the sampling rates higher the resolution. The band width (BW) of acquisition system should be greater than or equal to the five times of signal (ASW) frequency.

$1 / \text{temporal resolution} = \text{sampling rate}$ .

At a fixed band width (BW) and data length of oscilloscope, the ASW signals were collected at various time scales of 100, 500  $\mu\text{sec}$  and 1 m sec and presented in both time, frequency domain and presented in fig. 2.11 (a), (b).

For the data length of 1,25,000 points, smaller time scales (100  $\mu\text{s}/\text{div}$ ) has high temporal resolution (0.008  $\mu\text{s}$ ) due to its high sampling rate (125 Mega Samples/sec), whereas longer time scales (1 ms/div) has low sampling rate (12.5 MS/sec) and temporal resolution (0.08  $\mu\text{s}$ ) is low. So, to study the ASWs more precisely in time domain, lower time scales or high sampling rates are better choice. One more advantage is that reflected components from surrounding objects of source, can be avoided if you choose smaller time scales. Any real time signals are too complicated to reproduce. So we need more number of data points for reconstruction of signal. As presented in fig. 2.11 (a), 100  $\mu\text{s}/\text{div}$  time scale has more number of data points than the 500  $\mu\text{s}/\text{div}$  and 1 ms/div. The properties of ASWs doesn't change for these mentioned time scales of 100, 500  $\mu\text{s}$  and 1 ms.

The acoustic spectra corresponding to various time scales (sampling rates) are presented in fig. 2.11 (b). The acoustic spectrum of signal at 100  $\mu\text{s}$  has highest amplitude than the remaining time scales. The frequency components are more clearly separated in 500  $\mu\text{s}$  and 1 ms time scale spectra, shown in inset of fig. 2.11 (b). Smaller time scales (higher temporal resolution) causes the longer frequency scale in spectrums, whereas longer time scales (less temporal resolution) causes the shorter frequency scale, from Nyquist theorem, presented in table 3.

Total frequency scale =  $1 / 2 * \text{resolution in time domain signal}$ .

The parameters about data are clearly tabulated for various time scales in table 2-3. It gives the brief idea on time and frequency resolutions as time scale per division changes. Distribution of same data (62500 points) on larger frequency scale causes the large spacing between two consecutive data points in FFT than the smaller frequency scale. So, frequency resolution is very high for longer time scales (lower sampling rate).

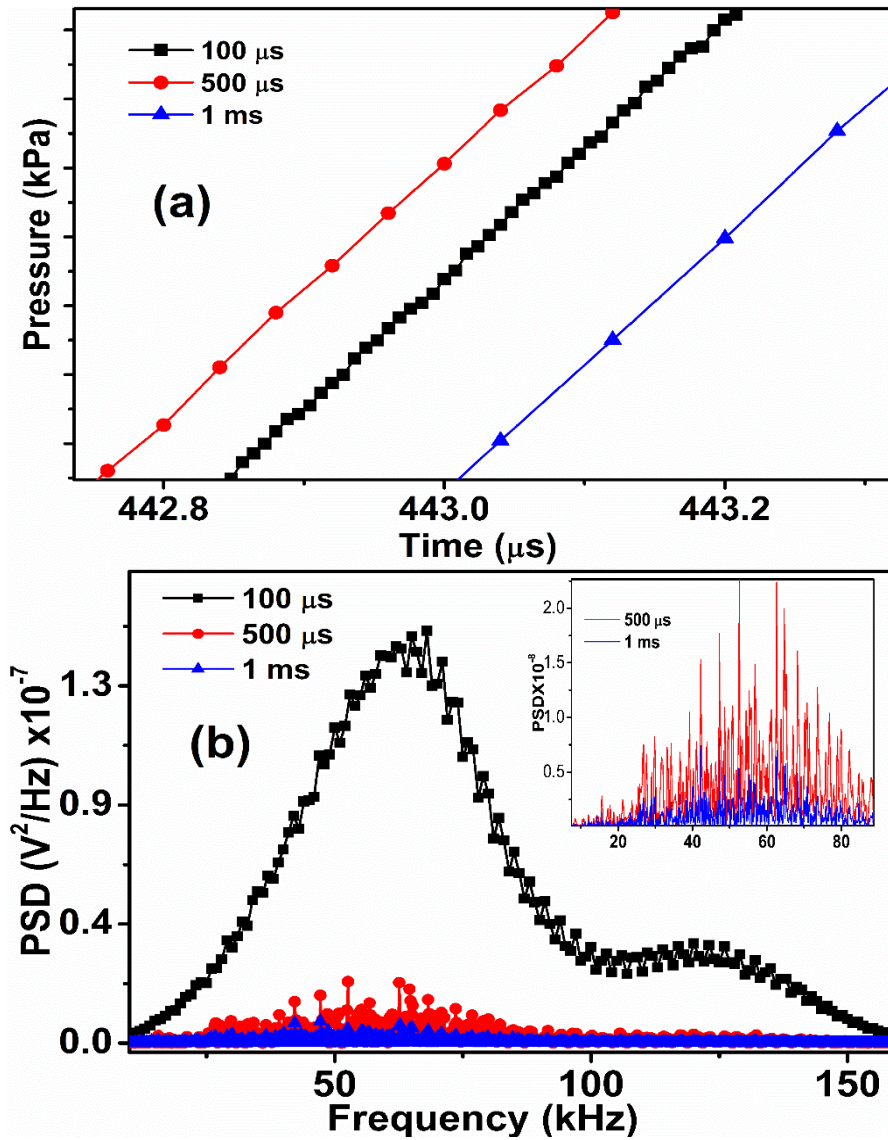


**Fig. 2.11.** For a fixed laser energy, ASW signals were collected at timescale of 100, 500  $\mu\text{s}$  and 1milli sec, (a) time domain representation of data points, temporal resolution is more for 100  $\mu\text{s}$  than the 500  $\mu\text{s}$  and 1 msec. (b) Frequency representation of data. Sampling rates are 125, 25 and 12.5 Mega samples/sec for 100, 500  $\mu\text{s}$  and 1 msec respectively. Frequency resolution is more for 1 msec than the 500, 100  $\mu\text{s}$ .

As we move from smaller to longer time scales (less to high frequency resolution), the amplitude of frequency peak will decrease up to 3 orders. Always time and frequency domains are reciprocal to each other. For better accuracy in time domain we have to compromise the frequency domain and vice versa. It is easy to reconstruct the signal if we have more number of data points. Lower time scales consist of more number of data points than the higher time scales/div, as shown in fig. 2.11.

**Table 2-3.** Relation between time scale, number of data points, sampling rate and frequency scales.

Time scale/ div [when data length is 125000 ]	Number of data points in frequency spectrum	Maximum frequency on scale of spectrum (M Hz)	Frequency resolution (Hz)	Total time scale (sec) [triggering at First division]	Time resolution ( $\mu$ s)	Sampling rate Mega samples/sec
50 $\mu$ s	62500	125	2000	0.00045	0.004	250
100 $\mu$ s	62500	62.5	1000	0.0009	0.008	125
500 $\mu$ s	62500	12.5	200	0.0045	0.04	25
1 m s	62500	6.25	100	0.009	0.08	12.5

## 2.5 References:

1. L. E. Kinsler, *Fundamentals of acoustics* (Wiley, 2000).
2. Brüel and Kjær, "Microphone Handbook," (1996).
3. S. L. Chin, D. K. Evans, R. D. McAlpine, and W. N. Selander, "Single-pulse photoacoustic technique for measuring IR multiphoton absorption by polyatomic molecules," *Appl. Opt.* **21**, 65-68 (1982).
4. J. Diaci and J. Mozina, "A study of blast waveforms detected simultaneously by a microphone and a laser probe during laser ablation," *Applied Physics A Solids and Surfaces* **55**, 352-358 (1992).
5. K.-H. Leitz, B. Redlingshöfer, Y. Reg, A. Otto, and M. Schmidt, "Metal Ablation with Short and Ultrashort Laser Pulses," *Physics Procedia* **12**, 230-238 (2011).
6. J. König, S. Nolte, and A. Tünnermann, "Plasma evolution during metal ablation with ultrashort laser pulses," *Opt. Express* **13**, 10597-10607 (2005).
7. S. Palanco and J. Laserna, "Spectral analysis of the acoustic emission of laser-produced plasmas," *Appl. Opt.* **42**, 6078-6084 (2003).
8. L. Grad and J. Možina, "Acoustic in situ monitoring of excimer laser ablation of different ceramics," *Applied Surface Science* **69**, 370-375 (1993).
9. E. Schwarz, S. Gross, B. Fischer, I. Muri, J. Tauer, H. Kofler, and E. Wintner, "Laser-induced optical breakdown applied for laser spark ignition," *Laser and Particle Beams* **28**, 109-109 (2010).
10. A. K. Rao, "Acoustic emission and signal analysis," *Defence Science Journal* **40**, 55-70 (1990).
11. C. Stauter, P. Gérard, J. Fontaine, and T. Engel, "Laser ablation acoustical monitoring," *Applied Surface Science* **109/110**, 174-178 (1997).
12. T. Bende and B. J. Jean, "Non-contact photoacoustic spectroscopy for photoablation control," (Google Patents, 2004).

13. S. J. Davies, C. Edwards, G. S. Taylor, and S. B. Palmer, "Laser-generated ultrasound: its properties, mechanisms and multifarious applications," *Journal of Physics D: Applied Physics* **26**, 329 (1993).
14. D. A. Hutchins, "Ultrasonic generation by pulsed lasers," in *Physical Acoustics V18: Principles and Methods*, W. P. Mason, ed. (Elsevier Science, 2012).

This page is intentionally left blank

## **CHAPTER 3 : ASW emissions from ns and ps-LIB of atmospheric air: Propagation of ASWs in surrounding atmosphere**

### **Abstract:**

Evolution of Acoustic shock waves (ASW) and their properties in the frequency range of 30-120 kHz generated during Laser Induced Breakdown (LIB) of ambient atmospheric air, using 7 ns and 30 ps pulse duration is presented. The specific frequency span and peak amplitude are observed to be different for ns and ps-LIB. The ASW frequencies for ps-LIB lie between 90 to 120 kHz, with one dominant peak whereas for ns-LIB, two dominant peaks with frequencies in the 30-70 kHz and 80-120 kHz range are observed. The radial and angular distribution of ASW is presented. These frequencies are observed to be laser pulse intensity dependent. With increasing energy of ns laser pulses, the acoustic frequencies move towards the audible frequency range. The variation in the acoustic parameters, peak-to-peak pressures, signal energy, frequency and acoustic pulse widths with laser energy and for two different pulse durations is presented in detail and compared. The acoustic emissions are observed to be high for ns-LIB than the ps-LIB, indicating higher conversion efficiency of optical energy into mechanical energy. The laser intensity is varied by changing focal geometry of ns and ps pulses. The ASW pressures are observed to follow the dynamic interplay between the plasma density and recombination of plasma species. The conversion of laser energy to acoustic energy increases when we move from loose to tight focusing conditions. The central frequencies move towards the lower side with increasing laser intensities for both ns-LIB (76 to 48 kHz) and ps-LIB (111.2 to 92.1 kHz). The angular distribution of acoustic emissions was observed to follow the laser induced plasma spark in both ns and ps-LIB.

### **3.1 Introduction**

The ASWs are similar to the pressure waves produced by micro-blasts, and are used to understand sonic booms under controlled conditions [1]. The plasma formed by lasers is more close to a spherical acoustic source (depends on laser pulse width and focal length of the lens used). Some of the applications of laser induced point acoustic source is in acoustic land mine detection and measuring the resonant frequency of metal tubes [2]. Laser induced plasma is a good acoustic source, for the acoustic landmine detection (ALD) [3] and this technique is more reproducible. The emitted pressure or stress waves go in to soil in multi directions when the laser is focused on the soil. These acoustic waves travel into the surface and reflect back. Knowing the speed of sound in soil and time taken for the reflected waves, gives the precise information about location of land mine (like SONAR in water). The ASWs from laser

generated plasma can be used to measure the resonant frequency of metal tubes and impedance tubes. Because of the good repeatability, broad frequency response, laser induced plasma (LIP) is used in scale models as an acoustic source, instead of using conventional methods like small loud speakers and electrical spark [4] to predict the acoustic behaviour of space (concert hall, streets etc.).

### **3.2 Radial distribution of acoustic shock waves**

When a laser beam is focused in air, breakdown happens when the supplied energies are greater than the breakdown threshold of air. It results in the generation of ions, neutrals, atomic and molecular clusters, which collectively constitutes a plasma. Plasma is highly energetic and dense, which while coming to an equilibrium, drives a shock wave into the surrounding atmosphere. As the shock wave propagates into ambient air, it decays in to acoustic shock waves. These can be detected by a condenser microphone. Measurements are triggered by the incident laser pulse to ensure better S/N ratio.

Spatio-temporal expansion of the plasma is well studied by using various techniques such as shadowgraphy, interferometry and Schlieren photography [5, 6]. The salient features of the plasma is that it has expansion towards incident laser direction at initial time scales, after 80  $\mu\text{s}$  the expansion is normal to the incident laser direction, and then after 200  $\mu\text{s}$  there is a small jet which comes out from the plasma and travels towards the incident laser direction [5, 7]. The aim of this chapter is to explore the feasibility of the acoustic diagnosis to understand the plasma due to LIB. The representation of ASW signal and the measurement of its parameters are presented earlier in chapter 2.

The ns LIB generates ASW of micro second pulsewidth. ASW is a transient pulse, whose peak to peak voltage and evolution time are characteristic of every signal and these parameters help us to measure the pressure and energy associated with that of the ASW [5]. The properties of ASWs vary along with the source receiver distance and incident energy per pulse. Arrival time ( $A_t$ ), peak-to-peak pressure ( $P_k$ ), acoustic pulse decay time ( $D_t$ ), and acoustic pulse duration ( $W_t$ ) are the parameters which helps to understand the ASW in detail manner. For better signal analysis one has to avoid the reflections of acoustic waves from surrounding objects of plasma. ASW pressures increased with incident laser energy indicating a good conversion of incident energy to acoustic shock energy. The maximum pressures of 4.5 kPa (167 dB ref. to 20  $\mu\text{Pa}$ ) and 7 kPa (170 dB ref. to 20  $\mu\text{Pa}$ ) observed at 20 mJ and 40 mJ of incident laser energies

respectively at a fixed distance of 6 cm, for f/10 focal geometry. These pressure levels are very high and sufficient to create non-linear acoustical effects [1, 8].

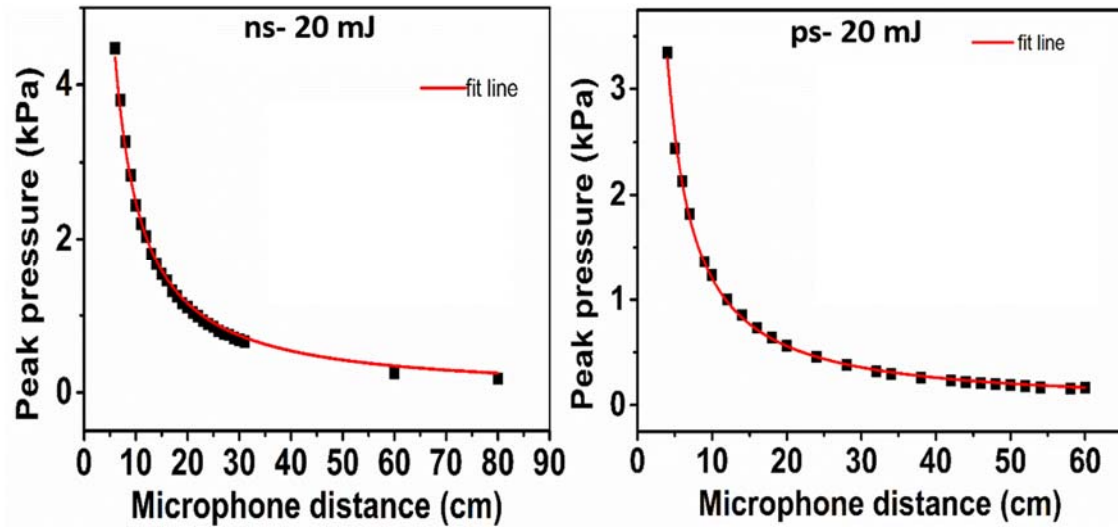


**Fig. 3.1.** ASW pressures produced by ns LIB of air, at 20 mJ, 40 mJ pulse energies under, (a) f/10 focal geometry and (b) f/19 focal geometry.

We varied source-receiver distance from 6 to 80 cm and observed the ASW behaviour. As separation distance increases the intensity of sound is observed to fall off, as shown in fig. 3.1. There is a fall in peak pressures with respect to distance of detector. These pressures were fitted to Allometric fit, which is :

$$y = a \cdot x^b$$

where  $a$ ,  $b$  are fitting parameters. ASW pressures are decay w.r.t microphone distance as shown in fig. 3.1, so  $b$  takes negative values. For f/10 focal geometry and for 20, 40 mJ of laser energies, the  $b$  values are -1.17, -1.25 respectively. For f/19 focal geometry and for 20, 40 mJ of laser energies, the  $b$  values are -1.24, 1.25 respectively. In both focal geometries, the  $b$  values are close to 1, it indicates that the, acoustic peak pressures follows the inverse square law [9]. Hence, we can say that, the ASW behaviour is varies with distance. Here we observed no non-linear acoustic effects (the power of  $x$  is  $b$ ,  $b > 2$ ) were observed along with the source-receiver distance. The slope of microphone distance vs arrival time of ASW gives the velocity, here 350 m/sec for 40 mJ of incident laser energy.

### 3.3 Angular distribution of ASWs

LIP is a mass-less and point size sound source, and the frequencies of ASWs in all directions (angles w.r.t plasma) has a common range of frequencies, shown in fig. 3.2. To study the

evolution of ASWs from plasma, we measured pressures at various angles of microphone w.r.t incident laser radiation around the plasma. This experiment was done at 10 mJ of laser energy and 3, 5, 8 cm microphone distances for both ns and ps-LIB of air.

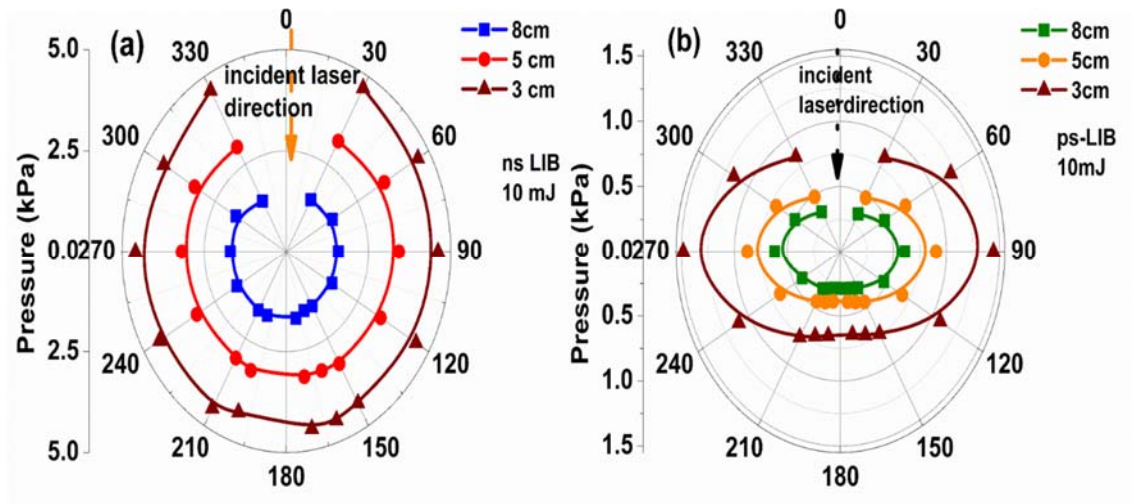


**Fig. 3.2.** Distribution of ASW pressures around plasma for both ns and ps LIB of air at three different radii of 3, 5, 8 cm and time scales for 10mJ of incident laser energy.

To know the spatial distribution of ASWs around plasma, the angular dependence is studied. Assuming plasma to be a spherical source (Debye sphere) of a finite radius, the microphone is moved at different angles around the plasma for a fixed separation between plasma (source) and detector (receiver) ( $r$ ). Later the separation  $r$  is varied to get the angular distribution.

As we mentioned earlier, the pressures from ns LIB are higher than the ps LIB of air, at three different separations of  $r$ . The peak pressures ( $P_k$ ) at  $90^\circ$  position of microphone for 8, 5, 3 cm of microphone distances from ps LIB and ns LIB are 0.61, 0.9, 1.4 kPa and 1.6, 3.4, 4.6 kPa respectively. As shown in fig. 3.2, the pressure distribution around the plasma is more or less spherical from ns LIB of air. Whereas, the ASWs from ps-LIB are more focused in the normal direction as compared to the incident laser direction. At three different separations studied, the pressures are high at  $90^\circ$ ,  $270^\circ$  i.e. perpendicular to the laser propagation direction which also happens to be along the polarization of the ps laser pulses.

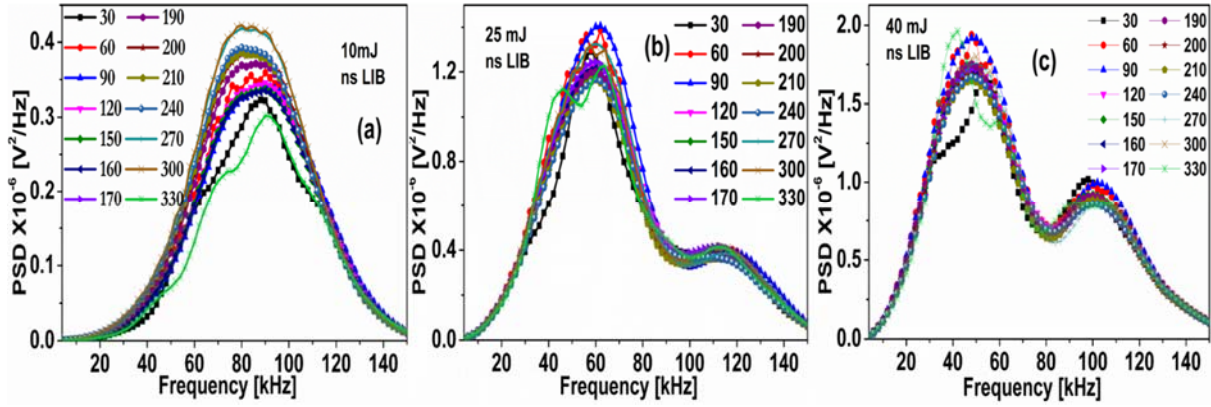


**Fig. 3.3.** Frequency response of ASWs from ns LIB of air, around the plasma at various angles of microphone w.r.t incident laser direction, (a) 10 mJ, (b) 25 mJ, (c) 40 mJ of incident laser energy.

The evolution of frequency response vs power spectral density (PSD) of ASWs from ns-LIB at different laser energies, in various angles of microphone with respect to incident laser direction are shown in fig. 3.3. The frequencies of ASWs are from audible to ultrasonic frequency range with high amplitudes. For a particular laser energy of 10 mJ, the peak frequencies are very close. The variation in PSD of peak is very less indicating the unchanging acoustic frequencies around the plasma. A similar trend is observed for second frequency peak also for 25, 40 mJ of energies. We observed that the frequency response of ASWs from plasma is independent of microphone position. Thus ASWs from LIB of air are useful for wideband acoustic signal propagation in the atmosphere [10]. The appearance of single peaks at lower energies and two at higher energies indicates the number of LIB sources generated in atmosphere [5].

## 3.4 Energy dependence of ASWs

### 3.4.1 nano second laser induced breakdown (ns-LIB) of Air

The behavior of plasma is different at different laser energies is a well-known fact. As the incident laser energy increases, we are dumping more and more energy at a very small focus point, so the medium will get ionized heavily and consequently the size, density and temperature of the plasma increases [5]. For ns-LIB the  $P_k$  value at 10 mJ of incident laser energy is 2.6 kPa (162 dB) whereas at 90 mJ the  $P_k$  is 5.1 kPa (168 dB), almost double the value. Sound pressure level >140dB creates nonlinear acoustical effects [1, 8]. So, it can be used as acoustic source for non-linear studies [1]. With increasing laser energy, the changes in the arrival times of the acoustic signals were presented in fig. 3.4. Along with the arrival times, the temporal shape of the acoustic pulse also changes.

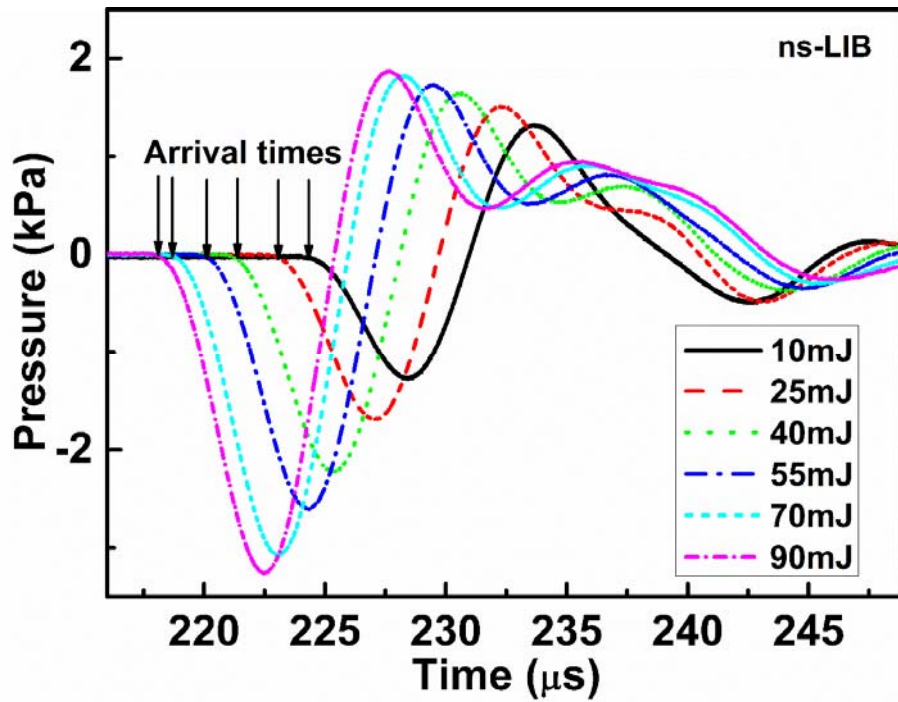


**Fig. 3.4.** ASW signals from ns-LIB of air at 10, 25, 40, 55, 70 and 90 mJ of laser energies per pulse, X-axis is time duration of the pulse, Y-axis is peak to peak pressure. Here the source-receiver distance is 8 cm.

With increasing laser energy, the arrival time of ASW is reduced. At 90 mJ of laser energy, the  $A_t$  is 218  $\mu\text{s}$  whereas at 10 mJ,  $A_t$  is 224.5  $\mu\text{s}$  indicating that, higher the laser energy, sooner the ASW reaches detector with high peak pressure. Table 3-1 summarizes energy dependent evolution of the important acoustic parameters from ns-LIB of atmospheric air at a fixed source-receiver distance of 8 cm.

**Table 3-1.** The ASW parameters from ns-LIB of atmospheric air at different input laser energies.

Laser energy (m J)	Peak-peak pressure $P_k$ (k Pa)	Arrival time, $A_t$ ( $\mu$ s)	Decay time, $D_t$ ( $\mu$ s)	Pulse Duration, $W_t$ ( $\mu$ s)	Signal energy, $E_s$ (a.u $\times 10^{-9}$ )
10	2.6	224.5	12.2	14.8	11
25	3.2	222.8	14.3	17.7	17
40	3.9	221.2	17.4	19.9	25
55	4.3	220	19	21.96	32
70	4.9	218.8	22.8	24.14	42
90	5.1	218	24.6	25.23	47

Thus, the arrival time depends on incident laser energy and distance of microphone from the plasma. There is considerable rise in signal energy along with incident laser energy; it distinctly indicates that there is good conversion of optical energy into mechanical energy (table 3-1). With increasing laser energy, the plasma is sustained for longer durations leading to a broader acoustic pulse resulting in higher  $W_t$  and  $D_t$  values. Similar results were reported during plasma initiated by solid aerosol particles [11], confirming that plasma size and acoustic pulse width are proportional to each other.

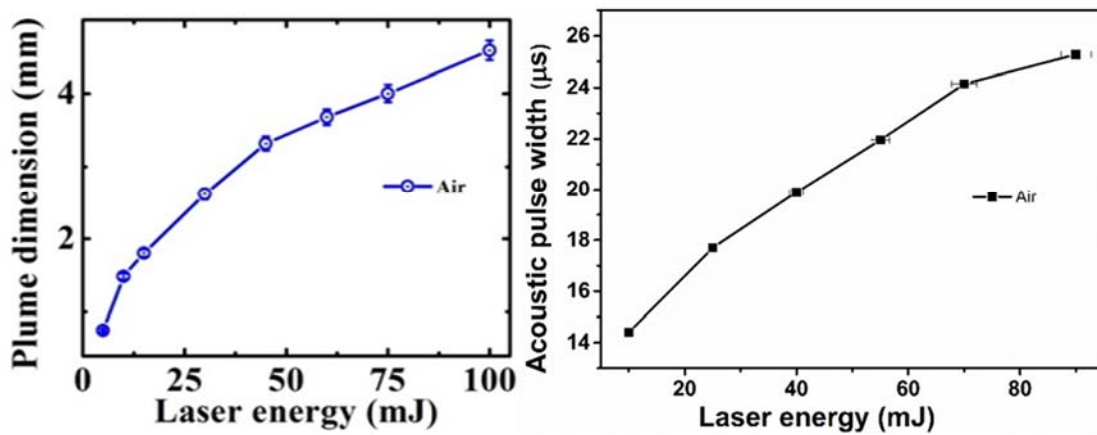


**Fig. 3.5.** During ns-LIB of air, plasma plume dimension (from CCD imaging) and ASW pulse width vs laser energy at same experimental condition.

Actual plasma dimensions were measured from CCD images [5]. It is clearly seen that, along with incident laser energy, plasma dimension also increases as shown in fig. 3.5. The increment in acoustic pulse duration follows a similar behaviour close to the increment in plasma dimension.

Apart from time domain information, evolution of frequency information and spectral density of ASWs is also essential to get a complete picture of acoustic emissions. The frequency components associated with the time domain ASW signals are obtained by applying Fast Fourier Transform, which shows the presence of several frequency components associated with the acoustic waves [6, 12, 13]. ASWs are transient signals so its frequency response range is broad. Fig. 3.6(a) shows the evolution of power spectral density as a function of frequency with laser energy from ns-LIB at a distance of 8 cm. At lower energies (<25 mJ) only a single dominant peak centered at 68 kHz is observed (termed as peak 1). With increasing energy (>25 mJ) another frequency peak is observed (termed as peak 2). With increasing laser energy, both

the peaks shift towards the lower frequencies with peak 1 approaching audible range. At the highest energy of 90 mJ used in the present study, two peaks centred at 34 kHz (peak 1) and 84 kHz (peak 2) with an amplitude ratio of 5:3 respectively are observed. Central frequency of peak 1 is observed to rapidly shift towards the audible range with increasing laser energy as shown in fig. 3.6 (b).

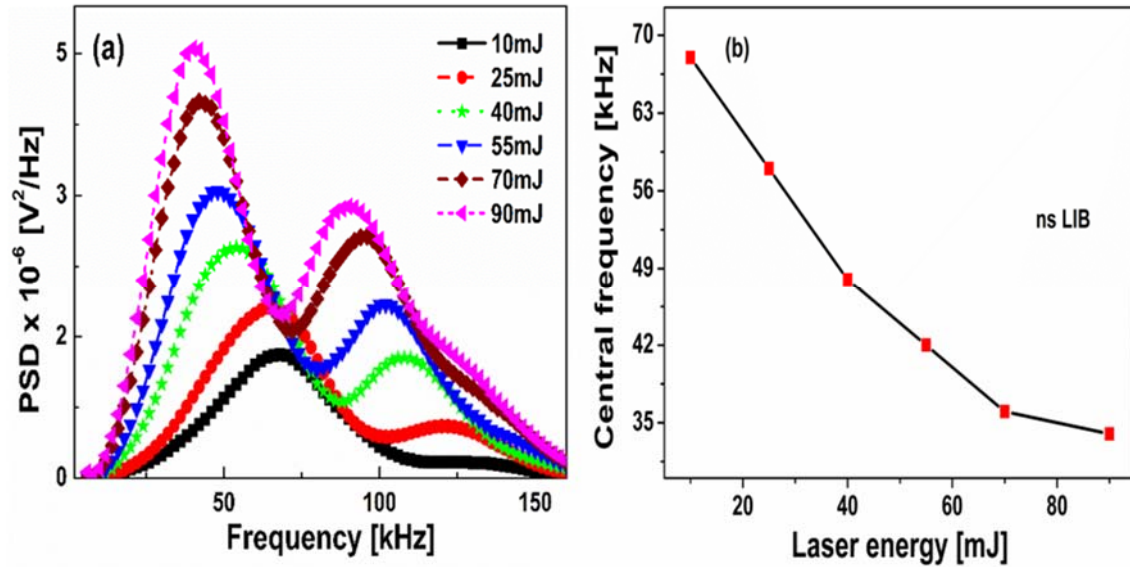


**Fig. 3.6.** Frequency spectrum of ASWs from ns-LIB of air, (a) at various incident laser energies, X-axis is frequency and Y-axis is Power Spectral Density (PSD), (b) shift in central frequency (peak 1) w.r.t laser energy.

With laser energy the shift of frequencies to the lower side is in good agreement with the increase in size of the plasma [14], because the natural frequency of resonance of any sound source is dependent of its flexural rigidity and inversely dependant on its density, mass and dimensions [15]. In our case, with increasing laser energy the dimension and number density of LIB induced plasma increases. Also, the collisions among the plasma will increase leading to increased ASW pulse duration. The following equation shows the dependence of frequency of ASW on plasma dimension [10, 11], here  $r_p$  is the size of the plasma,  $\tau_p$  is the ASW width in time domain,  $c$  is the velocity of sound in atmosphere.

$$f_{max} \cong \frac{c}{4r_p} \cong \frac{1}{2\tau_p} \quad \text{---- (1)}$$

So, from equation (1), as the  $r_p$  and  $\tau_p$  increases, the max frequency value decreases.

The full width half-maximum (FWHM) and area under the curve are extracted by fitting the acoustic frequency spectrum to a Lorentzian function and plotted against incident laser energy, shown in fig. 3.7. As laser energy increases, the frequency peaks become sharper with increasing amplitude,

indicating energy conversion to a dominant acoustic mode. With the appearance of high frequency peak (which has lower amplitude, peak 2) at laser energy >25 mJ, the FWHM and energy content of the low frequency peak (peak 1) in fig. 3.7 starts to saturate. This confirms the transfer of incident laser energy into the evolution of different acoustic modes.

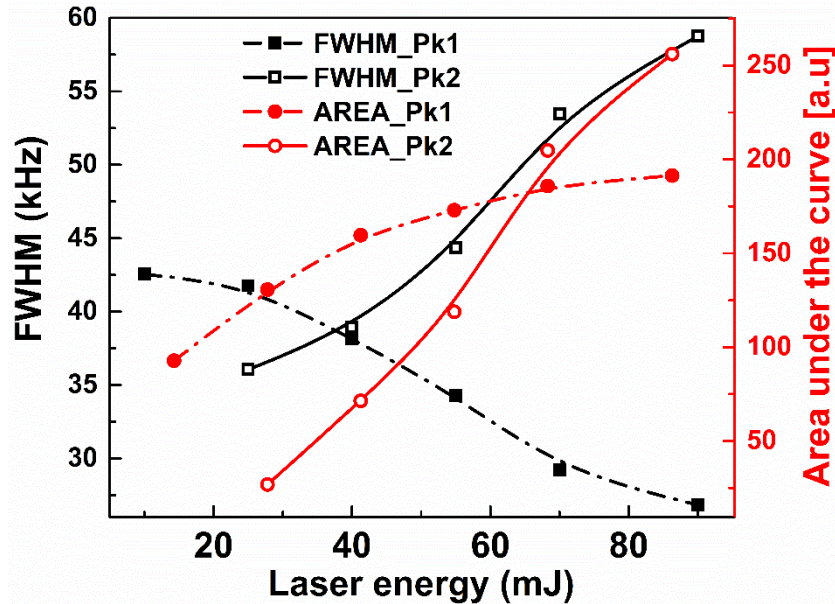


**Fig. 3.7.** For ns LIB of air, (b) the FWHM and area under the curve of spectrum for both peak 1 (low frequency) and peak 2 (high frequency). These are changing along with the incident laser energy.

For peak 1, the FWHM values decreases as laser energy increases, whereas for peak 2, FWHM values increases, as shown in fig. 3.7. As laser energy increases, the area under the curve values also increases, as shown in fig. 3.7. From fig. 3.7, the change in the slopes of area under the curve indicates the higher propagation velocities involved in ASWs. The response of these two peaks can be related to the different plasma expansion dynamics that takes place at higher input laser energies. The presence of two peaks can be attributed to the presence of two dominant plasma centers due to the leading and trailing edge of the ns laser pulse interacting with varying refractive index and electron density profiles along the propagation direction [5, 16]. A similar observation of two ionization centers along the propagation direction during vibrant evolution of ns laser–plasma interaction leading to two shock waves is reported [5].

### 3.4.2 pico second laser induced breakdown (ps-LIB) of Air:

Acoustic signals from ps-LIB of air for different laser energies are shown in fig 3.8. The time domain acoustic signals from ps-LIB have shown similar evolution with laser energy as that of ns-LIB. The parameters extracted are shown in table 3-2.

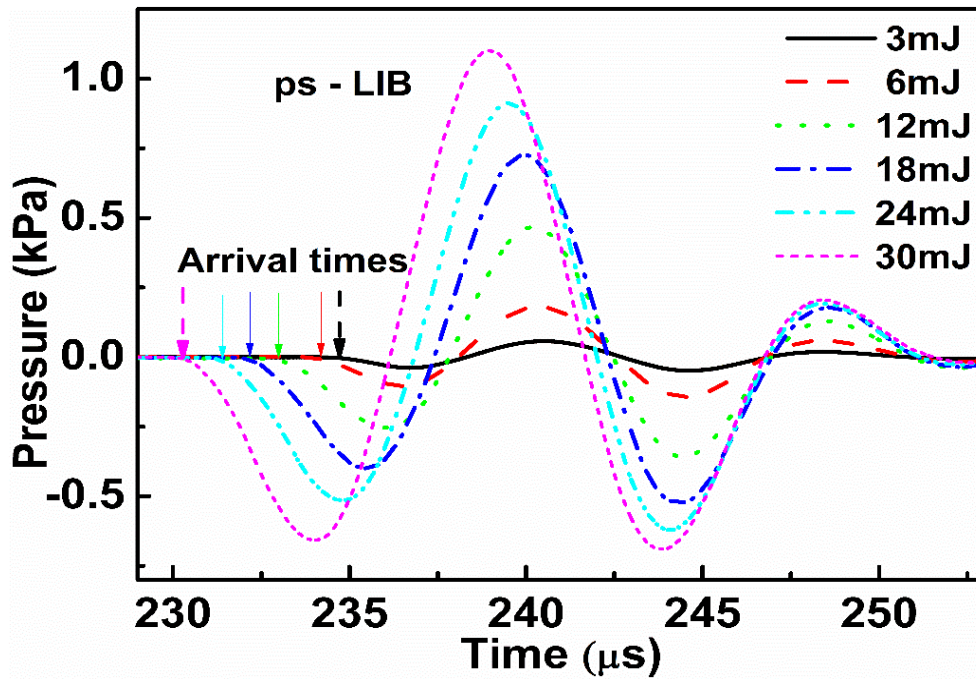


**Fig. 3.8.** ASW signals from ps-LIB of atmospheric air at 3, 6, 12, 18, 24 and 30 mJ of incident laser energies, X-axis is time duration of the pulse, Y-axis is pressure.

For 3 mJ and 30 mJ of incident pulse energies the maximum peak frequencies are 122 kHz and 94 kHz, respectively. Like ns-LIB spectrum, the peak frequency shifts towards lower frequency range with incident laser energy, but not closer to the audible range. At various incident laser energies, FWHM values and area under the curve values for the spectra of ps-LIB generated ASWs are presented in fig. 3.9. As shown in fig. 3.9(b), the FWHM values increases till 12 mJ and, then decays rapidly, which indicates the rapid rise in its peak height. This can be attributed to the ps-LIB which consists of a pool of electrons, ions, neutrals and molecular clusters [17] with huge temperature ( $\approx 10,000 - 15,000$  K) and density gradients compared to the surrounding atmosphere [13, 18, 19]. The time domain spectrum of ASWs from ps-LIB at a distance of 8 cm at various incident pulse energies are presented in fig. 3.8.

**Table 3-2.** ASW parameters from ps-LIB of air at various laser energies.

Laser energy (mJ)	Peak-to-peak pressure (k Pa)	Arrival Time, $A_t$ ( $\mu$ s)	Decay Time, $D_t$ ( $\mu$ s)	Pulse Duration, $W_t$ ( $\mu$ s)	Signal Energy, $E_s$ ( $a.u \times 10^{-6}$ )
3	0.106	234.6	10.8	8.35	0.015
6	0.324	234.1	10.8	8.8	0.14
12	0.825	233	10.9	9.6	0.9
18	1.25	232.3	11.6	10.07	2.3
24	1.54	231.6	12.5	10.8	3.7
30	1.79	230.4	13.7	11.25	5.5

With increasing laser energy, these gradients increase sharply leading to huge pressure differences between plasma and the surroundings. These temperature and density gradients generates acoustic transients [20] with high peak pressures [21, 22] that propagate with higher velocity in unperturbed ambient medium. In the case of ps laser pulses, the intensity of the pulse is higher, ensuring higher degree of ionization of the medium, which decreases the presence of neutrals in the plasma.

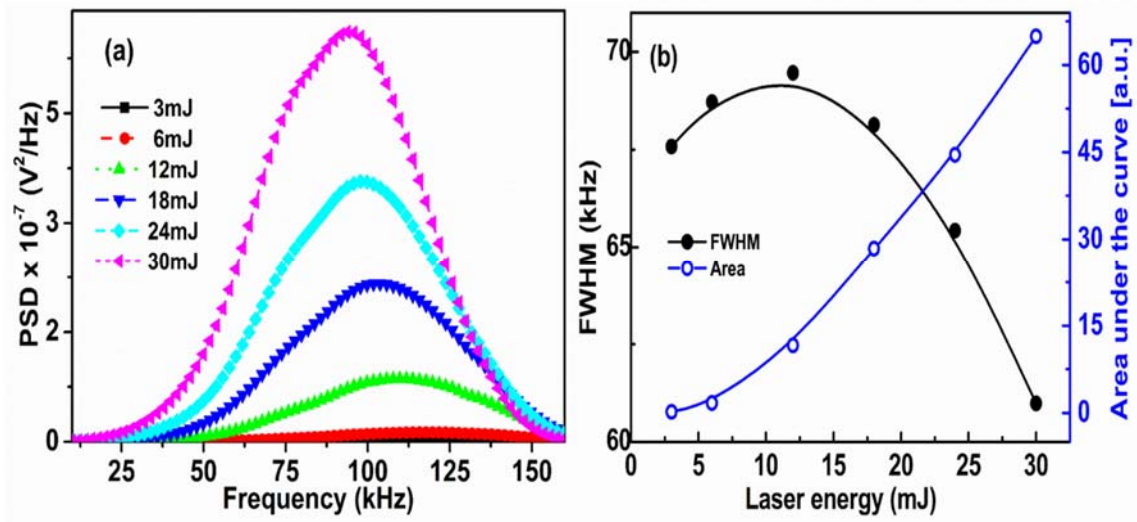


**Fig. 3.9.** Frequency spectrum of ASWs from ps-LIB of air, at different incident laser energies when microphone is at 8 cm distance from plasma, here X-axis is frequency and Y-axis is Power Spectral Density (PSD) (a), Incident laser energy versus FWHM and area (b).

FWHM represents the spectral energy of the acoustic signals. The acoustic signals are majorly due to the density gradient of electrons, ions and clusters within the plasma. With increasing laser intensity, the ionization will increase reducing the number of clusters within the plasma. This in turn will increase

the plasma frequency, localizing the energy to specific acoustic frequencies and reducing the FWHM. The increasing area under the curve supports the localization of acoustic frequencies and their increase with intensity. This eventually reduces the acoustic emissions. A similar amplitude reduction is observed in the case of RF emissions from ps-LIB of air [17].

The major difference between the acoustic SWs due to ns- and ps-LIB is that, (a) peak-to-peak pressures and  $E_s$  lower for ps-LIB, (b)  $A_t$  is slightly delayed, (c)  $D_b$ ,  $W_t$  are shorter. This is due to the fact that pico second pulses have high intensity and ns pulses have higher energy under similar experimental conditions which lead to plasma of different densities.

### 3.5 Effect of input intensity on the acoustic parameters

To understand the role of laser intensity on the ASW the generation of plasma and resulting effects, the photon flux, spot size and number of atoms in focal volume need to be studied. The estimated values for the focal geometries used in the studies are presented in table 3-3. We calculated the number of atoms in focal volume, assuming that laser energy is deposited in a cylindrical volume  $\pi\omega_0^2 Z_R$  where  $2\omega_0$  is the spot size at focal plane,  $Z_R$  is the Rayleigh length of the focused beam.

and the atomic density of air is  $10^{20}$  atoms/cm<sup>3</sup> at STP conditions [23]. At a fixed input laser beam diameter, increasing the focal length results in the increase of the focal number.

Spot size at focal plane is directly proportional to the focal length, when remaining parameters are fixed.

$$2\omega_0 = 1.27 * f * \lambda * \frac{M^2}{d} \text{-----(1)}$$

Where  $2\omega_0$  is the spot size (diameter),  $f$  is focal length of the lens,  $\lambda$  is incident wavelength and  $d$  is the laser beam diameter.  $M^2$  is beam divergence parameter of the given laser beam.

Varying focal length leads to varying spot size at focal plane ( $2\omega_0$ ) and varies the intensity accordingly.

The laser intensity is

$$I = \frac{2P}{\pi\omega_0^2} \text{-----(2)}$$

Where  $P$  is peak power of the pulse. The theoretical estimated peak intensity is order of  $10^{12}$  W/cm<sup>2</sup> for 80 mm focal length. However, from our experimental measurements the breakdown is observed at an intensity of  $10^{10}$  W/cm<sup>2</sup> in tune with the literature [24]. The theoretical calculated intensity values are always two orders higher as the role of impurities are neglected in the estimations [23].

The estimated spot size, intensity and number of atoms at focal volume are presented in table 3-3 for  $f/10, f/19, f/25, f/38, f/50$  focal geometries. These numerical values give a brief idea on the role of focal number that varies intensity, which in turn controls the breakdown. As shown in table 3-3, as the focal number increases, the intensity at focal point decreases. The number of photons per pulse for 40 mJ energy are  $11 \times 10^{16}$ . As focal number increases, the distribution of the same number of photons into larger focal volumes reduces the effective intensity at focal point and breakdown probability. For example at 80 mm focal length,  $3.2 \times 10^{11}$  W/cm<sup>2</sup> intensity is shared by  $1.6 \times 10^{10}$  atoms where as in 150 mm case,  $9 \times 10^{10}$  W/cm<sup>2</sup> intensity is shared by  $10.6 \times 10^{10}$  atoms. The mechanisms leading to breakdown is different for ns and ps pulses. With ns laser pulses the major breakdown mechanism is avalanche ionization where electrons interacting with the neutrals get multiplied under the influence of the laser electric field.

**Table 3-3.** Theoretically estimated spot size, intensity and number of air molecules in focal volume for different focusing conditions.

ns LIB 40 mJ	f=80 mm	f=150 mm	f=200 mm	f=300 mm	f=400 mm
Focal Number	$f/10$	$f/19$	$f/25$	$f/38$	$f/50$
Spot size ( $2\omega_0$ )	6.75 $\mu\text{m}$	12.66 $\mu\text{m}$	16.9 $\mu\text{m}$	25.3 $\mu\text{m}$	33.8 $\mu\text{m}$
Intensity (I) $\times 10^{10}$ W/cm <sup>2</sup>	31.9	9.07	5.09	2.27	1.27
Number of molecules in focal volume ( $\times 10^{10}$ )	1.6	10.6	20	84	200

While with ps laser pulses that have shorter pulse duration but higher intensities, ionization is the major mechanism leading to breakdown. The breakdown threshold for a material is given by [16]

$$I_{br} \propto \frac{mc\varepsilon_i(1+\omega^2\tau^2)}{2\pi e^2\tau} \left[ g + \frac{1}{\tau_p} \log \left( \frac{\rho_{cr}}{\rho_0} \right) \right] \text{-----(3)}$$

Where,  $\tau_p$  is the laser pulse duration,  $\omega$  is the optical frequency,  $\tau$  is the momentum transfer collision time, and  $\varepsilon_i$  is the ionization energy of the atoms or molecules,  $g$  is the rate of loss of electron,  $\rho_{cr}$  and  $\rho_0$  are the critical and pre-ionized densities of the medium. Hence, the breakdown threshold predominantly depends on the ionization energy ( $\varepsilon_i$ ) of the atoms or molecules of the medium. For a gaseous medium like atmospheric air containing N<sub>2</sub>, O<sub>2</sub> as major molecules with huge number of ambient impurities, the element with least  $\varepsilon_i$  generates the seed electrons for breakdown [16, 25].

Hence, the breakdown threshold with ns and ps pulses is observed to happen around  $10^{10}$  W/cm<sup>2</sup> and  $10^{12}$  W/cm<sup>2</sup>, respectively [23, 25].

Under different focusing conditions, the number of molecules of atmospheric air available at focal volume will vary drastically, leading to varying pre-ionized density ( $\rho_0$ ) of the medium. This in turn will change the breakdown threshold ( $I_{br}$ ). Under tighter focusing conditions having low focal volume, the ionization will be more due to higher ratio of photons to atoms in focal volume. At the same time, the electron loss due to diffusion out of focal volume is also more. Hence,  $g$  and  $I_{br}$  are relatively higher compared that of loose focusing conditions. By varying the intensity, the dynamic interplay between the plasma temperature and recombination of the plasma species ( $n_e, n_i$ ) will be different. This eventually leads to plasma with different initial temperatures that expand into ambient atmosphere in turn launching acoustic shock waves propagating with varying parameters. Therefore, the evolution of the ASW parameters at different laser intensities is presented here.

In both ns and ps-LIB, the arrival time decreases with increasing incident laser intensity as shown in fig. 3.10(a), (b). For ns-LIB, at f/19 focal number the arrival time decreases from 227.2 to 220.2  $\mu$ s. For ps-LIB, at f/14 focal number, the arrival time decreases from 234.8 to 232.4  $\mu$ s. With decay of plasma the  $A_t$  comes down. Acoustic pulse width ( $W_t$ ) indicates the duration over which plasma expansion is supersonic. With increasing laser energy (intensity),  $W_t$  increases monotonically. This is in agreement with the self-emission or plasma plume expansion with increasing laser energy [14]. For a given focal number, as the laser energy increases, the  $W_t$  increases, for both the ns and ps-LIB, shown in fig. 3.10 (a), (b).

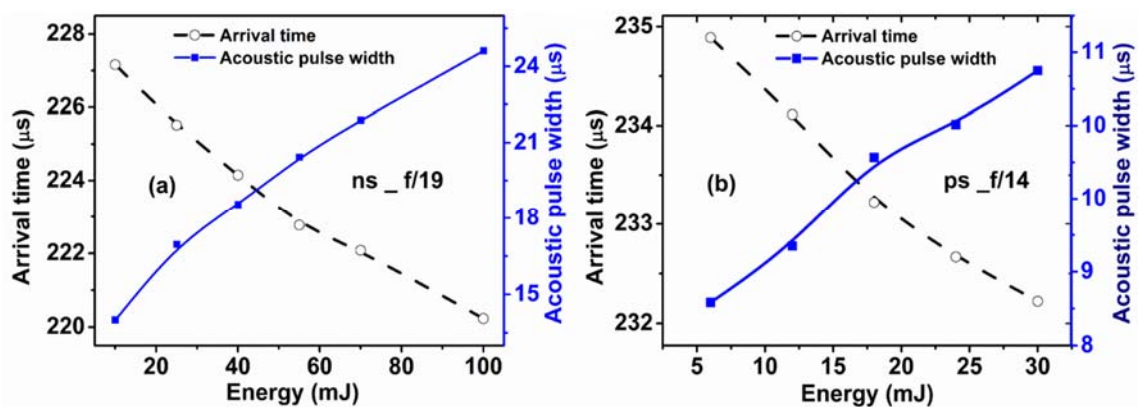


**Fig. 3.10.** Arrival time and acoustic pulse widths of ASW w.r.t incident laser energy. (a) ns LIB, f/19 and (b) ps LIB, f/14 focal geometry.

Arrival time ( $A_t$ ) is observed to be proportional to the lifetime of plasma and to its decay time due to diffusion or recombination.  $A_t$  and  $W_t$  shows the strength of the pressure gradient between plasma and

ambient atmosphere. At a given laser energy as focal number increase from  $f/10$  to  $f/38$ , acoustic pulse width and decay times are decreasing from 24.14 to 18.01  $\mu\text{s}$  and 22.8 to 14.34  $\mu\text{s}$ , respectively, indicating that life time and decay time of ASW are intensity dependent.

For ns-LIB, the ASW peak to peak pressures are 1.7, 2.7, 3.4, 3.8, 4.4 and 4.9 kPa at the laser energies of 10, 25, 40, 55, 70 and 100 mJ, respectively for  $f/25$ . This shows that as the laser energy increases, the peak to peak pressures also increase [24]. Similar behaviour is observed for all focusing conditions. The pressures from ps LIB are also proportional to incident laser energy, as observed with ns LIB. For  $f/14$  focal number, the pressures are 0.2, 0.5, 0.9, 1.2, 1.5 kPa at 6, 12, 18, 24, 30 mJ of laser energies, respectively. For ns-LIB, at a constant laser energy of 70 mJ, the pressures are 4.9, 4.43, 4.36 and 3.44 kPa for  $f/10$ ,  $f/18.7$ ,  $f/25$  and  $f/37.5$  focal numbers, respectively, shown in fig. 3.11(a). Whereas for ps-LIB, at 30 mJ of laser energy, the pressures are 1.79, 1.5 and 0.78 kPa for  $f/10$ ,  $f/14$ ,  $f/18$  focal geometries respectively, shown in fig. 3.11(b).

At a particular laser energy, the pressures are high for tighter focusing conditions and low for loose focusing. For tight focal lengths, the acoustic pressures are high because, smaller the focal length, the smaller the dimension of the focal volume, the greater the rate of diffusion of electrons out of it (and these electrons create pressures on surrounding gas molecules) and higher the threshold field [23]. Longer focal lengths are associated with larger spot sizes, lesser intensity, resulting in low acoustic pressures. At a particular focal geometry, as the laser energy increases, there is an increase in electron number density and the temperature gradients produced by plasma. These gradients affect the electromagnetic [25] and mechanical emissions [5] from plasma.

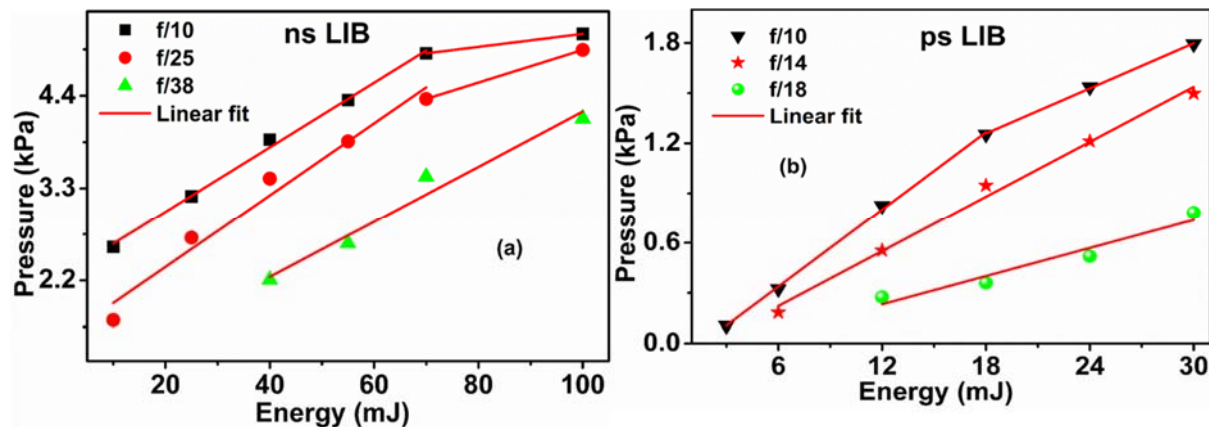


**Fig. 3.11.** ASW pressure variations and linear fits vs incident laser energy for different focal geometries. (a) ns LIB, (b) ps LIB of ambient air.

The peak acoustic pressures have shown an interesting energy dependent evolution. For ns-LIB till 70 mJ of input laser energy, the peak to peak pressure has increased linearly before saturating for higher

input energies. A similar trend is observed for ps-LIB also. Two linear fits with two different slopes for each f/10 and f/25 focal geometries, shown in fig. 3.11 (a). From 10-70 mJ of energy, the fitted line slopes are  $3.8 \times 10^{-2}$ ,  $4.2 \times 10^{-2}$  for f/10, f/25 focal numbers, whereas for f/38 focal number, the slope of fitted line is  $3.3 \times 10^{-2}$ . For f/10 focal number, from 70-100 mJ of energy, the slope is much smaller  $0.7 \times 10^{-2}$ , indicating the saturation of pressure. At lower input laser energies, for longer focal lengths breakdown is not observed. For example, f/38 at 25 mJ, no breakdown is observed and for f/50 condition breakdown is observed at 100 mJ. For ns-LIB the saturation of pressure occurred at 70 mJ for the tighter focal geometries as shown in fig. 3.11(a). While for ps-LIB, the saturation starts only for f/10 focal geometry. These observations are in line with the fact that peak intensities do play a critical role in the breakdown of the medium. At any given laser energy, the pressures come down, as focal number increases. This is due to the fact that, higher energies are required at larger focal numbers to induce breakdown and propagation through the medium. For f/50 focal geometry, at 100 mJ of incident laser energy the ASW pressure is 1.6 kPa. Below 100 mJ no breakdown is observed.

The threshold intensity of any medium mainly depends on the focal number [26]. The ASW parameters gives the information about plasma [24]. There is a change in all ASW parameters as we move from one focal number to another for a particular laser energy. As mentioned earlier, f/10 has more intensity than the other focal numbers. Hence, the ASW produced with high laser intensity reaches the microphone quickly than that produced with lower laser intensities.

The ASW parameters were tabulated for both ns and ps LIB of ambient air for a fixed laser energy of 25 mJ per pulse. As we move from left to right in table, the focal number increases and intensity decrease. As the focal number increases, we can see a clear change in ASW parameters. For f/38 focal geometry, at 25 mJ of energy, there is no ASW signal noticed at our experimental condition.

**Table 3-4.** ns LIB generated ASWs parameters at a fixed laser energy of 25 mJ, for various focal geometries.

<b>ns-LIB@25 mJ</b>	<b>f/10</b>	<b>f/19</b>	<b>f/25</b>	<b>f/38</b>
Arrival time ( $\mu$ s)	222.8	225.5	227	No ASW signal
Pressure (kPa)	3.2	3.1	2.7	
Pulse width ( $\mu$ s)	17.7	17	14.9	
Signal energy ( $\mu$ J)	3.4	3	2.1	
Decay time ( $\mu$ s)	14.3	13.5	12	

As focal number increases, the acoustic pulse width decreased for both ns and ps LIB generated ASWs, as shown in table 3-4 and 3-5.

**Table 3-5.** ps LIB generated ASW parameters at 25 mJ of incident laser energy.

<b>ps-LIB@25 mJ</b>	<b>f/10</b>	<b>f/14</b>	<b>f/18</b>
Arrival time (μs)	231.6	232.8	235.8
Pressure (kPa)	1.54	1.2	0.52
Pulse width (μs)	10.8	10.2	9.3
Signal energy (μJ)	0.5	0.3	0.05
Decay time (μs)	12.5	11	10.5

Signal energy is the energy carried by the ASW [27] and indicates the conversion efficiency of laser energy to acoustic energy. Higher the laser intensity, higher the signal energy and it is inversely proportional to the focal number. Though the values of ASW parameters are different, the evolution of the parameters is observed to follow the same trend for both ns- and ps-LIB.

Increase and decrease of selective ASW parameters indicates the growth in electron density, pressure, temperature inside the plasma. There is considerable rise in signal energy along with incident laser energy indicating a good conversion of optical energy into mechanical energy and it is valid for all focal numbers, as shown in fig. 3.12.

Conversion of laser energy into acoustic energy ( $\omega_{ac}$ ) can be estimated from ASW parameters using [10] the equation given below:

$$\omega_{ac} = \frac{4\pi r^2 p^2 \tau_{ac}}{\rho c} \text{ -----(4)}$$

Where,  $p$  is acoustic peak pressure,  $\tau_{ac}$  is acoustic pulse width,  $r$  is source to receiver distance and  $\rho c$  is the acoustic impedance of the medium. The incident laser energy is of the order of milli Joules (mJ), whereas the obtained acoustic energy from plasma is in micro Joules. The energy difference indicates that the laser energy is conserved by generating other forms of energy like heat, radiation, optical (scattering, transmissions), RF emissions, etc. [5-7, 25, 28, 29].

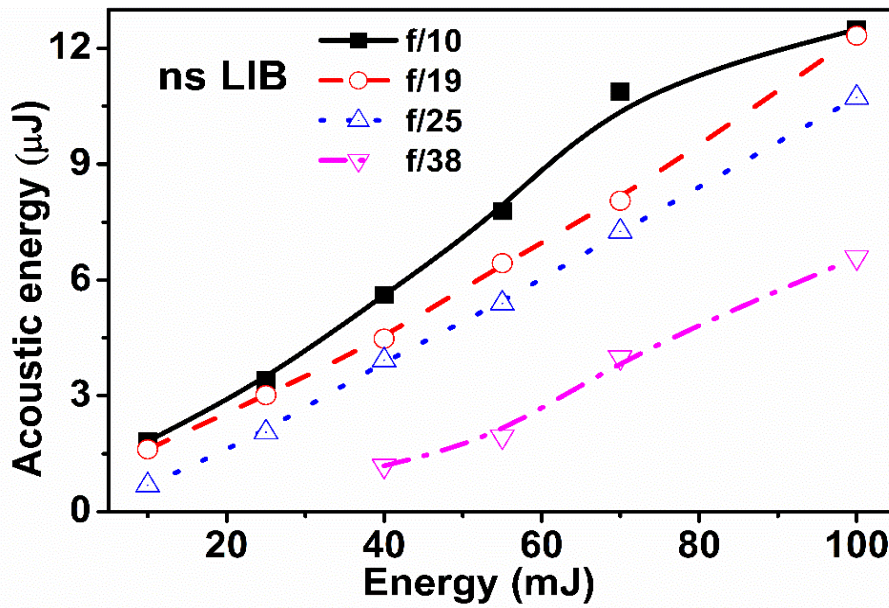


**Fig. 3.12.** Acoustic signal energy vs Laser energy at f/10, f/19, f/25, f/38 focal numbers, from ns LIB of air, lines are guided to the eye.

Though air is transparent at 532 nm, due to breakdown of air, the evolving plasma during the laser pulse and the diffusion and recombination of plasma density, absorption increases. The laser light absorbed by plasma increases the ionization of remaining neutrals and increases the energy of the ions. At very high incident laser energies (beyond the range of laser energies used in the study), plasma acts as a shield for incident light. However, a portion of the incident laser energy before focusing ( $E_{in}$ ) will transmit through the breakdown point as residual energy ( $E_R$ ). These residual energies are function of incident laser energy and wavelength [5]. Table 3-6 shows the residual energy and the percent of absorbed energy at the breakdown region.

**Table 3-6.** Residual energy of ps laser pulses after focal point at different laser energies at a given ps input laser pulse energies.

$E_{in}$ (mJ)	$E_R$ (mJ)	% of absorbed energy $\frac{E_{in}-E_R}{E_R} \times 100$ (532 nm)
3.21	3.01	6.3
5.93	5.44	8.27
11.4	9.71	14.83
17.6	15.1	14.21
23.3	19	17.4
31.1	25	19.62

At higher incident laser energy, the energy absorption by ps LIB of air is greater than the energy absorbed at lower laser energies (table 3-6). This absorption will represent higher conversion efficiency at higher laser energies, as shown in fig. 3.13(b). At higher intensities the distribution of plasma to surrounding atmosphere is more compared to the plasma formed at lower intensities [29]. At higher laser energies, the plasma density is more than the density formed at lower energies [6, 7], so these plasma species absorb more energy and allows less transmission of laser energy through the plasma. Ratio of the acoustic energy to the incident laser energy gives the gain or conversion factor [30].

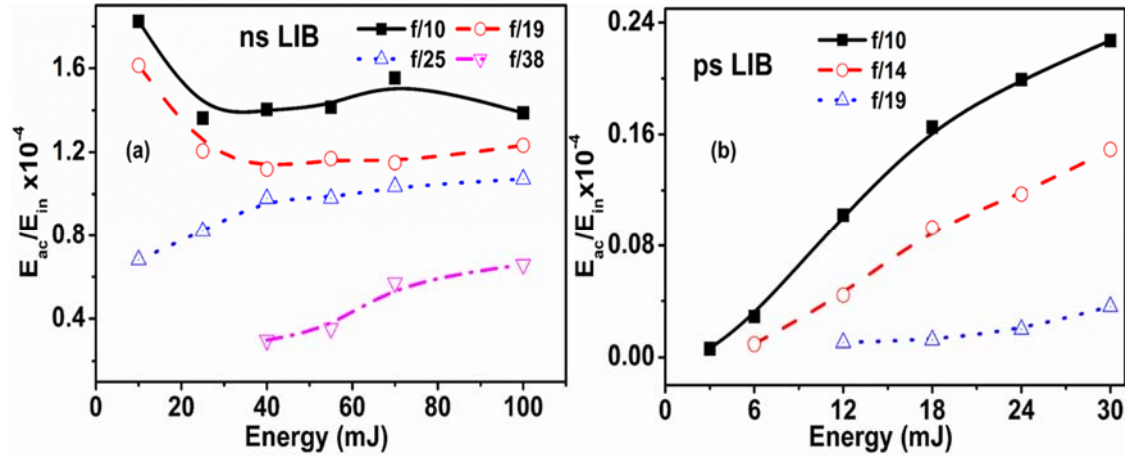


**Fig. 3.13.** Ratio of  $E_{ac}$  and  $E_{in}$ , (a) ns LIB, (b) ps LIB at various laser energies and focal numbers.

For ns-LIB, for loose focusing (f/38) the conversion efficiency of laser energy ( $E_{in}$ ) to acoustic energy increases from 40 to 100 mJ. While for f/25 focusing geometry, the  $E_{ac}/E_{in}$  increased linearly until 40 mJ before becoming constant. Interestingly, for f/19 and f/10 focusing conditions the  $E_{ac}/E_{in}$  decreases till 40 mJ before remaining almost constant. However, beyond 40 mJ, the  $E_{ac}/E_{in}$  increases by 2-5 times while traversing from loose focusing geometry (f/38) to tighter focusing geometry (f/10). This clearly indicates the role of laser intensity on the acoustic energy. In contrast to ns-LIB, for ps-LIB for all the focusing geometries, the  $E_{ac}/E_{in}$  increases with input laser energy, in agreement with earlier reports [30, 31]. The role of laser intensity on the increasing acoustic energy is evident as we traversed from f/19 to f/10 focusing conditions, with  $E_{ac}/E_{in}$  increasing by 4 times.

### 3.6 Frequency analysis

The upper frequency limit of the acoustics is determined by the mean free path of air molecules [34]. With increasing laser energy for any given focal geometry, two frequency peaks with different amplitudes were noticed in ns-LIB, whereas only one frequency peak was observed in ps-LIB.

Peak 1 and peak 2 of ns-LIB and ps-LIB decay with laser energy for all focal numbers, as shown in fig. 3.14(a), (b), (c). As laser intensity increases, the dimension of the plasma increases [5], this leads to rise in the acoustic pulse width, which is inversely proportional to the frequency of acoustic emissions [10, 32] due to which the peak frequency shifts towards the lower frequency side. The trend of change in frequencies for all focal numbers is presented in fig. 3.14. As focusing moves from tight to loose, the frequency range is increases, as shown in fig. 3.14. The spectral analysis of ASWs from LIB of air can be helpful for real time diagnostics of plasma parameters [10]. The ionization is a function of intensity. For ps-LIB, the pulse intensity is higher than the ns-LIB, the plasma constitutes more of electrons, ions and lesser neutrals [17, 18]. Therefore, interaction of neutral particles with surrounding ambient atmosphere is less. Therefore, it produces the low acoustic pressures than that of the ns-LIB. The broad spectral range of ASW frequencies cannot be obtained by other conventional sources of acoustic radiation [10].

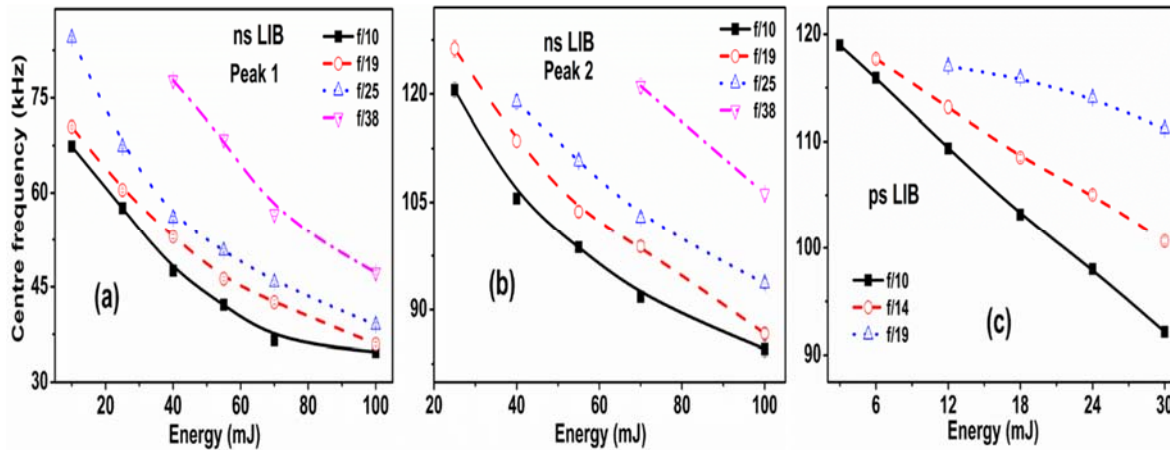


**Fig. 3.14.** Central peak frequencies for various laser energies for both (a) ns LIB peak-1, (b) ns LIB peak-2 and (c) ps LIB of air.

### 3.7 Summary:

Investigations on propagation of ASW from LIB by focusing ns and ps laser pulses in atmospheric air is presented. The analysis of microphone signal levels was done and compared for both ns and ps lasers. The studies have establish a relationship between the ASW parameters and laser pulse parameters in which the acoustic detection method can be used in real-time monitoring of laser matter interaction. Also the peak frequencies of both ns and ps acoustic pulses are observed to be distinct indicating the distinct plasma formation mechanisms. Under same laser energies, the ns pulses have shown better conversion of optical energy to acoustic frequencies compared to ps pulses. While with ps pulses, that deliver two orders of magnitude higher peak intensities than the ns laser pulses,

localization of acoustic spectrum towards higher frequencies (60-70 kHz) with less peak pressures is observed. This brings out the different decay mechanisms for the plasma generated using ns and ps pulses. The ASWs were found to be more intense and longer with increasing laser energy for both the cases.

Evolution of ASWs from ns and ps LIB of air, as a function of laser intensities achieved via different focusing conditions were presented clearly. The role of breakdown mechanism for ns- and ps-LIB are observed to play a major role in the acoustic properties and the evolution of the central frequencies that followed the plasma profile due to the breakdown. For any given laser energy, as we traversed from loose focusing conditions to tighter focusing conditions, the central frequencies were observed to remain almost same with increasing power spectral density. The spatial distribution of the ASWs around the breakdown region is found to be almost spherical with similar central frequencies. Moreover, the observed broad band frequencies are widespread in comparison with traditional acoustic sources with a uniform spatial distribution. Conversion ratio of the laser energy to acoustic energy is presented. We can optimize the ASW frequencies, which varies from audible to ultra-sonic range by varying the laser pulse energies and pulse-width.

These studies have established a relationship between the ASW parameters and laser pulse parameters in which the acoustic detection method can be used in real-time monitoring of laser matter interaction and can augment the traditional LIBS technique. Using ASW parameters, we can study the plasma properties from long distances.

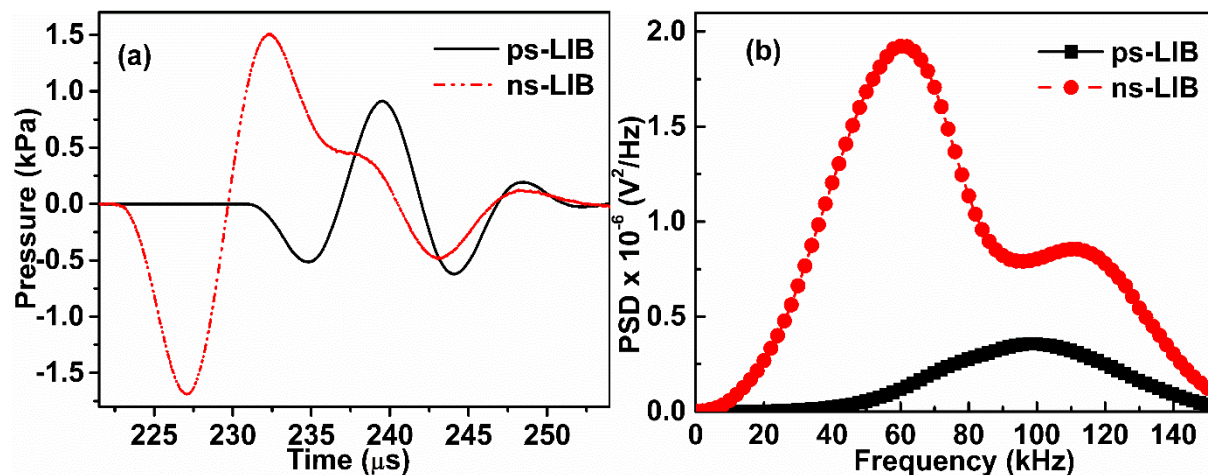


**Fig. 3.15.** ns- and ps- LIB generated ASWs, (a) temporal representation, (b) spectral representation.

### 3.8 References:

1. Q. Qin and K. Attenborough, "Characteristics and application of laser-generated acoustic shock waves in air," *Applied Acoustics* **65**, 325-340 (2004).
2. N. Hosoya, M. Nagata, and I. Kajiwara, "Acoustic testing in a very small space based on a point sound source generated by laser-induced breakdown: Stabilization of plasma formation," *Journal of Sound and Vibration* **332**, 4572-4583 (2013).
3. J. C. van den Heuvel, V. Klein, P. Lutzmann, F. J. M. van Putten, M. Hebel, and H. M. A. Schleijsen, "Sound wave and laser excitation for acousto-optical landmine detection," in (2003), 569-578.
4. J. Gomez Bolaños, V. Pulkki, P. Karppinen, and E. Hægström, "An optoacoustic point source for acoustic scale model measurements," *The Journal of the Acoustical Society of America* **133**, EL221 (2013).
5. C. Leela, S. Bagchi, V. R. Kumar, S. P. Tewari, and P. P. Kiran, "Dynamics of laser induced micro-shock waves and hot core plasma in quiescent air," *Laser and Particle Beams* **31**, 263-272 (2013).
6. E. Schwarz, S. Gross, B. Fischer, I. Muri, J. Tauer, H. Kofler, and E. Wintner, "Laser-induced optical breakdown applied for laser spark ignition," *Laser and Particle Beams* **28**, 109-109 (2010).
7. S. S. Shiva, C. Leela, P. P. Kiran, C. D. Sijoy, and S. Chaturvedi, "The effects of electron thermal radiation on laser ablative shock waves from aluminum plasma into ambient air," *Physics of Plasmas* **23**, 053107 (2016).
8. D. A. Webster and D. T. Blackstock, "Finite-amplitude saturation of plane sound waves in air," *The Journal of the Acoustical Society of America* **62**, 518-523 (1977).
9. E. Hecht, *Optics* (Addison-Wesley, 2002).
10. N. P. Krasnenko, S. V. Shamanaev, and L. G. Shamanaeva, "Propagation of laser-induced shock waves in the atmosphere," *IOP Conference Series: Earth and Environmental Science* **1**, 012013 (2008).
11. S. V. Shamanaev, "Sound generation by breakdown plasma formations initiated by solid aerosol particles upon exposure to laser radiation," *Russian Physics Journal* **44**, 1256-1262 (2001).
12. J. Diaci and J. Mozina, "A study of blast waveforms detected simultaneously by a microphone and a laser probe during laser ablation," *Applied Physics A Solids and Surfaces* **55**, 352-358 (1992).
13. S. Palanco and J. Laserna, "Spectral analysis of the acoustic emission of laser-produced plasmas," *Appl. Opt.* **42**, 6078-6084 (2003).
14. S. Conesa, S. Palanco, and J. J. Laserna, "Acoustic and optical emission during laser-induced plasma formation," *Spectrochimica Acta Part B: Atomic Spectroscopy* **59**, 1395-1401 (2004).
15. J. Holland, *Sound Waves and their Properties in the Surrounding Media* (American Sound Press, Lexington, 1985).
16. Y. R. Shen, *The Principles of Nonlinear Optics* (Wiley, 1984).
17. L. Vinoth Kumar, E. Manikanta, C. Leela, and P. Prem Kiran, "Spectral selective radio frequency emissions from laser induced breakdown of target materials," *Applied Physics Letters* **105**, 064102 (2014).
18. P. Mulser, R. Sigel, and S. Witkowski, "*Plasma production by laser*," *Physics Reports* **6**, 187-239 (1973).
19. X. Chen, L. Cheng, D. Guo, Y. Kostov, and F.-S. Choa, "Quantum cascade laser based standoff photoacoustic chemical detection," *Opt. Express* **19**, 20251-20257 (2011).

20. R. M. White, "Generation of Elastic Waves by Transient Surface Heating," *Journal of Applied Physics* **34**, 3559 (1963).
21. T. Zyung, H. Kim, J. C. Postlewaite, and D. D. Dlott, "Ultrafast imaging of 0.532- $\mu\text{m}$  laser ablation of polymers: Time evolution of surface damage and blast wave generation," *Journal of Applied Physics* **65**, 4548-4563 (1989).
22. W. P. Leung and A. C. Tam, "Noncontact monitoring of laser ablation using a miniature piezoelectric probe to detect photoacoustic pulses in air," *Applied Physics Letters* **60**, 23-25 (1992).
23. C. DeMichelis, "Laser induced gas breakdown: A bibliographical review," *Quantum Electronics, IEEE Journal of* **5**, 188-202 (1969).
24. E. Manikanta, L. Vinoth Kumar, P. Venkateshwarlu, C. Leela, and P. P. Kiran, "Effect of pulse duration on the acoustic frequency emissions during the laser-induced breakdown of atmospheric air," *Appl. Opt.* **55**, 548-555 (2016).
25. L. Vinoth Kumar, E. Manikanta, C. Leela, and P. Prem Kiran, "Effect of laser intensity on radio frequency emissions from laser induced breakdown of atmospheric air," *Journal of Applied Physics* **119**, 214904 (2016).
26. V.E. Mitsuk, V.I. Savoskin, and V. A. Chernikov, "BREAKDOWN AT OPTICAL FREQUENCIES IN THE PRESENCE OF DIFFUSION LOSSES," *ZhETF Pisma Redaktsiiu* **4**, 129-131 (1966).
27. L. Grad and J. Možina, "Acoustic in situ monitoring of excimer laser ablation of different ceramics," *Applied Surface Science* **69**, 370-375 (1993).
28. K.-H. Leitz, B. Redlingshöfer, Y. Reg, A. Otto, and M. Schmidt, "Metal Ablation with Short and Ultrashort Laser Pulses," *Physics Procedia* **12**, 230-238 (2011).
29. S. S. shiva, "Numerical Investigations of ns Laser Induced Shock Waves from Aluminum and Air," (University of Hyderabad, Hyderabad, india, 2016).
30. P. Cristian and A. W. David, "Time-resolved dynamics of nanosecond laser-induced phase explosion," *Journal of Physics D: Applied Physics* **42**, 155503 (2009).
31. F. Wang, Y. Zhang, H. Yao, and B. Yuan, "Real time NDE of laser shock processing with time-of-flight of laser induced plasma shock wave in air by acoustic emission sensor," *Applied Acoustics* **71**, 739-742 (2010).
32. S. Shamanaev and L. Shamanaeva, "Analysis of spectra of acoustic signals generated by high-power pulsed laser radiation propagating in the atmosphere. I. Spectra of local plasma formations," *Russian Physics Journal* **48**, 1188-1196 (2005).

This page is intentionally left blank

## **CHAPTER 4 : ASW emissions from LIB of various materials**

---

### **Abstract:**

In this chapter, the results from focusing laser pulses of both ns and ps duration on target materials of metals, dielectrics, insulators and compacted copper micro powders to generate LIB is presented. Under various experimental conditions we have presented the time domain and frequency domain analysis of the acoustic signals. The evolution of ASW parameters as a function of laser energy is presented for each material. The resulting ASW pressures are proportional to the crater dimensions. The ASW signal is divided into two parts and studied to understand the laser-matter interaction.

The relation between ASW strength and density fluctuations caused by ionized species in surrounding atmosphere was studied. Comparisons made between the fresh spot area of sample interaction (each laser pulse falls on virgin area of sample) and shot on shot method (selective number of laser shots are incident on same spot area). Lorentz fitted frequency peaks are plotted for various samples.

### **4.1 nano second LIB**

When nano second laser pulses have intensity above the breakdown threshold of a particular medium it results in breakdown and ablation of material [1]. In short pulse (nano second) laser ablation, the formation of plasma is associated with the processes of heat conduction, melting, melt expulsion, melt deposits, evaporation and creating a high pressure and temperature gradient, shown in fig. 4.1.

If the supplied laser fluence is greater than the breakdown threshold value of material, then breakdown is initiated and it further develops and forms a state of ionized species and finally forms the plasma plume above the target surface [2]. After breakdown, the electrons, ions, neutrals and high temperatures will develop within the plasma. Because of good thermal

conductivity of the metal, the heat generated at the focal point is transferred to surroundings including both metal and surrounding atmosphere. It causes melting, then vaporization and finally good amount of material is expelled from the focal spot and is called ablation. After saturation of the ablation, plasma works as a shield to the incident laser energy [3]. The ambient gas allows laser light (532 nm) through it, whereas the ionized gas absorbs and reflects the laser light. At this stage, the laser energy absorption takes place by the plasma and there is a huge rise in plasma density and temperature.

This discontinuity in pressure and temperature with respect to ambient atmosphere causes the plasma to expand into surrounding atmosphere [4, 5] with higher velocities and creates a large pressure and temperature gradient. This plasma in the initial time scales (upto few hundreds of ns) while coming to an equilibrium with surroundings, depending on the energy will generate mechanical stress which is dependent on the electrical and thermal conductivities of the metal targets. These high pressure gradients launch shock waves up to few 100 ns that are converted into acoustic shock waves (ASW) after a few tens to hundreds of microseconds due to air friction. The measurements associated with the acoustic emission are, the signal energy [6] and arrival time [7] of ASW, which were utilized to know the peening quality of the sample. Both thermal and dielectric breakdown of materials generate acoustic emissions, that can be captured by a calibrated microphone [8]. The acoustic detection technique is used to understand the laser-matter interaction to monitor ablation quality [9]. These intense pressure waves can be used in many critical places to trigger electronic devices and resonate complicated structure, conference halls [10], metal impedance tubes [11], scaled sealed structures etc. [12], laser cleaning (removal of encrustations) [13], surface treatment, underground land mine detection, [14] to name a few.

So, here we present ASW parameters such as peak pressures, arrival times, acoustic pulse width, decay time, signal energy and central frequencies as a function of laser energy and target materials. We attempted to establish a relation between material properties and the ASW parameters. These ASWs from material plasma are different from air plasma. The major difference is in the plasma temperature and density. These two parameters decide the energy dynamics and their relaxations via collisions, which in turn determine the emissions.

Understanding of LIB of materials is more complicated than LIB of air. The plasma species such as number of electrons, ions, neutrals and plasma temperatures are very high in a material plasma in comparison with air plasma. During ns-LIB of solid targets the plasma formed will

lead to melt expulsion, and deposition and the heat conduction through the material that can form cracks etc. all these phenomena will make the dynamics of emissions more challenging compared to the plasma dynamics from gaseous samples.

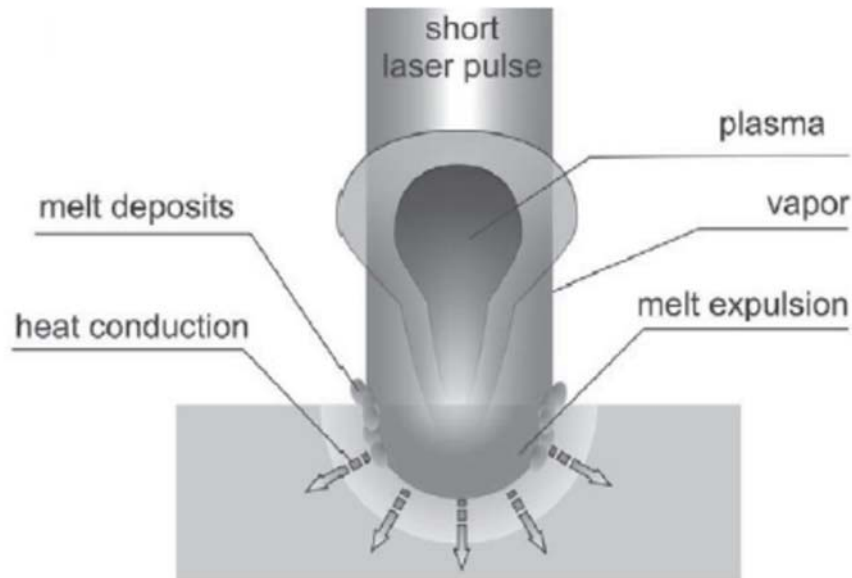


**Fig. 4.1.** nano second laser pulses and target sample interaction [15]. During laser matter interaction, the associated phenomena are also presented.

Target samples used to study the laser matter interaction through the acoustic emissions are conductors (Al, Cu, Brass, and SS-304), insulators (PVC, Teflon, Alumina-90% dense), dielectrics (Mica, Barium Titanate, Zirconium Tin Titanate,  $\text{LiNbO}_3$ ) and copper powder pellets of various densities and particle sizes (2, 425  $\mu\text{m}$ ). The properties of materials like melting and boiling points influences the threshold fluence for ablation [16]. The threshold fluences for Al and Cu are 1.30 and 1.61  $\text{J}/\text{cm}^2$ , respectively at 532 nm wavelength. Cabalin et.al, reported the, saturation fluences for Al and Cu as 6.6 and  $>40$   $\text{J}/\text{cm}^2$  [16]. The fluences we have used are in the range of (26 to 265  $\text{J}/\text{cm}^2$ ) and higher than the above literature reported values. The fluence range used in our study allowed us to understand the ASWs from breakdown threshold and beyond the saturation fluences. If enough laser energy is incident on any metal sample surface, the layer of metal is heated and vaporized. This vapour gets ionized by absorbing the trailing edge of the laser pulse and forms plasma. The vapour which is adjacent to plasma can launch a strong shock wave into the neighbouring atmosphere. The propagation of shock also causes the breakdown of molecules for stronger shock. This is the phenomena of laser supported detonation (LSD) waves [17]. This makes our experiments mimic the laser supported micro detonation wave in lab scale.

Metals are surface absorbers, with low ionization potential, high absorption coefficient and high electron number density. Hence, the LIB of metals generates more electron density, ion density and plasma temperature than the LIB of a gas medium.

In this section the ASW from ns-LIB of metallic/alloys samples is studied under similar experimental conditions (input laser energy, focusing geometry and source-receiver distance) to understand the role of material parameters on ASW. The physical properties of samples we have used are tabulated in table 4-1.

**Table 4-1.** Physical properties of materials from literature.

Sample	Density g/cm <sup>3</sup>	Electrical conductivity (S/m)	Thermal conductivity (W/m.K)	Melting point (M) K
SS 316 LN	7.4	1.35 * 10 <sup>6</sup>	16.2	1633
SS304	7.92	1.4 * 10 <sup>6</sup>	16.2	1633
Brass	8.56	1.67 * 10 <sup>7</sup>	111	1170-1210
Aluminium	2.70	3.5 * 10 <sup>7</sup>	204	933
Copper	8.96	5.96 * 10 <sup>7</sup>	386	1356
Alumina (Al <sub>2</sub> O <sub>3</sub> )	3.95	10-15	30	2345
Naphthalene (C <sub>10</sub> H <sub>8</sub> )	1.16	10-16	0.12	353
PVC (C <sub>2</sub> H <sub>3</sub> Cl) <sub>n</sub>	1.38	10-14	0.19	373-473
Teflon (C <sub>2</sub> F <sub>4</sub> ) <sub>n</sub>	2.2	10-24	0.25	600
Glass (Borosilicate)	2.203	10-13	1.05	1921
Mica	1.9	10-15	0.71	1773
Lithium Niobate (LiNbO <sub>3</sub> )	4.63	10-12	4	1513
Barium Titanate (BaTiO <sub>3</sub> )	4.49	10-9	2.85	1898
Zirconium Tin Titanate (ZrSnTiO <sub>4</sub> )	4.33	10-6	-	-

Literature reported thermal conductivity [16], electrical conductivity, density [18], melting point, boiling point of Al, Cu, Brass and SS [19] are used to understand the laser mater interaction phenomena. It helps to compare the material properties to the ASW parameters.

### 4.1.1 Metals and alloys

In this section, the ASW properties due to LIB of commonly used metals (Al, Cu) and alloys (Brass, SS 304) are presented. The focal length of the lens (80 mm) and the microphone distance from LIB source is kept constant at 7.5 cm for all samples. Here the experimental schematic is different from the LIB of ambient air setup. In LIB of air, the microphone is placed normal to the plasma at a distance. For the material targets the microphone is at  $45^\circ$  w.r.t incident laser direction and target. The targets are mounted on a translation stage to ensure that each laser pulse interacts with a fresh target surface. The experimental schematic is presented in fig. 4.2

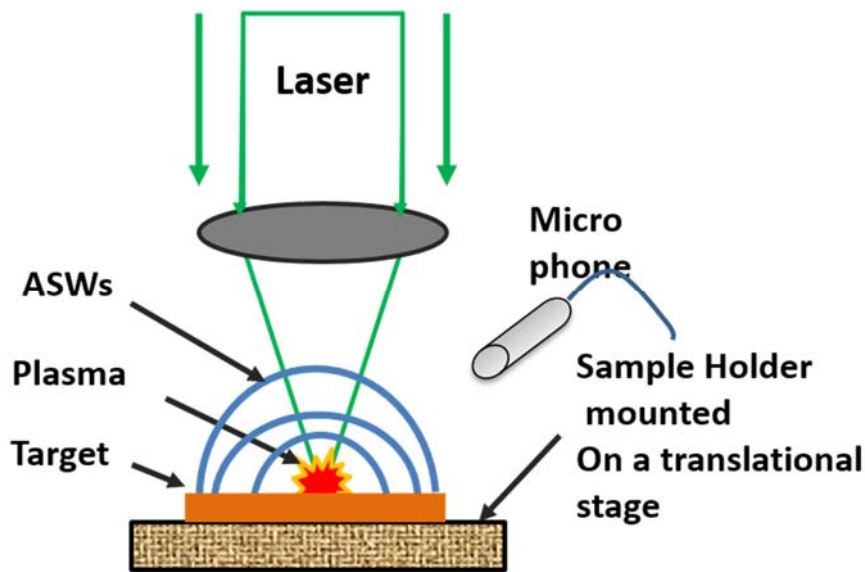


**Fig. 4.2.** Schematic of LIB of materials. The position of microphone, target, sample holder (mounted on a translation stage), ASWs are shown.

Ambient air at atmospheric pressure is the background gas. The emitted ASW signal from ns-LIB of aluminium (Al) target from the plasma at 100 mJ of laser energy, is presented in fig. 4.3. The method of taking measurements of ASW signal, is as presented in Chapter 2. These ASWs are acoustic radiations emitted from plasma, so the associated changes in acoustic parameters reflects the source characteristic properties from long distances.

The acoustic signal consists of two portions, a positive and a negative peak. The line zero in fig. 4.3, is the ambient pressure (100 kPa) and upper, lower part of signal are the fluctuations due to LIB of material about the atmospheric pressure. The ASW pressures we measure are the dynamic pressures caused by the plasma, with reference to atmospheric pressure. As shown

in fig. 4.3, positive upper portion (+ve part) and negative lower portion (-ve part) are taken into account for further analysis of signals.

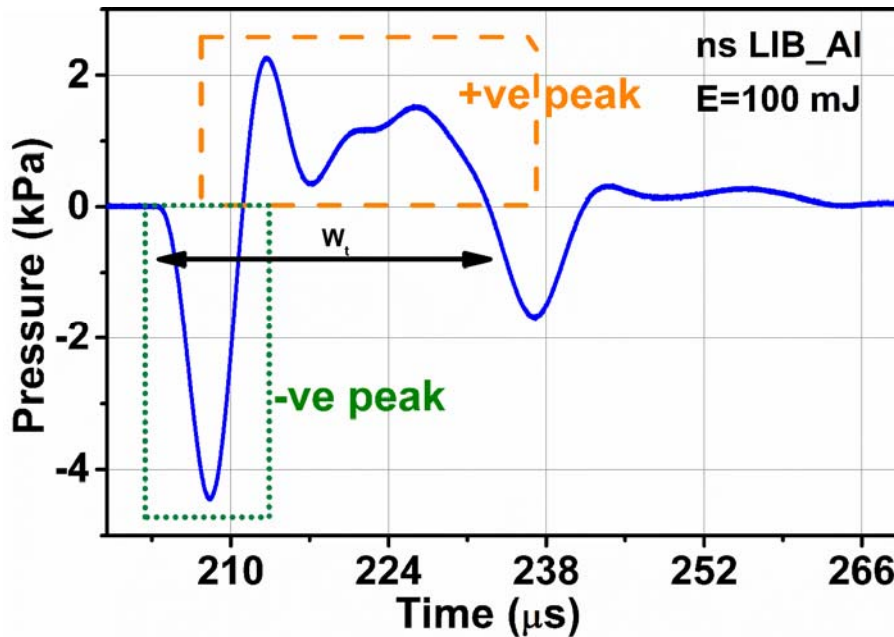


**Fig. 4.3.** Typical time domain ASW signal from ns LIB of Aluminium target at 100 mJ of laser energy per pulse. Plasma- microphone distance is 7.5 cm. X-axis is time and Y-axis is pressure.

The second -ve peak (dip comes at latter time scales) depends on the sample dimension, if the sample is larger in dimension (50 mm or 25 mm), then the height of second -ve peak is observed to increase. Hence, we considered the first -ve and +ve peak (one full wave) for analysis. As shown in fig. 4.3, the two portions have different amplitudes (heights) and widths (difference between the arrival time and the time of +ve peak touching the ambient (zero) pressure line) at different laser parameters. The properties of -ve and +ve parts of ASW signal with respect to incident laser energy are presented in fig. 4.4 and 4.5. The sharp rise in the first -ve peak represents the arrival time of ASW which gives the velocity of ASW. The arrival time of ASW from LIB of Al at different input laser energies, under fixed experimental conditions, is shown in fig. 4.4. The ASW peak pressures emitted from ns- LIB generated Al plasma are 3.67, 5.59, 5.9 and 6.7 kPa and the arrival times are 218.8, 207.2, 206 and 203.6  $\mu\text{s}$  for laser energies of 20, 60, 80, 100 mJ, respectively. As the incident laser energy increases, the ASW pressures from plasma also increases and the arrival time decreases. Lower values of arrival time indicates that ASW is reaching microphone faster. So, the velocity of ASW is increasing [20, 21] with increasing laser energy for a fixed distance of 8 cm between source and microphone. When compared with the LIB of ambient air, ASW pressures of materials are

very high and arrival times are very less under similar experimental conditions. It shows the effect of material target on the ASW properties apart from the incident laser energy. In general, solids have very low threshold values than the ambient air, so a small portion of incident laser energy is used to breakdown the material, the remaining energy is utilized to enhance the plasma. The signal energies of ASWs from ns-LIB of Al are 2.8, 5.59, 6.66,  $10.2 \times 10^{-5}$  (a.u) for 20, 60, 80, 100 mJ energies, respectively. The signal energies are not saturated until 100 mJ and is observed to increase linearly with incident laser energy, so we can achieve pressure signals with good strength by simply increasing laser energy up to 100 mJ.

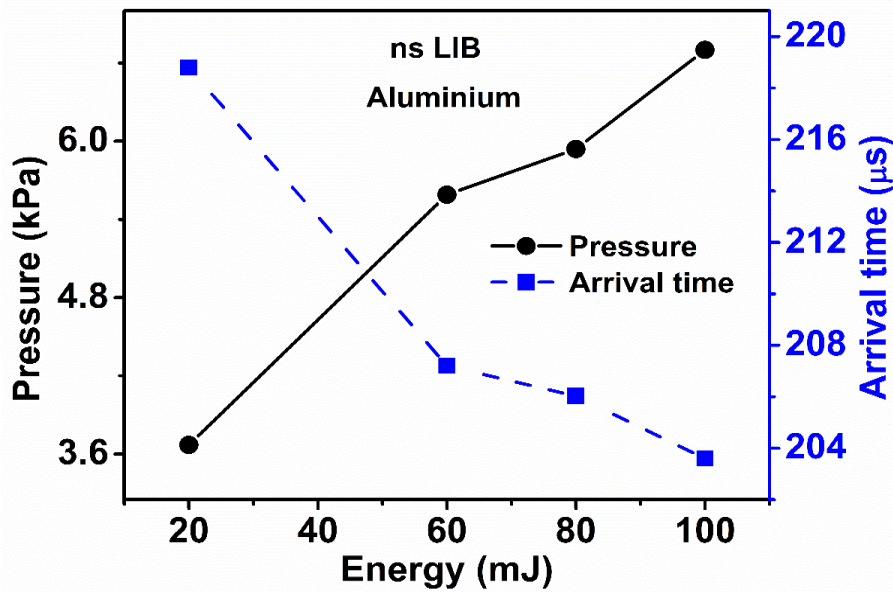


**Fig. 4.4.** Peak pressures and arrival times of ASWs emitted from ablation of Aluminium sample at 20, 60, 80 and 100 mJ energies.

The response of ASWs are different at higher laser energies than the lower energies [22, 23]. As we increase the incident laser flux the following phenomena takes place, surface heating without melting, surface melting and vaporization, linear absorption (ablation), non-linear absorption (ablation), highly dense plasma formation and plasma shielding [21]. These phenomena can be observed through acoustic studies. Change in laser energy affects the plasma properties such as plasma temperature, density and plasma expansion with respect to surrounding atmosphere [24].

The measurements of both  $-ve$  and  $+ve$  portions of ASW signal are different at various experimental conditions, so these give the distribution of information regarding LIB of medium. As the laser energy increases the change in plasma parameters affects the associated acoustic emissions, these changes are represented by peak heights (pressure) and widths of

ASWs. Heights of both +ve and –ve peaks were plotted at various laser energies, shown in fig 4.5. The rate of rise in +ve height is less compare with that of the –ve peak. The height difference is considerable between –ve and +ve parts at any particular laser energy, as presented in fig. 4.5. The –ve peak height varies from 2.23 to 4.46 kPa, i.e almost doubled with increase of input laser energy from 20 to 100 mJ by almost five times. While the +ve peak has varied from 1.44 to 2.26 kPa.

During laser matter interaction, from the conservation of momentum, acoustic signals are generated both inside [25] the material and into the ambient atmosphere. The generation of the acoustic signal inside the target sample is due to thermal expansion and momentum transfer from the ejected particles of the ablated target (plasma) to its surface [26]. Piezo electric transducers are used to detect these acoustic signals, generated inside the material and these are in the range of ultra-sonic frequency range. But here we are interested in ASWs and their properties in ambient atmosphere.

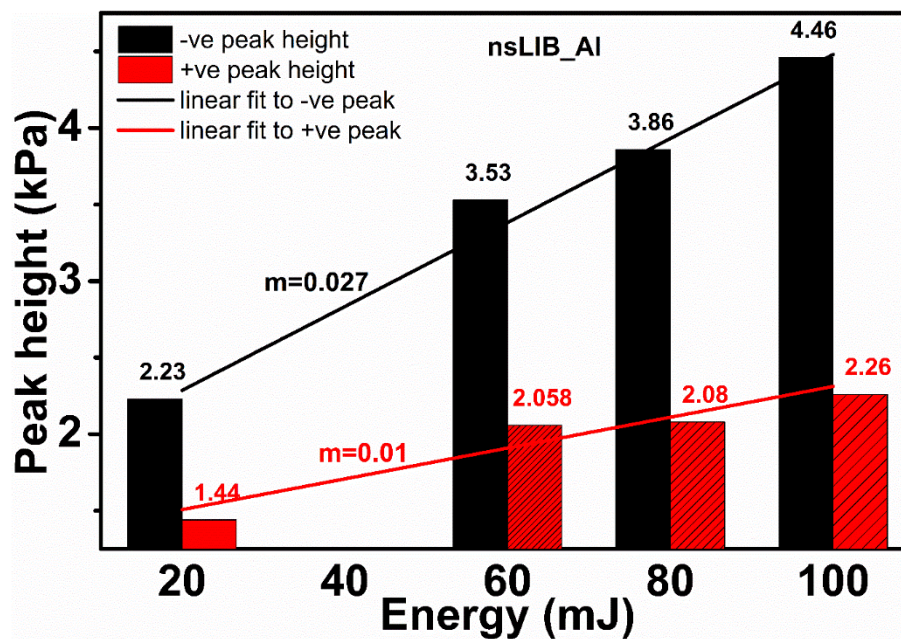


**Fig. 4.5.** Peak heights of –ve and +ve portions of ASW signal at 20, 60, 80 and 100 mJ of incident laser energies for the Al target sample. X- Axis is incident laser energy, Y-axis is Peak height (pressure). The slope of –ve and +ve peak heights are 2.7 and  $1.0 \times 10^{-2}$  respectively as shown by solid lines.

As shown in fig. 4.6, +ve peak width increases from 14.58 to 21.69  $\mu$ s as energy increases from 20 to 100 mJ, respectively. Whereas, the width of –ve portion representing the pressure generated is almost constant with laser energy. So, increasing laser energy enhances

the ablation and results in the density fluctuations in surrounding atmosphere resulting in longer duration of the +ve portion. These density fluctuations are indicated by the +ve peak width of ASW.

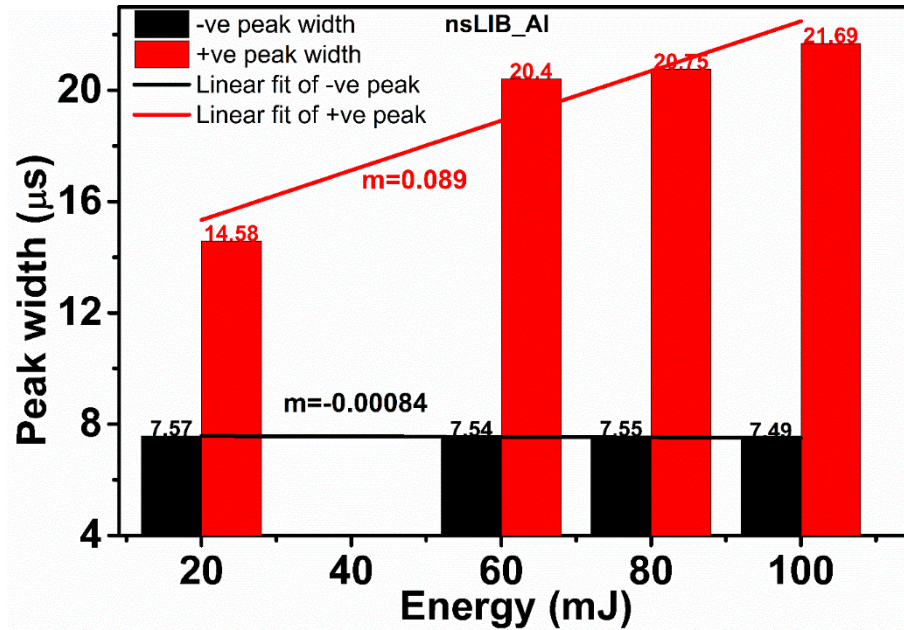


**Fig. 4.6.** Peak widths of both positive (+ve) and negative (-ve) portions of ns-LIB of Al generated ASW. X- Axis is incident laser energy, Y-axis is Peak width. The slopes of -ve and +ve peaks are  $-0.08$  and  $8.9 \times 10^{-2}$ . The slope of -ve peak is almost flat, very close to zero compare with the +ve peak.

Peak height and width together representing the area under the curve of -ve and +ve portions are observed to increase continuously with respect to incident laser energy, as presented in fig. 4.7. The increased rate of area under the curves of both portions is almost similar. This area under the curve is observed to be comparable with the volume of the crater. ns laser pulses form the craters [27] and around the crater, corona formation takes place, depending on the incident laser pulse energy [28]. The liquid phase expulsion and plasma recondensation [29] together causes the crater corona. Since, the experiment is performed in ambient air, the recondensation is high. Crater depth may be saturated at higher laser energies, but the crater volume increases with the increase of laser energy [28]. The area under the curve of +ve peak representing the ablation efficiency increases linearly with increased input laser energy.

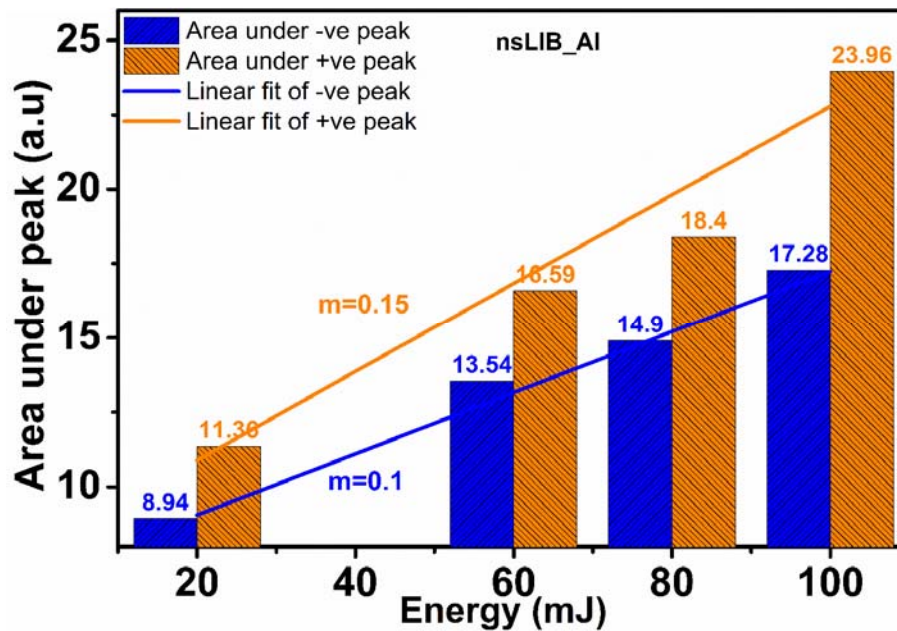


**Fig. 4.7.** Area under both positive (+ve) and negative (-ve) portions of time domain ASW signal, which is radiated from the ns-LIB of Al target sample. X- Axis is laser energy, Y- axis is Area under the curve. The slopes of area under the -ve and +ve peaks are  $10.2 \times 10^{-2}$  and  $14.9 \times 10^{-2}$  respectively. Both are having increasing slopes.

The amplitude of the acoustic signal is proportional to the total amount of material vaporised for each laser pulse [30] when sample is held in a closed chamber. The crater depth and diameters are associated with the absorption of incident laser energy [27] with increasing laser energy the amount of laser energy coupled to the target is observed to increase in our study. From Laser induced breakdown spectroscopy (LIBS) study, the emission signal increases with the incident fluence, it indicates that the amount of ablated material is increased [31].

#### **Comparisons of ASW parameters from LIB of metals and alloys at an energy of 20mJ:**

At a fixed energy of 20 mJ, ASW pressures for ns LIB of Al, Cu, Brass and SS 304 target samples are shown in fig. 4.8. The produced heat energy at focal point doesn't transfer to target surroundings, so target material reaches the boiling point soon and dielectric breakdown will occur and formation of plasma takes place. Metals with high thermal conductivity (Cu), will have lower breakdown threshold, large heat dissipation volume, hence irradiated surface gets vaporized easily. Further laser energy breaks the vapour molecules and forms high temperature plasma [1].

After breakdown, the electrons, ions and neutrals will develop within the plasma. Because of the good thermal conductivity of Cu, the heat generated at the focus point is transferred to the surrounding metal rapidly, melting and evaporating, leading to a good amount of material ablation.

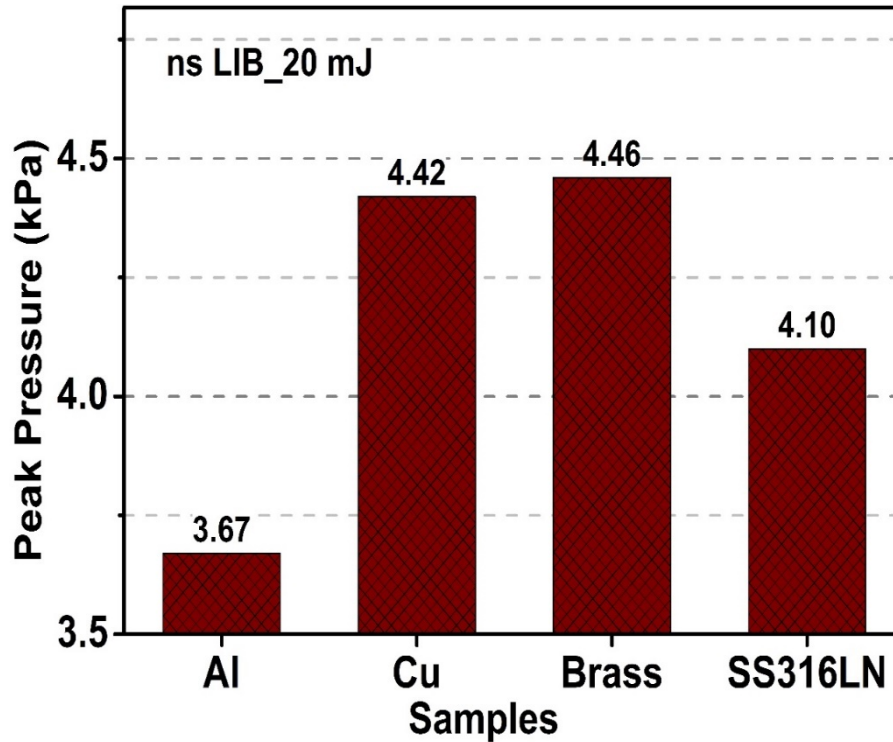


**Fig. 4.8.** Peak pressures from ns-LIB of Al, Cu, Brass and SS 316LN at a fixed energy of 20 mJ at 7.5 cm distance of microphone from plasma. Samples are dimensions of 5 cm × 5 cm, with samples.

Lower thermal conductivity of sample will have higher threshold fluences. In our case, the supplied laser fluences to sample targets is very high than the threshold values. So, the question is where the given extra laser energy is going? Is it leading to high ablation rates or heat radiation or shock pressure conversion? At high fluence, a high temperature plasma is formed and more laser energy can be absorbed effectively into the target surface even if the linear reflectivity is high [31].

Literature reported thermal conductivity [16], electrical conductivity, density [18], melting point, boiling point of Al, Cu, Brass and SS [19] are used to understand the laser material interaction phenomena. It helps to compare the material properties to the ASW parameters.

ASW parameters of LIB of Al, Cu, Brass, SS 316LN samples at input laser energy of 20 mJ, were presented in table 4-2. As presented in table 4-2, peak pressures and –ve peak height

follows the order, such as brass, Cu, SS, Al. Whereas the +ve peak width representing ablation following the order Cu > Brass > Al > SS. This is in line with the electrical and thermal conductivity of the materials that play crucial role in laser absorption and in ablation.

**Table 4-2.** ASW parameters of Al, Cu, Brass and SS316LN samples at a fixed energy of 20mJ.

Sample	Peak-peak Pressure (k Pa)	Arrival time (μs)	Signal energy ( $\times 10^{-5}$ ) a.u	-ve peak height (k Pa)	+ve peak height (k Pa)	-ve peak width (μs)	+ve peak width (μs)
Al	3.67	218.8	2.8	2.23	1.44	7.48	14.58
Cu	4.42	220.5	3.57	2.69	1.73	7.8	20.49
Brass	4.46	219.9	3.4	2.72	1.74	7.63	15.82
SS316	4.1	223	3.66	2.35	1.76	7.33	12.74

Thermal conductivities of SS316LN, brass, Al and Cu are 16.2, 111, 204 and 386 W/m K. Melting points of Al, Cu, Brass and SS316LN are 933, 1356, 1170-1210 and 1645-1670 K. Arrival time is directly following the order of melting point of conductors, i.e SS>Cu>Brass>Al. while the other parameters of  $E_s$ , -ve peak height are not following any specific property. Melting of the material being the first process during laser ablation of the materials the melting point has direct correlation to  $A_r$ .

If we consider only pure metals such as Al, Cu then order of all properties of metals follows the every ASW parameter order. Thermal conductivity, electrical conductivity, density, melting point, boiling point are high for Cu when compare with the Al. As presented in table 4-2, all acoustic parameters are high for Cu than the Al. However, any property of material alone is not effecting ASW parameters, but collectively effects the ablation [15].

Apart from the possible mechanisms discussed in chapter 1, photo chemical mechanism is contrast to photo thermal mechanism which is caused due to longer pulse duration [32]. Ablation rates has great scope in bio research also [33, 34] . Here we are trying to understand the ablation rates by studying acoustic parameters. The delay in arrival time of acoustic wave w.r.t laser pulse helps to estimate the ablation rate [35] more precisely when a PZT is used. The rate of ablation is not always linear to incident laser flux, after a particular flux, ablation varies rapidly then saturates [35]. In our experiments also such a saturation is observed at very high input laser energies.

### 4.1.2 Alloys

As the incident laser energy increases the peak to peak pressures also increases in both of alloys such as Brass and Stain less steel (SS 304). Comparatively, LIB of Brass has ASW pressures and higher area under the curve than the SS304 at higher energies whereas at 10 mJ SS has the more pressure than the Brass.

With increasing laser energy Brass and SS have shown different  $P_k$ - $P_k$  pressures and the evolution of +ve part of acoustic signal. This is in tune with the fact that the acoustic signals indicates the rise in ablation rate [9]. The laser parameters such as spot size, laser fluence and material properties such as target thickness, effects the ablation of material. With increasing laser energy, the ASW parameters increase linearly but with different slopes.

**Table 4-3.** Area under the -ve and +ve portions of ASW signal for both Brass and SS at various laser energies.

Energy (mJ)	Brass		SS	
	Area under -ve part $\times 10^{-6}$	Area under +ve part $\times 10^{-6}$	Area under -ve part $\times 10^{-6}$	Area under +ve part $\times 10^{-6}$
10	10	13.26	9.89	13.5
25	11.97	14.53	10.9	13.8
40	12.79	14.6	13.58	15.94
70	18.32	21.31	16.64	18.5
100	21.36	24.43	18.5	16.13

As the energy increases, the areas under the both -ve and +ve portions increases for both Brass and SS, as shown in table 4-3. At 10 mJ of energy, Brass and SS have same areas of both -ve (10) and +ve (9.89) parts. The difference starts from 25 mJ and continues till 100 mJ. The difference in these areas indicates the different ablation rates under same experimental conditions.

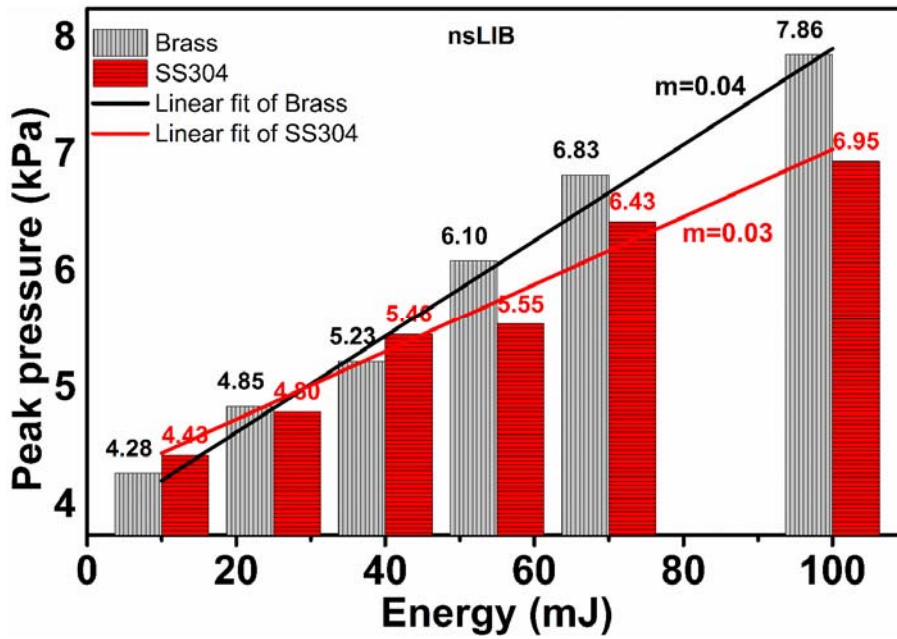


**Fig. 4.9.** Peak-peak pressures of ASWs emitted from the ns-LIB of Brass and SS 304 solid target samples at 10, 25, 40, 55, 70 and 100 mJ of laser energies per pulse. The slopes of Brass and SS304 peak pressures are 4.1,  $2.9 \times 10^{-2}$  respectively. Both materials are having increasing slopes.

### 4.1.3 Dielectrics

In this section we present the ASW parameters from dielectrics Mica,  $ZrSnTiO_4$ ,  $LiNbO_3$ . First we will see the ASW parameters from LIB of Mica as the incident laser energy increases. The thickness layer having  $k^{-1}$  (inverse of absorption coefficient of a dielectric material) is heated and vaporized due to leading edge of laser pulse. Trailing edge of laser pulse will lead to partially ionized hot vapour [17].

As the laser energy increases from 10 to 100 mJ, the peak pressures increases from 4.37 to 7.8 kPa, the arrival time decreases from 230.5  $\mu s$  to 222.9  $\mu s$ , the acoustic pulse width increased from 21.1 to 34.89  $\mu s$  and the signal energy increases from 3.63 to 13.4 (a.u). The sum of  $-ve$  and  $+ve$  peak pulse width is the total acoustic pulse width. The linear fit to arrival time shows the slope of -0.11. The peak pressures and acoustic pulse width are fitted to a linear equation with different slopes, shown in fig. 4.10. The slopes are 0.038 for peak pressure and 0.15 for acoustic pulse width. The signal energy is directly proportional to the square of the pressure [36]. The slope of linear fit to signal energy is 0.11.

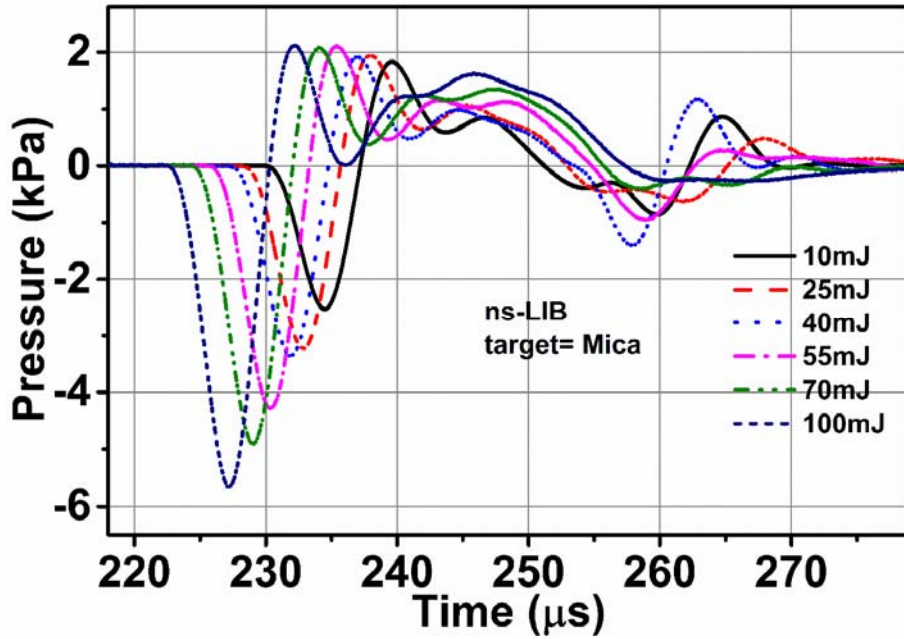


**Fig. 4.10.** Time domain signals of ns-LIB of Mica generated ASWs at various laser energies of 10, 25, 40, 55, 70 and 100 mJ.

The response of ASW parameters follows the same trend with respect to incident laser energy for all dielectrics. The only difference is with the acoustic parameters for various target samples under fixed experimental conditions, as shown in table 4-4.

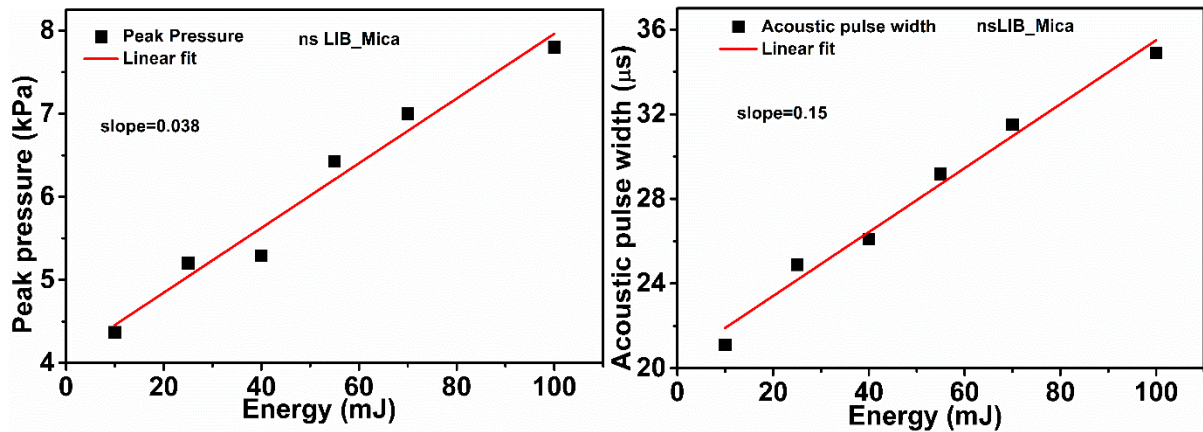


**Fig. 4.11.** Peak pressures and acoustic shock wave pulse width w.r.t incident laser energy for Mica target sample. The linear fit for data is indicated with a line. The slopes are 0.038, 0.15.

Mica has more peak pressure than the  $\text{ZrSnTiO}_4$  and  $\text{LiNbO}_3$ . Signal energy and  $-ve$  peak height follows the peak pressure order.  $+ve$  peak width is high for  $\text{LiNbO}_3$  than the remaining two. FWHM values do not follow the trend of peak pressure and  $+ve$  peak width. Table 4-4 indicates that at a fixed energy the variation in ASW parameters are a function of

other material properties also. For dielectrics, melting point and arrival time follow the same order as observed for metal/ alloy presented in table 4.1

**Table 4-4.** ASW parameters from LIB of dielectrics at 25 mJ of laser energy.

Sample	Peak pressure (kPa)	Arrival time ( $\mu$ s)	Signal energy ( $\times 10^{-5}$ ) a.u	-ve peak height (kPa)	+ve peak height (kPa)	-ve peak width ( $\mu$ s)	+ve peak width ( $\mu$ s)	FWHM of -ve peak ( $\mu$ s)
Mica	5.2	228.8	5.17	3.24	1.95	7.66	17.23	3.86
ZrSnTiO <sub>4</sub>	4.45	234.14	4.06	2.77	1.67	7.42	16.68	3.88
LiNbO <sub>3</sub>	4.39	227.8	3.26	2.69	1.7	7.33	17.8	3.84

### 4.1.4 Insulators

The insulators we have studied are PVC, Teflon, Alumina and Naphthalene. With increasing incident laser energy, the variation in ASW parameters of LIB of PVC is presented in fig. 4.12. As we increase the laser energy, the acoustic pressures from PVC are increasing from 3.5 to 7.83 kPa.

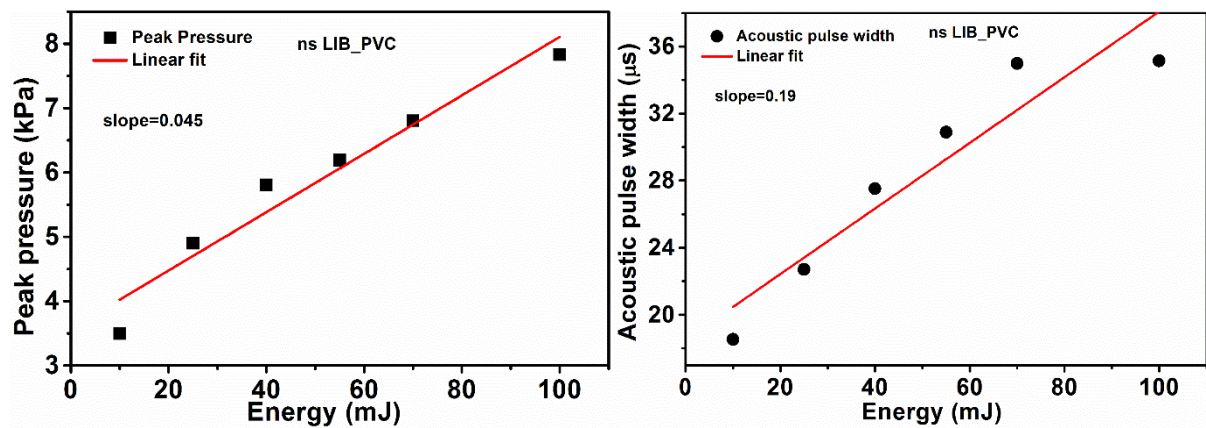


**Fig. 4.12.** Laser energy vs peak pressure and acoustic pulse width for LIB of PVC sample. The slopes are 0.045, 0.19 for peak pressure and acoustic pulse width respectively. Data is fitted to linear equation.

This indicates that there is good conservation of optical energy into acoustic energy. As we have seen in dielectrics, the -ve peak width and +ve peak height are varying differently with laser energy. Amplitude of +ve peak and +ve peak width (duration) changes from one sample to another [37], which indicates that ablation is different for different samples. The

mass removed per pulse is proportional to the incident laser energy [38]. Whereas, the +ve peak width increasing from 11.68 to 27.28  $\mu\text{s}$  and -ve peak height also increases from 1.86 to 5.65 kPa. Increments in ASW parameters such as peak pressure, acoustic pulse width are shown in fig. 4.12. As the laser energy increases the arrival time decreases from 234.8 to 223.7  $\mu\text{s}$ , with a slope of the value -0.11. The slope for linear fit of signal energy is 0.12. The signal energy varied from 2.03 to  $12.77 \times 10^{-5}$  (a.u) by almost six times with laser energy.

**Table 4-5.** ASW parameters from LIB of insulators at 10 mJ of laser energy.

Sample	Peak pressure (kPa)	Arrival time ( $\mu\text{s}$ )	Signal energy ( $\times 10^{-5}$ ) a.u	-ve peak height (kPa)	+ve peak height (kPa)	-ve peak width ( $\mu\text{s}$ )	+ve peak width ( $\mu\text{s}$ )	FWHM of -ve peak ( $\mu\text{s}$ )
PVC	3.49	234.8	2.03	1.86	1.61	6.85	11.68	3.69
Teflon	4.35	231.5	3.12	2.5	1.84	7.17	14.39	3.76
Alumina	3.46	234.7	2.15	1.81	1.65	6.8	11.23	3.66
Naphalene	4.24	232.6	3.28	2.55	1.69	7.25	15.78	3.86

At the laser energy of 25 mJ, the ASWs parameters of insulators were tabulated in table 4-6.

**Table 4-6.** ASW parameters from ns- LIB of insulators at 25 mJ of laser energy.

Sample	Pressure (kPa)	Arrival time ( $\mu\text{s}$ )	Signal energy ( $\times 10^{-5}$ ) a.u	-ve peak height (kPa)	+ve peak height (kPa)	-ve peak width ( $\mu\text{s}$ )	+ve peak width ( $\mu\text{s}$ )	FWHM of -ve peak ( $\mu\text{s}$ )
PVC	4.9	231	4.32	2.95	1.95	7.33	15.38	3.81
Teflon	4.99	229.7	4.54	3.13	1.85	7.42	17.08	3.86
Alumina	4.81	228.6	5.99	3.39	1.99	7.36	17.99	3.85
Naphalene	4.74	230.1	4.41	2.94	1.8	7.54	16.87	3.91

At a particular energy of 100 mJ the ASWs from the LIB of all insulators are presented in table 4-7. PVC and Teflon have almost the same pressure, arrival time, signal energy, -ve peak height, FWHM and +ve peak width.

At higher laser energies, most of the ASW parameters are not changed considerably. It may be due to the saturation of parameters and the ablation.

**Table 4-7.** ASW parameters from LIB of insulators at 100 mJ of laser energy.

Sample	Pressure (kPa)	Arrival time ( $\mu$ s)	Signal energy ( $\times 10^{-5}$ a.u)	-ve peak height (kPa )	+ve peak height (kPa )	-ve peak width ( $\mu$ s)	+ve peak width ( $\mu$ s)	FWHM of -ve peak ( $\mu$ s)
PVC	7.83	223.7	12.77	5.65	2.18	7.86	27.28	3.96
Teflon	7.83	223.2	12.75	5.67	2.17	7.73	26.63	3.97
Alumina	7.34	223.62	12	5.07	2.27	7.94	21.2	3.91
Naphthalene	7.19	224.7	10.9	5.03	2.16	7.93	24.39	4.03

The trend of variation in ASW parameters at higher energies (100 mJ) is not following the same order as that of lower energies (10, 25 mJ), it can be noticed in table 4-5, 4-6, 4-7. If the threshold intensity is lower for a material, then its acoustic signal is more energetic at a laser intensity [39].

The ASW parameters of various materials are different, it indicates the material properties plays a role in ablation. So, here our aim is to find out why these ASW parameters are changing w.r.t energy. The acoustic signal emitted from the laser matter interaction can be helpful for remote chemical detection [40]. Detection of material from long range depends on the incident laser wavelength, material properties and it needs more theoretical and experimental studies.

Free carriers on the surface will be relatively higher for metals/conductors/alloys and dielectrics compared to insulators. The leading edge of the laser pulse interacts with the surface triggering the generation of free electrons which lead to melting and vaporisation of the material. Hence, in the case of metals/alloys, dielectrics the arrival time of the shock wave and melting point have shown a nice correlation at the input laser energies used in our studies. The relatively larger thermal and electrical conductivities will lead to faster ablation rate. While in insulators the threshold to create the initial free electrons is higher and lower thermal, electrical conductivities will not lead to a rapid ablation and expansion of the plasma resulting in a saturation of the acoustic parameters. Tables 4-5, 4-6, 4-7 shows the acoustic parameters from insulators at input laser energies of 10, 25 and 100 mJ per pulse respectively. At lower input

energies of 10 mJ, though there is a slight variation in peak-peak pressures, with increasing laser energies the  $A_t$ ,  $P_k$  are almost similar. The peak width is continuously increasing and the arrival time has reduced with laser energy as expected. The explicit dependence of the material properties on the ASW were not obvious in insulators with ns-LIB.

### 4.1.5 Cu powders

We extended our work from bulk materials to powders of different particle sizes, compacted into pellets of different densities. Copper powders of four different average sizes (2, 15, 40, 420 microns) compacted into pellets of three different packing densities are studied. The aim of this study is used to understand the effect of packing density and particle sizes on acoustic shock waves (ASW).

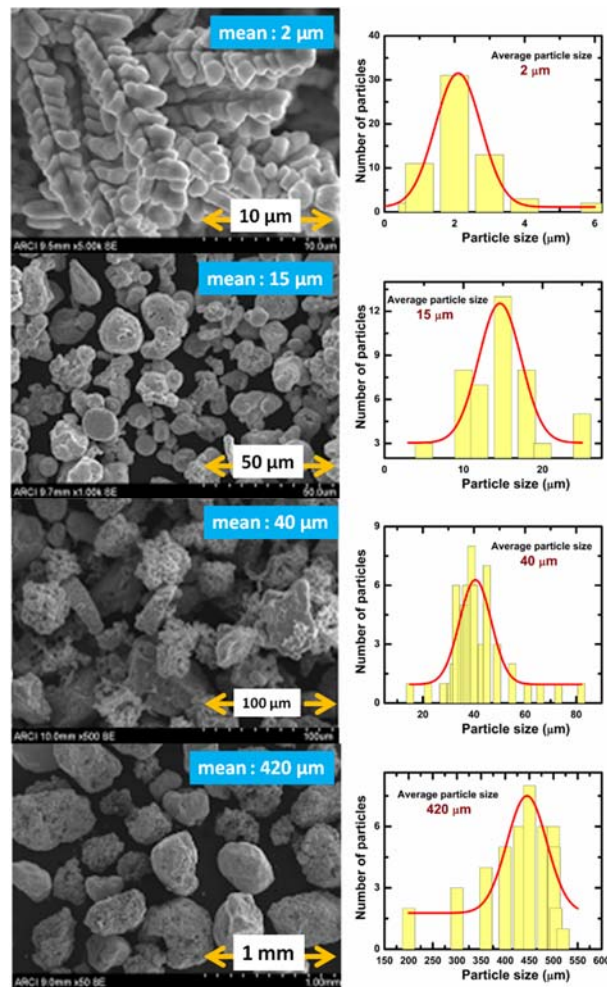


**Fig. 4.13.** SEM images of copper powders and their corresponding particle size distribution fits.

The effect of particle size on ASW has been reported in the literature. The ablated particles expected to be of nanometer sizes from a bulk target are reported to lead to phase explosion during ns to  $\mu$ sec time scale [41]. Various sizes of liquid droplets/ aerosols formed using nanoparticles have shown a spectrum shifted towards lower acoustic frequencies with varying ratio of +ve and -ve peak amplitudes and ration of +ve and -ve pulse widths [42, 43]. Our attempt is to study the effect of solid particles of different sizes and packing on the ASW from ns-LIB.

By changing the surface structure of the target sample, the resultant laser matter interaction will change in terms of amount of laser energy coupled to the target and it leads to the variation in the properties of emissions from the LIB. Surface area of sample formed due to the smaller particles is four orders greater than the bulk sample. It results in more laser energy transfer to the sample during laser matter interaction. Copper powders with range of particle sizes 2-420 micron were procured from the Sigma Aldrich (company). The images of powder particles taken using SEM (scanning electron microscope) to confirm the size distribution. Results were presented in fig. 4.12. From each SEM image, we have taken the average of particle size and those are 2, 15, 40 and 420 micron, shown in fig. 4.13.

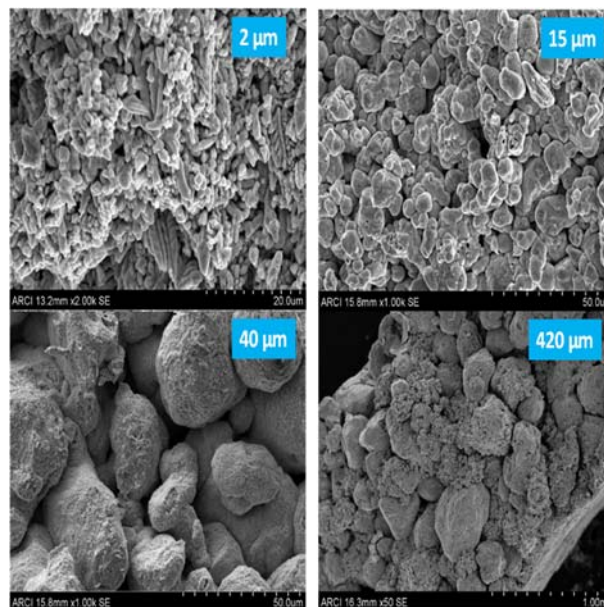


**Fig. 4.14.** SEM images of copper samples heat treated at 600°C.

The powders of different particle sizes were made into pellets of 3 cm square shape at applied pressures range of 55- 165 MPa. The heat treatment to these pellets below the melting point temperature (1085<sup>o</sup> C) will increase the mechanical properties. Each set of samples (2,

15, 40 and 420 micron) were heated at various temperatures of 400°C, 500°C and 600°C at a heating rate of 30°C/min. The SEM images of copper target samples of four particle sizes at a temperature of 600°C is, shown in fig 4.14. Heat treatment to samples, causes no grain growth, changes in its original mechanical properties.

Here we have used four distinct particle sizes with three different packing densities (12 samples) for ns-LIB experiments. We applied pressure and heat treatment to vary the density of pellets. The heat treated sample packing density is estimated by using well known Archimedes technique, these are presented in table 4-8.

**Table 4-8.** Pressure and temperature used to prepare the compacts.

Particle size (µm)	(60±2) % of theoretical density		(70±2) % of theoretical density		(80±2) % of theoretical density	
	Temperature (°C)	Pressure (MPa)	Temperature (°C)	Pressure (MPa)	Temperature (°C)	Pressure (MPa)
2	500	55	500	165	600	165
15	400	165	500	110	600	110
40	400	110	500	55	600	55
425	400	55	400	165	500	165

As shown in table 4-8, we made pellets of copper powders with three different packing densities (60%, 70%, and 80%) for four particle sizes such as 2, 15, 40, 420 micron. Sample processing and details of making pellets are presented elsewhere [18]. This study was used to understand the effect of incident laser energy, packing density and particle sizes on acoustic shock waves (ASW). At a particular packing density of 60, 70 and 80 %, as the incident laser energy increases from 10 to 70 mJ, the peak to peak ASW pressures are increasing for each particle sizes of 2, 15, 40 and 420 micron, shown in fig 4.15. At all packing densities, the increment in peak pressures w.r.t laser energy indicates that the energy conversion from optical to acoustical is also increasing.

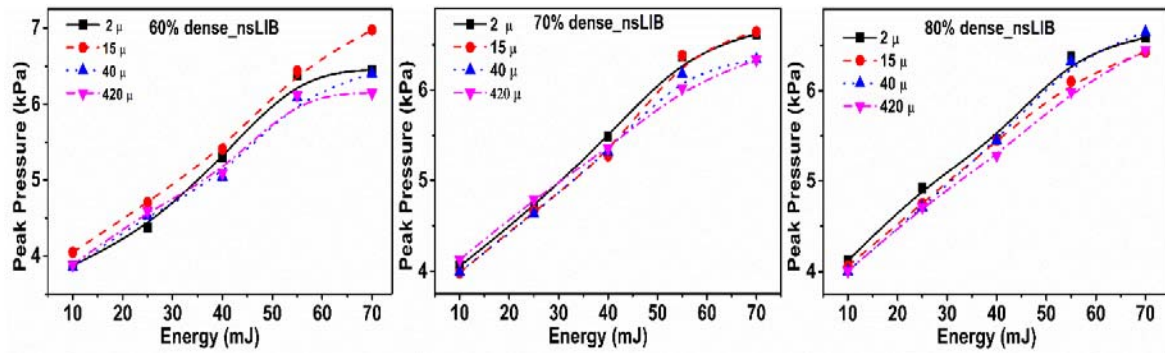


**Fig. 4.15.** Incident laser energy vs peak pressures for 2, 15, 40 and 420 micron size particles. At three packing densities of 60, 70 and 80 %, peak pressures are plotted for 10, 25, 40, 55 and 70 mJ laser energies. The pressures are increased w.r.t incident laser energy.

We focused on 2 and 420 micron particle sizes in further analysis, because 2 micron particle is too smaller than 50  $\mu\text{m}$ , typical grain size of a metal and pellets made of 420  $\mu\text{m}$  size are treated as equivalent to bulk target as both the grain size (50  $\mu\text{m}$ ) as well as laser focal spot size ( $\approx 150 \mu\text{m}$ ) on pellet surface are smaller than that of the powder size. The variation in peak pressures of these ns-LIB of two particle sizes gives a fair idea of particle size dependence on ASW. For pellets of 2  $\mu\text{m}$  size particles at a laser energy of 10 mJ, the peak pressures are 3.87, 4.05, 4.12 kPa at three packing densities of 60, 70, and 80 % respectively, shown in fig. 4.16. Similarly, at 40, 70 mJ of laser energies, the peak pressures are different at three packing densities. Even though the pressures values are different at three packing densities for a particular laser energy, they are following a trend of higher packing density giving more peak pressure than the lower one.

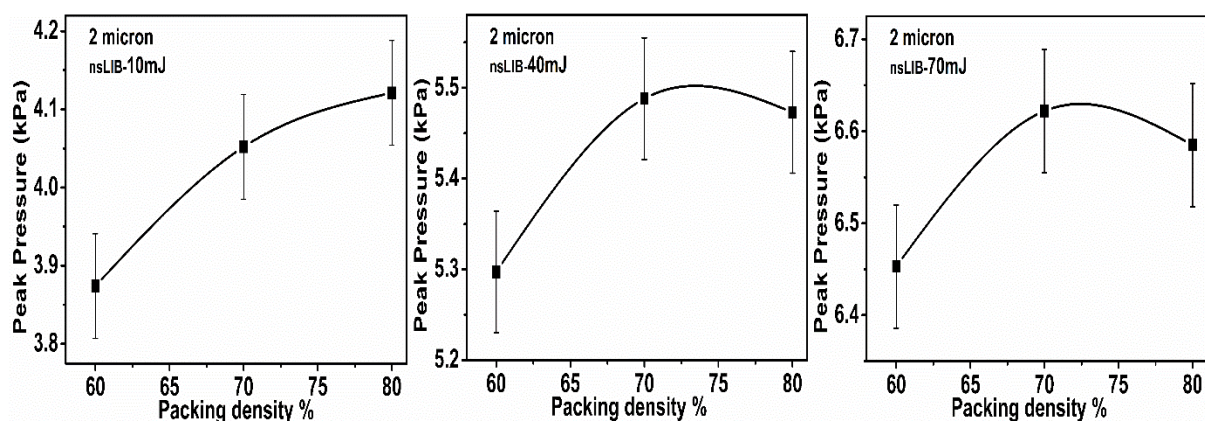


**Fig. 4.16.** Packing density vs peak pressures for 2 micron size particles at 10, 40 and 70 mJ of laser energies.

For 420 micron particle size, the peak to peak pressures are different at three packing densities. Packing density of 70% has more peak pressure than the 60 % for 10, 40 mJ laser

energies whereas 80 % packing density shows higher value than the remaining densities at 70 mJ.

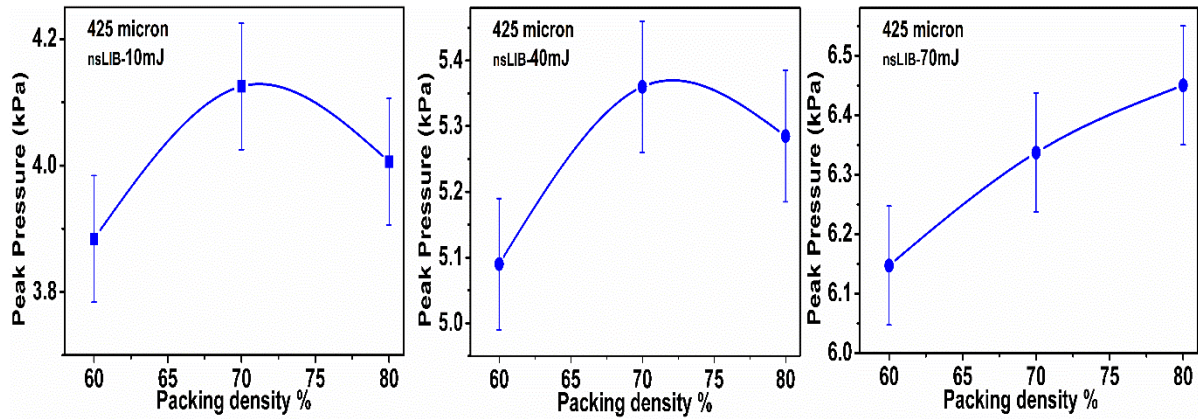


**Fig. 4.17.** Packing density vs peak pressures for 420 micron size particles at 10, 40 and 70 mJ of laser energies.

From fig. 4.15, 4.16, at 60%, 70% and 80% packing densities the peak pressures are different for both 2, 420 micron particle sizes.

In order to show the effect of particles size, we have taken the ratio of +ve peak width and -ve peak height of a ASWs for 2, 420 micron particle sizes at all energies and packing densities. At each packing density, the ratio of +ve peak width and -ve peak height (PW/NH) are distinct for a particular laser energy.

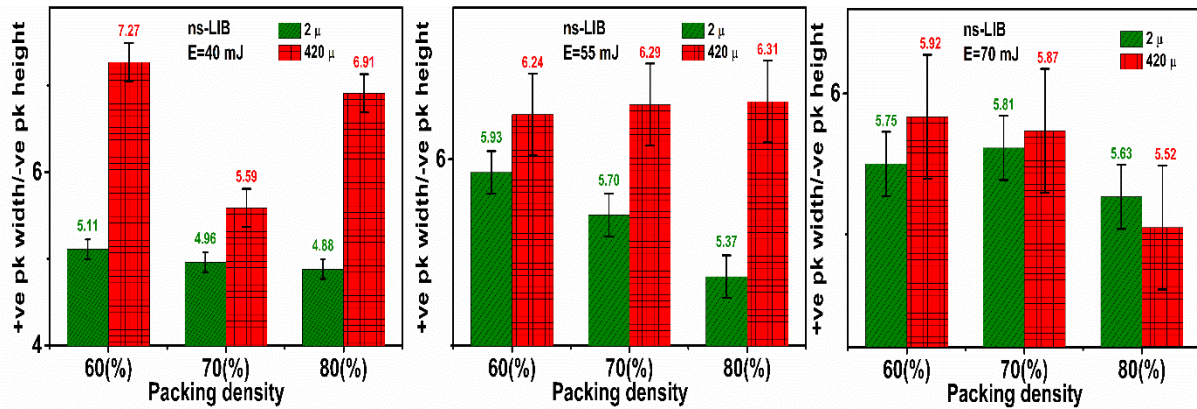


**Fig. 4.18.** Packing density vs ratio of +ve peak width and -ve peak height for 2, 420 μm particle sizes for the laser energies of 40, 55, 70 mJ. At each packing density, the 420 μ particle size having higher value of ratio than the 2 μ except 80 % packing density and laser energy of 70 mJ. Units of ratio is (μsec/kPa), error is absolute value.

At an energy of 40 mJ, the ratio values (PW/NH) for 2, 420 μm are 5.11, 7.27 for a packing density of 60 %. The ratio value (PW/NH) is greater for 420 μm particle size. For 55,

70 mJ laser energies, ratio value of 420  $\mu\text{m}$  particle size is higher than the 2  $\mu\text{m}$  for the packing densities of 60%, 70%, 80%. For three packing densities and three laser energies the function of particle size on ratio of +ve peak width and -ve peak height (PW/NH) presented in fig 4.18.

For twenty individual laser shots, acoustic data was collected and we calculated the error from the measurements. From this fig. 4.18, we can say that, particle size and packing density effect is clearly presented in ASW parameters.

At lower laser energies, such as 10, 25 mJ also the ratio values are distinct for 2, 425  $\mu\text{m}$  particle sizes for all packing densities. At 25 mJ, for 60% packing density, the ratio values for 2, 420  $\mu\text{m}$  are 5.55, 4.87 whereas for 80% packing density, the values are 5.03, 5.38 respectively. This is different from the case of higher laser energies such as 40, 55, 70 mJ. These values are clearly tabulated in table 4-9.

**Table 4-9.** At 10, 25 mJ laser energies, the ratio of +ve peak width and -ve peak height for the packing densities of 60, 70, 80%.

Particle size	Packing density					
	10mJ			25 mJ		
	60%	70%	80%	60%	70%	80%
2	5.55	4.63	5.2	5.55	4.72	5.03
425	5.54	5.05	5.03	4.87	4.69	5.38

### 4.1.6 Comparison among various materials

The time domain signals of ASWs, which are emitted from the ns-LIB of Brass, Teflon, Mica, PVC at 10 and 40 mJ of laser energy are presented in fig 4.19. It helps to see the difference in samples at a fixed experimental conditions.

Even though laser energy is the same 10 mJ, the width of +ve peaks are different for samples. As we increase the laser energy, the ablation increases with which the plasma species will also increase and resultant shock pressure and density rises. The difference in +ve peak widths of sample signals is clearly visible in fig. 4.19.

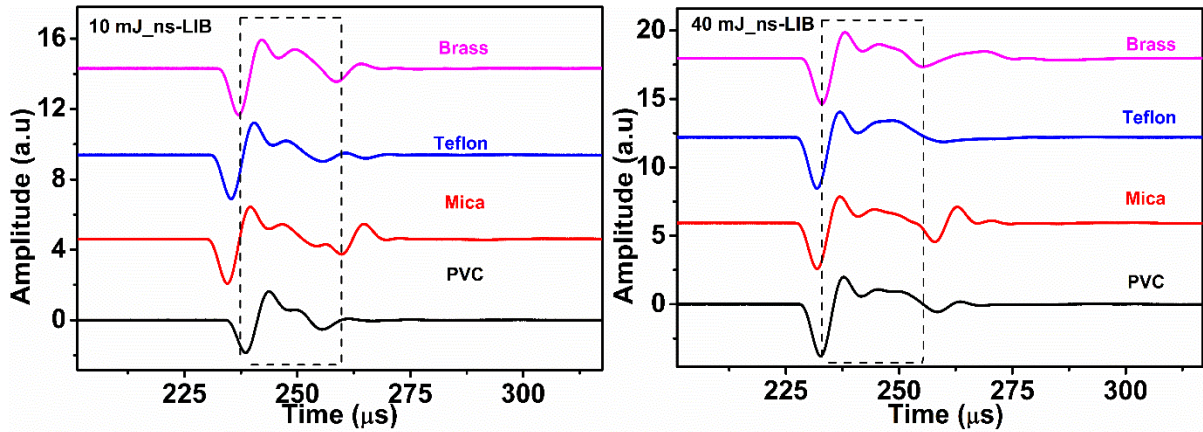


**Fig. 4.19.** The time domain signals of ASWs emitted from the ns-LIB of Brass, Teflon, Mica, PVC at 10 and 40 mJ of incident laser energies.

The +ve peak widths of samples at 40 mJ are higher than the 10 mJ values, presented in table 4-10. This clearly indicates that the acoustic signals do represent the different ablation rates of different materials.

**Table 4-10.** +ve peak lengths of ASWs emitted from ns-LIB of Brass, Teflon, Mica and PVC samples at 10 and 40 mJ of laser energies are presented in this table.

Sample	+ve peak length ( $\mu\text{s}$ )	
	10 mJ	40 mJ
Brass	15.4	16.7
Teflon	14.4	21.2
Mica	14	18.8
PVC	11.9	20.1

### 4.1.7 Frequency analysis

From the time domain signals the frequency distribution of the emitted acoustic signals are obtained by applying Fast Fourier Transform (FFT) [22, 39] as explained in Chapter 2. The FFT of ASW signal gives the spectrum consisting of few number of peaks. Fig 4.20 shows the evolution of dominant frequencies of brass with varying laser pulse energy. The frequencies are observed to be in the ultrasonic range.

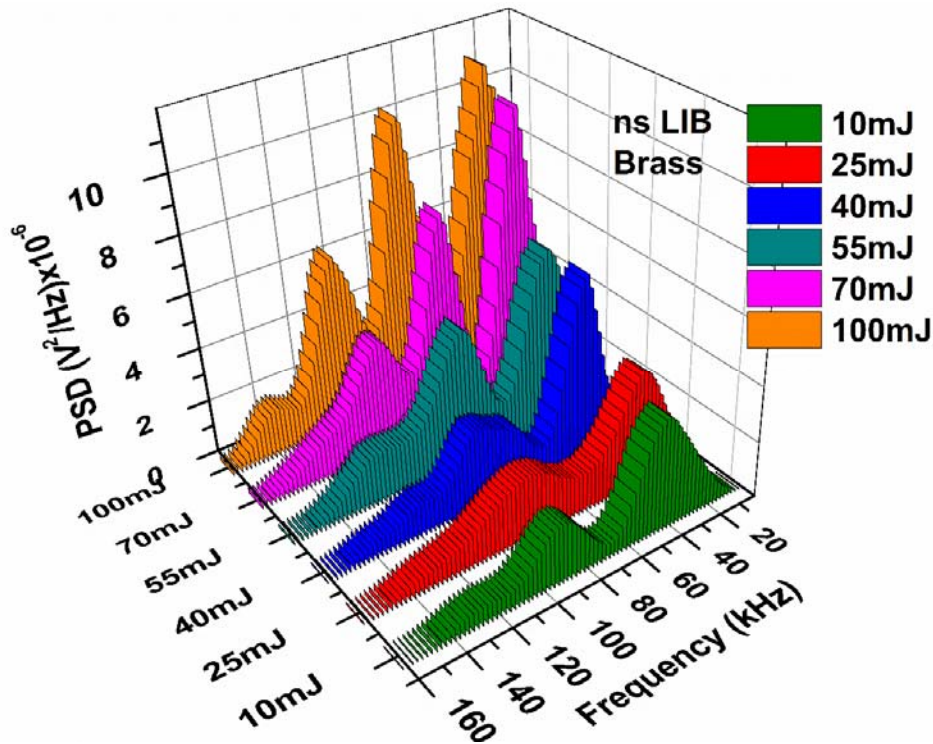


**Fig. 4.20.** Spectral distribution of ASW emitted from the ns LIB of Brass target at various laser energies. X- Frequency, Y-laser energy and Z- power spectral density (PSD).

At 10 mJ of laser energy, only two frequency peaks with different power spectral density (PSD) values are observed in spectrum. At 40 mJ of laser energy, a third peak around 120 kHz has appeared. With increasing energy up to 70 mJ the third peak has become dominant. At 100 mJ, fourth peak at  $\sim 140$  kHz is observed, shown in fig. 4.20. The spectral features mainly are the function of laser intensity [39]. Energy carried by ASW increases with incident laser energy, under fixed experimental conditions for all samples. Observed frequency peaks are fitted to a Lorentzian function to extract the central peaks and the full width at half maximum, shown in fig. 4.21(a). The fitting parameters are central frequency, peak width, area under the curve and height of the peak. One of these fitting parameters, central frequency of peak 1, 2, 3 are plotted at various laser energies for brass sample, are shown in fig. 4.21(b). Peak 1 is the frequency which has highest PSD in spectrum, peak 2 is the second highest frequency in spectrum. It is also observed that the observed peaks are not the harmonics of the fundamental frequency (peak with highest PSD).

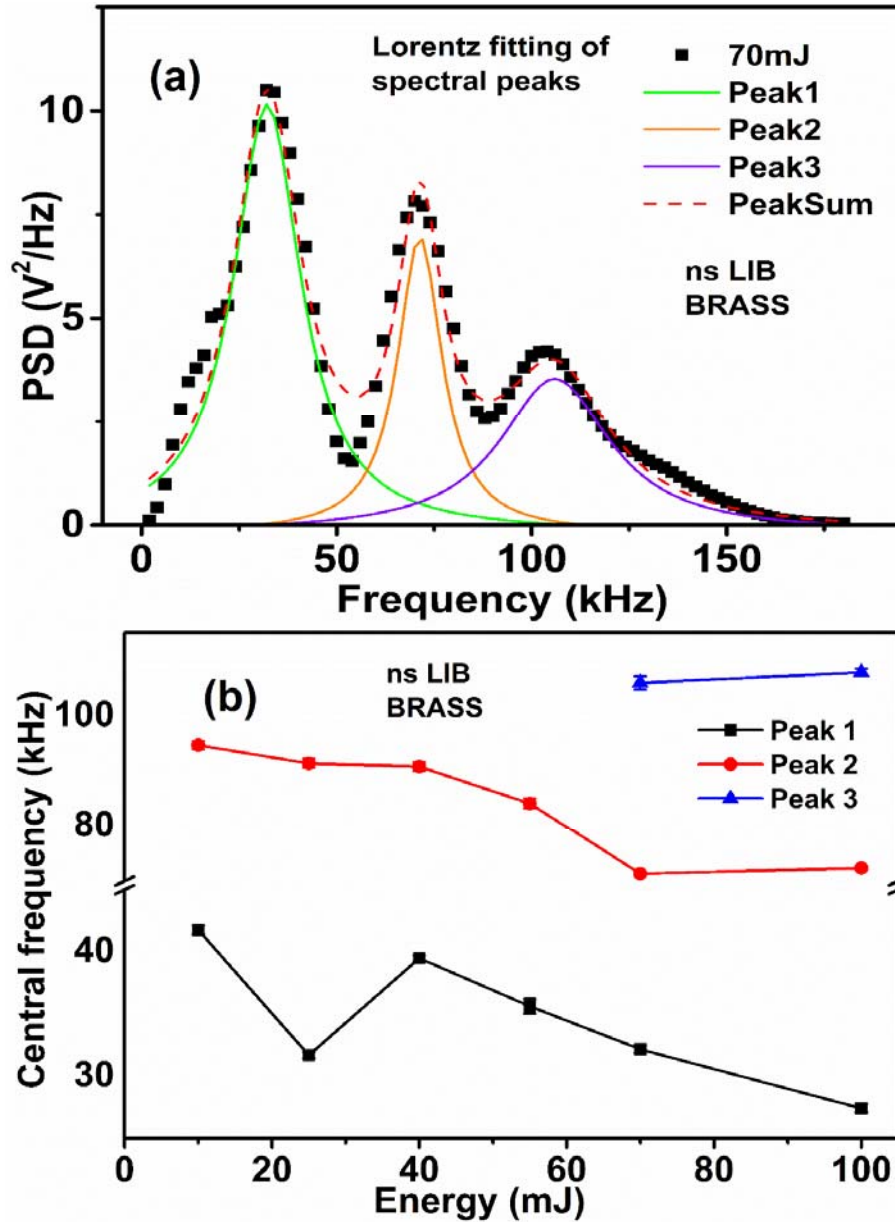


**Fig. 4.21.** (a) Lorentzian fitting for spectral peaks of ns LIB of Brass spectrums. X- Axis is frequency, Y-axis is power spectral density (PSD), (b) central frequencies of peak 1, 2, 3 with respect to incident laser energy.

As the laser energy increases, the frequency moves towards the lower frequency side (audible range) with increasing amplitude. The maximum frequency ( $f_{max}$ ) [44] in the acoustic spectrum is a function of plasma parameters:

$$f_{max} = \frac{c}{4 \cdot r_p} = \frac{1}{2\tau_p} = \frac{1}{4\tau_+}$$

where  $c$  is velocity of sound in ambient atmosphere,  $r_p$  is radius of the plasma plume in the high pressure region,  $\tau_p$  is duration of acoustic pulse and  $\tau_+ = \tau_p/2$  is the duration of its

positive half period. The frequency of the acoustic spectrum is reported to be inversely proportional to the radius of the plasma [45]. The number of peaks and their characteristics (central frequency, peak width and amplitude) are observed to be material dependent.

For 70 mJ of laser energy, the spectrum of ASW consists of three different frequency components. The Lorentzian fitting of the observed frequencies is presented in fig 4.21(a). The central frequencies of peak 1, 2 and 3 are plotted in fig 4.21(b) against the incident laser energy. The central frequency of the observed peak is found to move towards lower frequency with increasing laser energy. The peak 1 is observed to vary from 42 to 27 kHz, peak 2 from 95 to 71 kHz and peak3 from 108 to 106 kHz as shown in fig 4.21 (b).

LIB of materials is a unique reproducible source of high power wide band acoustic frequencies [44]. The spectral analysis of the acoustic signals helps in the real-time diagnosis of the laser spark parameters. In order to understand the significance of the material parameters, the frequency components of the acoustic signals for all the category of materials is compared under similar experimental conditions (laser energy and focusing geometry).

The central frequency obtained from Lorentzian fittings of peak 1 and peak 2 are plotted w.r.t samples and their PSD values. The two peaks (peak1 and peak2) observed at all input laser energies have shown distinct frequency features.

The central frequencies, their widths and the ratio of these two parameters of the corresponding peaks of the acoustic spectrum obtained at an input laser energy of 25 mJ are tabulated in table 4-11 for comparison.

In case of the peak 1 frequencies, for all samples the frequency spread is all over 22.4 to 48.76 kHz. Though some frequency components are closer to each other, their PSD values are different. This shows the role of material properties in the acoustic emissions which can be used to distinguish the materials. Peak 2 frequencies are varied from 51.95 to 96.82 kHz for all the samples. These peak1 and peak2 frequencies w.r.t their power spectral densities (PSD) for all the samples are shown in fig. 4.22.

**Table 4-11.** At 25 mJ laser energy, the Lorentz fitted central frequency, spectral width and their ratios for all the samples.

Samples	Peak 1			Peak 2		
	Central frequency (kHz) ( $\omega_1$ )	Width (kHz) ( $\Delta\omega_1$ )	$\Delta\omega_1/\omega_1$	Central frequency (kHz) ( $\omega_2$ )	Width (kHz) ( $\Delta\omega_2$ )	$\Delta\omega_2/\omega_2$
Brass	31.69	25.57	0.807	91.40	67.66	0.740
SS	48.76	22.24	0.456	96.82	17.01	0.176
Alumina 90	34.96	20.09	0.575	70.32	17.50	0.249
Alumina 99	35.10	17.95	0.511	68.15	13.23	0.194
PVC	43.32	40.21	0.928	95.71	22.81	0.238
Teflon	35.78	31.24	0.873	93.01	79.37	0.853
Mica	35.44	18.45	0.521	70.89	121.48	1.714
ZrSnTiO4	35.41	20.52	0.580	89.97	30.70	0.341
LiNbO3	25.71	18.87	0.734	95.43	89.54	0.938
BaTiO3	22.48	18.95	0.843	78.62	33.89	0.431
Al	38.53	17.21	0.447	51.95	12.37	0.238
Cu	30.62	19.56	0.639	66.68	18.27	0.274

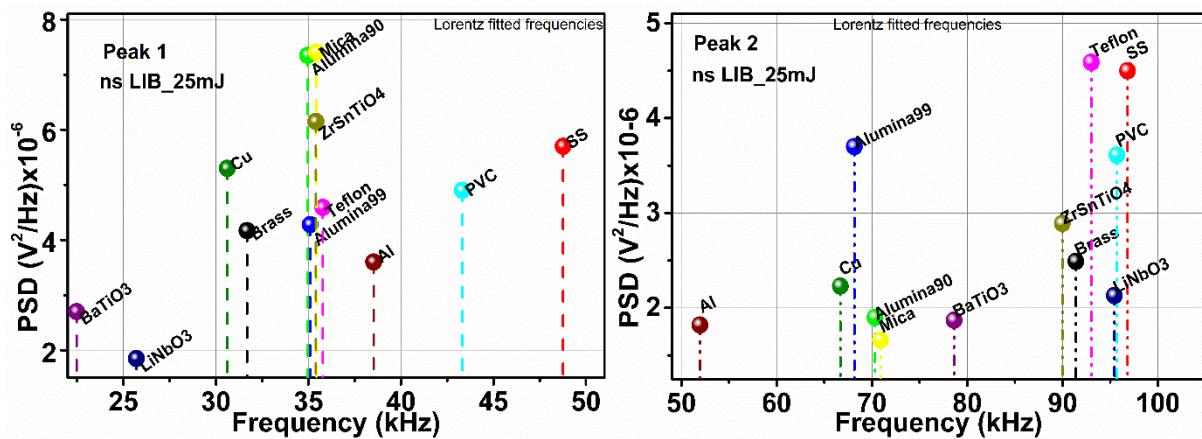


**Fig. 4.22.** Lorentz fitted peak1 and 2 frequencies due to ns LIB of material samples with their PSD values are plotted for all the samples at a fixed energy of 25 mJ. Each colour sphere is a data point. (a) Peak 1, (b) peak 2 frequencies vs their corresponding PSDs.

For some of the samples peak 3, 4 have also appeared, which are not presented in this plot. Of all the materials Mica has highest PSD for peak 1 whereas Teflon has the highest PSD

for peak 2. In case of peak 2 frequencies, except Al all other samples have a peak after 60 kHz frequency with different PSDs. From fig 4.22 we can observe that the studied insulators and dielectrics can be separated with respect to each other. However, the conductors appear to have acoustic signals spread across wide frequency range.

From fig 4.22 (b), the peak 2 of all the conductor samples studied is fairly localized closer to 90-100 kHz; while the frequencies corresponding to dielectrics and insulators are widely spread. Between the dielectrics and insulators, insulators have higher PSD values. Though the present data cannot clearly classify different categories of materials, but points towards the need for better algorithms and more parameters to classify the materials analogous to standard LIBS.

### Frequency analysis of Cu powders

FFT of time domain signal gives the acoustic spectrums of that corresponding signal. Frequency analysis gives the information which is hidden in time domain. In time domain, as the peak - peak pressure increases with the laser energy, the amplitude of frequency spectrum increases with laser energy, shown in fig. 4.23.

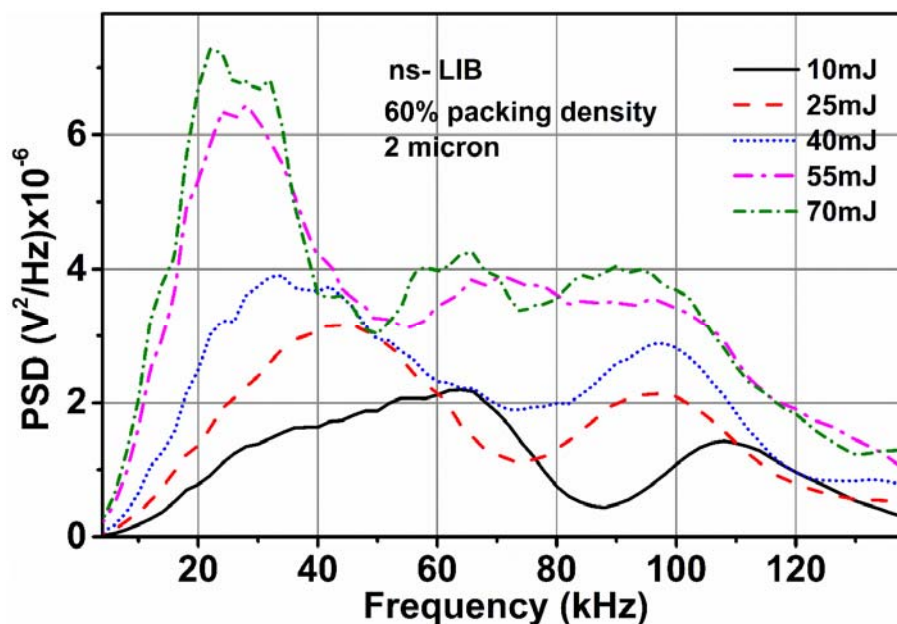


**Fig. 4.23.** Frequency spectrums of ASWs emitted from the ns-LIB of Cu powder pallet of 2  $\mu$  particle size. At various laser energies of 10, 25, 40, 55 and 70 mJ at a fixed packing density 60% and 2 micron particle size.

For a particle size of 2  $\mu$ m and packing density of 60%, the spectral peak shifts towards the lower frequency side and rises in its amplitude (PSD) as the incident laser energy increases

from 10 to 70 mJ, shown in fig. 4.18 At lower energies, the acoustic frequency spectrum is broader whereas at higher laser energies, the acoustic spectrum becomes narrower with higher amplitude. The same shifting of peak frequency to audible range w.r.t incident laser energy is observed for remaining packing densities also such as 70 % and 80%. Along with peak 1 frequency, secondary frequency peaks also increase in their amplitudes w.r.t laser energy. At 10 mJ the peak frequency is 68.36 kHz with an amplitude of  $2.79 \times 10^{-6}$  V<sup>2</sup>/Hz whereas at 70 mJ it is 20 kHz with  $4.36 \times 10^{-6}$  V<sup>2</sup>/Hz amplitude. We have observed a similar shifting of peak frequency with laser energy in LIB of air and various materials (presented in chapter 3). At all packing densities of materials as the laser energy increases, the spectrum shifts towards lower side.

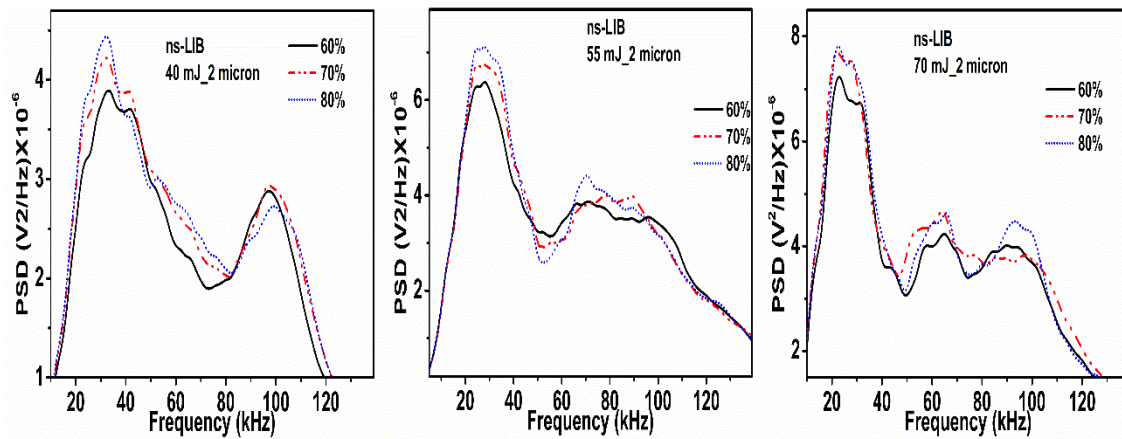


**Fig. 4.24.** The frequency responses of ASWs from 60, 70, 80 % dense copper pallets at 40, 55, 70 mJ of laser energies for a 2 micron size particles. Amplitude of PSD is maximum for 80% dense cu pallets than the 60, 70% dense.

At 40, 55, 70 mJ of laser energies, the 80% dense copper pellets shows maximum PSD than the 70%, 60% dense, as shown in fig. 4.24.

## 4.2 pico second LIB

The ns and ps-LIB both have their own advantages and disadvantages, which find relevant applications in fields, like material processing, analytical chemistry, LIBs etc. Generally ns laser pulses were used in LIBS studies, due to its reheating phenomena that leads to higher temperature plasma. Whereas in material drilling and processing, ps or shorter lasers were used, because of its ablation quality and less thermal damage than the ns LIB. Lower pulse widths generate high peak intensities, leading to non-linear multi-photon absorption process. Ultrashort pulse laser ablation mechanism is used to understand phase explosion

model, in which extreme pressures, densities and temperatures rise up and ionized species comes out with greater velocities [15] along with a shock wave. The schematic of interaction of ultrashort laser pulse with material is presented in fig. 4.25.

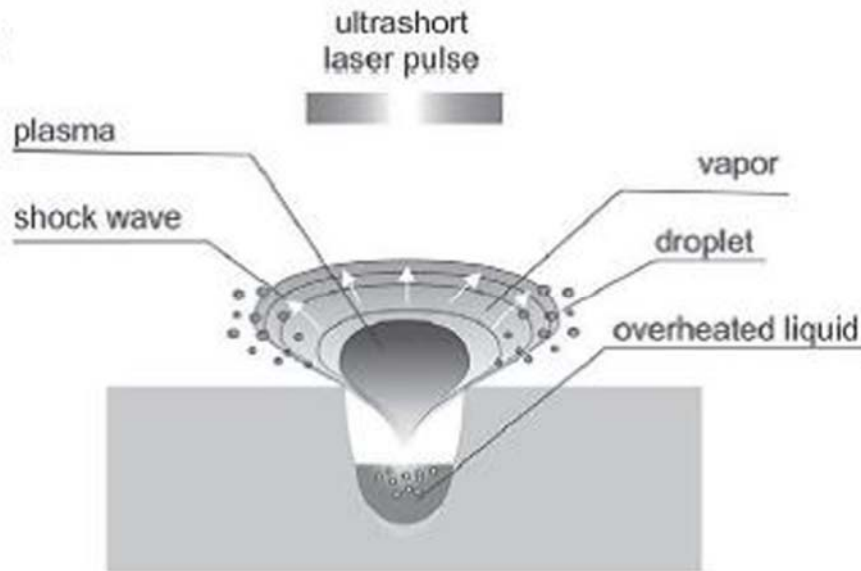


**Fig. 4.25.** Schematic of interaction of ultrashort pulse with material [15].

After detachment from plasma, shockwave propagates with supersonic velocity [36, 46] in to the surrounding atmosphere. Behind the shock wave, the density is more than the normal density of the medium. The shock wave and the ejected particles both together influence the density of surrounding medium and it is reflected in the microphone response. So, the parameters of ASW are used to study the ablation rate qualitatively [21]. At higher laser energies, the generated acoustic shock waves have high pressures and travel with higher speeds than the normal sound.

Both thermal and non-thermal mechanisms exist in pico second (ps) LIB [ $10^{10} - 10^{13} \text{ W/cm}^2$ ] [3]. For ps and fs laser pulses interaction with matter, there exist no reheating of the plasma as in the case of ns pulse [47]. During ps laser pulse induced breakdown the ejected particles will be less compared to the ns ablation. In ultrafast laser pulse ( $<2 \text{ ps}$ ) matter interaction, there is no time for thermal interaction and the electronic phenomena are dominant. The ASWs from samples studied in section 4.1 using ns-LIB are studied with ps-LIB and the following sections describe the ASW from them.

## 4.2.1 Conductors

All the experiments are done in ambient air medium, no buffer gases were used. The influence of buffer gas on the ablation rates is well studied [48]. As mentioned earlier, LIB of material generates acoustic emissions. ASW studies indirectly indicate that the properties of the plasma and laser-matter interaction. The physical properties of the materials studied are tabulated in table 4-1. These will help to correlate the ASW properties with the material characteristic properties. In this section, 30 ps laser pulses are irradiate on Al, Cu, Brass and SS 316 LN target samples.

The ASW parameters were plotted against the incident laser energy for different conductor samples. Here we can see the effect of material and laser energy on ASWs. The properties of metals (Al, Cu) and alloys (Brass, SS) are compared in fig. 4.26 respectively. The pressures and arrival times are distinct for Al and Cu samples at different laser energies.

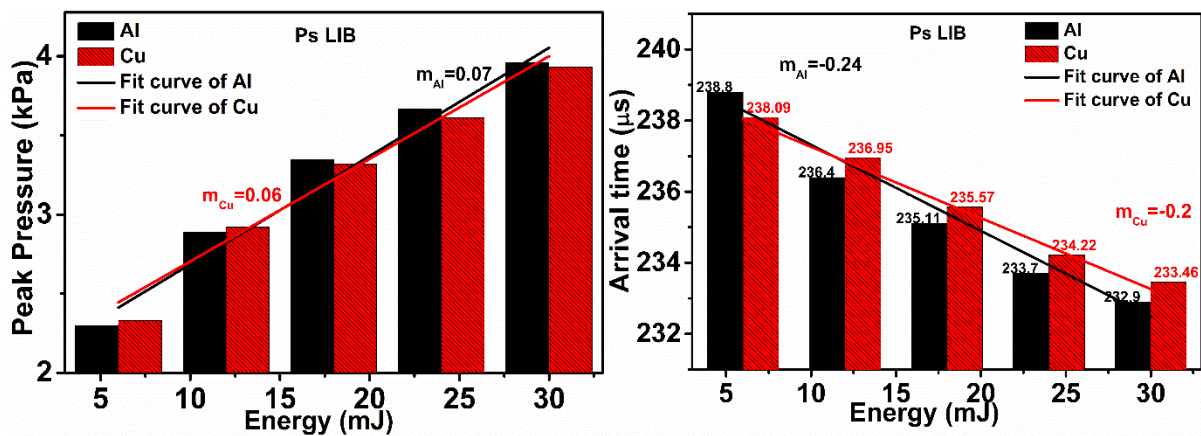


**Fig. 4.26.** Pressures and arrival times for Al and Cu samples, at various input energies of 6,12,18,24 and 30 mJ. The slopes of peak pressures for Al, Cu samples are 0.068, 0.065 respectively. The slopes of arrival times for Al, Cu samples are -0.24, -0.20 respectively.

As laser energy increases, the peak-peak pressure ( $P_k$ ) increases and arrival time (or transit time) [1] decreases. Decrease in arrival time at a fixed distance of microphone indicates the rise in ASW velocity. The  $P_k$  pressures and arrival times at 24 mJ for Al and Cu samples are 3.67, 3.81 kPa and 233.7, 234.2  $\mu$ s respectively. The density of Cu (8.96 g/cm<sup>3</sup>) is more than the density of Al (2.7 g/cm<sup>3</sup>). The melting points of Cu > Al. Under same experimental conditions the  $A_t$  for Cu  $\geq$  Al with increasing input laser energy. For brass (combination of Cu and Zinc) and SS-304 (combination of Fe, Ni, Cr etc.), the pressures and arrival times are 3.81, 3.73 kPa and 232.9, 231.6  $\mu$ s respectively at 24 mJ of energy.

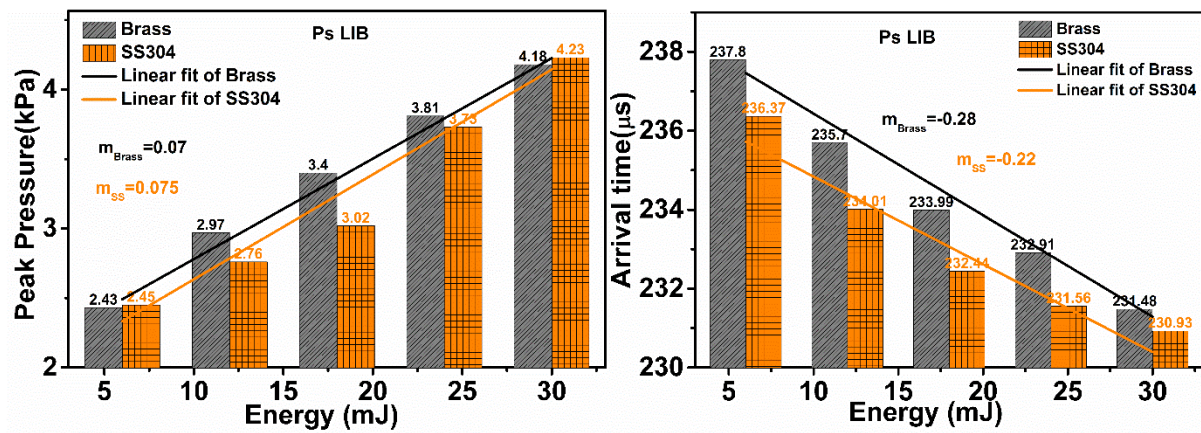


**Fig. 4.27.** Peak to peak pressures and arrival times for Brass and SS 304 at 6, 12 and 24 mJ of laser energies. The slopes of peak pressures for Brass, SS304 samples are 0.072, 0.075 respectively. The slopes of arrival times for Brass, SS304 samples are -0.26, -0.22 respectively.

From fig. 4.27 we can see the difference between pure metals and alloys. For conductors the ASW pressures are increasing linearly with input energy with almost a constant slope of  $0.07 \pm 0.005$ . The arrival time of ASWs from pure metals is slightly faster than the alloys while the peak pressures are slightly lower.

These acoustic pressures generated by ps LIB are less when compared with the ns-LIB of same materials. ns-LIB of Al at 20 mJ produces the 3.67 kPa pressure whereas ps-LIB of Al produces 3.67 kPa at 24 mJ of laser energy. For long laser pulses (nano second), the trailing edge of pulse interacts with the medium ablated by the leading of the same laser pulse. It causes the plasma reheating, resulting in a rise in plasma species. In ps-LIB, the time for reheating to form plasma is less. Hence, in ps-LIB, less thermal energy is dissipated in the target, ablation is more efficient [26]. Hence, between ns & ps pulse LIB, the electron and ion number density  $n_e$  and  $n_i$  will be completely different. The dynamics of  $n_e$  and  $n_i$  will play a crucial role in ASW. So, we can expect the variation in ASW parameters between ns and ps LIB of same target sample.

Now we move on to understand the acoustic signatures of acoustic pulse width, signal energy and their relevance to ps ablation. First we focus on one pure material, then we can extend to other materials. The ASW signals from ps LIB of Al at various laser energies are shown fig. 4.28 (a). Increasing laser energy causes the increment in  $P_k$  pressure of overall signal. Here the noticeable point is that, the contribution of -ve and +ve peak pressures are different to total  $P_k$  pressure at different energies.

Fig. 4.28 (b) indicates that with increasing laser energy, the height of the -ve peak is increasing more rapidly than the height of the +ve peak. This rise is much faster compared to the ns-LIB. This clearly indicates that the ablation due to ns and ps laser pulses can be distinguished using acoustic signals.

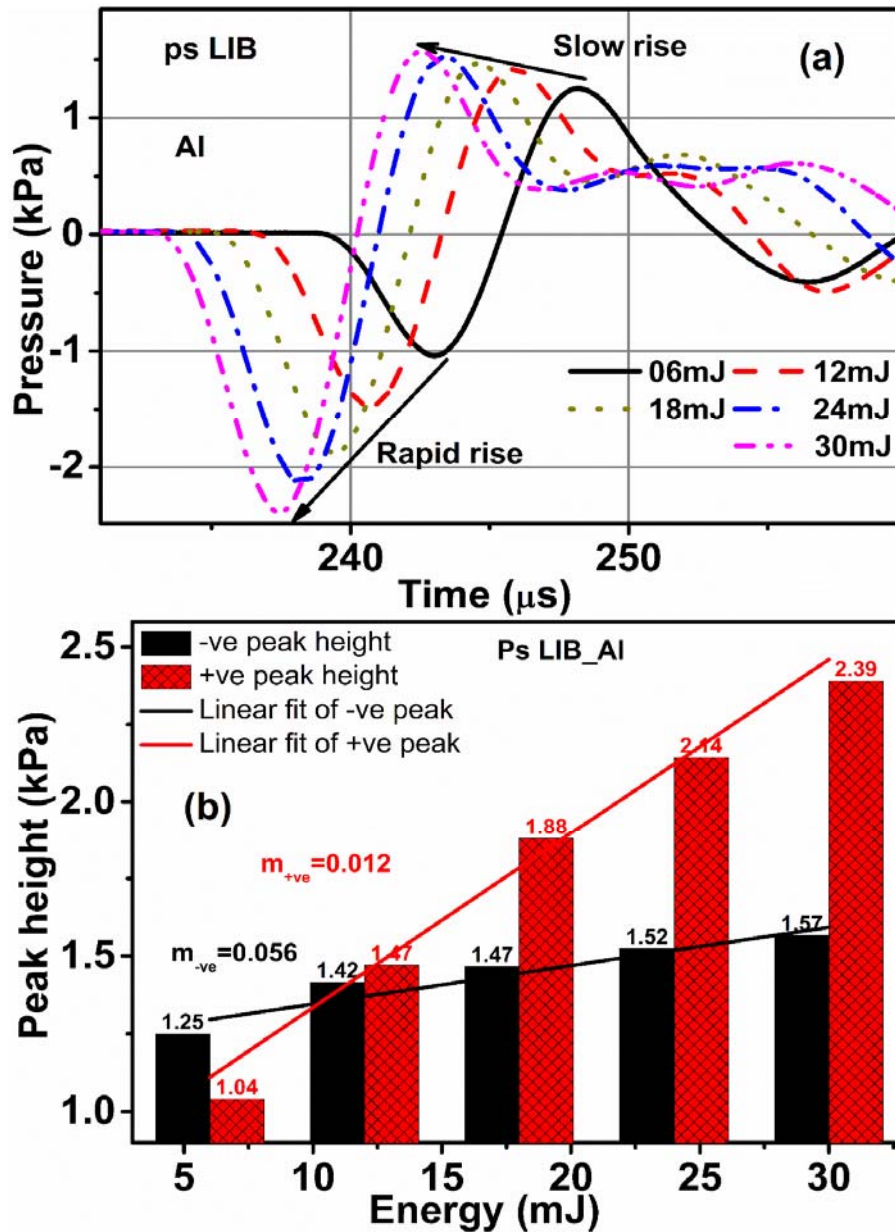


**Fig. 4.28.** For Al sample, (a) comparison of ASW signals, (b) +ve and -ve peak heights w.r.t incident laser energy. The slopes of +ve and -ve peak heights are 0.012 and 0.056 respectively.

For a particle size of  $2 \mu\text{m}$  and packing density of 60%, the spectral peak shifts towards the lower frequency side and rises in its amplitude (PSD) as the incident laser energy increases from 10 to 70 mJ, shown in fig. 4.18 At lower energies, the acoustic frequency spectrum is broader whereas at higher laser energies, the acoustic spectrum becomes narrower with higher

amplitude. The same shifting of peak frequency to audible range w.r.t incident laser energy is observed for remaining packing densities also such as 70 % and 80%. Along with peak 1 frequency, secondary frequency peaks also increase in their amplitudes w.r.t laser energy. At 10 mJ the peak frequency is 68.36 kHz with an amplitude of  $2.79 \times 10^{-6}$  V<sup>2</sup>/Hz whereas at 70 mJ it is 20 kHz with  $4.36 \times 10^{-6}$  V<sup>2</sup>/Hz amplitude. We have observed a similar shifting of peak frequency with laser energy in LIB of air and various materials (presented in chapter 3). At all packing densities of materials as the laser energy increases, the spectrum shifts towards lower side.

As shown in fig. 4.28, the signals at various laser energies, the +ve peak height is rising slowly, whereas the -ve peak height is increasing rapidly. At lower energies the +ve peak height is greater than the -ve peak height. As laser energy increases, the -ve peak height is gradually increasing and finally it overcomes the +ve peak height. Increase in -ve peak pressures (heights) represents rise in shock pressures. It indicates that there is a good conversion of incident laser energy in to acoustic energy. For Al target sample it is clearly shown in fig 4.28.

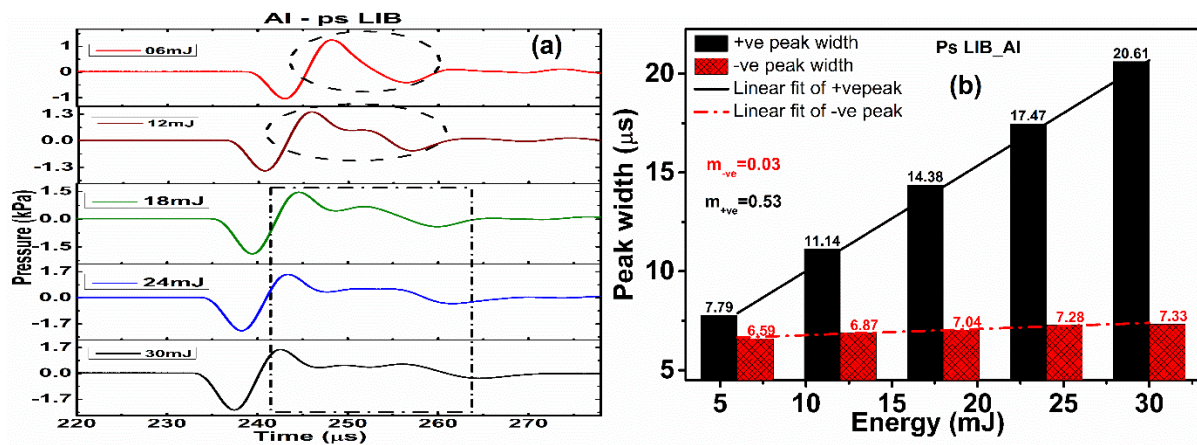


**Fig. 4.29.** (a) The ASW signals from Al target at various incident laser energies of 6,12,18,24 and 30 mJ. Highlighted circles and boxes indicates the changes in signals due to variation in laser ablation. (b) The slopes of +ve and -ve peak widths are 0.53 and 0.03 respectively.

Along with peak heights, peak widths (different from the total acoustic pulse width) of both +ve and -ve are also presented in fig. 4.29 (b). As the laser energy increases, the +ve peak width is increasing than the -ve peak width. These peak parameters helps to understand the laser matter interaction. Fluctuations in +ve peak represents the density fluctuations in surrounding medium [49] created by ablative plasma. The elongation or stretch in +ve peak of ASW represents the ablation efficiency [49].

Laser matter interaction is different at various laser energies for same set of samples, due to changes in material ablation. Here, observation is focused on the width of positive peak, shown in fig. 4.29. At 6 mJ of energy, there is no distortion in +ve portion of signal. At 12 mJ of laser energy, distortion or stretch has initiated, clearly shown in fig. 4.29. As the energy is increasing from 18 to 30 mJ the acoustic +ve peak width is increasing. The length of stretch in positive peak provides the duration of ablated matter in a given ambient atmosphere. As incident laser energy increases, there is change in laser-matter interaction, it is causing the distortions in ASW signals, shown in fig. 4.29 (a).

## 4.2.2 Comparison of ASW parameters of conductors

At all energies (6, 12, 24 mJ) SS 304 has lower arrival time than all metals, so the ASW velocity from LIB of SS 304 sample is higher than all samples. The response of SS 304 is different from Al, Cu and Brass at lower and higher energies because of its too many elements (Cr, Mo, Ni, Ti, Cu, C, and N). The breakdown threshold of such an alloy will vary depending on the composition and typically being decided by the material with lowest breakdown threshold. In mixture of material, the breakdown will happen at lower energies and the remaining energy is utilized for plasma growth. Brass is a combination of both copper and zinc. ps LIB of alloys has more pressures and less arrival times than the pure metals because alloys have low breakdown threshold energies and majority of the incident energy is converted into acoustic energy. Signal energy and acoustic pulse width increase as the incident laser energy increases.

**Table 4-12.** ASW parameters of Al, Cu, Brass and SS316LN samples at a fixed energy of 30 mJ.

Sample	Pressure (kPa)	Arrival time ( $\mu$ s)	Signal energy (a.u)	-ve peak height (kPa)	+ve peak height (kPa)	-ve peak width ( $\mu$ s)	+ve peak width ( $\mu$ s)	Area under curve (a.u)	
								-ve part	+ve part
Al	3.96	232.9	2.75	2.39	1.567	7.325	20.61	9.06	12.56
Cu	3.93	233.46	2.76	2.38	1.54	7.45	20.49	9.17	12.41
Brass	4.18	231.48	3.29	2.6	1.57	7.81	20.79	10.12	14.07
SS316	4.23	230.93	3.36	2.619	1.62	7.265	19.38	10.10	13.99

Decrease in mass removal per unit laser energy is reported when the fluence of ps laser pulses increases for copper target material at 1064 nm wavelength [28]. Whereas for 532 and

266 nm, crater volume has increased with laser energy for ps laser pulses [28]. Our experiments are performed at 532nm wavelength, so the increase in ASW parameters indicates the crater volume. The ASW parameters of Al, Cu, Brass and SS samples at a fixed energy of 30 mJ were presented in table 4-12. This table gives the idea of effect of material on acoustic parameters.

### 4.2.3 Dielectrics

The dielectrics we have used are Glass, Mica, Barium Titanate ( $\text{BaTiO}_3$ ), Zirconium Tin Titanate ( $\text{ZrSnTiO}_4$ ). The peak pressures, arrival times of these dielectrics samples were presented in fig. 4.30, at three different laser energies of 6, 12, 24 mJ.

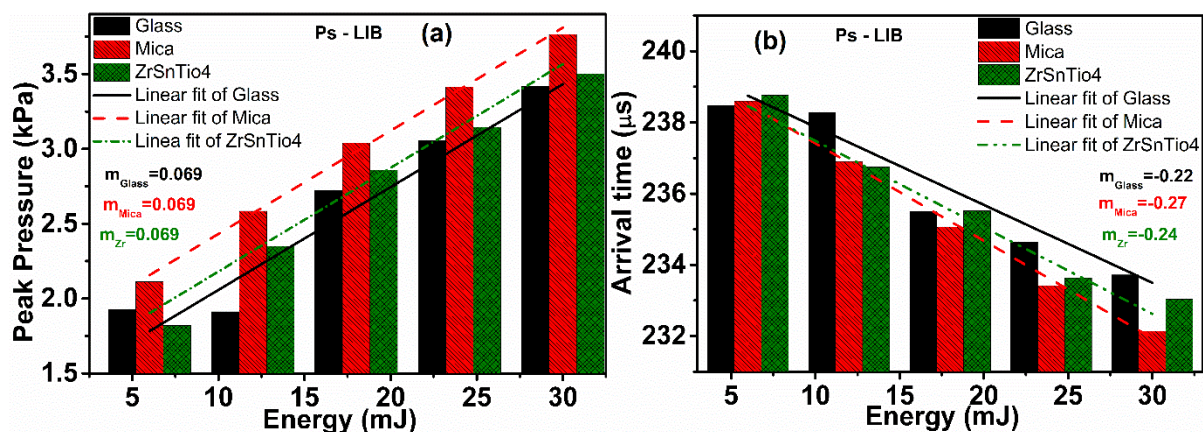


**Fig. 4.30.** (a) Peak to peak pressures and arrival times of ASWs at 6, 12 and 24 mJ of energies for dielectric samples. (b) The slopes of peak pressures for glass, Mica, ZrSnTiO<sub>4</sub> samples are 0.069, 0.069, 0.069 respectively. The slopes of arrival times for glass, Mica, ZrSnTiO<sub>4</sub> samples are -0.22, -0.27, -0.24 respectively.

The behaviour of varying peak pressures and arrival time are observed to be similar. Glass has almost the same pressures and arrival times at 6 and 12 mJ of laser energies. We can't observe large difference at 6 and 12 mJ, as shown in fig. 4.30. Glass is transparent to 532nm wavelength light, so majority of the energy is transmitted at 6, 12 mJ energies, whereas a rapid rise in pressure at 24 mJ is observed. This result indicates that the laser-matter interaction mechanism is different at lower and higher energies. Other than glass, the peak pressures of remaining samples are increasing and arrival times are decreasing with laser energy, shown in fig. 4.30 (a), (b). As we move to higher energies the laser matter interaction is non-linear. Idea on ablation rates is important to choose the optimum laser parameters for various sample characterization [50] and to understand environment effects on the ablation rates [50]. The acoustic parameters from LIB of dielectrics at 12 mJ, were presented in table 4-13. The values are distinct for different samples.

**Table 4-13.** ASW parameters from LIB of dielectrics at 12 mJ of laser energy.

Sample	Signal energy (a.u)	-ve peak height (kPa )	+ve peak height (kPa )	-ve peak width ( $\mu$ s)	+ve peak width ( $\mu$ s)	Area under curve (a.u)	
						-ve part	+ve part
ZrSnTiO4	0.886	1.198	1.152	7.65	11.7	4.54	5.94
Glass	0.662	0.794	1.12	6.72	6.65	2.71	4.527
Mica	1.097	1.332	1.248	6.825	10.72	4.865	6.43
BaTiO3	2.06	1.38	1.37	6.79	8.7	4.99	6.88

#### 4.2.4 Insulators

PVC, Teflon, Alumina (Al 90% dense) are the insulators we have used here to form the plasma and studied the associated effects acoustic emissions. As laser energy increases, the pressures and signal energy increases and arrival time decrease for both PVC and Teflon as expected, shown in fig. 4.31.

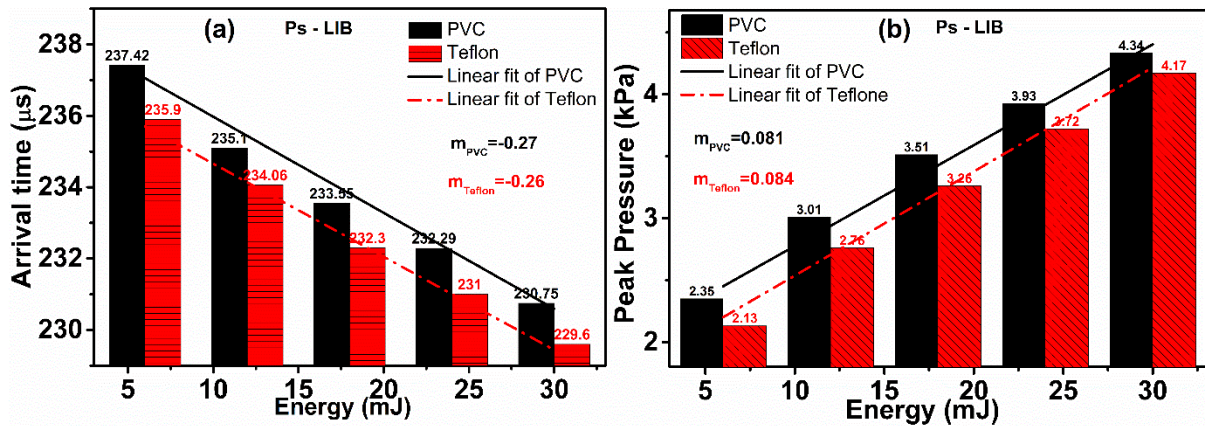


**Fig. 4.31.** (a) Pressures, (b) arrival times for PVC, Teflon at all laser energies of 6, 12, 18, 24, and 30 mJ. The slopes of peak pressures for PVC, Teflon samples are 0.081, 0.084 respectively. The slopes of arrival times for PVC, Teflon samples are -0.27, -0.26 respectively.

Signal energy is proportional to the square of the peak pressures. Even though both are insulators, the ASW parameters are different. Both have different chemical structure and properties. At all input laser energies the ASWs from ps LIB of PVC and Teflon shows similar evolution with incident laser energy. ps LIB of PVC show more peak pressures than the Teflon

at all laser energies, shown in fig. 4.31. Arrival times of ASWs from Teflon are less than the PVC at all energies. Due to sample constraint, for Al 90, experiment was done at 6, 12 mJ of laser energies only. Acoustic measurements are tabulated in table 4-14.

**Table 4-14.** ASW parameters of ps LIB of Alumina at 6, 12 mJ of laser energies.

Energy (mJ)	Pressure (kPa)	Arrival time (μs)	Signal energy (× 10 <sup>-5</sup> ) V <sup>2</sup> .sec	peak height (kPa)		peak width (μs)		Area under curve (×10 <sup>-6</sup> ) a.u	
				-ve portion	+ve portion	-ve portion	+ve portion	-ve portion	+ve portion
6	2.337	237.15	0.93	1.153	1.183	6.725	10.1	4.16	5.95
12	2.939	234.25	1.48	1.618	1.32	7.495	12.81	6.07	8.18

Area under the curves of –ve and +ve portions for Al 90 sample are increasing with laser energy, shown in table 4-14. It implies that either peak heights or peak widths or both are increasing along with laser energy. Decrease in arrival time indicates the rise in acoustic shock velocity. For PVC and Teflon, the area under the curves of both –ve and +ve portions were tabulated in table 4-14. As the laser energy is increasing, the areas representing higher ablation are increasing. It indicates the increase in crater volume with respect to laser energy.

**Table 4-15.** Area under -ve and +ve portions of PVC and Teflon samples, at various laser energies.

Energy (mJ)	PVC		Teflon	
	Area under –ve part × 10 <sup>-6</sup>	Area under +ve part × 10 <sup>-6</sup>	Area under –ve part × 10 <sup>-6</sup>	Area under +ve part × 10 <sup>-6</sup>
6	3.71	5.58	3.63	5.2
12	5.93	8.56	5.51	7.081
18	7.73	10.4	7.08	8.24
24	9.18	11.96	8.5	9.89
30	10.52	13.2	10.06	11.39

### 4.2.5 Compacted Cu powders

The same set of copper powder pellets were used for the ps-LIB also. Temporal ASW parameters were presented in fig. 4.32 as we have seen in ns-LIB, copper powder pellets with different packing densities shows the different peak pressures with less amplitude (peak pressure) difference. Here, the microphone to plasma distance is 73 cm. To avoid the particle

accumulation on the microphone holes, target was kept at a safe distance. The low peak to peak pressures are due to this long source-receiver distance.

The effect of incident laser energy on the ASW peak pressures from pellets made out of 2  $\mu\text{m}$  and 420  $\mu\text{m}$  particle sizes were presented here. As the laser energy increases the peak pressures are increasing at all packing densities, as shown in fig. 4.32. Linear fits to peak pressures for both 2, 420  $\mu\text{m}$  particles are presented in fig. 4.32. For 2  $\mu\text{m}$ , the peak pressure is increasing linearly with a slope of 5.1, 6.4, and 5.8 for packing densities of 60, 70, and 80 % respectively. For 420  $\mu\text{m}$  powder pellet, the slopes are 4.7, 6.4, and 3.8 for packing densities of 60, 70, and 80 % respectively.

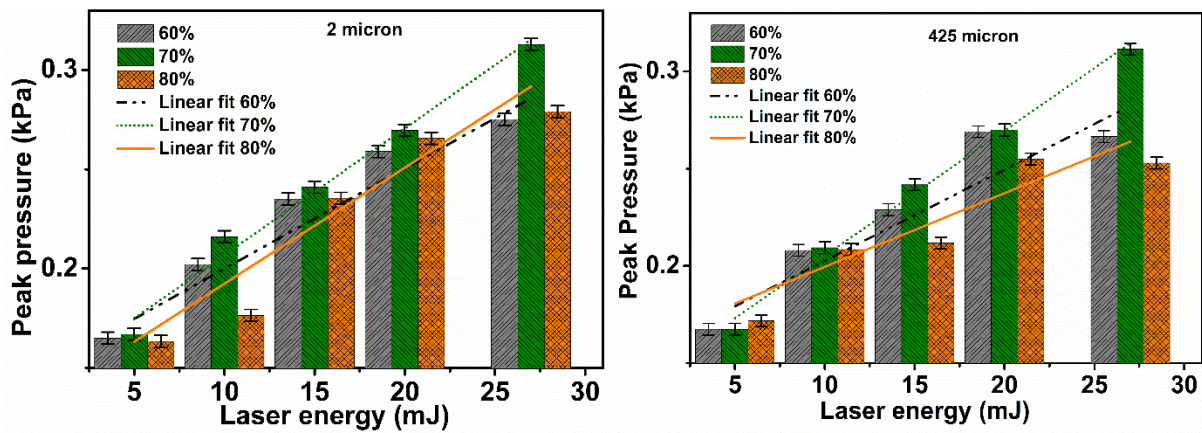


**Fig. 4.32.** Laser energy vs peak pressures and their linear fits for packing densities of 60, 70, 80% for the particle sizes of 2 and 425 micron. Peak pressure are proportional to the incident laser energy.

Interaction of laser pulse with copper powder pellet made with the 2  $\mu\text{m}$  size particles is different from the 425  $\mu\text{m}$  size at a fixed laser energy, shown in fig. 4.33.

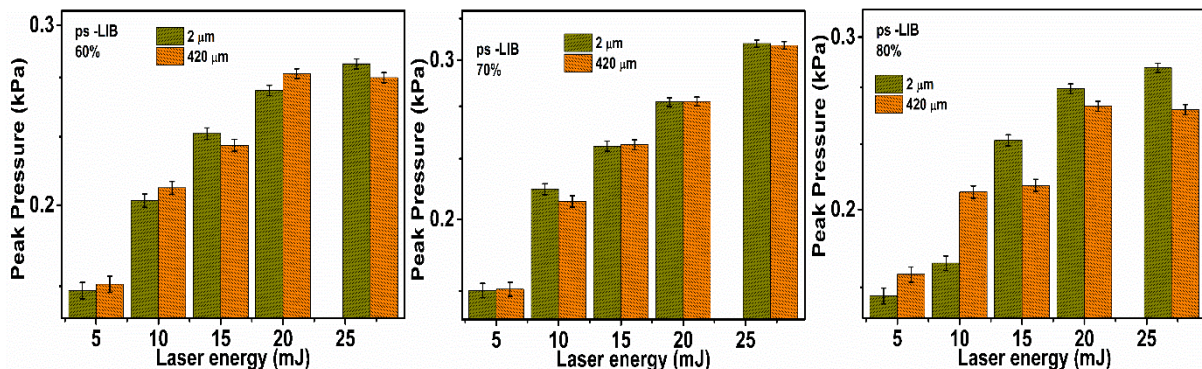


**Fig. 4.33.** Laser energy vs peak pressures for particle sizes of 2, 425  $\mu\text{m}$  at each packing density of 60, 70, and 80 %. At each packing density, interaction of laser pulse with each particle size is different.

The peak pressures are very close to each other at some of laser energies and packing densities. At 80% density, the peak pressures for 2, 420  $\mu\text{m}$  are very different from each other, shown in fig. 4.33.

The ratio of +ve peak width to that of -ve peak height indicating the material ablation duration and the resulting ablative pressure (fig 4.34) shows that at a given laser energy the material ablation is happening over a longer duration for 420  $\mu\text{m}$  powder pellets with increasing laser energy the 2  $\mu\text{m}$  powder pellets will get ablated much quickly due to increased coupling of laser energy to the pellets. This is evident from fig. 4.34 (a) and (b).

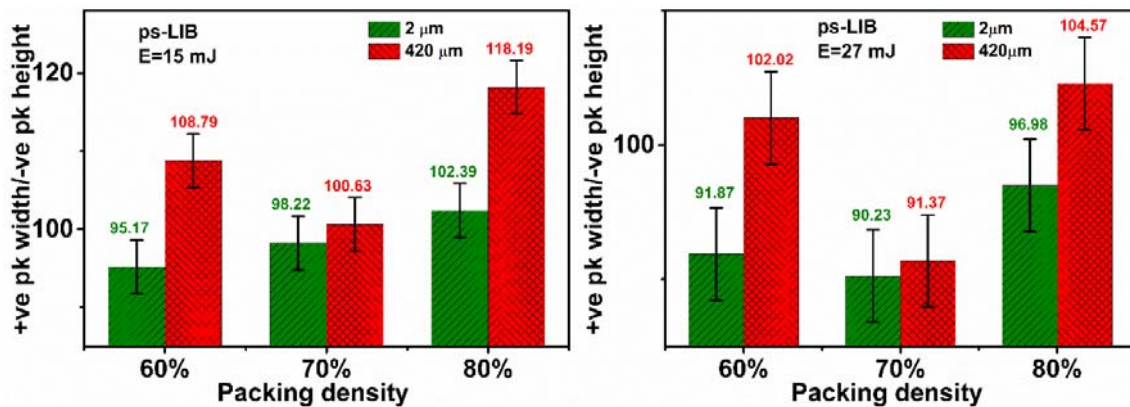


**Fig. 4.34.** Packing density vs ratio of +ve peak width and -ve peak height for 2, 425  $\mu$  particle sizes for the laser energies of 15, 27 mJ. At each packing density, the 425  $\mu$  particle size having higher value of ratio than the 2  $\mu$ . Units of ratio is ( $\mu\text{sec/kPa}$ ), error is absolute value.

#### 4.2.6 Comparison among various materials

To understand the role of material on the ASW from LIB, the time domain signals are compared under similar experimental conditions. At 6 mJ of laser energy, there is not considerable stretch in positive peak of Glass, PVC, SS, Al, shown in fig 4.35. At 12 mJ of energy, the stretch in positive peak has increased for all the materials except for glass. As Glass transmits 532 nm wavelength of laser light the amount of laser energy deposited is less compared to the remaining samples that are opaque for 532 nm light. So, the amount of energy used to form the plasma, decides the density fluctuations in surrounding atmosphere.

As we increase the laser energy, the plasma absorbs incident energy and develops its constituents, which are represented by the ASW parameters. We can see a stretch in glass signal also at 18 mJ of energy along with the other samples, shown in fig. 4.35. The length of this stretch is different for different samples. The remaining parameters are also distinct for various samples. Change in some of the acoustic parameters are visually observable like length of +ve

peak and depth of –ve peak. Remaining parameters we will calculated from known formulae and function fitting.

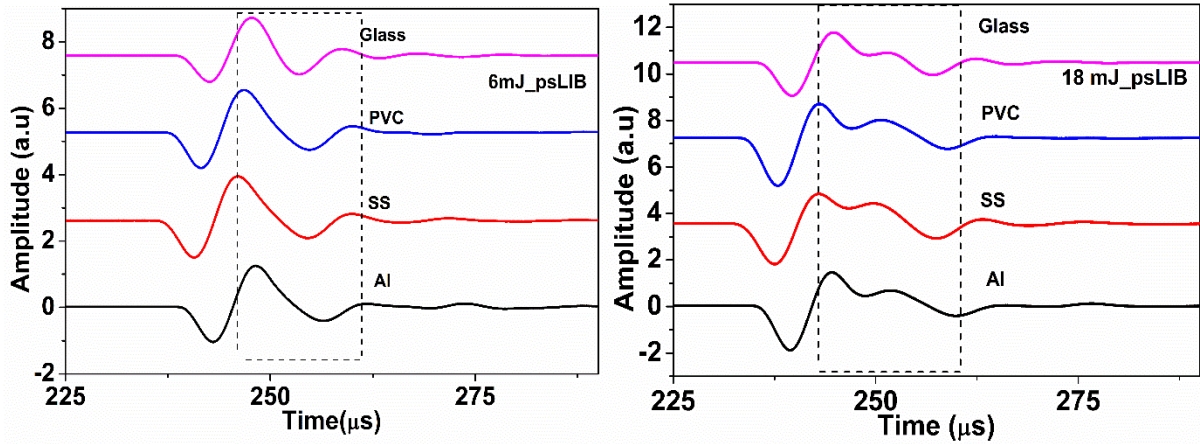


**Fig. 4.35.** ASW signals from ps LIB of various samples at (a) 6 mJ, (b) 18 mJ of incident laser energies.

The change in ablative widths are compared in table 4-16.

**Table 4-16.** +ve peak lengths of ASWs emitted from ps-LIB of Al, SS, PVC and Glass samples at 6 and 18 mJ of laser energies are presented in this table.

Sample	+ve peak length (μs)	
	6mJ	18mJ
Al	7.78	14.37
SS	8.08	13.66
PVC	7.5	15
Glass	6.19	11.89

The length (or stretch) of +ve peak is doubled when laser energy is 3 times increased, for all the samples which is in line with the fact that ablation increases with input laser energy.

### 4.2.7 Frequency analysis

The FFT of ASW time domain signal gives the spectrum, consisting of frequency information of acoustic signals. Spectral frequencies are fitted to Lorentzian function, shown in fig. 4.36. Peak 1, peak 2, peak 3 are three dominant frequencies which were considered for analysis. Highest PSD is peak 1, the peak number follows the amplitude of PSD.

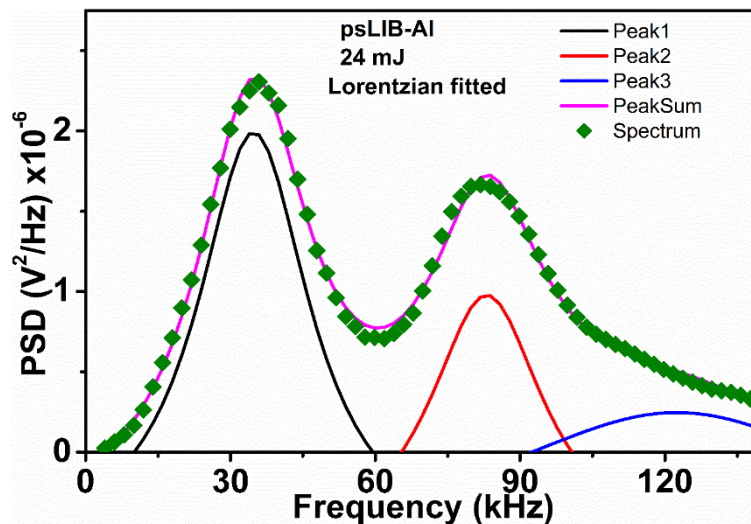


**Fig. 4.36.** Acoustic spectrum of ps-LIB of Al target sample at 24mJ of laser energy. Frequencies are fitted to Lorentzian function with three different frequencies (peak1 to 3), actual spectrum is super imposed on the peak sum of fitting, and it shows the fitting is good.

The values of  $R^2$  square (coefficient of determination (COD)) is 0.9964 for this fitting, indicating a good fit. The peak sum (shape) has to be very close to the original spectrum. In order to get this, we have used Lorentz multiple peak fitting. Three peaks of different frequency and PSDs have appeared in Lorentz multiple peak fitted spectrum (fig. 4.36). The Lorentzian peak fit parameters are central peak frequency, width of that peak, height and area under the curve of fitted curve. These parameters helps to understand the ASWs emitted from LIB of materials. The frequency analysis for Aluminium (Al), Copper (Cu), Brass, Stainless steel (SS), PVC, Teflon, Mica, Glass, ZrSnTiO<sub>4</sub> are presented here.

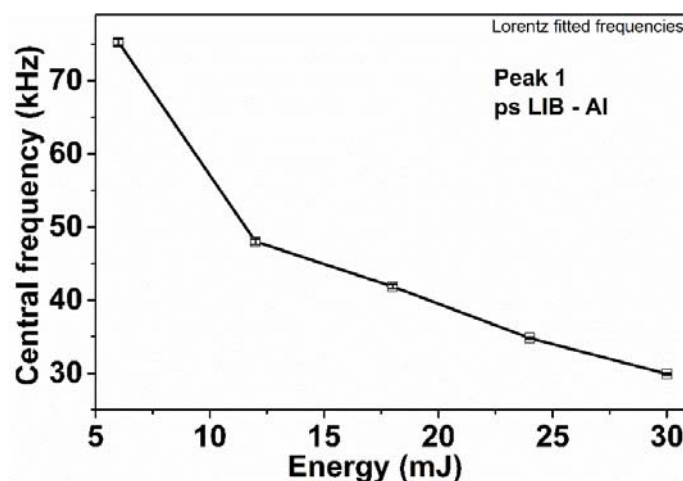


**Fig. 4.37.** Peak 1 frequency vs incident laser energy, for ps LIB of Al target sample. Central fitted peak frequency decreases as the laser energy increases from 6 to 30 mJ.

As the laser energy increases the central frequency of peak 1 for Al is shifted from 75 to 30 kHz, indicating presence of near acoustic frequencies with increasing laser energy. A similar behaviour is observed to the remaining peak frequencies. For a particular laser energy of 24 mJ, the peak 1, peak 2 frequencies are plotted for all the samples, shown in fig. 4.38.

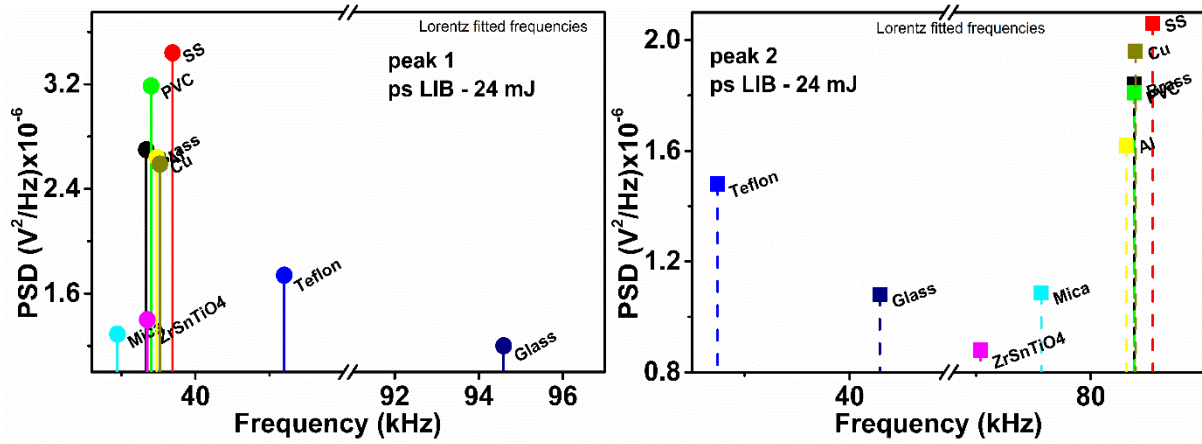


**Fig. 4.38.** Peak 1 and peak 2 frequencies of ps – LIB of various samples at 24 mJ of laser energy.

Since we are working in audible to ultrasonic frequencies in ambient air, there are some constraints which needs to be considered. In audible range, general noises will limit the acoustic parameters, at the same time, attenuation of higher frequency components comes into picture in the ultrasonic range [51].

A clear difference in the peak frequencies with corresponding PSD values is observed in ns-LIB and ps-LIB. This is mainly due to the shorter 30 ps pulse which minimizes the interaction of the trailing edge of the laser pulse with the initial free electrons. Despite the very close peak frequencies, different PSD values from samples is an advantage to utilize ASW from ps-LIB under lab conditions. The central peak frequencies, peak widths and their ratios are presented in table 4-17 for all the samples at 24 mJ of laser energy.

**Table 4-17.** The Lorentz fitted central frequency, FWHM and its ratios for all the samples for ps LIB of various samples at 24 mJ laser energy.

Samples	Peak 1			Peak 2		
	Central frequency (kHz) ( $\omega_1$ )	Width (kHz) ( $\Delta\omega_1$ )	$\Delta\omega_1/\omega_1$	Central frequency (kHz) ( $\omega_2$ )	Width (kHz) ( $\Delta\omega_2$ )	$\Delta\omega_2/\omega_2$
Brass	33.37	19.92	0.597	83.82	29.37	0.350
SS	36.93	33.27	0.901	85.40	41.06	0.481
PVC	34.03	32.35	0.951	83.81	30.63	0.365
Teflon	51.97	29.77	0.573	27.41	33.39	1.218
Mica	29.50	24.07	0.816	75.68	23.47	0.310
ZrSnTiO4	33.50	41.21	1.230	70.38	36.93	0.525
Al	34.80	28.17	0.809	83.08	28.72	0.346
Cu	35.20	29.04	0.825	83.91	28.27	0.337
Glass	94.59	30.08	0.318	42.86	14.63	0.341

To understand the energy dependence on acoustic frequencies produced by LIB of materials, the spectral components at 12 mJ laser energy are compared as shown in fig. 4.39. The frequency components are well separated in either the frequency scale or its amplitude (PSD).

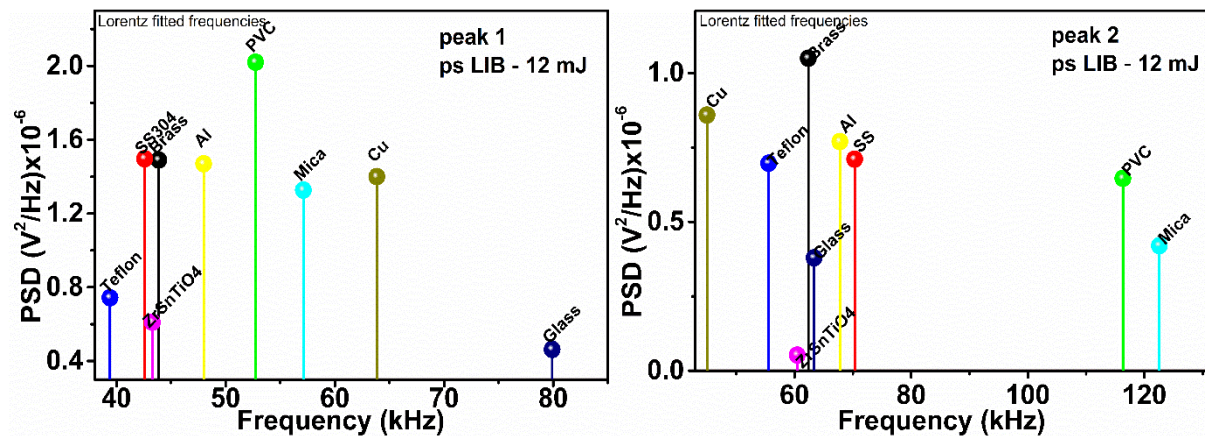


**Fig. 4.39.** Peak 1 and peak 2 frequencies of ps – LIB of various samples at 12 mJ of laser energy.

The frequency components are well separated as we observed for 24 mJ of laser energy. The acoustic peaks and spectral widths are tabulated in table 4-18. The ratios are also distinct from

sample to sample, though distinct nature of acoustic parameters is not so explicitly observed for all incident laser energies. Fig. 4.38 and 4.39 show the dependence of laser energy on the ASW from ps-LIB. Pulse energy  $\sim 24$  mJ seems to be better to distinguish the acoustic signals and their PSDs in our studies.

**Table 4-18.** At 12 mJ laser energy, the Lorentz fitted central frequency, peak width and its ratios for all the samples for ps LIB of various samples.

Samples	Peak 1			Peak 2		
	Central frequency (kHz) ( $\omega_1$ )	Width (kHz) ( $\Delta\omega_1$ )	$\Delta\omega_1/\omega_1$	Central frequency (kHz) ( $\omega_2$ )	Width (kHz) ( $\Delta\omega_2$ )	$\Delta\omega_2/\omega_2$
Brass	43.87	29.81	0.679	62.37	18.95	0.304
SS	42.58	30.16	0.708	70.30	12.86	0.183
PVC	52.75	38.09	0.722	116.32	39.42	0.339
Teflon	39.41	30.42	0.772	55.55	40.38	0.727
Mica	57.12	42.19	0.739	122.57	44.46	0.363
ZrSnTiO4	43.29	33.95	0.784	60.47	26.07	0.431
Al	48.00	34.43	0.717	67.79	19.43	0.287
Cu	63.85	30.18	0.473	44.98	24.70	0.549
Glass	79.90	28.02	0.351	63.36	34.22	0.540

### 4.3 Repetitive ablation

In addition to the regular LIBS, where each laser pulse interacts with a pristine surface, we have studied ASWs due to repetitive ablation of materials. In this mode, multiple laser pulses are allowed interact with pre irradiated sample surface. The first laser pulse ablates pristine surface and the subsequent pulses will interact with the ablated surface containing crater with recondensed ablated material in the form of solidified particles in some cases. This will lead to increased crater dimensions (depth and width) with increasing number of pulses before the ablation efficiency reaches saturation. This entire process will affect the ASW from the successive pulses. To understand the saturation of the ablation efficiency, acoustic signals are picked up after 32, 64 and 128 laser shots at laser energies of 60, 80 and 100 mJ. The time domain signals and their corresponding acoustic spectrums are presented in fig. 4.40 (a), (b).

Change in acoustic signals (-ve peak height, arrival time) and the associated spectrums are clearly identified in fig. 4.40 (a) and (b) respectively.

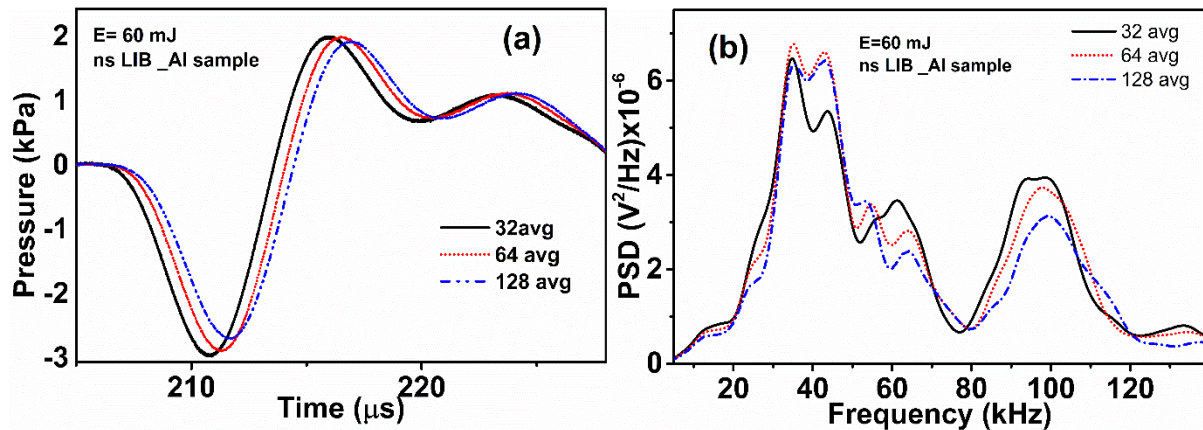


**Fig. 4.40.** Time domain signals (a) and its corresponding acoustic spectrums (b) of 32, 64 and 128 averaged ASW signals at laser energy of 60 mJ.

A clear reduction in the ASW parameters (peak pressure) and FWHM of -ve peak are observed as shown in fig. 4.41.

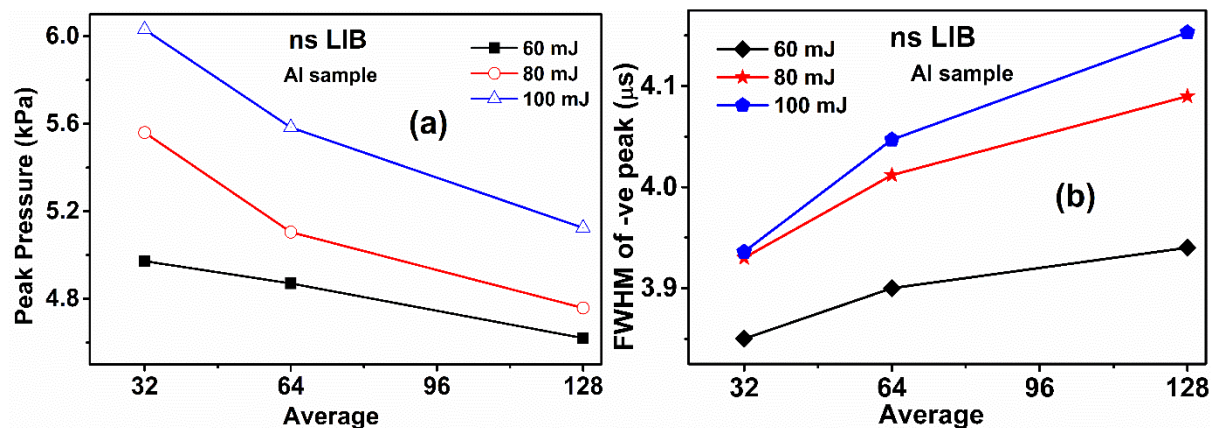


**Fig. 4.41.** (a) Peak-to- peak pressures and (b) FWHM of -ve peak of emitted ASW from the LIB of Aluminium sample for consequent laser shots of 32, 64 and 128 on same spot at 60, 80 and 100 mJ energies.

As the laser energy increased from 60 to 100 mJ, the peak pressure rises from 4.97 to 6 kPa, respectively, shown in fig. 4.38 at a particular average (32 or 64 or 128) of incident laser pulses. At 32 shots average, 2.97, 3.55, 3.93 kPa are the -ve peak heights for 60, 80, 100 mJ of laser energies, respectively. It indicates that the good amount of incident laser energy is converted into acoustic energy despite multiple laser shots interacting with material.

At 60 mJ of laser energy, the peak pressures are 4.97, 4.87 and 4.62 kPa for 32, 64 and 128 average of laser shots, respectively. The pressures decay as the number of laser shots increases at the same spot. The similar decrease in peak pressures were observed for remaining energies of 80 and 100 mJ laser energy, shown in fig. 4.41 (a).

At fixed laser energy of 60 mJ, for fixed number of shots average 32, 64 and 128 the +ve peak widths 14.87, 14.49 and 14.11  $\mu$ s, respectively. The same trend is observed for remaining laser energies 80 and 100 mJ also. It means that, the density fluctuations effected by ablated particles is less. As the number of shots falling on same spot increases, the ablation rate decreases.

At 80 mJ of laser energy, the FWHM of –ve peak values are 3.93, 4.01, 4.09  $\mu$ s for 32, 64, 128 shots average, respectively. As the number of shots on a same area increases, the FWHM of –ve peak also increases, for all energies (60, 100 mJ). Here FWHM is increasing with the increasing number of incident laser pulses at any incident laser energy, shown in fig 4.41 (b). Generally, as we focus more number of laser pulses on a same area, more ablation takes place. It will happen only when the target moves towards the incident laser direction according to ablation rate. But, here, target is not moving towards the laser, it is fixed at the focal point for all the 32 laser shots. The pulse to pulse time gap is 1 sec and the pulse width is nano second. The ablated species exists at focal point up to a few microseconds, so the subsequent laser shot is not interacting with the ionized species at crater. After the few pulses interaction, there is formation of molten, solidified material around and inside the crater. So, interaction of laser pulses with the less dense molten or solidified material generates the less intense ASWs (low pressure waves) than the first stage of ablation, as shown in fig. 4.41.

After few pulses of interaction with material, there is a formation of craters. The dimensions of the crater will tell the amount of laser energy coupled to the target material [27]. The next pulses are focused in craters, in which laser pulse will interact with crater edges also. Then laser pulses doesn't interact with material, completely and the generated heat is transferred to crater edges and transferred to surrounding atmosphere. This leads to lower pressure at 128 shots average. We can see the difference in pressures for ablation of virgin spot area (average of shots) and different number of laser shots on same spot area, at various laser energies of 60, 80, 100 mJ presented in fig. 4.42.

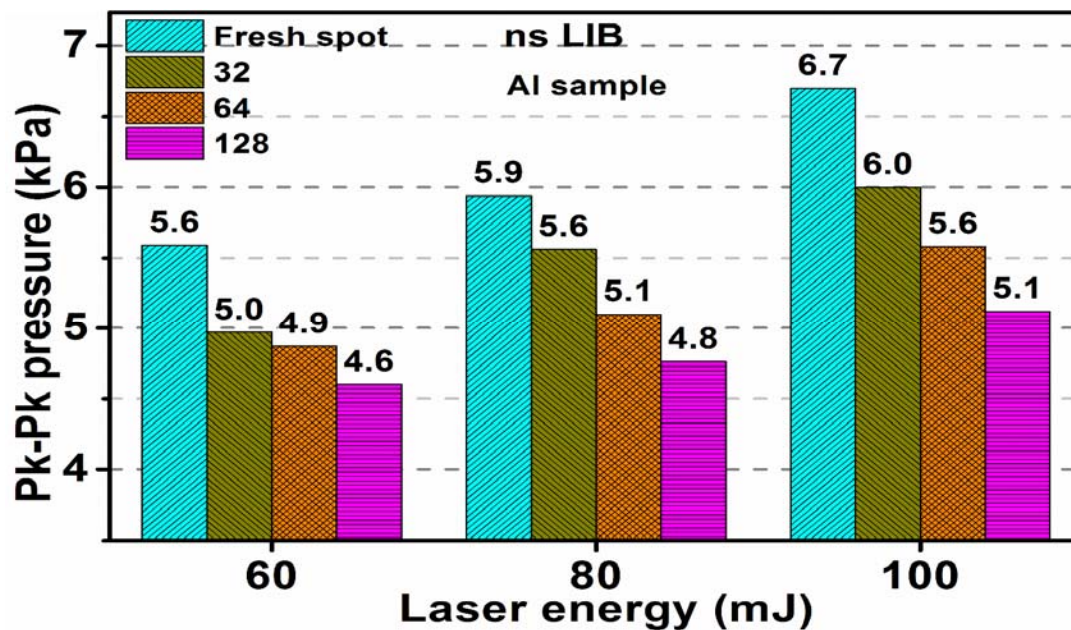


**Fig. 4.42.** Comparison of ASW peak pressures between the fresh spot area ablation and the ablation due to different number of shots on same spot area at 60, 80, 100 mJ of energies.

As presented in fig. 4.42, the fresh spot ablation generated more peak pressures than the multiple shots ablation on same spot area. Multiple laser shot ablation is reported to increase the x-ray emission up to 5 to 7 laser shots beyond which the x-ray emissions is observed to decrease drastically.

## 4.4 Summary

ASW emissions from ns & ps-LIB of various target samples has been studied at various incident laser energies. Peak pressures, arrival times, area under the curve of both –ve and +ve peaks are plotted w.r.t incident laser energy. The increment in slopes of peak pressures w.r.t laser energy indicates the conversion of optical energy into acoustic energy. With increasing laser energy decrease in arrival times were observed, indicating the rise in acoustic shock velocities along with laser energy.

The LIB of metals (Al, Cu, SS, Brass), dielectrics (Mica, Zirconium tin titanate, Lithium niobate, Barium titanate), insulators (PVC, Teflon, Napthalene, Alumina 90, 99) were studied through the temporal and spectral ASW parameters.

Of all the physical parameters like thermal conductivity, electrical conductivity, density, melting point and boiling point the time domain acoustic parameters follow predominantly the order of melting point. For all the different category of materials studied the acoustic parameters peak pressure and +ve peak width are increasing with increasing input laser energy. The peak

frequencies obtained using FFT to time domain signal of ns- & ps- LIB have given multiple peaks. The important peaks and their PSD values have shown that, the materials can be separated. Repetitive ablation of Al using ns-LIB has shown that the peak pressures are reducing with number of laser shots. Though the peak pressure has reduced, the frequencies are observed to be remain unchanged. This makes acoustic emissions a useful tool to augment standard LIBS.

## 4.5 References

1. S. Petzoldt, J. Reif, and E. Matthias, "Laser plasma threshold of metals," *Applied Surface Science* **96**, 199-204 (1996).
2. Y. F. Lu, M. H. Hong, and T. S. Low, "Laser plasma interaction at an early stage of laser ablation," *Journal of Applied Physics* **85**, 2899-2903 (1999).
3. J. P. Singh and S. N. Thakur, *Laser-Induced Breakdown Spectroscopy* (Elsevier Science, 2007).
4. Y. B. Zel'dovich and Y. P. Raizer, *Physics of Shock Waves and High-Temperature Hydrodynamic Phenomena* (Dover Publications, 2012).
5. M. Tański, R. Barbucha, M. Kocik, K. Garasz, and J. Mizeraczyk, "Investigation of the laser generated ablation plasma plume dynamics and plasma plume sound wave dynamics," in *Laser Technology 2012: Applications of Lasers*, (Proc. SPIE, 2013),
6. B. M. Davis, R. D. McClain, U. W. Suh, and S. R. Mannava, "Real time laser shock peening quality assurance by natural frequency analysis," (Google Patents, 2005).
7. J. B. Deaton, F. H. Azad, M. N. Azer, and T. J. Rockstroh, "Laser shock peening system with time-of-flight monitoring," (Google Patents, 2011).
8. Q. Qin and K. Attenborough, "Characteristics and application of laser-generated acoustic shock waves in air," *Applied Acoustics* **65**, 325-340 (2004).
9. C. Stauter, P. Gérard, J. Fontaine, and T. Engel, "Laser ablation acoustical monitoring," *Applied Surface Science* **109/110**, 174-178 (1997).
10. J. Gómez Bolaños, V. Pulkki, P. Karppinen, and E. Hægström, "An optoacoustic point source for acoustic scale model measurements," *The Journal of the Acoustical Society of America* **133**, EL221 (2013).
11. N. Hosoya, I. Kajiwara, T. Inoue, and K. Umenai, "Non-contact acoustic tests based on nanosecond laser ablation: Generation of a pulse sound source with a small amplitude," *Journal of Sound and Vibration* **333**, 4254-4264 (2014).
12. J. G. Bolaños, V. Pulkki, P. Karppinen, and E. Hægström, "An optoacoustic point source for acoustic scale model measurements," *The Journal of the Acoustical Society of America* **133**, EL221-227 (2013).
13. K. G. Watkins, C. Curran, and J.-M. Lee, "Two new mechanisms for laser cleaning using Nd:YAG sources," *Journal of Cultural Heritage* **4**, **Supplement 1**, 59-64 (2003).
14. G. D. Larson, J. S. Martin, and W. R. S. Jr., "Investigation of microphones as near-ground sensors for seismic detection of buried landmines," *The Journal of the Acoustical Society of America* **122**, 253-258 (2007).
15. K.-H. Leitz, B. Redlingshöfer, Y. Reg, A. Otto, and M. Schmidt, "Metal Ablation with Short and Ultrashort Laser Pulses," *Physics Procedia* **12**, 230-238 (2011).
16. L. Cabalin and J. Laserna, "Experimental determination of laser induced breakdown thresholds of metals under nanosecond Q-switched laser operation," *Spectrochimica Acta Part B: Atomic Spectroscopy* **53**, 723-730 (1998).
17. L. J. RADZIEMSKI, *Lasers-Induced Plasmas and Applications* (Taylor & Francis, 1989).

18. L. V. Kumar, "Radio Emissions from Laser Induced Breakdown of Materials," (University of Hyderabad, 2016).
19. D. R. H. Jones and M. F. Ashby, *Engineering Materials 2: An Introduction to Microstructures, Processing and Design* (Elsevier Science, 2005).
20. J. G. Fujimoto, "Time-Resolved Studies of Nd : YAG Laser-Induced Breakdown," 1771-1777 (1985).
21. D. Dogas, T. Efthimiopoulos, C. Andreouli, and M. Campbell, "Acoustic wave monitoring of the excimer laser ablation of YBCO high-Tc superconductor," *Appl Phys A* **73**, 287-294 (2001).
22. Y. F. Lu, M. H. Hong, S. J. Chua, B. S. Teo, and T. S. Low, "Audible acoustic wave emission in excimer laser interaction with materials," *Journal of Applied Physics* **79**, 2186-2186 (1996).
23. F. Wang, Y. Zhang, H. Yao, and B. Yuan, "Real time NDE of laser shock processing with time-of-flight of laser induced plasma shock wave in air by acoustic emission sensor," *Applied Acoustics* **71**, 739-742 (2010).
24. P. Mulser, R. Sigel, and S. Witkowski, "*Plasma production by laser*," *Physics Reports* **6**, 187-239 (1973).
25. S. J. Davies, C. Edwards, G. S. Taylor, and S. B. Palmer, "Laser-generated ultrasound: its properties, mechanisms and multifarious applications," *Journal of Physics D: Applied Physics* **26**, 329 (1993).
26. H. Hébert, F. Vidal, F. Martin, J.-C. Kieffer, A. Nadeau, T. W. Johnston, A. Blouin, A. Moreau, and J.-P. Monchalín, "Ultrasound generated by a femtosecond and a picosecond laser pulse near the ablation threshold," *Journal of Applied Physics* **98**, 033104 (2005).
27. P. Venkateshwarlu, P. Yella, R. K. Buddu, K. B. SankaraRao, R. P.M, K. V. Rajulapati, and P. P. Kiran, "Structural Modification of Stainless Steel Surface Using Pulsed Lasers," *Technology Letters* **10**, 5-8 (2014).
28. A. Semerok, C. Chaléard, V. Detalle, J. L. Lacour, P. Mauchien, P. Meynadier, C. Nouvellon, B. Sallé, P. Palianov, M. Perdrix, and G. Petite, "Experimental investigations of laser ablation efficiency of pure metals with femto, pico and nanosecond pulses," *Applied Surface Science* **138–139**, 311-314 (1999).
29. R. Kelly and A. Miotello, "Laser-pulse sputtering of atoms and molecules Part II. Recondensation effects," *Nuclear Instruments and Methods in Physics Research Section B: Beam Interactions with Materials and Atoms* **91**, 682-691 (1994).
30. H. M. Pang, D. R. Wiederin, R. S. Houk, and E. S. Yeung, "High-repetition-rate laser ablation for elemental analysis in an inductively coupled plasma with acoustic wave normalization  
" *Anal. Chem* **63**, 390–394 (1991).
31. L. M. Cabalín and J. J. Laserna, "Experimental determination of laser induced breakdown thresholds of metals under nanosecond Q-switched laser operation," *Spectrochimica Acta Part B: Atomic Spectroscopy* **53**, 723-730 (1998).
32. D. Albagli, M. Dark, L. T. Perelman, C. von Rosenberg, I. Itzkan, and M. S. Feld, "Photomechanical basis of laser ablation of biological tissue," *Opt. Lett.* **19**, 1684-1686 (1994).
33. M. Klasing, M. Werner, and M. Ivanenko, *Acoustic monitoring of bone ablation using pulsed CO<sub>2</sub> lasers* (2004).
34. M. Ivanenko, M. Werner, S. Afilal, M. Klasing, and P. Hering, "Ablation of hard bone tissue with pulsed CO<sub>2</sub> lasers," *Medical Laser Application* **20**, 13-23 (2005).
35. T. Efthimiopoulos, E. Kritsotakis, L. Naomidis, H. Kiagias, and E. Helidonis, "Ablation rate and threshold flux of cartilage irradiated by a XeCl excimer laser," *Journal of Applied Physics* **87**, 2020-2025 (2000).

36. E. Schwarz, S. Gross, B. Fischer, I. Muri, J. Tauer, H. Kofler, and E. Wintner, "Laser-induced optical breakdown applied for laser spark ignition," *Laser and Particle Beams* **28**, 109-109 (2010).
37. S. V. Shamanaev, "Sound generation by breakdown plasma formations initiated by solid aerosol particles upon exposure to laser radiation," *Russian Physics Journal* **44**, 1256-1262 (2001).
38. Y. Cai and N. H. Cheung, "Photoacoustic monitoring of the mass removed in pulsed laser ablation," *Microchemical Journal* **97**, 109-112 (2011).
39. S. Palanco and J. Laserna, "Spectral analysis of the acoustic emission of laser-produced plasmas," *Appl. Opt.* **42**, 6078-6084 (2003).
40. M. Harris, G. N. Pearson, D. V. Willetts, K. Ridley, P. R. Tapster, and B. Perrett, "Pulsed Indirect Photoacoustic Spectroscopy: Application to Remote Detection of Condensed Phases," *Appl. Opt.* **39**, 1032-1032 (2000).
41. C. Porneala and D. a. Willis, "Time-resolved dynamics of nanosecond laser-induced phase explosion," *Journal of Physics D: Applied Physics* **42**, 155503-155503 (2009).
42. S. Shamanaev and L. Shamanaeva, "Analysis of spectra of acoustic signals generated by high-power pulsed laser radiation propagating in the atmosphere. I. Spectra of local plasma formations," *Russian Physics Journal* **48**, 1188-1196 (2005).
43. S. Shamanaev, "Opto-acoustic effects accompanying laser-induced breakdowns on monodisperse solid aerosol particles," in *Proc. SPIE*, 2000), 225-230.
44. N. P. Krasnenko, S. V. Shamanaev, and L. G. Shamanaeva, "Propagation of laser-induced shock waves in the atmosphere," *IOP Conference Series: Earth and Environmental Science* **1**, 012013 (2008).
45. S. Conesa, S. Palanco, and J. J. Laserna, "Acoustic and optical emission during laser-induced plasma formation," *Spectrochimica Acta Part B: Atomic Spectroscopy* **59**, 1395-1401 (2004).
46. C. Leela, S. Bagchi, V. R. Kumar, S. P. Tewari, and P. P. Kiran, "Dynamics of laser induced micro-shock waves and hot core plasma in quiescent air," *Laser and Particle Beams* **31**, 263-272 (2013).
47. A. W. Miziolek, Vincenzo Palleschi, and e. Israel Schechter, *Laser Induced Breakdown Spectroscopy* (Cambridge University Press, 2006).
48. Y. Reg, K.-H. Leitz, and M. Schmidt, "Influence of Processing Gas on the Ablation Quality at ns-Laser Beam Ablation," *Physics Procedia* **12**, 182-187 (2011).
49. W. P. Leung and A. C. Tam, "Noncontact monitoring of laser ablation using a miniature piezoelectric probe to detect photoacoustic pulses in air," *Applied Physics Letters* **60**, 23-25 (1992).
50. I. Horn, M. Guillong, and D. Günther, "Wavelength dependant ablation rates for metals and silicate glasses using homogenized laser beam profiles — implications for LA-ICP-MS," *Applied Surface Science* **182**, 91-102 (2001).
51. A. K. Rao, "Acoustic emission and signal analysis," *Defence Science Journal* **40**, 55-70 (1990).

This page is intentionally left blank

# CHAPTER 5 : Acoustic shock waves from high energy materials

---

## Abstract:

The properties of ASWs from the ns-LIB of high energy materials are presented in this chapter. ns-LIB of the Ammonium Nitrate (AN), Di Nitro Toluene (DNT), Tri Nitro Toluene (TNT), 3-Nitro-1,2,4-triazol-5-one (NTO) samples and ambient Air is studied at two laser energies of 25, 40 mJ. ASW reproducibility is presented in both time and frequency domain. Huge peak-peak pressure difference between target samples and the Air breakdown is observed. Acoustic spectral peak frequencies of DNT have the highest amplitude than the remaining samples at 25 mJ of laser energy. Acoustic parameters from the breakdown in Air, Nitrogen ( $N_2$ ) and Argon (Ar) as ambient gases were performed. The increment in ASW parameters are observed from the ns LIB of Ar gas than  $N_2$  and Air. ASWs from ns-LIB of 4-Nitro imidazole, Bismuth nitrate ( $Bi(NO_3)_2$ ) and Lead nitrate ( $Pb(NO_3)_2$ ), in the presence of Air and Ar background gasses is presented. By changing the background ambient gas, we can control the associated ASW properties. ps-LIB of RDX, CL-20, TNT and  $NaN_3$  are also presented at two different laser energies. Variation in acoustic parameters were presented at a fixed laser energy, it indicated the effect of sample properties on ASW emissions. The peak frequencies are well separated from one sample to another sample.

## 5.1 Introduction

High energy materials (HEMs) play a crucial role in advancement of civilization. Mines of lime stone, metals and coal can be dug deeper quickly, faster infrastructure development expansion of roads, fast clearance of older buildings and expansion of harbours and rocket motors (propellants) that launch satellites that played crucial role in communication revolution. For all these applications, engineering of HEMs is essential. Explosives can be used for the dark side also, in IED's, bombs and in guns to increase the velocity of bullet.

To take control of both good and bad sides of explosives, it is essential to detect HEMs from long range distance. Various techniques are available for the detection and identification of explosives some of them are Laser induced breakdown spectroscopy (LIBS), Raman spectroscopy, terahertz, and photoacoustic techniques etc. [1-4]. Out of various available detection techniques, laser based detection is in focus as the beams can propagate over long ranges. People have reported, LIBS of RDX, HMX, TNT, and NTO with laser pulses of different widths [5-7]. Detection of isomers were also reported by using LIBS [8].

High energy materials (HEM) (explosives), when detonated undergo a fast chemical reaction and generate large amount of heat and exert a high pressure on its surroundings. Classification of explosives [9] is presented in fig 5.1 and their few important properties are mentioned in following sections.

Explosives are classified into three types, high explosives, propellants and pyrotechnics, shown in fig. 5.1. High explosives lead to detonation. Propellant does not detonate, but these combust or deflagrate and are mostly used as fuel in rockets. Pyrotechnics are materials capable of undergoing self-contained and self-sustained exothermic chemical reactions and produces effects such as explosion, fire, light, heat, smoke, sound, or gas emission [9]. Some desirable characteristics of HEMs are stability, oxygen balance, impact sensitivity, friction sensitivity, heat of formation, velocity of detonation and detonation pressure. High explosives are again classified into three types [10] which are primary, secondary and intermediate explosives depending on their chemical properties. Primary explosives will create detonation, this can be initiated by heat or strong shock wave. Detonation of these primary explosives creates large amount of heat or mechanical pressure waves in surrounding medium, these are used in triggering devices. Lead azide, mercury fulminate, silver azide, diazo di nitro phenol etc. are some of primary explosives.

Secondary explosives are not able to detonate as primary explosives. The heat or shock generated by primary explosives can ignite the secondary explosives. These are very insensitive unlike primary explosives. PETN is considered as a reference explosive in this category. If any explosive is more sensitive than the PETN then it is considered as a primary explosive [9]. Tertiary explosives can work as blasting agents. These are very insensitive to shock. Intermediate explosive booster of secondary explosives ignites these. Best examples are ammonium nitrate (AN) and ammonium perchlorate (AP). A flame can ignite the propellants. These do not explode whereas burning takes place at higher rate [10], so low intense explosion

will takes place. These are good to drive out projectiles from the weapons. Pyro technics are a mixture of combustible materials. Generally they contain a fuel, oxidizer and binder to perform some special functions like releasing a specific amount of heat, specific coloured emission, and specific gaseous products.

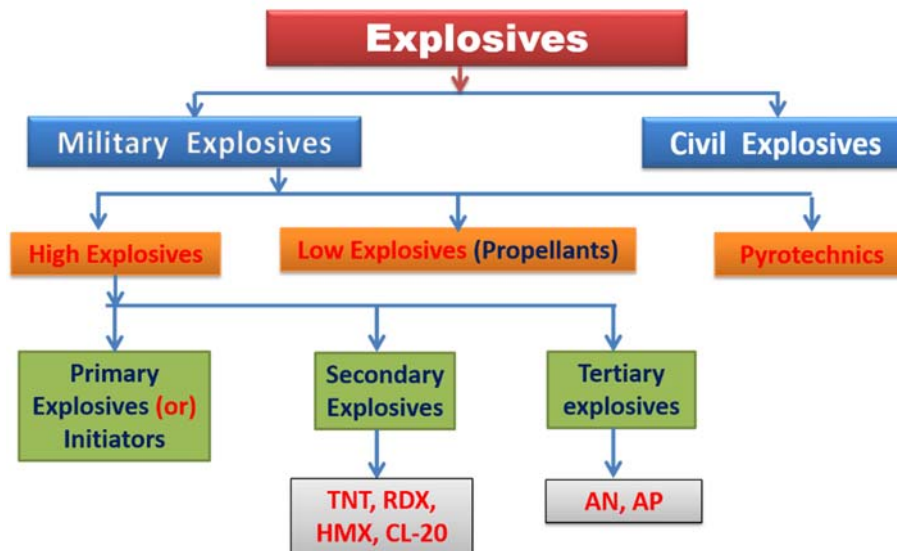


**Fig. 5.1.** Classification of explosives [9].

LIB creates a plasma which mimics a micro explosion or a micro detonation that launches shock/ blast waves into ambient atmosphere. These blast waves propagates with velocities in the range of 8 km/sec or higher [10, 11]. So, studying the plasma generated pressure waves helps to understand the detonation waves produced during explosion. Due to the limited availability of HEM samples, different samples are studied using ns-LIB and ps-LIB. Only TNT was studied using both ns-LIB and ps-LIB to understand effect of pulse duration.

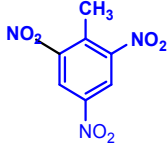
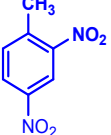
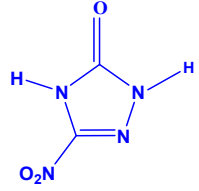
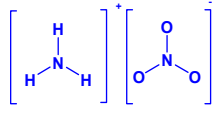
## 5.2 ns-LIB of AN, DNT, TNT, NTO and Air

Ammonium nitrate (AN) is tertiary explosive, generally used for mining and tunnelling purposes. But the mixture of TNT and AN called Amatol, which is very useful and covers the shortage of TNT. For under water explosions, Amatol in addition with aluminium called ammonal is used. TNT has a melting point of 84°C and decomposition temperature of 300°C, so it is named as melt cast explosive or explosive binder. It is in the molten condition for comparatively high period of times [10]. Lower grade of TNT is used for commercial purpose whereas its ultrapure form is for military applications. DNT is used as coolants and surface moderants in gun propellant elements [9]. The mixtures of AN and TNT/DNT are good water resistant. NTO is less sensitive than RDX, HMX and more stable than TNT and RDX. NTO

is used in explosive formulations, gas generators for auto mobile air bag systems. In solid rocket propellants NTO salt derivatives are good energetic additives. TNT is an alternate for Ammonium perchlorate (AP)/AN in rocket propellants, burning rate modifier for composite propellants replacing RDX, HMX and increasing the work of gun propellants [10]. RDX and HMX are greatly used in low vulnerability ammunition (LOVA) of gun propellants [12, 13].

The materials we have studied here are ambient Air, Di Nitro Toulene ( $C_7H_6N_2O_4$  - DNT), Tri Nitro Toulene ( $C_7H_5N_3O_6$ -TNT), Ammonium Nitrate ( $N_2H_4O_3$  - AN) and NTO ( $C_2H_2N_4O_3$ ). Molecular structures [14], formulae and names are mentioned in table 5-1. The experimental schematic of ns-LIB of these materials are presented in chapter 2.

**Table 5-1.** Molecular formula, structures and number of Nitro groups of the HEMs used.

Sample Name	Chemical Formula	Structure	IUPAC nomenclature
<b>TNT</b>	$C_7H_5N_3O_6$		2-Methyl-1,3,5-trinitrobenzene
<b>DNT</b>	$C_7H_6N_2O_4$		Di Nitro Toulene
<b>NTO</b>	$C_2H_2N_4O_3$		3-Nitro-1,2,4-triazole-5-one
<b>AN</b>	$N_2H_4O_3$		Ammonium nitrate

### 5.2.1 Reproducibility

For all these applications, reproducibility of the expected parameters is essential. As LIB mimics a micro explosion detonation/detonation/a small scale reaction reproducibility of LIB signals is studied.

To account for the fluctuations in laser energy and ambient atmospheric conditions where LIB is generated, we usually take average of data sets generated by number of laser shots. The changes in acoustic signals from 20 laser successive laser pulses is presented in fig. 5.2.

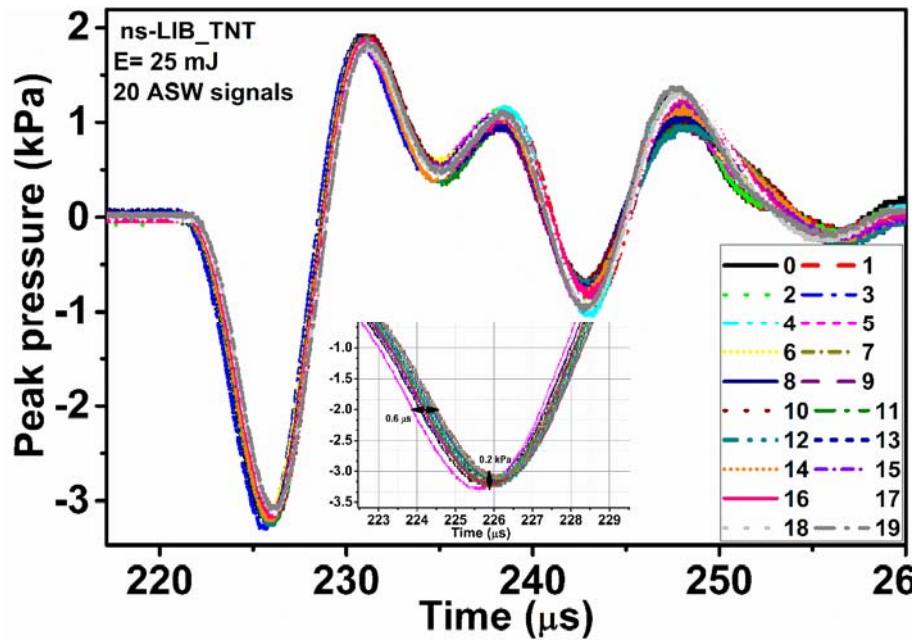


**Fig. 5.2.** ASW signals from LIB of TNT sample, for 20 consecutive laser pulses at 25 mJ of laser energy. Inset shows the image of negative peak (lower) of all 20 ASW signals. X-axis is time, Y- axis is pressure. The maximum deviation in X-axis is  $\approx 0.6 \mu\text{sec}$ , Y-axis is 0.2 kPa.

For ns LIB of TNT, at 25 mJ of laser energy, the average peak to peak pressure of ASWs of ten successive laser shots is  $5.014 \pm 0.073 \text{ kPa}$ . The error in peak pressures is very minimal as in the case of LIB of ambient air. As shown in fig. 5.2, the shift in pressure (vertical shift-Y-axis) and arrival time (horizontal shift-X-axis) are very less (with in error bars). It confirms the, repeatability of ASWs in time domain irrespective of sample characteristics. In general, repeated loading of any material is reported to give acoustic waves [15, 16] with large fluctuations. When compared with the mechanical generated acoustics, laser generated acoustic waves have better reproducibility and used in applications including remote sensing of pressure variations.

The above shown twenty time domain signals (20 laser shots data sets) of TNT sample are used to check the frequency response. The Fast Fourier transform (FFT) of any time domain signal generates its spectrum. Top peak frequencies are chosen for analysis according to their order of amplitude. Lorentz fitted peak frequencies of all twenty laser shots spectrums are presented in fig. 5.3. The actual acoustic spectrum and fitted peaks are shown in fig. 5.3 (a).

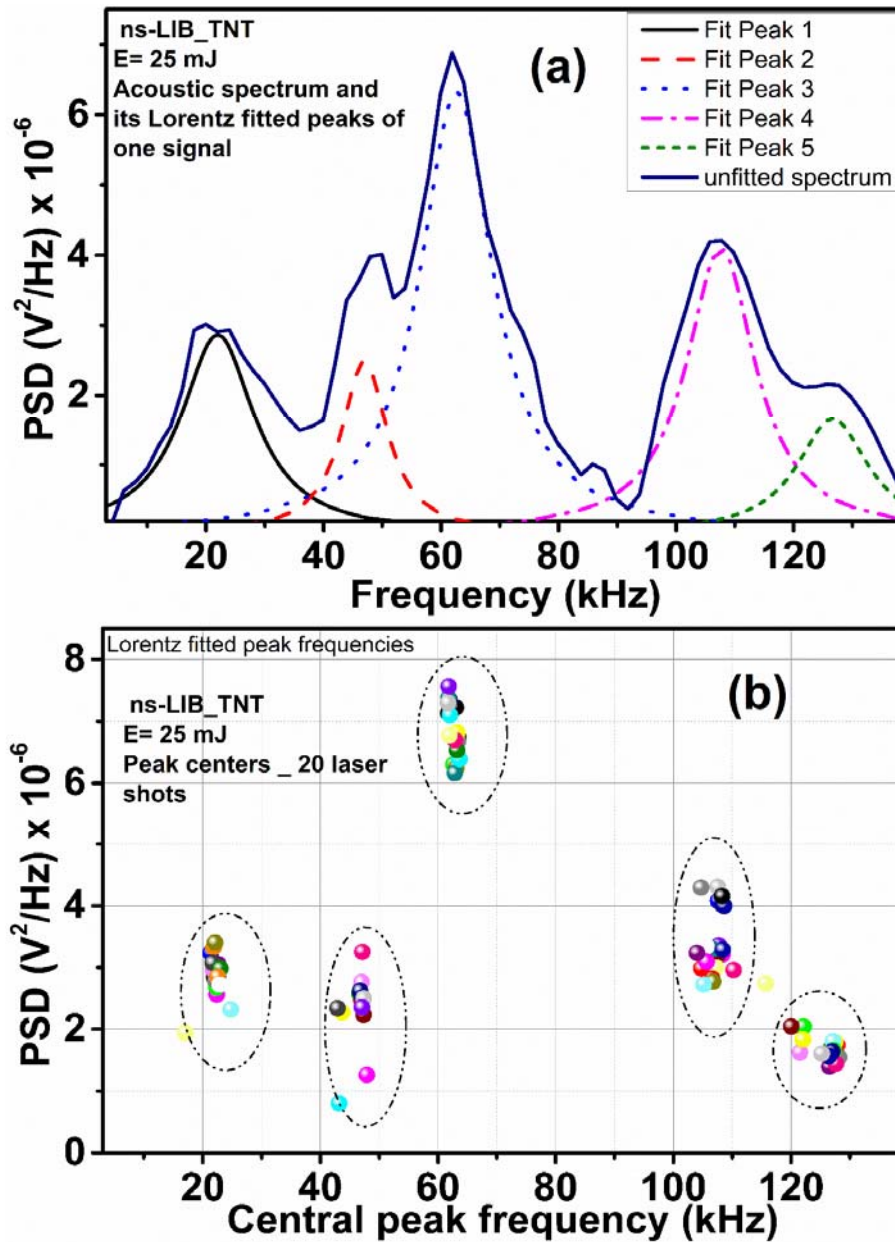


**Fig. 5.3.** (a) Actual spectrum and fitted peaks (five) of single ASW signal. (b) Spectral peak frequencies of twenty successive ns laser shots on TNT target sample, shown with different colours. Lorentz fitted peak frequencies of twenty laser shots data is presented. Here the laser energy is used is 25 mJ per pulse.

Each laser shot on sample generates one acoustic spectrum, each spectrum consists of different number of peak frequencies with slightly different PSD values and all symbols (peak frequencies) are at same frequency. Circled areas in fig. 5.3 shows the frequencies which overlapped on each other with slightly variable frequency and PSD values.

From fig. 5.3, it is evident that the laser-material interaction is reproducible in frequency domain also. The average spectrum of all twenty spectrum, shows the peak frequencies of

$62.88 \pm 0.204$ ,  $106.8 \pm 0.4$ ,  $22.05 \pm 0.35$ ,  $46.73 \pm 0.53$ ,  $125.16 \pm 0.9$  with their PSDs of 6.81, 3.29, 3.06, 2.15,  $1.62 \times 10$  V<sup>2</sup>/Hz respectively. The variation in frequency components of peak 1 and its PSD (Y-axis amplitude) from twenty shots is very less as shown in fig. 5.3. The amplitude variation is within allowed errors. It shows the unchanging spectral response of material with respect to fluctuations in laser energy. Hence fluctuations in laser energy doesn't influence the spectral response of material as much, it is evident from the fig. 5.2 and 5.3.

Now we move to the next step, where all target samples are exposed to incident laser pulses under fixed experimental conditions. The density, melting point, boiling point, number of nitrogen, oxygens and number of nitro groups are given in below table 5-2. These parameters helps to link the ASW properties to that of sample characteristics.

**Table 5-2.** Density, Melting point, Boiling point, number of nitrogen, oxygens etc., properties of samples are given here.

Sample	Density	Melting point (°C)	Boiling point (°C)	No of nitrogens	No of oxygens	No of nitro (NO <sub>2</sub> ) groups
<b>DNT</b>	1.52	70	300	2	4	2
<b>TNT</b>	1.55	80.35	295	3	6	3
<b>AN</b>	1.73	169	210	2	3	-
<b>NTO</b>	1.93	273	247	4	3	1

The breakdown of these target samples were done at both 25 and 40 mJ of laser energies. As expected the peak pressures are high for 40 mJ of laser energy than the 25mJ. The remaining acoustic parameters are tabulated in table 5-3. The difference in peak pressures between air and remaining target samples is ~2 kPa, shown in table 5-3. This clearly indicates the role of HEMs on the ASW properties. These samples are in pellet form and exposed to laser pulses under similar experimental conditions (laser energy, source-receiver distance, target position on translational stage etc.). Here the separation distance between plasma to microphone is fixed at 8 cm, the laser pulses are focused using a lens of 100 mm focal length. ASW parameters at 25 mJ of laser energy are tabulated in table 5-3. Measurements of arrival time, +ve acoustic pulse width, signal energy are done as explained chapters 2&3.

**Table 5-3.** ASW parameters of ns-LIB of Air, DNT, TNT, AN and NTO at 25 mJ laser energy, microphone distance is 8 cm from the plasma.

Sample	Peak pressure (kPa)		Arrival time ( $\mu$ s)		Signal energy ( $V^2 \cdot sec$ ) $\times 10^{-5}$		+ve peak width ( $\mu$ s)		Velocity m/sec	
	25 mJ	40 mJ	25 mJ	40 mJ	25 mJ	40 mJ	25 mJ	40 mJ	25 mJ	40 mJ
<b>Air</b>	3.05	3.77	225.6	222.35	1.77	2.56	11.5	14.91	354.6	359.8
<b>DNT</b>	5.14	6.03	220.7	217.8	5.75	7.84	13.9	18.09	362.4	367.3
<b>TNT</b>	4.99	5.69	221.35	218.8	4.97	6.91	12.36	11.52	361.4	365.6
<b>AN</b>	4.89	5.97	220.9	217.7	5.1	8.2	12.03	14.22	362.1	367.5
<b>NTO</b>	4.84	5.66	220.85	218.2	5.06	8.3	12.22	19.63	362.2	366.4

The peak-peak pressures are around 5 kPa for 25 mJ and 6 kPa for 40 mJ of laser energies respectively. With respect to incident laser energy, we can see the rise in all acoustic parameters such as, signal energy, +ve peak width, velocity, shown in tables 5-3.

Low melting point HEMs generate more peak pressures. HEMs have lower melting point compared to the other solid targets presented in chapter 4. Having lower melting point allows most of the laser pulse to interact with pre heated material leading to a higher temperature LIB plasma resulting in higher peak pressures.

For laser energy of 25 mJ, Lorentz fitted central frequency peaks of ns LIB generated acoustic spectrums of AN, TNT, DNT, NTO samples and Air are presented in fig. 5.4. Since peak pressures from ns LIB of air are low, the number of spectral peaks of air acoustic spectra are also very less in amplitude (PSD) when compared with the remaining samples. It is indicating that, time domain and spectral domain features are proportional to each other in the case of spectral amplitudes. These frequencies with their PSDs are shown in fig 5.4. The peak 1 and peak 2 frequencies of samples spectra are well separated from each other. At 25 mJ of laser energy, the frequencies of peak 1 are 48.3, 49.9, 54.3, 61.3, 62.9 kHz for NTO, DNT, Air, AN, TNT respectively. Whereas, the peak 2 frequencies are 63.1, 99, 106.8, 109.7, 110.4 kHz for NTO, DNT, TNT, AN, Air respectively. The order of peak 1 frequencies w.r.t samples are not followed by the peak 2.

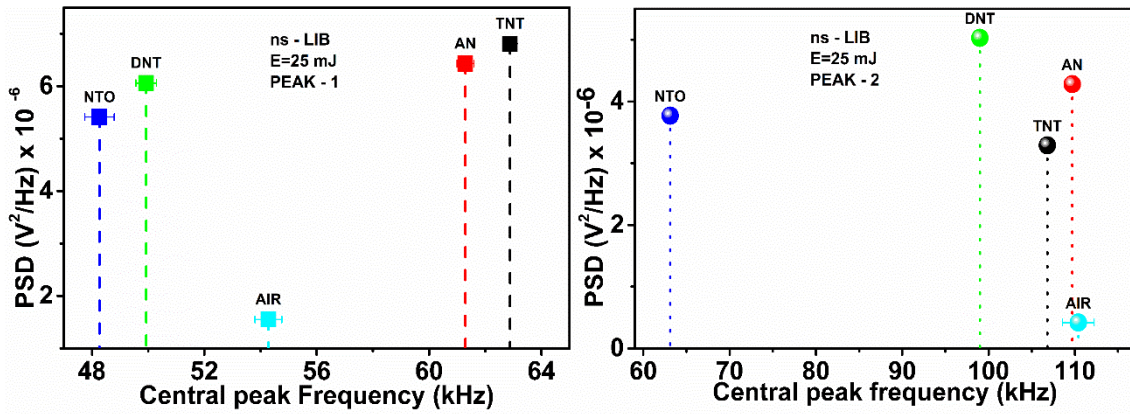


**Fig. 5.4.** Lorentz fitted acoustic spectral central peak frequencies vs their PSD (power spectral density) at 25 mJ laser energy for ns LIB of AN, DNT, TNT, NTO and Air. (a) Peak 1 frequencies, (b) peak 2 frequencies, here frequency is on X-axis, PSD is on Y-axis.

At the laser energy of 40 mJ, the spectral frequencies and their PSDs are plotted in fig. 5.5. DNT spectral peak frequencies are having highest amplitude than the remaining samples at 40 mJ of laser energy. The frequency peaks have also extended into ultrasonic side for DNT compared to other HEMs. At 40 mJ of laser energy, the frequencies of peak 1 are 33.2, 43.2, 52.9, 59.9, 73 kHz for NTO, Air, AN, TNT, DNT respectively. The central frequencies of peak 2 are 19.9, 35, 79, and 97.1, 99.6 kHz for TNT, DNT, NTO, and Air respectively. These frequencies with their PSDs are shown in fig. 5.5.

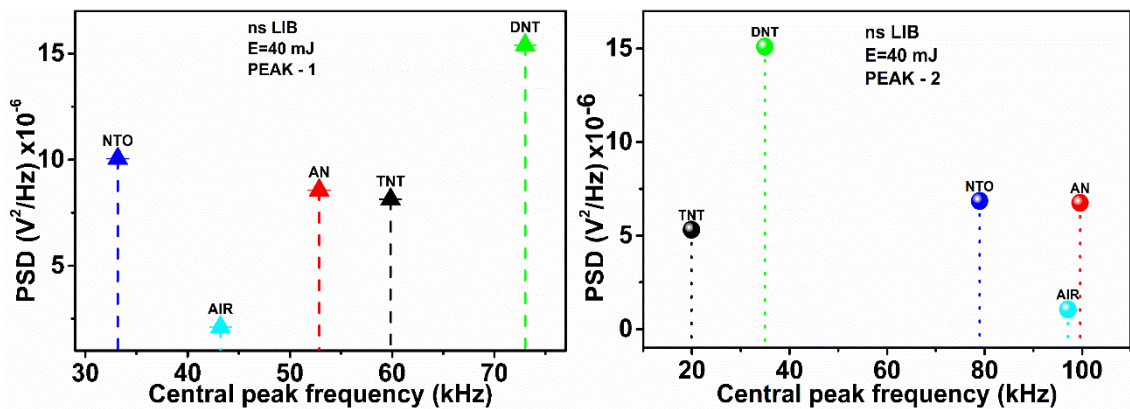


**Fig. 5.5.** Lorentz fitted acoustic spectral central peak frequencies vs their PSD (power spectral density) at 40 mJ laser energy for AN, DNT, TNT, NTO and Air. (a) Peak 1 frequencies, (b) peak 2 frequencies, here frequency is on X-axis, PSD is on Y-axis.

As expected the spectral frequencies of 40 mJ energy are having higher amplitudes than the 25 mJ, indicating higher conversion of laser energy to acoustic energy. So, higher laser energies enhances the peak frequency amplitudes under fixed experimental conditions.

### 5.3 ns-LIB of 4-Nitro Imidazole, Lead nitrate, Bismuth Nitrate

Nitroimidazoles has usage in many fields such as, medicines [17], radio sensitizers and military applications (as explosives) [18-20]. Lead nitrate advances the burning of combustible substances. High amount and longer duration of exposure to fire of lead nitrate, initiates explosion. Lead and bismuth nitrates (metal nitrates) are impressive reagents for nitration of aromatic compounds. The samples of 4-Nitro Imidazole, Lead nitrate ( $\text{Pb}(\text{NO}_3)_2$ ), Bismuth Nitrate ( $\text{Bi}(\text{NO}_3)_3$ ) are taken in pellet form. Each sample is exposed to incident nano second laser pulses in various gas environments such as ambient Air, Nitrogen ( $\text{N}_2$ ) and Ar. The experimental scheme of laser-target samples interaction in the presence of gases are shown in fig. 5.6. Target is (no gas chamber has used) mounted to target holder, then the gas flow is allowed towards the focal point in such a way that, focal point is surrounded by gas and sample breakdown takes place in the presence of applied gas only. The air above the sample was flushed by pressurised Argon or  $\text{N}_2$  gas, then it allows breakdown of sample only and Argon or  $\text{N}_2$  gas confine the plasma.

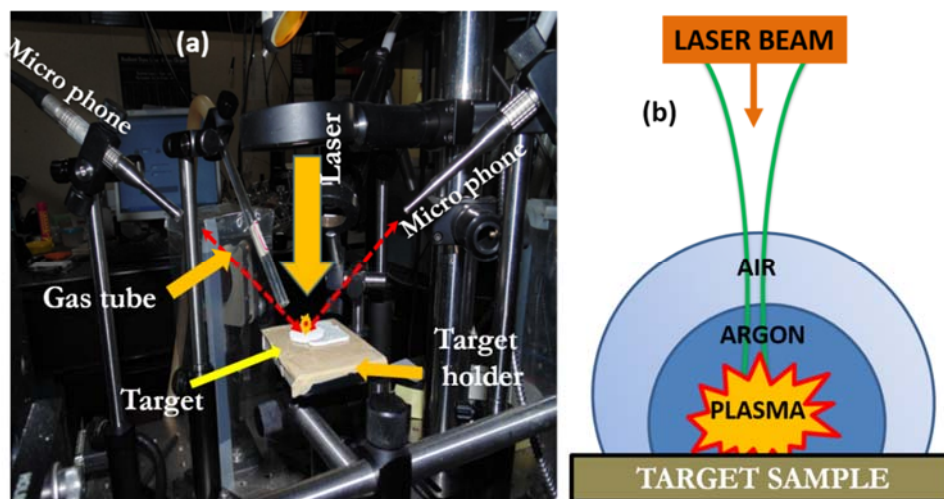


**Fig. 5.6.** Experimental schematic of laser interaction with HEMs in the presence of Nitrogen, Argon gases and Air (a), the actual arrangements of air, argon and plasma above the target sample. Here laser is incidenting on the sample from the top, which is normal to the target sample as shown in (b).

Here no ambient air /Ar / $\text{N}_2$  gas breakdown takes place at the sample breakdown point. The LIB of samples in presence of Air, Argon gases can be visualized like a three concentric hemi spheres, outer one (first one) is air, second one is Argon gas and last one

(inside or focal point) is plasma, shown in fig 5.6 (b). Microphone is positioned at an angle (40 - 60°) w.r.t target sample and laser direction, shown in fig 5.6 (a).

### 5.3.1 ns- LIB of Argon, Nitrogen and Ambient air

Breakdown of gases itself is studied prior to the study of LIB of target samples in gases environment. These gases (Ar, N<sub>2</sub> and Air) are made to breakdown under the same focal geometry what we have used for above experiments. ns LIB of ambient air, Nitrogen and Argon gases generates the ASWs, and the properties are presented in table 5-4. Here the target sample is gases only. The density and thermal conductivities of gases is also presented along with acoustic parameters in the table 5-4. Peak pressures from these three gaseous breakdown shows that, LIB in presence of Ar is radiating stronger ASW than the N<sub>2</sub> and Air environment. Time domain and frequency domain analysis is presented here. The acoustic signal energy due to LIB in N<sub>2</sub> and Ar ambient is observed to be higher by ~ 1.5 and ~2 times respectively, compared to the emissions from Air ambient.

**Table 5-4.** Measurements of ASWs which are emitted from the ns LIB of air, nitrogen and argon gases at 32 mJ of laser energy. Here plasma to microphone distance is 9 cm. Here the target is gas itself. Density and thermal conductivities of Ar, N<sub>2</sub> and Air.

Sample	P <sub>k</sub> (kPa)	E <sub>s</sub> (x10 <sup>-6</sup> ) V <sup>2</sup> .sec	+ve peak width (μs)	A <sub>t</sub> (μs)	Velocity (m/sec)	Total acoustic pulse width D <sub>t</sub> (μs)	Density (kg/m <sup>3</sup> )	Thermal conductivity (W/m.K)
Air	1.85	6.14	8.35	257.5	349.5	18.33	1.66	0.026
Nitrogen	2.24	9.1	9.98	261.5	344.2	16.81	1.17	0.026
Argon	2.6	11.1	10.1	258.5	348.2	17.26	1.18	0.017

Peak width of +ve portion, area under the -ve and +ve portions in time domain, supports that the breakdown of Ar emits the strong acoustic shock waves than the remaining ones. For better view of comparison between Air, Argon and Nitrogen gases breakdown, these acoustics parameters are plotted in fig. 5.7. Lower thermal conductivity of Argon gas compared to the N<sub>2</sub> and Air leads to better confinement of the plasma to the target surface, resulting in a rapid increase in the plasma density and have a stronger SW into the surrounding atmosphere. So, argon environment confines the plasma for a longer time than the N<sub>2</sub> and Air [21]. It results

in a plasma with higher density that leads to stronger density discontinuity and launches ASWs into the surrounding atmosphere.

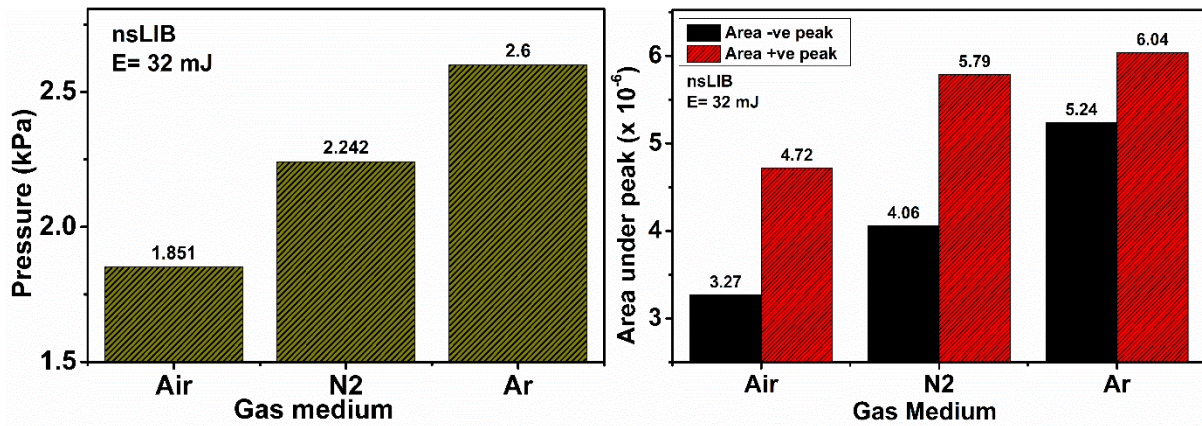


**Fig. 5.7.** ASW parameters of acoustic signals emitted from the breakdown of only Ar, N<sub>2</sub>, Air gases at 32 mJ of laser energy.

The effect of background gas [21] on spectroscopic emissions were studied by several authors [22]. If the laser breakdown of materials occurs in ambient atmospheric air, the plasma properties (its expansion, electron density etc.) are effected by ambient pressure. This results in change of interactions between the atomic and molecular species with in the plasma and surrounding ambient atmosphere. Ambient atmosphere plays a crucial role in LIBS measurements [21]. At low atmospheric pressures, the ablation is improved, uniform craters and improvement in LIBS signal is reported. Aguilier et al. reported the role of background gases of Ar, He, Air, on the temperature and electron densities of LIB plasma from steel [23].

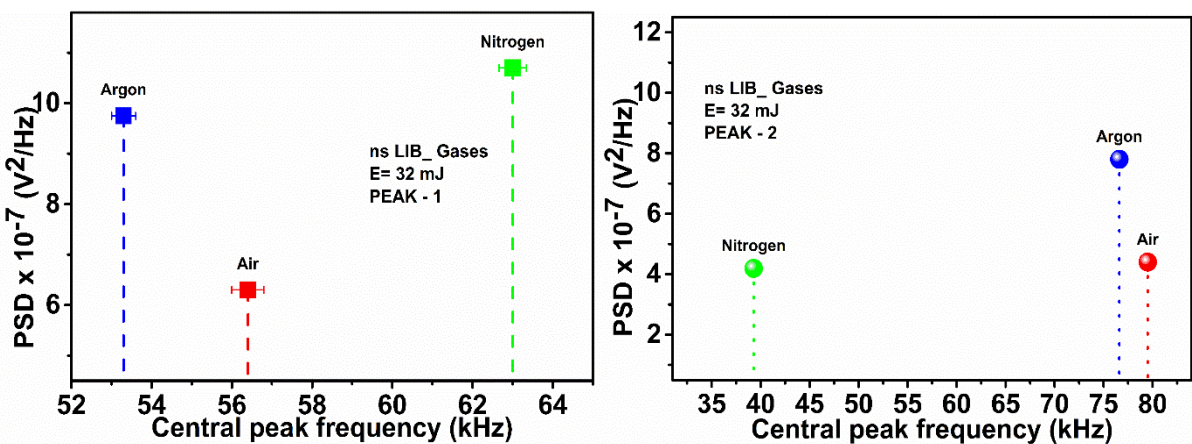


**Fig. 5.8.** The central peak frequencies and their PSDs for ns LIB of ambient AIR, Argon and Nitrogen at an energy of 32 mJ per pulse.

The background gas of Ar results in more plasma temperature and electron density than He and Air. Since argon has very less thermal conductivity whereas He has more, the plasma in Ar atmosphere decays very slowly than that from He [22]. Along with temporal analysis, spectral analysis is presented to bring out the role of background gas. The Lorentz fitted peak frequencies of acoustic spectra of ns LIB of gases of Ambient air, Argon and Nitrogen are presented in fig 5.8 w.r.t their power spectral densities (PSD). For peak 1, the Argon and N<sub>2</sub> PSDs are close to each other, whereas for peak 2, Ar has higher PSD and N<sub>2</sub> and Air PSDs are close to each other.

### 5.3.2 Effect of background gases on LIB:

To study the effect of background gas on ASW from LIB of target samples is presented. For Bismuth nitrate, Lead nitrate and the ASW peak pressures are high for Ar background, than the Air, shown in fig. 5.9. Breakdown of samples in Argon environment generates the more acoustic pressures.

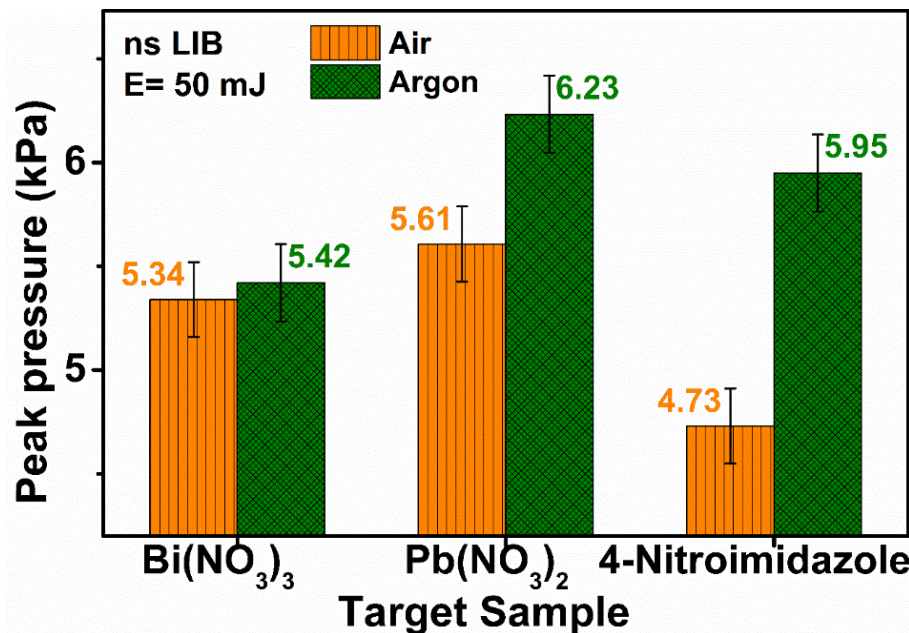


**Fig. 5.9.** The variation in peak pressures of 4-N-Imidazole, Bismuth and Lead nitrate samples in Argon and Air environment at a fixed laser energy of 50 mJ.

In Argon environment, the acoustic data from three samples (4-Nitro Imidazole, Bismuth Nitrate (Bi(NO<sub>3</sub>)<sub>3</sub>), Lead Nitrate (Pb(NO<sub>3</sub>)<sub>2</sub>)) were collected and corresponding acoustic spectrums are analysed. Effect of backing gas or background gas on ASW signals is studied in time domain, now we move into the spectral studies. The FFT of these time domain signals gives the corresponding acoustic spectrum. Breakdown of HEMs in ambient air

environment at 50 mJ of laser energy and the peak 1 and peak 2 frequencies and their PSDs are presented in fig. 5.10.

The central peak frequencies from the spectra of 4-Nitroimidazole,  $\text{Bi}(\text{NO}_3)_3$ ,  $\text{Pb}(\text{NO}_3)_2$  in Air backing gas environments is presented in fig 5.10. Peak 1 frequency of  $\text{Bi}(\text{NO}_3)_3$  (29.6 kHz) is close to audible frequency whereas  $\text{Pb}(\text{NO}_3)_2$  (66.9 kHz) and 4 N-imidazole (72.6 kHz) frequencies are in ultrasonic frequency. For peak 2, the  $\text{Pb}(\text{NO}_3)_2$  (29.8 kHz) and 4 N-imidazole (33.9 kHz) frequencies are close to audible and  $\text{Bi}(\text{NO}_3)_3$  (71 kHz) is in ultrasonic frequency range.

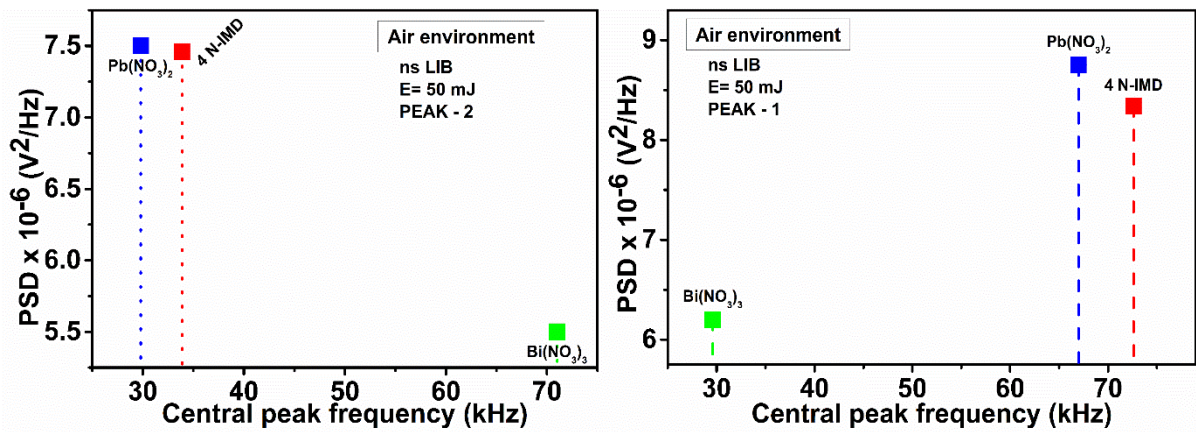


**Fig. 5.10.** The Lorentz fitted central peak frequencies and their PSDs (power spectral density) for the materials of Bismuth nitrate, Lead nitrate and 4-Nitro Imidazole at 50 mJ of laser energy. Here the LIB of material environment is ambient air.

The LIB of samples in Argon backing gas and their spectral peak frequencies are presented in fig. 5.11.

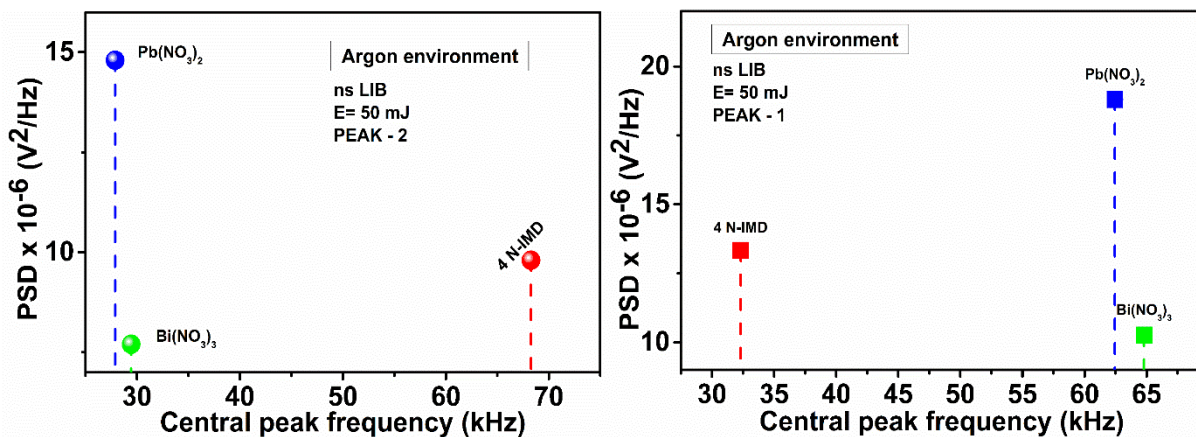


**Fig. 5.11.** The Lorentz fitted central peak frequencies and their PSDs (power spectral density) for the materials of Bismuth nitrate, Lead nitrate and 4-Nitro Imidazole at 50 mJ of laser energy. Here the LIB of material environment is Argon.

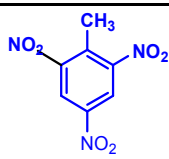
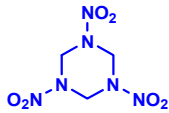
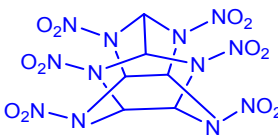
In Argon background, peak 1 frequencies of 4-Nitro Imidazole,  $\text{Bi}(\text{NO}_3)_3$ ,  $\text{Pb}(\text{NO}_3)_2$  are 32.3, 64.8, 62.4 kHz respectively. Peak 2 frequencies of 4-Nitro Imidazole,  $\text{Bi}(\text{NO}_3)_3$ ,  $\text{Pb}(\text{NO}_3)_2$  are 68.2, 29.4, 27.9 kHz respectively. In argon backing gas, the lead nitrate and bismuth nitrate are separated each other on frequency scale.

In Air background gas,  $\text{Bi}(\text{NO}_3)_3$  peak frequencies of peak1 and peak 2 are separated from the  $\text{Pb}(\text{NO}_3)_2$  and 4 N-imidazole, shown in fig. 5.10. Where as in argon backing gas, 4 N-imidazole is separated from the remaining, shown in fig. 5.11. In both Air and Argon environments, if the peak 1 lies close to audible range then peak 2 frequencies are in ultrasonic, this is vice versa. From these observations, even though we are using same target samples under similar experimental conditions, the background gas environment is playing role to optimize the central peak frequencies of both peak 1 and peak 2.

## 5.4 ps LIB of RDX, CL-20, $\text{NaN}_3$ and TNT:

In this section the effect of increased intensity using shorter laser pulses on the acoustic emissions from HEMs is presented.

**Table 5-5.** Structure, molecular formula, and number of Nitro groups of TNT, RDX, CL-20 and Sodium Azide.

Sample Name	Chemical Formula	Structure	IUPAC nomenclature	Number of Nitro groups
TNT	$\text{C}_7\text{H}_5\text{N}_3\text{O}_6$		2-Methyl-1,3,5-trinitrobenzene	3
RDX	$\text{C}_3\text{H}_6\text{N}_6\text{O}_6$		1,3,5-Trinitroperhydro-1,3,5-triazine	3
CL-20	$\text{C}_6\text{N}_{12}\text{H}_6\text{O}_{12}$		2,4,6,8,10,12 - hexanitro - 2,4,6,8,10,12 - hexaazaisowurtzitane	6
Sodium Azide	$\text{NaN}_3$	$\text{Na}^+$ 	Sodium Azide	-

The samples used here are RDX (research developed explosive), TNT, CL-20 (2,4,6,8,10,12 - hexanitro-2,4,6,8,10,12- hexaazaisowurtzitane), Sodium Azide ( $\text{NaN}_3$ ). The chemical formulae, structure and number of nitro groups are tabulated in table 5-5. Powders of these samples were taken and made into pellets.

In this section we present the ASWs due to ps-LIB of HEMs commonly known as RDX, CL-20,  $\text{NaN}_3$  and TNT. The IUPAC nomenclature, structure and chemical formula are given in table 5-5. 1,3,5-Trinitroperhydro-1,3,5-triazine commonly known as RDX (Research Developed Explosive) is developed during world war II and is reported to be more stable both chemically and thermally compared to other HEMs like PETN, TNT, Picric acid.

Sodium azide used in car air bags, airplane escape chutes and it is a good precursor for inorganic azide substances like lead azide and silver azide which are primary explosives.

Here, laser is incident on the sample from top, as shown in fig. 5.6. Here we have used the 110 mm focal lens and the microphone to plasma distance is 8.5 cm. Since we are using ps laser pulses, the intensities at focal point are two orders of magnitude more than that with nano second laser pulses. Since we are using HEMs, care was taken to avoid any sympathetic detonation causing physical damage of optics. The acoustic emissions of these explosives at two different laser energies of 6 and 12 mJ is studied. The ASW parameters at 6 and 12 mJ of laser energy were tabulated in table 5-6.

**Table 5-6.** ASW parameters of ps-LIB of RDX, CL-20, TNT and Sodium Azide at 6 and 12 mJ of laser energy.

Sample	Peak pressure (kPa)		Arrival time ( $\mu\text{s}$ )		Signal energy $\text{V}^2.\text{sec} \times 10^{-5}$		+ve peak width ( $\mu\text{s}$ )		Velocity m/sec	
	6 mJ	12 mJ	6 mJ	12 mJ	6 mJ	12 mJ	6 mJ	12 mJ	6 mJ	12 mJ
<b>RDX</b>	2.44	2.89	235.4	234.2	1.246	1.66	12.51	13.42	361.1	362.9
<b>CL-20</b>	2.51	2.77	235.6	232.7	1.33	1.67	7.01	10.31	360.8	365.3
<b>TNT</b>	2.53	3.27	235.8	233.3	1.22	2.14	8.28	11.94	360.5	364.3
<b><math>\text{NaN}_3</math></b>	2.46	3.16	237.4	234.3	1.32	2.31	8.74	11.99	358.0	362.8

A faster arrival time of ASW from RDX, CL-20, TNT compared to  $\text{NaN}_3$  can be attributed to the presence of  $\text{NO}_2$  group which is reported to dissociate at lower temperatures [24]. The laser matter interaction is different at various laser energies. At 6 mJ of laser energy the TNT

produces 2.53 kPa pressure whereas at 12 mJ, 3.27 kPa peak pressure is produced. Rise in peak pressures with laser energy is presented in fig. 5.12. The +ve peak width of ASWs at 6 and 12mJ laser energies follows the order RDX > NaN<sub>3</sub> > TNT > CL-20. Whereas this order is not followed by the peak pressures at two energies. The peak pressure, arrival time, signal energy, +ve peak width and velocity of ASWs are presented in table 5-6.

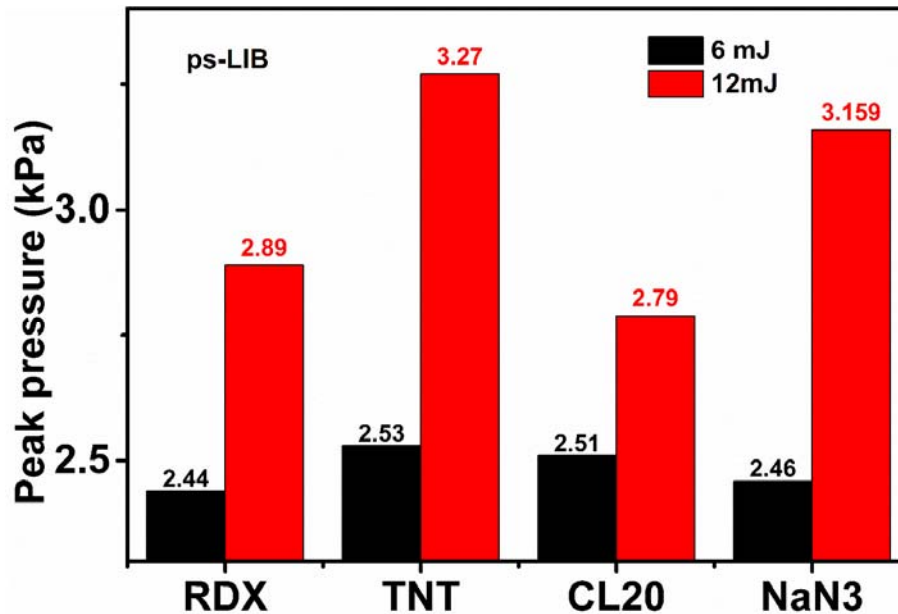


**Fig. 5.12.** Peak pressures for RDX, TNT, CL20 and Sodium Azide (NaN<sub>3</sub>) for 6, 12 mJ laser energies.

The acoustic shock waves generated from the ps LIB of HEMs, has higher velocities than the sound velocity of 335 m/sec at ambient atmosphere. There is a rise in ASW velocities w.r.t incident laser energy. The acoustic peak pressures are plotted for both 6 and 12 mJ of laser energies. Peak pressures are high for 12 mJ laser energy than the 6 mJ, shown in fig 5.12. As the laser energy is increased from 6 to 12 mJ, the frequency peak shifts from ultrasonic to towards audible range. The behaviour of spectrum is almost same for all the samples at both energies, but peaks and their amplitudes are different. Fig. 5.13 shows the spectrum of CL-20 obtained for the two energies used.

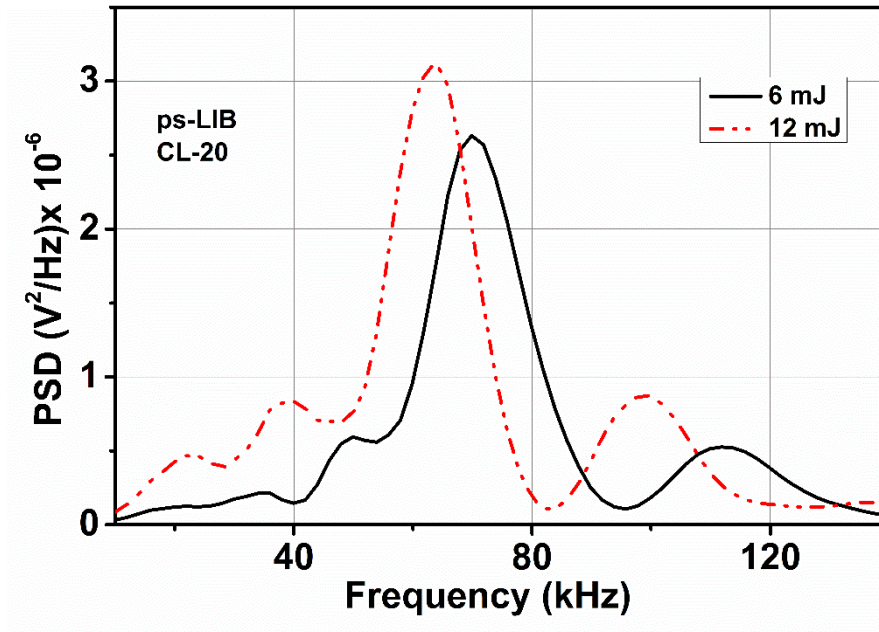


**Fig. 5.13.** Spectrum of ps-LIB of CL-20. The spectrums at two laser energies of 6, 12 mJ. The spectral response is same for both energies. PSD value is high for 12 mJ spectral peak than the 6 mJ.

If a spectrum contains three fitted frequency peaks, the peak with highest PSD is considered as peak 1, as presented in earlier chapters. The same order is applied for remaining peak also like peak 2, peak3. For 6 mJ of laser energy, we presented the peak1 and peak2 frequencies vs their PSDs for four samples, fig. 5.14.

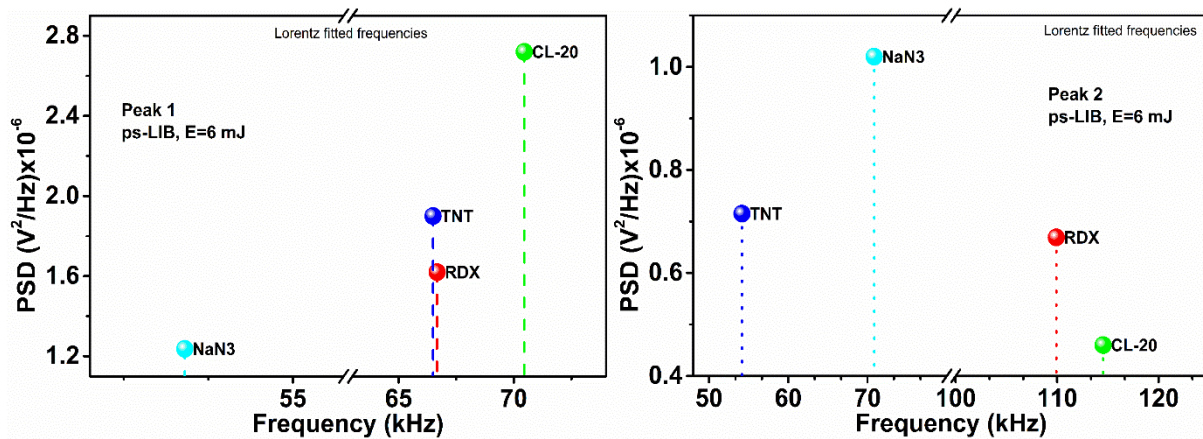


**Fig. 5.14.** Peak frequencies (Lorentz fitted) vs PSD values presented in spectrums of ps LIB of RDX, TNT, CL-20 and Sodium azide ( $\text{NaN}_3$ ) samples, at a fixed energy of 6 mJ.

Clearly peak frequencies are well separated from each other for all samples at 6 mJ energy. Peak 1 frequencies are observed over range of 51 to 72 kHz, whereas peak 2 covers over 50 to 115 kHz range.

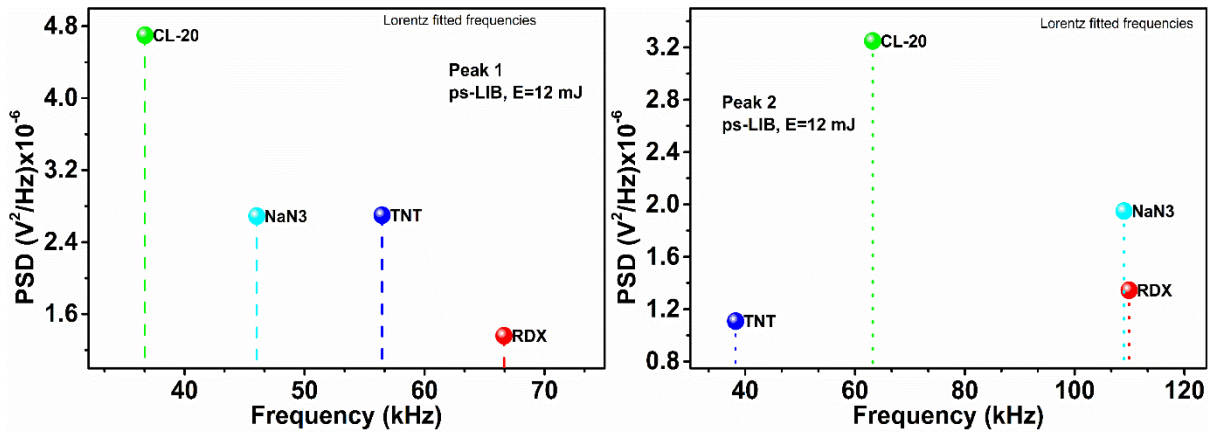


**Fig. 5.15.** Peak frequencies (Lorentz fitted) vs PSD values presented in spectrums of ps LIB of RDX, TNT, CL-20 and Sodium azide (NaN<sub>3</sub>) samples, at a fixed energy of 12 mJ. Each data point is a different colour sphere.

At 12 mJ, the peak1 and peak2 frequencies with their PSDs are presented in fig 5.15. For RDX, NaN<sub>3</sub>, the peak 2 frequencies are close to each other, but their amplitudes are different. At 12 mJ laser energy also, the peak frequencies are well distinguished from each other.

## 5.5 ns-vs ps- LIB of TNT

TNT sample is exposed to both ns and ps laser pulses at 12, 25 mJ energies respectively.

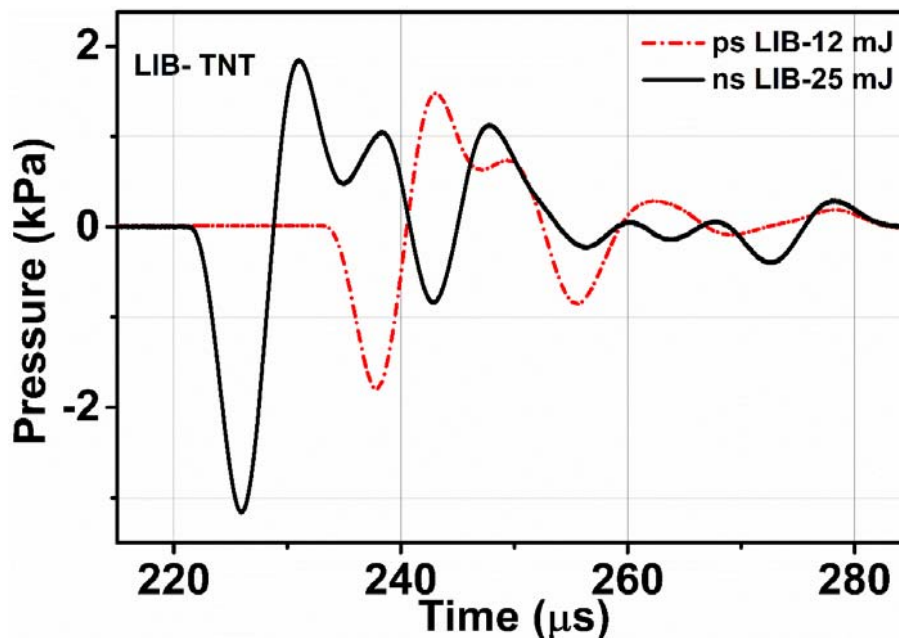


**Fig. 5.16.** Time domain signals, of ns and ps -LIB of TNT sample at 25 mJ and 12 mJ of laser energies respectively.

ns-LIB and ps-LIB of TNT sample generated acoustic signals and their corresponding acoustic spectra were presented in fig. 5.16 and 5.17 respectively. Here laser energy for ns

pulses is 25 mJ and for ps pulses is 12 mJ. This fig. 5.17 shows the effect of laser pulse duration on ASWs. ns LIB generates more acoustic pressures than the ps LIB of same sample under similar focusing geometry. The +ve peak width for ns-LIB of TNT produced ASW is 11.52  $\mu$ s whereas 8.28  $\mu$ s is for ps-LIB. There is difference in remaining acoustic parameters also.

The spectral amplitude is higher for ns-LIB of TNT than the ps-LIB, shown in fig. 5.17. The range of spectral response is same but, the peak frequencies are different.

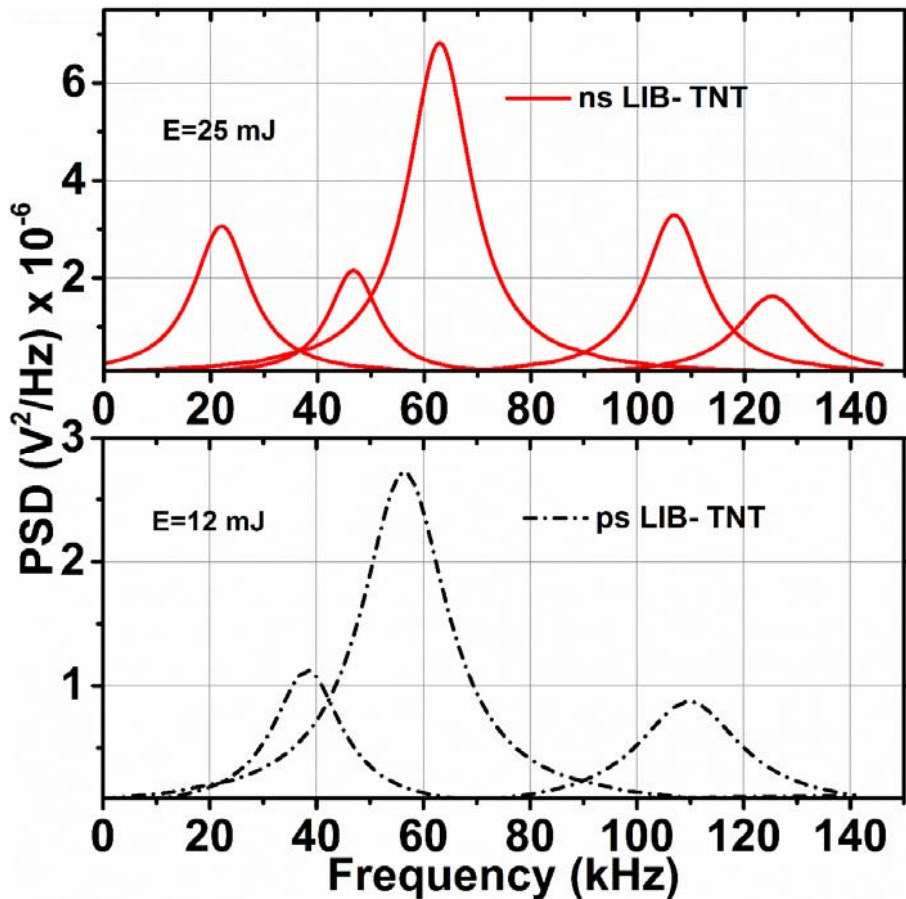


Fig. 5.17. Lorentz fitted spectral peak frequencies for both ns, ps LIB of TNT sample.

## 5.6 Summary:

We presented the time domain acoustic parameters of ASW such as peak to peak pressure, signal energy, +ve peak pulse width, velocity for the HEMs available to us. Acoustic parameters are obtained to be dependent on the material properties.

ns and ps-LIB of HEMs in pellet form studied, have shown higher peak pressures longer +ve peak width and higher acoustic shock velocity compared to that of atmospheric air.

LIB of Argon gas generates the more acoustic peak pressures than the N<sub>2</sub> and Air. The lower thermal conductivity of Ar gas confines the plasma more than the remaining background gases, resulting in enhancement of acoustic parameters. The laser induced breakdown of 4-Nitro Imidazole, Lead nitrate (Pb(NO<sub>3</sub>)<sub>2</sub>), Bismuth Nitrate (Bi(NO<sub>3</sub>)<sub>2</sub>) samples were done in background gases of Ar and ambient Air. We observed that, peak pressure and peak frequencies are enhanced in Argon background gas environment than the ambient Air. Distinct spectral features were noticed from one gas environment to another one for a particular sample. In Air as background gas, Bi(NO<sub>3</sub>)<sub>2</sub> peak frequencies of peak1 and peak 2 are separated from the Pb(NO<sub>3</sub>)<sub>2</sub> and 4 N-imidazole. Where as in Argon ambient, 4 N-imidazole is separated from the remaining.

ns LIB of AN, DNT, TNT and NTO were presented at two laser energies of 25, 40 mJ. The ASW parameters are function of laser energy because higher laser energy rises the plasma species and leads increase in pressure and temperature gradients. ps-LIB of RDX, CL-20, NaN<sub>3</sub> and TNT were presented at two laser energies of 6, 12mJ. The acoustic parameters were tabulated clearly. The peak frequencies of target samples are well separated at two laser energies.

## 5.7 References:

1. D. A. Cremers and L. J. Radziemski, *Handbook of Laser-Induced Breakdown Spectroscopy* (Wiley, 2006).
2. P. M. Pellegrino, E. L. Holthoff, and M. E. Farrell, *Laser-Based Optical Detection of Explosives* (CRC Press, 2015).
3. M. R. Leahy-Hoppa, J. Miragliotta, R. Osiander, J. Burnett, Y. Dikmelik, C. McEnnis, and J. B. Spicer, "Ultrafast Laser-Based Spectroscopy and Sensing: Applications in LIBS, CARS, and THz Spectroscopy," *Sensors* **10**, 4342 (2010).
4. K. S. Rao, A. K. Chaudhary, and F. Yehya, "Investigation of thermal stability and fingerprint spectra of energetic 1,2,3-triazole using pulsed photoacoustic pyrolysis technique," *Appl Phys B* **121**, 375-384 (2015).
5. S. Sreedhar, M. A. Kumar, G. M. Kumar, P. P. Kiran, S. P. Tewari, and S. V. Rao, "Laser-induced breakdown spectroscopy of RDX and HMX with nanosecond, picosecond, and femtosecond pulses," in *SPIE Defense, Security, and Sensing*, (SPIE, 2010), 12.
6. V. R. Soma, S. S., A. K. M., P. K. P., S. P. Tewari, and M. K. Gundawar, "Laser induced breakdown spectroscopy of high energy materials using nanosecond, picosecond, and femtosecond pulses: challenges and opportunities," in *International Conference on Fiber Optics and Photonics*, (SPIE, 2011), 10.
7. A. Kumar Myakalwar, N. Spegazzini, C. Zhang, S. Kumar Anubham, R. R. Dasari, I. Barman, and M. Kumar Gundawar, "Less is more: Avoiding the LIBS dimensionality curse through judicious feature selection for explosive detection," *Scientific Reports* **5**, 13169 (2015).
8. A. K. Myakalwar, S. K. Anubham, S. K. Paidi, I. Barman, and M. K. Gundawar, "Real-time fingerprinting of structural isomers using laser induced breakdown spectroscopy," *Analyst* **141**, 3077-3083 (2016).
9. J. P. Agrawal, *High Energy Materials: Propellants, Explosives and Pyrotechnics* (Wiley, 2010).
10. J. Akhavan, *The Chemistry of Explosives* (Royal Society of Chemistry, 2007).
11. P. W. Cooper, *Explosives engineering* (Wiley-VCH, 1996).

12. R. R. Sanghavi, P. J. Kamale, M. A. R. Shaikh, S. D. Shelar, K. S. Kumar, and A. Singh, "HMX based enhanced energy LOVA gun propellant," *Journal of Hazardous Materials* **143**, 532-534 (2007).
13. A. G. S. Pillai, R. R. Sanghavi, C. R. Dayanandan, M. M. Joshi, S. P. Velapure, and A. Singh, "Studies on RDX Particle Size in LOVA Gun Propellant Formulations," *Propellants, Explosives, Pyrotechnics* **26**, 226-228 (2001).
14. M. W. Smith, M. D. Cliff, Aeronautical, M. R. Laboratory, Aeronautical, M. R. L. W. S. Division, D. Science, and T. Organisation, *NTO-based Explosive Formulations: A Technology Review* (DSTO Aeronautical and Maritime Research Laboratory, 1999).
15. "<Vaporization and Plasma Shielding during High Power Nanosecond Laser Ablation of Silicon and Nickel.pdf>."
16. A. K. Rao, "Acoustic emission and signal analysis," *Defence Science Journal* **40**, 55-70 (1990).
17. P. J. Jenks, "CHAPTER 24 - Nitroimidazoles A2 - Finch, Roger G," in *Antibiotic and Chemotherapy (Ninth Edition)*, D. Greenwood, S. R. Norrby, and R. J. Whitley, eds. (Content Repository Only!, London, 2010), pp. 292-300.
18. L. Larina and V. Lopyrev, *Nitroazoles: Synthesis, Structure and Applications* (Springer New York, 2009).
19. J. P. Agrawal and R. Hodgson, *Organic Chemistry of Explosives* (Wiley, 2007).
20. E. N. Rao, P. Mathi, S. A. Kalam, S. Sreedhar, A. K. Singh, B. N. Jagatap, and S. V. Rao, "Femtosecond and nanosecond LIBS studies of nitroimidazoles: correlation between molecular structure and LIBS data," *Journal of Analytical Atomic Spectrometry* **31**, 737-750 (2016).
21. T. Delgado, J. M. Vadillo, and J. J. Laserna, "Acting Role of Background Gas in the Emission Response of Laser-Induced Plasmas of Energetic Nitro Compounds," *Applied Spectroscopy* **70**, 1364-1374 (2016).
22. A. J. Effenberger and J. R. Scott, "Effect of Atmospheric Conditions on LIBS Spectra," *Sensors (Basel, Switzerland)* **10**, 4907-4925 (2010).
23. J. A. Aguilera and C. Aragón, "A comparison of the temperatures and electron densities of laser-produced plasmas obtained in air, argon, and helium at atmospheric pressure," *Appl Phys A* **69**, S475-S478 (1999).
24. K. S. Rao, F. Yehya, A. K. Chaudhary, A. S. Kumar, and A. K. Sahoo, "Thermal stability study of nitro-rich triazole derivatives using temperature dependent time resolved pulsed photoacoustic (PA) technique," *Journal of Analytical and Applied Pyrolysis* **109**, 132-139 (2014).

# **CHAPTER 6 : ASW emissions from interaction zone of two counter propagating laser generated shock waves in air**

---

## **Abstract:**

The acoustic emissions due to interaction of two counter propagating laser induced ablative shock waves is presented in this chapter. These two laser plasma induced shock waves were formed by focussing two counter propagating ns laser beams derived from a common laser source. The laser energies of two incident laser beams were varied with respect to each other. The distance between two plasma sources is changed by moving the focusing lenses towards and away from each other. The acoustic features at various separation distances between the two plasma sources were presented. The interaction between two shock sources (plasmas) is observed to effect the peak-to-peak pressure of resulting acoustic shock wave. The characteristics of interacting shock waves studied through the acoustic diagnostics are observed to give an insight into distribution of plasma into surrounding atmosphere.

## **6.1 Introduction:**

Laser generated acoustic shock waves (ASW) are analogous to small sized blast waves and simulate the sonic booms and associated propagation effects in a laboratory scale effectively. These waves have more reproducibility than other existing methods such as electrical spark, hence can be used as a better diagnostic tool for characterization of a single or multiple blasts and their interactions.

Dual plasma method is being used by researchers in various laser based processes such as pulsed laser deposition (PLD) technique [1, 2], signal enhancement in LIBs based analytical techniques [3], simulating Astrophysical conditions on a table top [4], inertial confinement of laser fusion. Various methodologies like varying background gases, laser intensity, pulse width etc. are used to enhance the plasma parameters that in turn have increased the efficiency of various processes. One of the good method to enhance the plasma is dual plasma or double plasma. There are different schemes to form dual plasmas like, cross-beam [1, 2], parallel

propagating plasmas in which time delay between two incident laser pulses (pre and main laser pulse) is varied [3, 5], two laser beams producing plasmas normal to each other with varying spatial separation between two plasmas. Theoretical and experimental studies were also performed on the colliding plasmas or dual plasma [6] that were analysed by CCD imaging, ion emission analysis and optical emission spectroscopy [7, 8]. The interaction of two shock waves (SW) emitted from the dual plasma can also be considered as an interaction of two fluids with high velocities. During the expansion of two plasmas w.r.t time and space, the meeting point of two plasma called as stagnation layer, at which the density and temperature lasts for a longer duration due to an interesting dynamics of the energy conservation are reported [9]. However acoustic studies on the two plasma sources produced by two counter propagating laser beams are not present. Hence in this chapter, the effects of interaction of two counter propagating SWs were studied and analysed by using acoustic shock wave (ASW) detection. This interaction of two plasmas and their shock waves resembles the interaction two fluids with variable impedances (impedance,  $Z = \rho u$ ,  $\rho$  is density,  $u$  sound velocity). Here the density of the plasma sources is varied by varying the laser energy resulting in SWs of varying pressures. ASWs due to interaction of two plasmas having equal and un-equal densities, is presented here. The parameters of ASWs helps to understand the both plasma and shock wave interaction at the interaction zone.

## **6.2 Experimental details**

Two laser beams in a counter propagation geometry forms two LIB created plasmas. Two lenses  $L_1$  and  $L_2$  of same focal length of 78 mm are used to focus incident laser pulses.  $S_1$  and  $S_2$  are the two micro blasts or plasmas formed by lens  $L_1$  and  $L_2$  respectively. These plasmas were collinear and spatially separated by a distance ( $d$ ). The two lenses  $L_1$  and  $L_2$  are placed on two individual micro controller translational stages in order to vary the separation distance ( $d$ ) between two plasmas as shown in fig. 6.1. Both the laser beams/pulses are propagated such that both the counter propagating beams travel same optical path after the beam splitter (BS). This ensured that both the pulses overlap in time at the interaction zone  $d=0$ . When two plasma plumes are superimposed on each other,  $d$  is zero. The separation distance varied from 0 to 15 mm. The plane where two shock wave interacts is named as interaction zone, which is normal to the incident laser propagation direction. The microphone is placed at 8 cm away along normal to the laser propagation (fig. 6.1). Microphone is connected to oscilloscope for data acquisition.

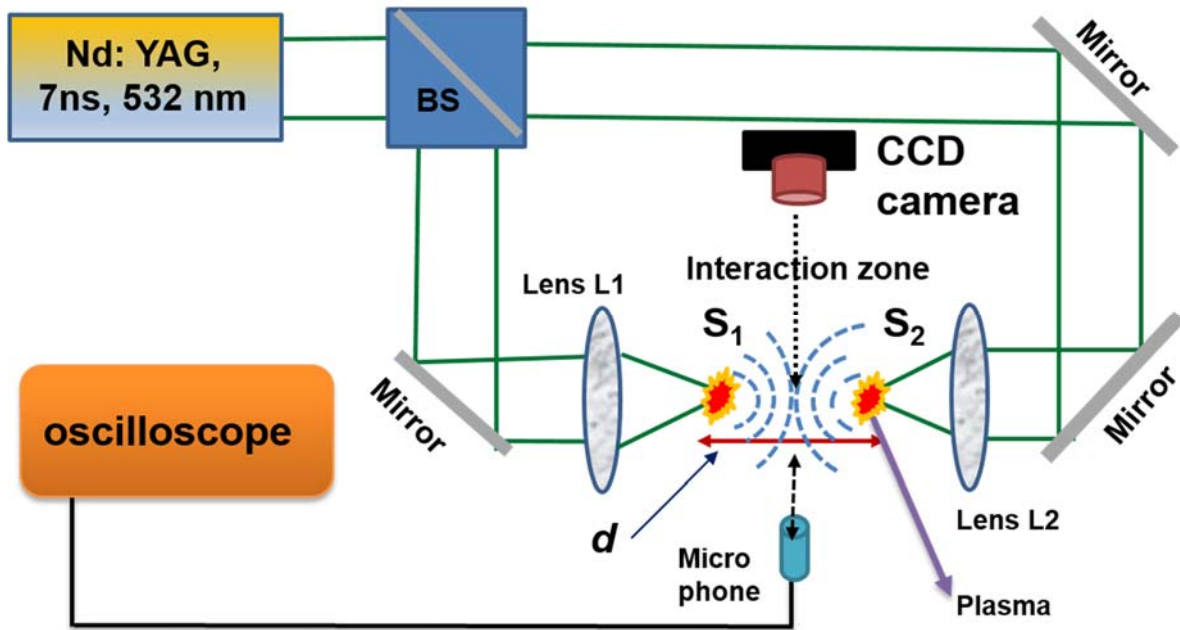


**Fig. 6.1.** Experimental schematic of counter propagation of two shock waves. BS is beam splitter, L1 and L2 are two Plano convex lenses of focal length 78 mm. Separation distance between two plasmas is  $d$ , it is variable. Microphone is fixed at a distance of 8 cm from the laser propagation axis. Interaction zone, where two plasmas meet each other.

The spatial evolution of plasma plumes and their separation is imaged using a CCD camera (SP620U) placed perpendicular to the laser propagation direction. Here the laser energy is measured before the lenses to know the exact laser energy creating the plasma sources.

An ICCD camera based imaging of the spatio temporal evolution of plasma plume and blast wave generated using shadowgraphy technique [10] is also performed to correlate the ASW to that of plasma induced SWs. Some of the representative shadowgrams of the dual plasma (counter wave propagation) are shown in fig. 6.2.

The shadowgrams are presented for better understanding of the process and clear visualization only. The shock properties are out of the scope of the thesis, hence are not presented. Plasma one ( $S_1$ )-plasma two ( $S_2$ ) interaction takes place at lower separation distances ( $d$ ), clearly shown in fig. 6.2. Shock front (SF), Contact front (CF) and Interaction zones are clearly highlighted in fig. 6.2. Interaction of SF1 and SF2, CF1 and CF2s of two plasmas is observed at the interaction zone. The evolution of interaction zone w.r.t time (at various time scales, shadowgrams) is observed in an entire series of shadowgrams and is presented elsewhere [11]. As the separation distance increases, then the shock wave-shock wave interaction starts.

As shown in experimental schematic, laser beam passes through the beam splitter (BS) resulting in two counter propagating laser beam before they are focused at two different points forming plasma ( $S_1$  and  $S_2$ ). Our aim is to understand the evolution of ASW due to interaction of two plasmas with equal and un-equal impedances. In order to achieve this, we have used different beam splitters with R: T of 50:50, 40:60 and 20:80.

By using a beam splitter with R: T= 50:50 similar laser energy is used to form plasma sources, images are shown in first row of fig. 6.2. This scenario is mentioned as case of equal impedances where impedance,  $z = \rho u$ . When the beam splitters with R: T of 40:60 and 20:80 are used the two plasmas were not same in their properties, then we call them as case of un-equal impedances, images are presented in second and third rows of fig. 6.2. Each laser energy forms a plasma with particular properties. Plasma properties are function of incident laser energy and pulse width [12]. The cases of equal and unequal impedances is studied by varying the total input laser energy.

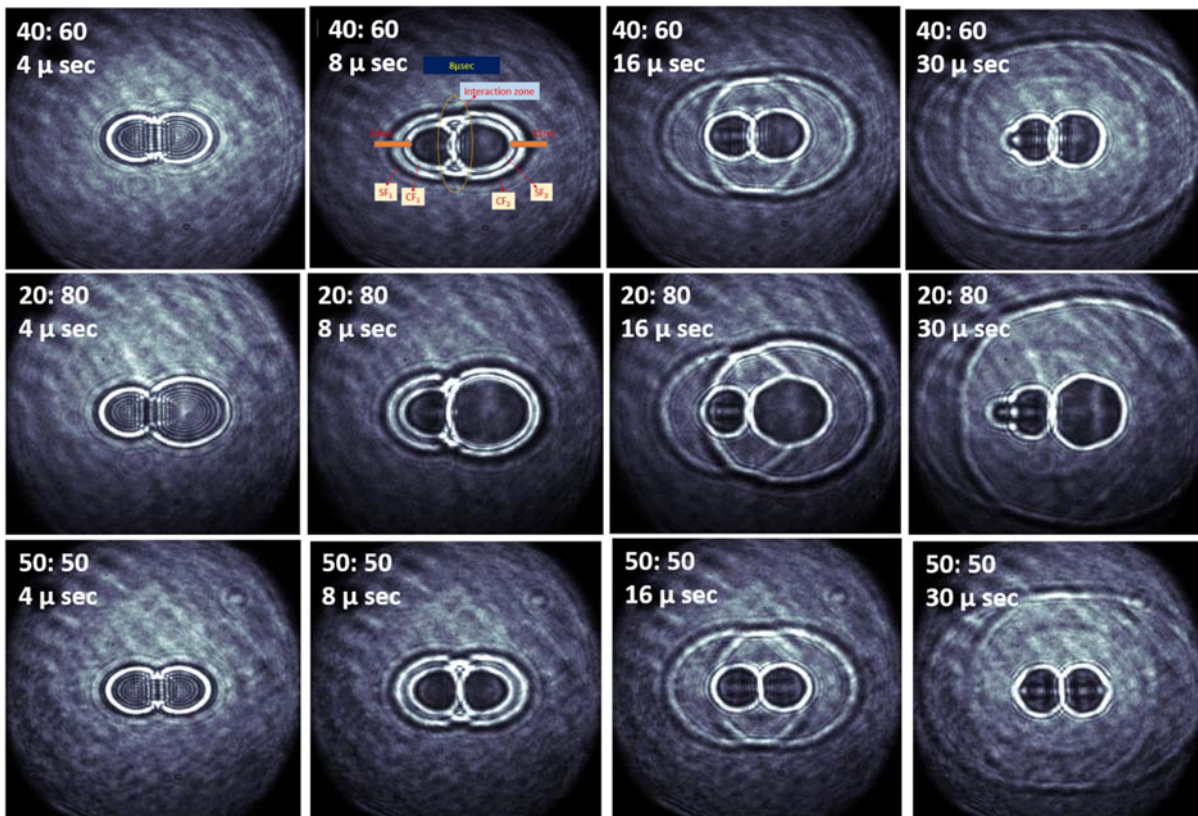


**Fig. 6.2.** Shadwographic images of dual plasma, formed due to counter propagation of two ns laser beams. Experiments are done with three beam splitters of 40: 60, 20:80 and 50:50 and at time scales of 4, 8, 16 and 30 μ secs. First row is 40:60 BS (left plasma formed due to 21 mJ of laser energy whereas right one formed with 42 mJ). Interaction zone is clearly highlighted in first row second image, this image is taken at 8 micro sec from the laser pulse. Second row is 20:80 and third row is 50:50 BS.

## 6.2.1 Optimization of microphone position w.r.t plasma

As the plasma sources are cylindrically symmetric, positioning the microphone at an appropriate distance is essential to understand interaction of plasma sources. For this the experimental schematic as shown in fig. 6.3 is adopted,  $z=0$  is chosen as the focal planes of the lenses and is aligned to be the normal of the microphone diaphragm. Microphone and line joining plasmas are separated by 80 mm distance. Now the microphone is moved along a line parallel to the line which joins the two plasmas as shown in fig. 6.3 (a). When source 2 ( $S_2$ ) presents (source 1 absent), we performed the acoustic scan of plasma from -10 to 10 mm ( $z$ - position) distance.

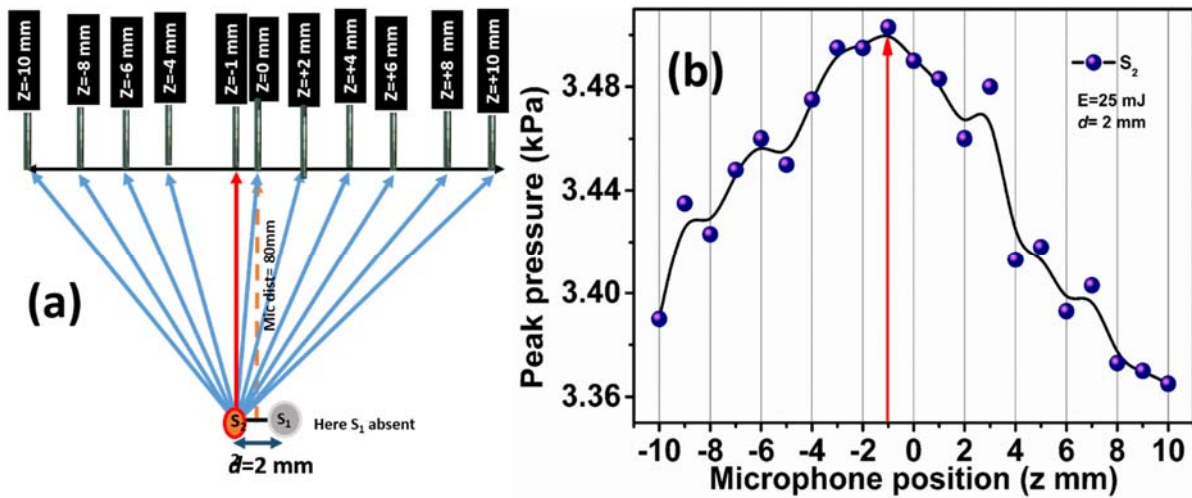


**Fig. 6.3.** (a) Microphone position vs the peak pressure for a single source ( $S_2$  plasma) at laser energy of 25 mJ ( $S_{1+2} = 50$  mJ). Microphone scan starts from  $z = -10$  mm to  $+10$  mm. (b) Source ( $S_2$ ) is exactly at  $z = -1$  mm position of microphone (indicated with red line), so peak pressure is maximum at this point.

As shown in fig. 6.3, when microphone is exactly straight to the plasma (here  $z = -1$  mm) then the peak pressure is maximum than the remaining positions of microphone. Once microphone is moved away from the vicinity of the plasma (shown in fig. 6.3 (a)), then pressure response will decrease rapidly, shown in fig. 6.3 (b). The same behavior of pressures is showed by the dual plasma also w.r.t microphone position, presented in fig. 6.4. Here for the dual plasma the acoustic measurements are taken when microphone is at  $z = 0$  position, i.e. interaction zone of two plasmas or shock waves, as shown in experimental scheme of fig. 6.1. For dual plasma, the position of microphone with respect to interaction zone is clearly shown in fig. 6.5 (a). The peak pressure is maximum from the dual plasma ( $S_{1+2}$  is 50 mJ) at microphone position of  $z = 0$ , shown in fig. 6.5 (b).

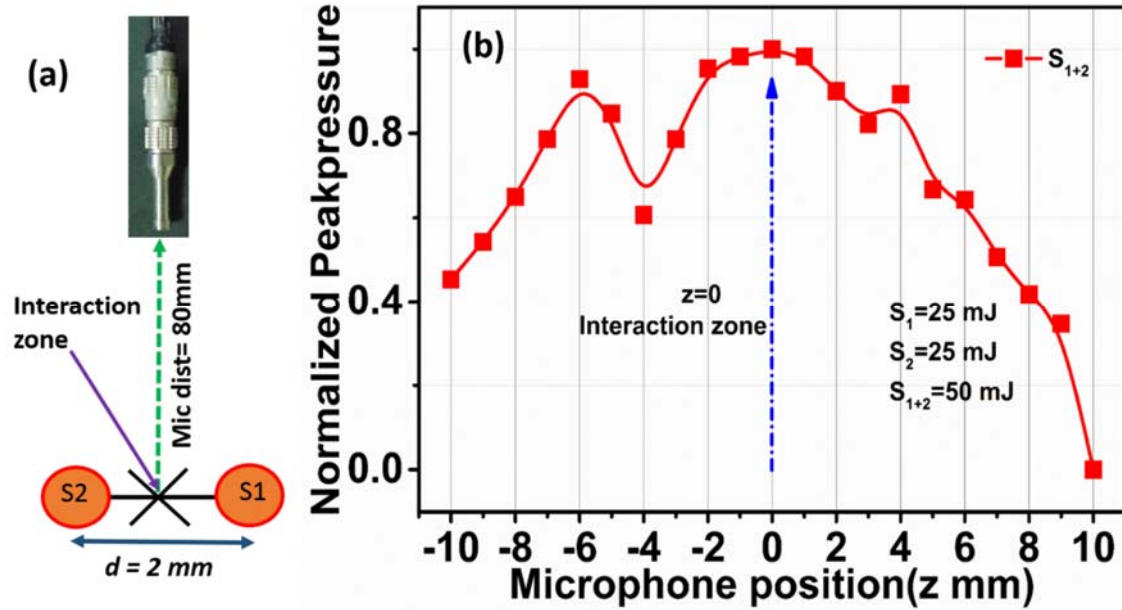


**Fig. 6.4.** (a) Position of microphone from the interaction zone point of two shock waves, (b) normalized peak pressures from the dual plasma (two plasmas are present and separated by 2 mm distance) at various positions of microphone. Peak pressure is maximum at  $z=0$  microphone position for 50:50 BS and laser energy of  $S_{1+2}$  is 50 mJ.

For dual plasma also, the pressure fall off as move away from the plasma as observed for single source. The way two sources interact is presented in fig. 6.2 at various time scales.

**Table 6-1.** Arrival times information of single and dual plasma at 2 and 22 mm separation distances. Here the total energy is 100 mJ.

Source	Arrival time ( $\mu\text{sec}$ )	
	Separation distance = 2mm	Separation distance=22mm
$S_1$	224.58	226.3
$S_2$	224.5	226.5
$S_{1+2}$	220.9	226.16

The given laser energy of 100 mJ is distributed equally and forms two plasmas. Since these two plasma or sources are formed at same experimental conditions (same focal geometry and laser energy) these two sources are having similar properties. When two plasmas are separated by 22 mm ( $d$ ) distance the arrival time of ASWs from the  $S_1$ ,  $S_2$ ,  $S_{1+2}$  are 226.33, 226.5 and 226.16  $\mu\text{sec}$  respectively. Whereas, at a distance of 2 mm, the arrival time of ASWs from the  $S_1$ ,  $S_2$ ,  $S_{1+2}$  are 224.58, 224.5 and 220.9  $\mu\text{sec}$  respectively.

This clearly indicates that at a lower separation distance, the interaction of plasma/SWs is higher leading to higher acoustic pressures. With increasing distance the plasma interaction has reduced resulting in a smaller peak pressure. When two plasmas are present, the arrival time of dual plasma is less than the individuals at two separation distances. From this we can say that, the ASW received by microphone is from the interaction zone of two SWs and the gross features of interacting plasma plumes/SWs can be understood by acoustic measurements. As shown in the shadowgraphic image (fig. 6.2) of dual plasma, as the time evolves, two SWs meet at interaction zone and travel towards the microphone with higher velocities.

### 6.3 Case of Equal impedances

Here we have used beam splitter of R: T = 50:50 to get two equal plasmas with similar properties that expand similarly, hence two plasmas are taken to have equal impedances. Acoustic properties from single, plasma source and that of two plasma sources are compared to explicitly bring out the interaction of plasma sources.

#### 6.3.1 Comparisons between single and dual plasma

Single plasma source at 50 mJ of incident laser energy generated ASWs with pressure of 4.7 kPa. The incident laser energy 50 mJ is divided into two sources each of 25 mJ and focused through lenses of same focal length (78 mm). The individual pressures from plasma1, plasma2 are 3.38, 3.44 kPa respectively. This resulted in two plasmas with equal impedances. As mentioned above, the resultant pressure varies as a function of separation distance. A maximum ASW pressure of 6.49 kPa at 14 mm separation distance is observed in this case.

As we increase the separation distance between two plasmas, the resultant ASW pressure starts increasing from 4.9 kPa and reaches to 6.59 kPa. This ASW pressure 6.59 kPa is greater than the 4.7 kPa, which is produced by single plasma source. The time domain signals due to single source ( $S_1$  or  $S_2$ ) and due to dual plasma ( $S_{1+2}$ ) at a separation distance  $d=14$  mm is shown in fig 6.5. Arrival time of ASW from single plasma of 50 mJ is 224.58  $\mu$ s, whereas 225.03  $\mu$ s is the arrival time from dual plasma (25 mJ+25 mJ) source. For single 25 mJ plasma, the arrival time is 227.6  $\mu$ s. The variation of arrival times clearly indicates the dependence of input laser energy on the acoustic signals [12]. From fig. 6.5 it is evident that the arrival time of ASW at detector due to dual plasma source is slightly smaller, however, the peak pressure is larger by 1.84 kPa. This confirms that a simple acoustic signal can point out the variations due to interacting atmosphere plasmas.

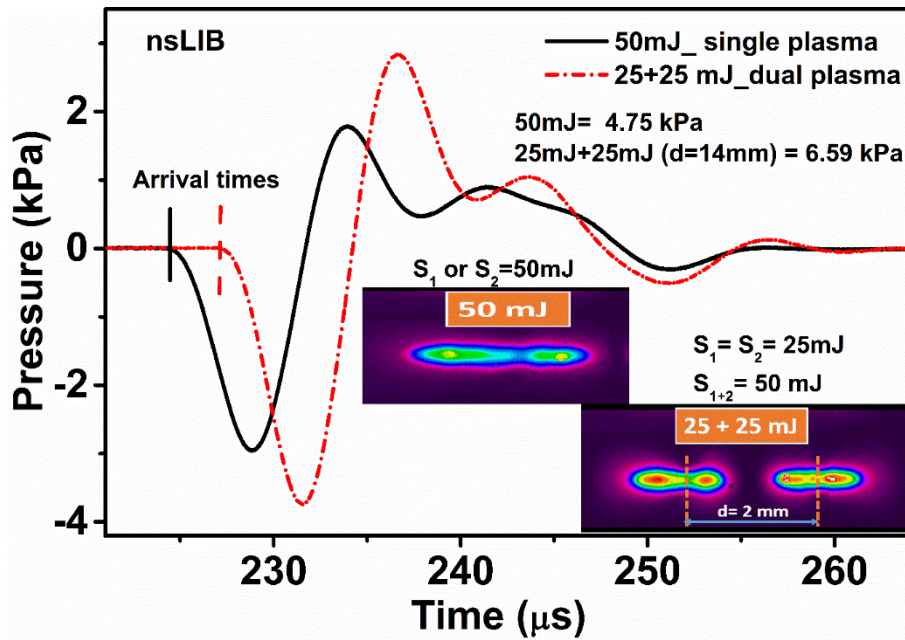


**Fig. 6.5.** ASW time domain signals from LIB of air at laser energies of 50 and 25+25 mJ for a separation distance of 14 mm. Peak pressures of single and dual plasma are 4.75 and 6.59 kPa, respectively. Dual plasma generates the more acoustic pressures than the single plasma under fixed laser energy. Inset shows the plasma plume image integrated over 32 ms. CCD images are at 2 mm separation distance.

For the detection of materials one of the good spectroscopy technique is laser induced breakdown spectroscopy (LIBS). In this LIBS studies, enhancement in signal is more in the case of dual plasma than that of a single plasma [3]. Dual plasma generated ASWs are more intense than the single plasma produced ASWs, shown in fig. 6.5. In the case of 100 mJ laser energy generated 6.8 kPa pressure at the detector whereas dual plasma due to 50 mJ+50 mJ sources produced the 10 kPa at 28 mm separation distance as is shown in fig. 6.6.

Arrival time of ASW from single plasma of 100 mJ is 219.6  $\mu$ s whereas from the dual plasma of 50 mJ+50 mJ is 227.9  $\mu$ s at a separation distance of 28 mm. The arrival time due to dual plasma is more than the single plasma even though acoustic pressures are higher for dual plasma. Here the separation distance is 28 mm, so the arrival time of 50+50 mJ is greater than 100 mJ. As the separation distance increases the arrival time also increases. Because the ASW has to reach the interaction zone and interact with the second ASW (the ASW path is shown in fig. 6.1). At interaction zone pressure is enhanced and then it travels to the microphone. So, as the distance increases, the arrival time increases and pressure varies accordingly.

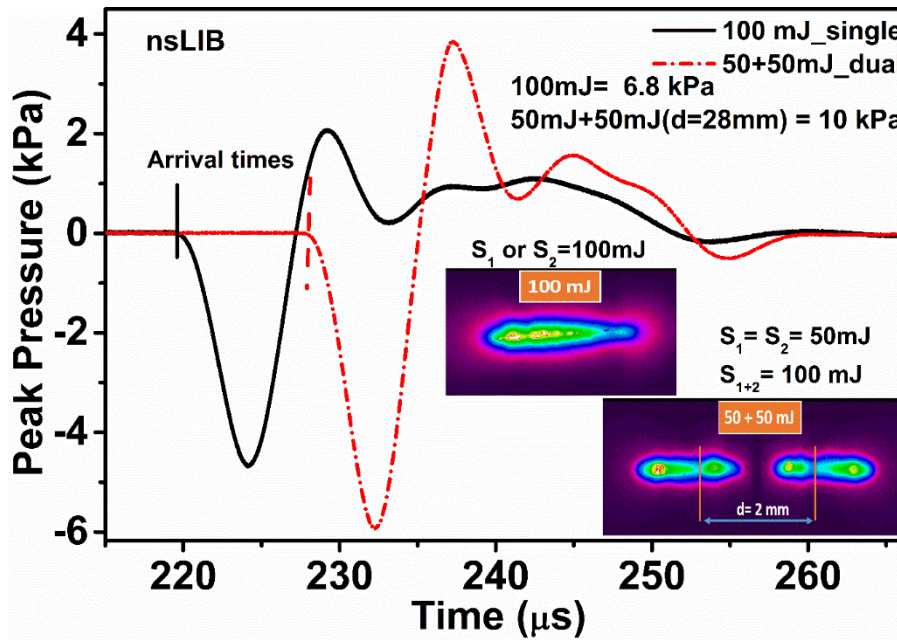


**Fig. 6.6.** ASW signals from LIB of air at laser energies of 100 and 50 mJ+50 mJ for a separation distance of 25 mm. Peak pressures of single and dual plasma are 6.8 and 10 kPa respectively. Dual plasma generates more acoustic pressures than the single plasma under fixed laser energy. Inset shows the plasma plume image integrated over 32 milli sec. CCD images are at 2 mm separation distance.

### 6.3.2 Total energy 100 mJ ( $S_{1+2}$ )

Here we present the evolution of acoustic properties due to equal energies of 50 mJ to both the sources  $S_1$  and  $S_2$  to form plasmas of equal densities and temperatures.

The acoustic peak pressure, arrival time, signal energy of ASWs emitted from single plasma and dual plasma for  $d= 2$  cm are tabulated in table 6-2. The detector is placed at 80 mm from the interaction zone. Since we are using same energy for both the sources, the acoustic parameters are also same for individual plasmas. The resultant peak pressure from dual plasma when two plasmas are separated by 2 mm is 6.55 kPa. The variation in peak pressures w.r.t separation distance is presented in fig. 6.7. The interaction of dual shock waves captured using shadowgraphic imaging is presented in inset of fig. 6.7.

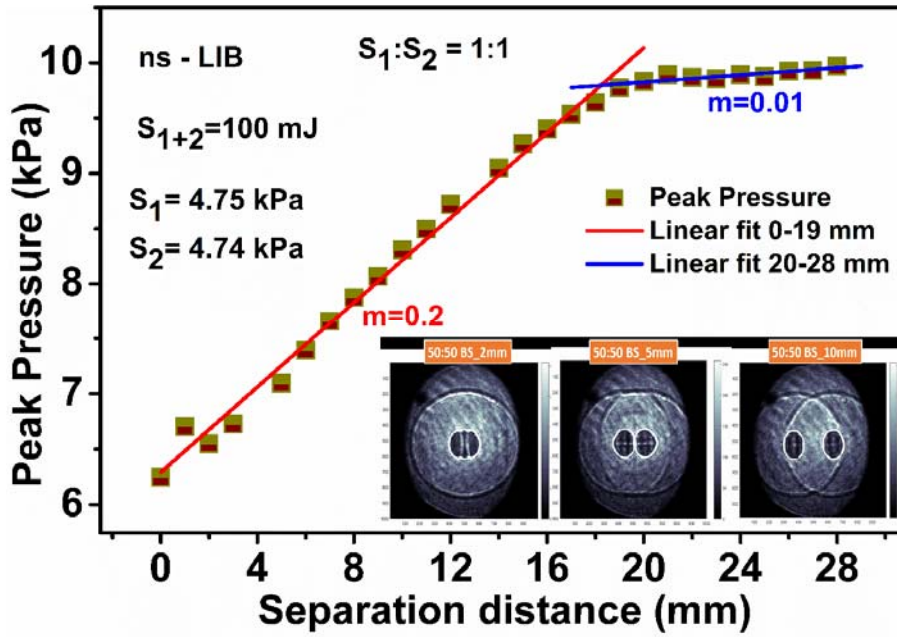


**Fig. 6.7.** Separation distance vs peak pressures from dual plasma for 50:50 beam splitter. Linear fits with two slopes are mentioned in above graph. From 0-19 mm and 20-28 mm the slopes of linear fits are 0.2 and 0.01 respectively. In set shows that the shadowgraphic image of interaction of counter propagating two shock waves at 2, 5, 10 mm separation distances. Images are presented here are taken at 30  $\mu$ sec time from the plasma initiation.

The arrival times at various separation distances of dual plasmas shown in fig. 6.8. A simple linear fit with slope of 0.27 shows that plasma sources keep interacting continuously for a longer separation distances. For  $d=0$  to 19 mm, the pressures are increasing linear with the slope of 0.2. The maximum peak pressure from dual plasma is 9.97 kPa, which is greater than the sum of individual pressures ( $4.75+4.75= 9.5 \text{ kPa} < 9.97 \text{ kPa}$ ). After 20 mm the pressures are almost saturated, indicating stagnation of plasma interactions. This confirmed by the shadowgraphic images also. As the separation distance increases the arrival time also increases. This is due to

the fact that the ASW from each source has to travel an extra distance which is  $\sqrt{80^2 + \left(\frac{d}{2}\right)^2}$  as shown in fig. 6.3. So, as the distance increases, the arrival time also increases, shown in fig. 6.8 (a).

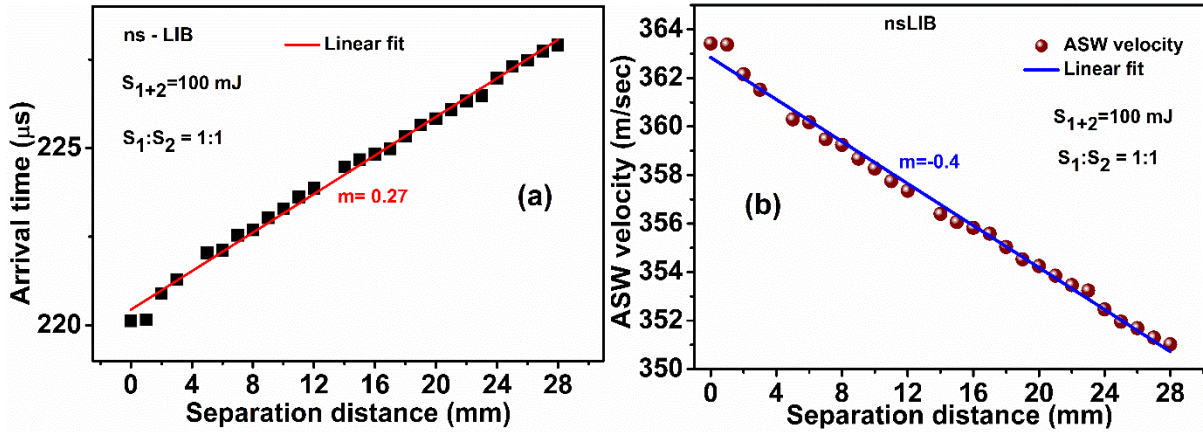


**Fig. 6.8.** Separation distance vs arrival time of ASW from the dual plasma for 50: 50 beam splitter. Here total energy is 100 mJ.

At a separation distance of 1 mm, the ASW velocity is 363.4 m/sec, it is more than the sound velocity (344 m/sec at STP). This velocity is decreasing from 363.4 to 351 m/sec as the separation distance increases from 1 to 28 mm. The linear fit to the ASW velocity is with decreasing slope of 0.4, shown in fig. 6.8 (b).

### 6.3.3 Total energy is 50mJ ( $S_{1+2}$ )

In this subsection, we present the evolution of acoustic properties when total laser energy of 50 mJ is divided into 25 mJ each forming plasmas having equal impedances. The acoustic parameters ASWs from individual and dual plasma, are tabulated in table 6-2.

**Table 6-2.** The ASW parameters of independent  $S_1$ ,  $S_2$  sources and  $S_{1+2}$  with a separation of 2 mm. The laser energies supplied to two sources is 50 mJ and 100 mJ respectively.

	ASW parameters					
	Peak pressure (kPa)		Arrival time ( $\mu$ s)		Signal energy $\times 10^{-5} V^2 \cdot sec$	
	$S_{1+2}=50$ mJ	$S_{1+2}=100$ mJ	$S_{1+2}=50$ mJ	$S_{1+2}=100$ mJ	$S_{1+2}=50$ mJ	$S_{1+2}=100$ mJ
$S_1$	3.378	4.75	227.6	224.6	1.86	3.9
$S_2$	3.44	4.74	227.3	224.5	1.92	3.9
$S_{1+2}$	4.97	6.55	223.8	220.9	4.38	8.09

ASW pressures from two individual plasmas are having same values with in the limitations of the experimental errors. ASW pressure, signal energy is high from dual plasma than from the individual

plasmas. The peak pressures from dual plasma vs separation distance were presented in fig. 6.9 for 50:50 beam splitter.

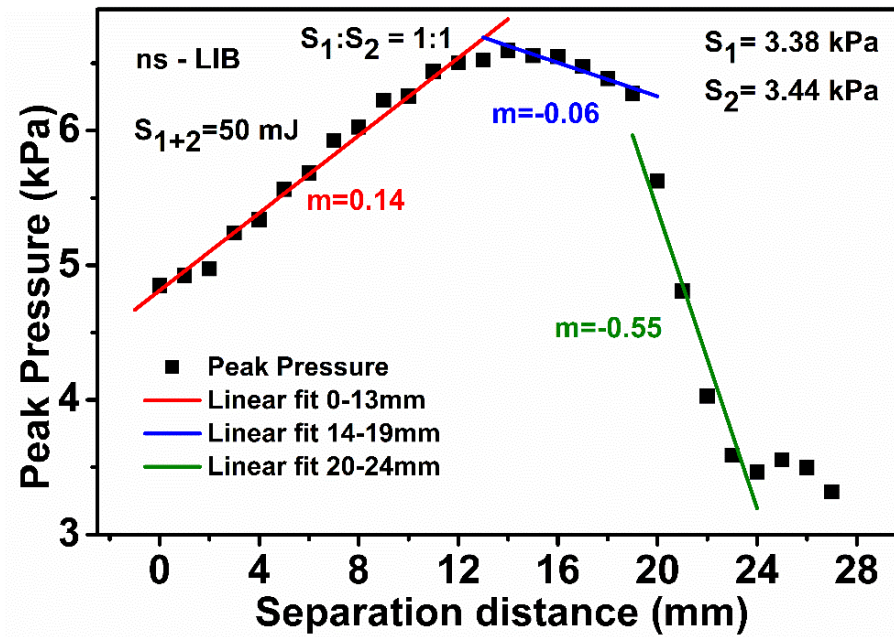


**Fig. 6.9.** Separation distance vs acoustic peak pressures for 50:50 beam splitter, at total energy of 50 mJ. ASW peak pressure behaviour is fitted to three lines of slopes 0.14, -0.06, -0.55.

The peak pressures increase with separation distance up to 14 mm. The actual sum of the peak pressures of individual ASWs is 6.8 kPa. At the separation distance of 14 mm, the peak pressure from the dual plasma is 6.59 kPa. After this 14 mm, the peak pressures have started falling with different slopes, as shown in fig. 6.9. The peak pressures have started saturating between 14-20 mm and have reduced drastically beyond 20 mm. This clearly indicates that the plasma interaction is minimal beyond a separation of 20 mm.

The separation distance vs arrival times of ASW from the interaction zone are presented in fig. 6.10 (a). As the separation distance increases, the arrival time increases. From 0 to 15 mm, the arrival times are increasing with slope of 0.29. Whereas after 15 mm, the slope is close to straight line with slope of 0.02. The stagnation of interaction is indicated by saturation of  $A_t$  or velocity.

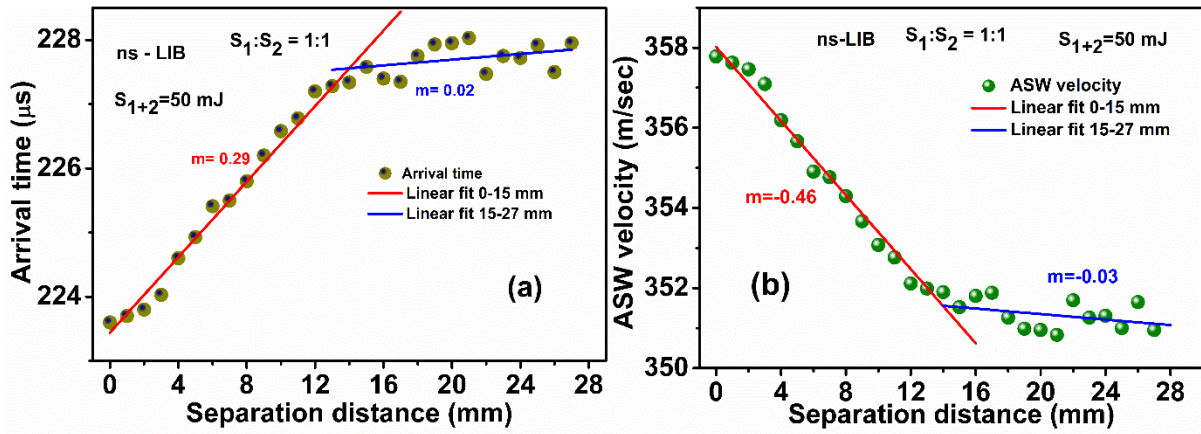


**Fig. 6.10.** Separation distance vs arrival time of ASWs from dual plasma. Here total energy is 50 mJ.

The ASW velocities were decreased from 1 mm to 15 mm separation distance, after that it becomes close to saturation. The ASW velocities at 1mm, 15 mm separation distances are 357.6, 351.5 m/sec respectively. Here the linear fit to decrement in velocity has the slope of -0.46 till 15 mm, it indicates the rapid fall of velocity whereas the slope is -0.03 from 15 mm to 28 mm, which is close to zero and it indicates the saturation of velocity, as shown in fig. 6.10 (b). The velocities are less for 50 mJ of laser energy than the 100 mJ, it is due to the fact that higher laser energies generates the plasma with higher pressures, densities and temperatures.

Spectral response of ASWs for the case of equal impedance with individual laser energies (S<sub>1</sub> or S<sub>2</sub>) of 25, 50 mJ, and S<sub>1</sub>+S<sub>2</sub> is shown in fig. 6.11. Since we are using the same laser energy to form individual plasmas, the spectra of both S<sub>1</sub>, S<sub>2</sub> are superimposed on each other, shown in fig 6.11.

In the case of each source having 25 mJ, the peak1 from both the sources of S<sub>1</sub> and S<sub>2</sub> is centered at 54 kHz. Whereas the frequencies of peak2 are centered at  $\approx 109$  kHz for S<sub>1</sub> and S<sub>2</sub> respectively. When the dual plasma source (S<sub>1</sub>+S<sub>2</sub>) present the peaks have shifted towards lower frequencies of 40 kHz and 94 kHz. While in the case of plasma sources generated using 50 mJ source, each source emitted frequencies of peak 1 is centered at 36 kHz. Whereas the frequencies of peak2 are centered at 89 kHz for S<sub>1</sub> and S<sub>2</sub> respectively. When the two plasmas are interacting the emitted frequencies shifted towards 30 kHz and 76 kHz respectively.

In the case of dual plasmas both the peak frequencies has shift to lower acoustic frequency. This clearly indicates the interaction of plasmas/SWs leading to localization of acoustic frequencies/energies. When 50 mJ of laser energy is used in each source due to interaction of plasmas an additional acoustic frequency  $\approx 110$  kHz is confirmation of interaction of plasma/ SWs. With

increasing energy of individual source the second peak has shifted towards the lower acoustic frequencies as expected [12].

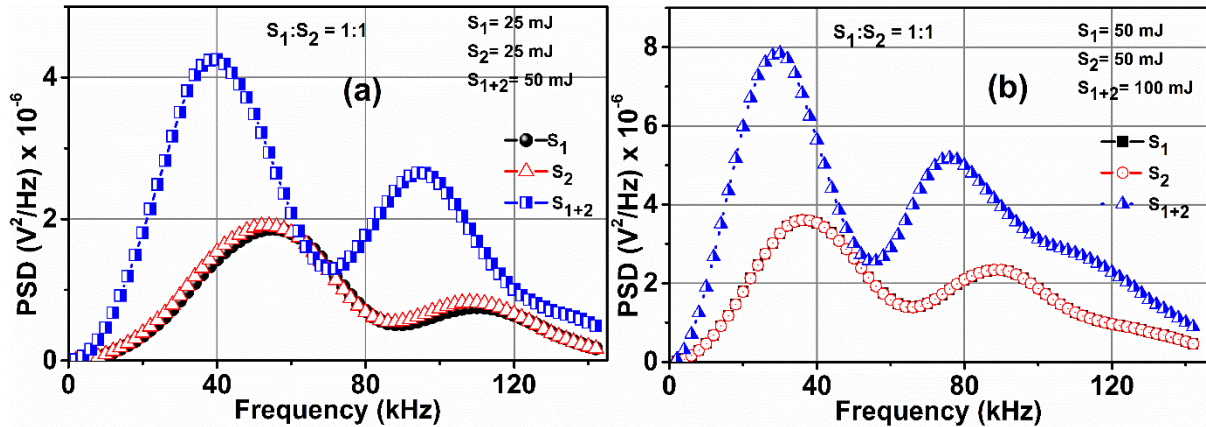


**Fig. 6.11.** Spectral response of ASWs for 50:50 beam splitter and individual laser energies of 50, 25 mJ. Two individual plasmas are having same spectral peak. The separation distance is 2 mm for dual plasma in this case.

## 6.4 Un-equal impedances (un-equal densities)

In this section, acoustic properties due to interaction of two plasma sources of different properties are presented. These two sources were generated using different input laser energies. Hence they will have different densities and lead to SWs of different velocities. These in turn will have different impedances. In order to get two plasmas with un-equal impedances, we have used two different beam splitters with R: T=40:60 and 20:80.

### 6.4.1 Ratio of $S_1: S_2= 1: 1.5$

In this case the laser energy of 65 mJ is distributed into two beams of 24 mJ and 41 mJ and focused using two lenses  $L_1$  and  $L_2$ . Plasma formed by  $L_1, L_2$  are named as  $S_1, S_2$  respectively. When two plasmas were present, it is indicated by  $S_{1+2}$ . Acoustic data taken with only one plasma source ( $S_1$  or  $S_2$ ) is present compared with the data when two plasmas ( $S_{1+2}$ ) are present. The time domain ASW signal from two individual sources  $S_1, S_2$  compared to that of  $S_{1+2}$  is shown in fig. 6.12. The acoustic signals and their arrival times are shown clearly in above fig. 6.12. With increasing laser energy from 24 mJ ( $S_1$ ) to 41 mJ ( $S_2$ ), the arrival time ( $A_t$ ) of ASW has reduced from 234 to 231  $\mu$ s, while due to counter propagating shock waves ( $S_{1+2}$ ) the  $A_t$  has come down to 229  $\mu$ s.

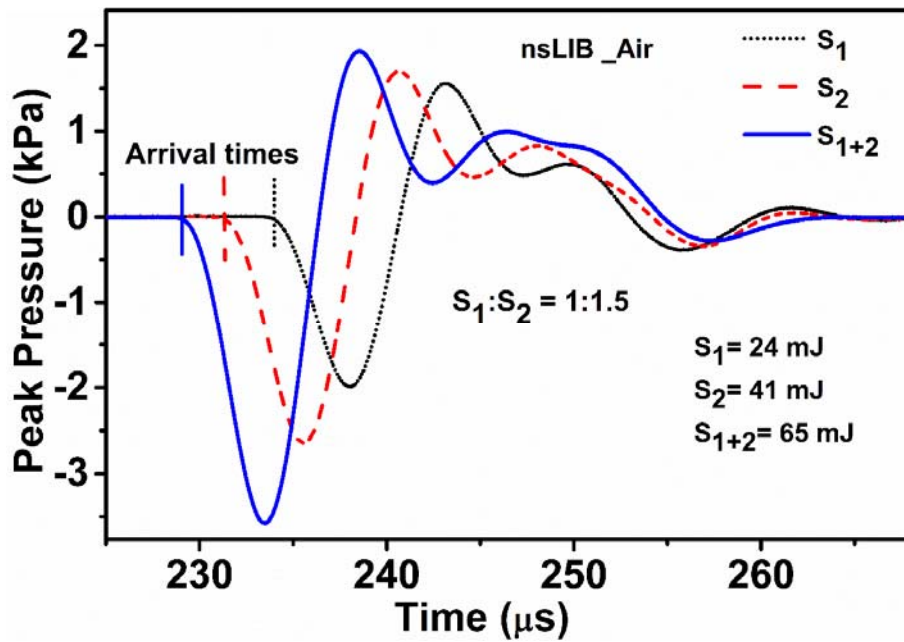


**Fig. 6.12.** Time domain signals of ASWs emitted from the single plasma ( $S_1$  and  $S_2$ ) and dual plasma ( $S_{1+2}$ ). Laser energies of 24, 41 mJ used to form first plasma ( $S_1$ ) and second plasma ( $S_2$ ) respectively. Arrival times are indicated with coloured lines on signals. Here the separation distance between two plasmas is 2 mm.

In addition the  $P_k$ , signal energy has also increased due to the counter propagating SWs indicating increased energy deposition and the interaction of the SWs. Higher laser energies produces the high acoustic peak pressures [12], that’s why  $S_2$  radiates the acoustic signal with 4.34 kPa pressure. When both the plasmas are present, the ASW pressure is 5.5 k Pa and it is more than the acoustic pressure produced by either  $S_2$  or  $S_1$ . From this we confirm that, ASW emitted from the interaction zone is higher than that of the individual plasmas table 6-3 summarizes the important ASW parameters due to  $S_1$ ,  $S_2$  and  $S_{1+2}$ .

**Table 6-3.** The ASW parameters of independent  $S_1$ ,  $S_2$  sources and  $S_{1+2}$  with a separation of 2 mm. The laser energies supplied are 24 and 41 mJ respectively.

	ASW parameters		
	Peak pressure (kPa)	Arrival time ( $\mu$ s)	Signal energy $\times 10^{-5} \text{ V}^2.\text{sec}$
$S_1$	3.55	234	2.1
$S_2$	4.34	231	3.2
$S_{1+2}$	5.52	229	5.5

The signal energy from  $S_{1+2}$  is almost equal to sum of the signal energy from individual sources  $S_1$  and  $S_2$  [ $S_{1+2} \approx S_1 + S_2$ ]. At lower separation distances, interaction between the two-plasma sources takes place but not that of the shock waves, as shown in fig. 6.2. When both plasmas are present, the resultant peak-to-peak pressure at interaction zone is higher than that of individual sources. Now we change the separation distance between the two plasmas and presented the resultant ASW pressure from the interaction zone, shown in fig. 6.13. Acoustic and shadowgraphic data was collected simultaneously. To show the separation distance between the plasmas, the shadowgraphic images at various separation distances of 2, 5, 10, 12 mm are presented in the inset of fig. 6.13.

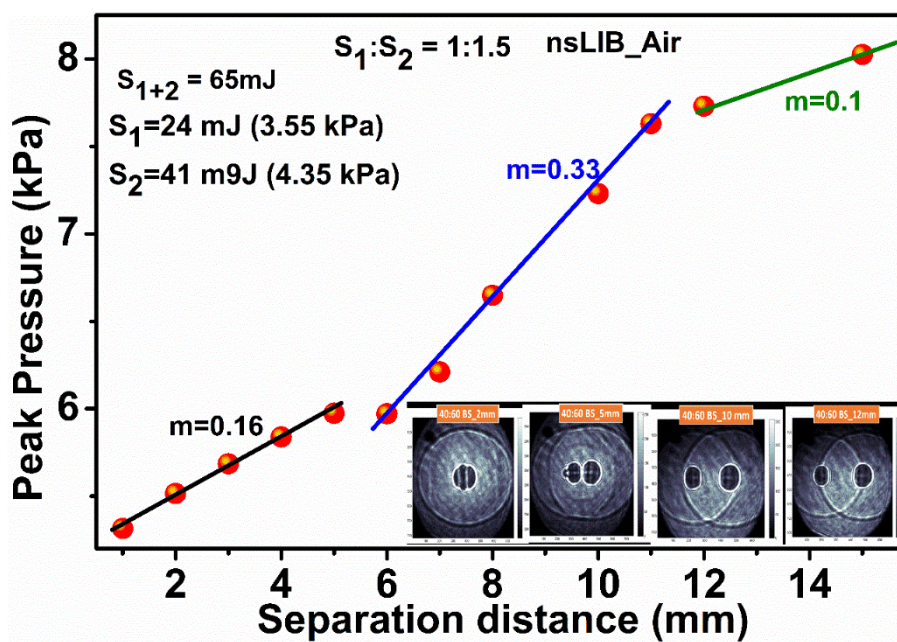


**Fig. 6.13.** Separation distance between two plasmas vs acoustic shock wave peak pressure. The slope is positive. The slopes are different for different distances. For the separation distances of 1 to 5 mm, 6 to 11 mm and 12 to 15 mm the slopes ( $m$ ) are 0.16, 0.33, and 0.1 respectively. In set shows that the shadowgraphic image of interaction of counter propagating two shock waves at 2, 5, 10, 12 mm separation distances. Images are presented here are taken at 30  $\mu$ sec time from the plasma initiation.

We observed that the ASW pressure increases as separation distance ( $d$ ) increases from 1 mm to 15 mm. Shock waves were fully developed at larger distances of separation ( $> 6$  mm) resulting in the interaction of two shock waves (blast waves). At these distances of separation, there is sufficient time to build up shock pressure or strength in the interaction zone. This leads to larger peak pressures with increasing separation between the shock sources. At 2 mm of separation, the  $P_k$  is 5.5 kPa whereas at 15 mm separation, the  $P_k$  is 8 kPa, confirming a rise in acoustic pressure increasing with  $d$ . The increment in acoustic pressure is not linear

indicating that the interaction of two shock waves is a nonlinear phenomenon. The rise in pressures with  $d$  is fitted to linear plot and it is showing three different slopes from 1 to 15 mm. For the separation distances of 1 to 5 mm, 6 to 11 mm and 12 to 15 mm the slopes ( $m$ ) are 0.16, 0.33, and 0.1 respectively.

For the separation distance of 1 to 5 mm the interaction is majorly due to the plasma plumes while beyond 6 mm the interaction of shock waves plays a dominant role. The evolution of ASW pressures due to  $S_{1+2}$  with distance clearly indicates that the resultant pressure due to interaction of SWs for a separation distance of 6 to 11 mm is higher.

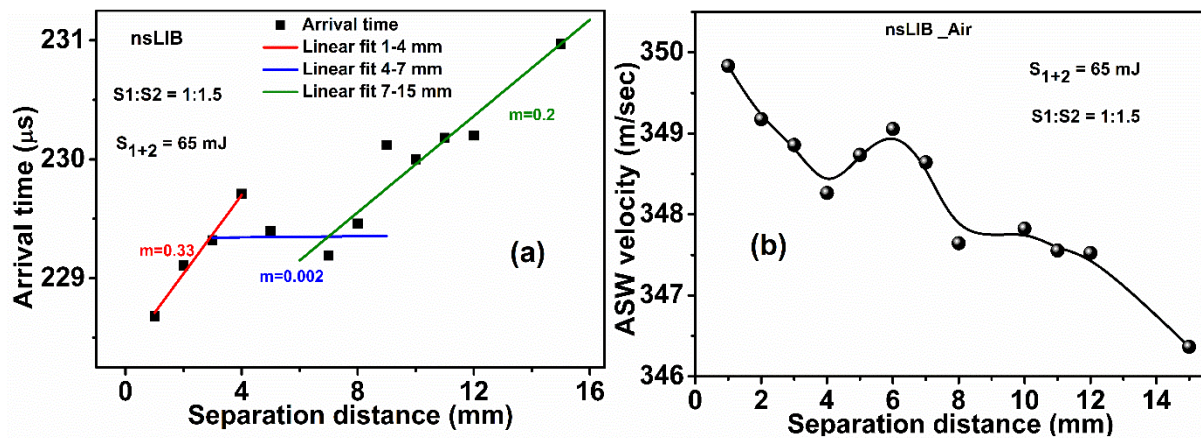


**Fig. 6.14.** Separation distance vs arrival time and velocity of ASWs, from the dual plasma, for the beam splitter of 40:60 (1:1.5). Three linear fits for arrival times, with slopes of 0.33, 0.002 (saturation), 0.2 for 1-4mm, 4-7mm, 7-15mm respectively. Here the total laser energy is 65 mJ and divided into 24 and 41 mJ. ASW velocity is decreasing with separation distance.

As the separation distance increases the variation in arrival times and ASW velocities are presented in fig 6.14. The arrival times first increased rapidly from 0-4 mm with a slope of 0.33, then saturated from 4-7 mm with the slope very close zero (0.002), then increased again till 15 mm from 7 mm with slope of 0.2, shown in fig 6.14 (a). The change in ASW velocities w.r.t separation distance are presented in fig. 6.14 (b). Rapid fall in velocities from 1 to 4 mm, then a small hump form 4 to 8 mm, then decreasing very slowly till 15 mm, shown in fig. 6.14 (b). The arrival time ( $A_t$ ), acoustic shock velocity and  $P_k$  pressure increase for  $d= 4$  to 8 mm confirms the interaction of SWs for specific separation distances.

The spectral response of single and dual plasma ASWs is shown in fig. 6.15. The spectral amplitude is increasing with increasing input laser energy from  $S_1$  and  $S_2$ . A shift of central frequency towards lower frequency side is observed as expected [12]. With both sources  $S_1$  and  $S_2$  together the spectral amplitude (PSD) of all the peaks have almost doubled, as summarized

in table 6-4. Higher laser energy generates frequencies closer to audible range with large amplitudes.

**Table 6-4.** Lorentz fitted frequency peaks parameters for the ASWs generated from the dual plasma which are distributed in the ratio of  $S_1:S_2 = 1: 1.5$ .

Source	Peak1		Peak 2	
	Central frequency± FWHM	Height PSD x 10 <sup>-6</sup>	Central frequency± FWHM	Height PSD x 10 <sup>-6</sup>
S <sub>1</sub>	50.8±36.7	1.98	108.62±30.58	0.77
S <sub>2</sub>	40.23±30.8	2.85	95.3±39.6	1.6
S <sub>1+2</sub>	33.48±25	4.73	87.6±50	2.83

The Lorentz fitted central frequencies of peak 1 for S<sub>1</sub>, S<sub>2</sub>, S<sub>1+2</sub> are 50.8, 40.23, 33.48 kHz and their corresponding FWHM values are 36.7, 30.8, 25 kHz respectively. The frequency and FWHM are proportional to each other for peak 1, whereas for peak 2, dual plasma (S<sub>1+2</sub>) has more FWHM than the S<sub>1</sub> and S<sub>2</sub>, presented in table 6-4. In the case of S<sub>1+2</sub> an additional frequency ~ 120 kHz is observed.

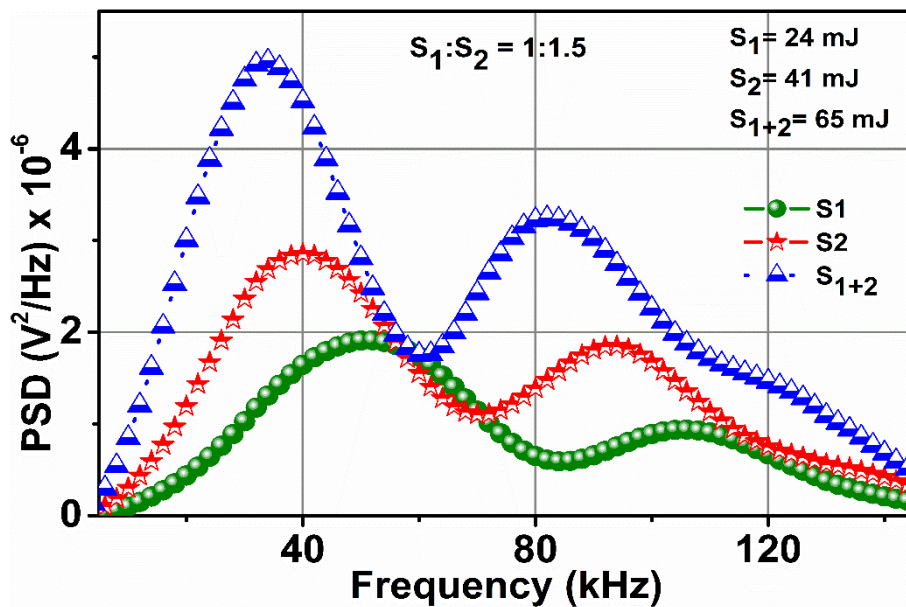


**Fig. 6.15.** The acoustic spectra for ASWs emitted from single plasma and dual plasma. The peak frequencies are 52, 40, 34 kHz for S<sub>1</sub>, S<sub>2</sub>, S<sub>1+2</sub> respectively.

### 6.4.2 Ratio of $S_1: S_2 = 1:4$

In this subsection we present the results of ASW when a total laser energy of 140 mJ is split into two beams such that  $\approx 24.5 \pm 2.1$  mJ is focused by  $L_1$  and  $101.7 \pm 1.5$  mJ is focused by  $L_2$ . This results in forming of two plasmas with different properties, i.e plasma temperature and density hence with different expansion into the ambient.

When two plasmas were present, the acoustic peak pressures, arrival times, signal energies etc, will be varied w.r.t plasma–plasma separation distance. Plasmas of  $S_1$  and  $S_2$  generates the peak pressures of 3.9 and 6.76 kPa respectively. When the two plasmas ( $S_{1+2}$ ) were present with a separation distance of 2 mm, the peak pressure is 7.9 kPa and it is greater than the peak pressure produced by either of the breakdown plasma. Its arrival time is 218.5  $\mu$ s which is less than the both individual arrival times, shown in table 6-5. The signal energy is also more for ASW generated by dual plasma than the remaining two individual values.

**Table 6-5.** The ASW parameters of independent  $S_1$ ,  $S_2$  sources and  $S_{1+2}$  (dual plasma present) with a separation of 2 mm. The laser energies supplied to  $S_1$  and  $S_2$  are  $24.5 \pm 2.1$  and  $101.7 \pm 1.5$  mJ respectively. The microphone is kept at a distance of 80 mm.

	ASW parameters		
	Peak pressure (kPa)	Arrival time ( $\mu$ s)	Signal energy * $10^{-5}$ V <sup>2</sup> .sec
$S_1$	3.92	234	2.57
$S_2$	6.76	219.6	8.71
$S_{1+2}$	7.9	218.5	12.2

Table 6-5 shows that, the dual plasma produces the shock waves with different features than the single plasma generated ASWs. The evolution of ASW pressures with separation is plotted in fig. 6.16. The interaction of the two plasma sources is analogous to interaction of two fluids with different densities. We are observing the ASW parameters at interaction zone. The pressure starts at 7.54 kPa and increases up to 8.47 kPa then decreases to 7.69 kPa and again rises continuously up to 9.79 kPa as shown in fig. 6.15. The entire behaviour of peak pressures w.r.t distance is fitted to four linear fits with four different slopes. From 0 to 7 mm, 7 to 9 mm, 9 to 13 mm, 13 to 19 mm the slopes are 0.1 (+ve), ( $\approx 0$ , straight-line), -0.19 (-ve), 0.4 (+ve) respectively. The pressures are increasing rapidly from 13 to 19 mm separation distance. After 19 mm we have not carried out measurements, due to threshold limitation of microphone.

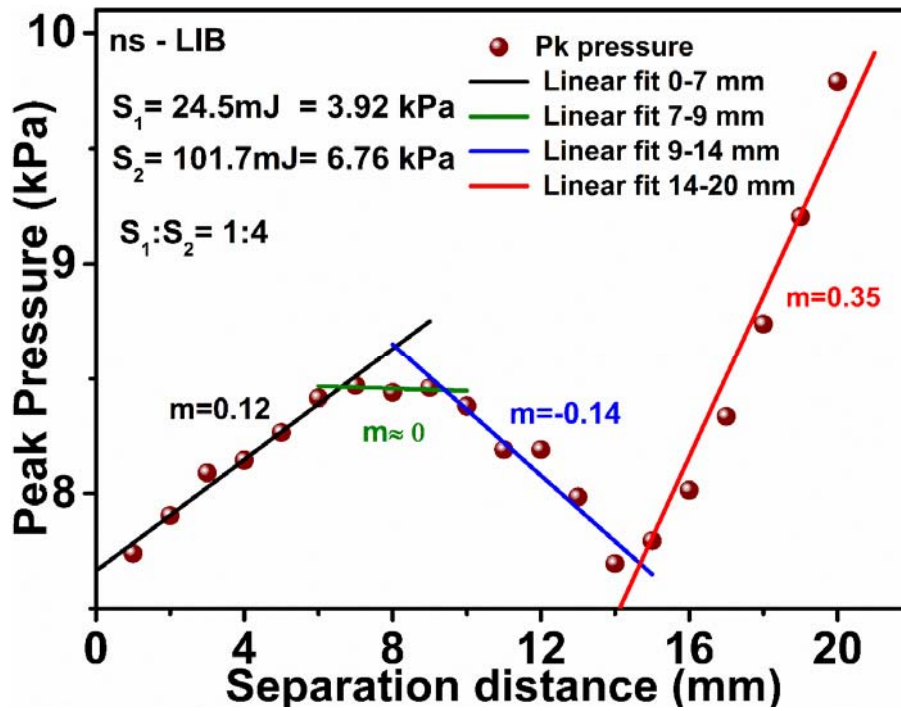


**Fig. 6.16.** Separation distance vs peak pressures for the interaction of plasma sources with 1:4 impedances. Individual laser energies of 24.5, 101.7 mJ forms the two plasmas of  $S_1$ ,  $S_2$ .

The separation distance vs arrival times of ASW from the interaction zone were plotted in fig. 6.16. The ASW from the interaction zone takes more time to reach the microphone as we increase  $d$ . During the expansion of plasma, the SW leaves the plasma and propagates into surrounding atmosphere with higher velocity. At longer time scales, it appears as a spherical wave. Since we are increasing the separation distance between two plasma, along with their major axis, SW takes more time to interact with each other leading to pressure variations. This ASW has to reach microphone from the interaction zone. Hence the arrival time is increasing as we increase the plasma-plasma separation distance, shown in fig. 6.17 (a). This also confirms that the interaction will be controlled dominantly by the source with higher energy  $S_2$ . With increasing separation distance ( $d$ ) the arrival time was observed to increase at two different rates. Up to 12 mm separation the arrival time increased with a lesser slope ( $m= 0.19$ ) indicating that the shock velocity is reducing slowly ( $m=-0.32$ ) while beyond a separation of 12 mm  $A_t$  increased with a higher slope (0.48) indicating that shock velocity has started reducing drastically ( $m=-0.78$ ), shown in fig 6.17 (b). This clearly indicates that the interaction of SWs from  $S_1$  and  $S_2$  is predominantly occurring beyond a separation of 12 mm for the present ratios of  $S_1$  &  $S_2$ . The ASW velocities behaviour also plotted w.r.t separation distance

and fitted to linear function. Variation in velocities w.r.t separation distance were presented in fig. 6.17 (b).

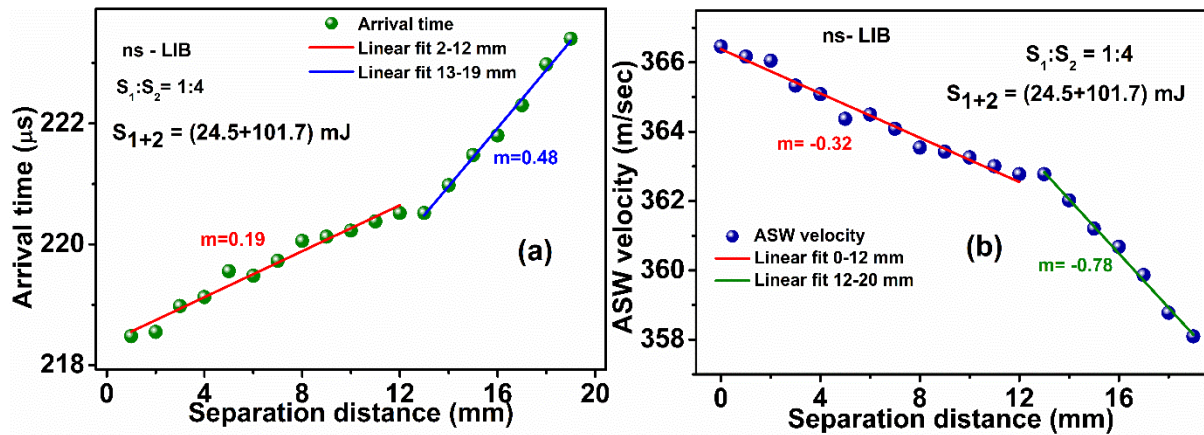


**Fig. 6.17.** Separation distance vs arrival time and velocity of ASW emitted from dual plasma for the 20:80 (1:4) beam splitter. Rise in arrival time linear fit shows the two slopes of 0.19, 0.48. Linear fit to the velocity shows the two slopes of -0.32, -0.78. Slopes are indicated with letter ‘m’.

The spectral response of ASWs from single and dual plasma for  $S_1:S_2=1:4$  is presented in fig. 6.18. The spectrum with lower energy source  $S_1$  has two peaks centered at 48 kHz and 100 kHz while the spectrum due to higher energy source  $S_2$  has three peaks centered at ~24 kHz, 70 kHz and 96 kHz.

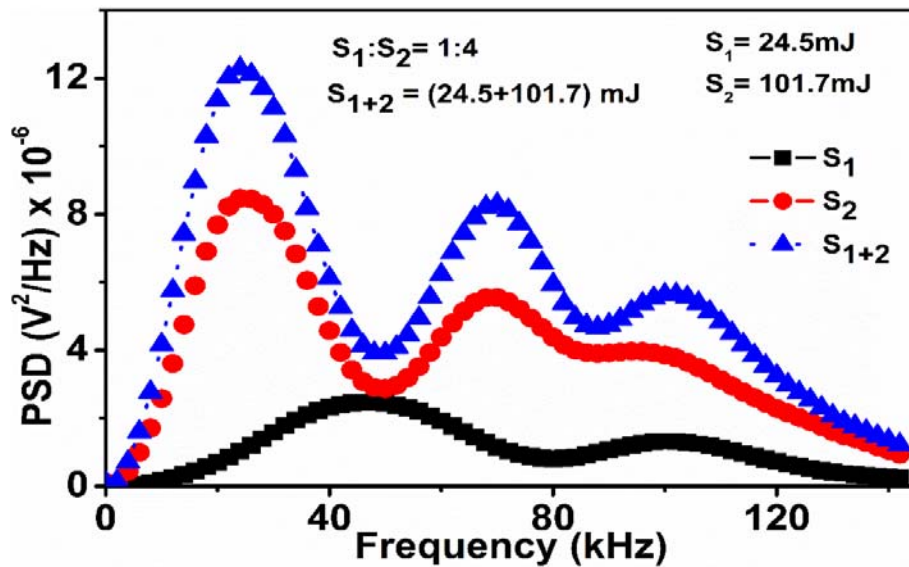


**Fig. 6.18.** Spectra for the ASWs, emitted from single and dual plasma. The separation between the sources is 2 mm. The peak frequencies of spectra are 48, 24, 24 kHz for  $S_1$ ,  $S_2$ ,  $S_{1+2}$  respectively.

With increasing input laser energy the PSD has increased with the peaks moving towards audible range. In this case the peaks due to  $S_{1+2}$  are same as that due to  $S_2$  with higher PSD. This clearly indicates that in the case of  $S_1:S_2=1:4$  the interaction is dominated by  $S_2$  completely. The evolution of spectrum with varying separation is shown in fig. 6.18. The same spectra are fitted to Lorentz peak function and peak parameters that were tabulated in table 6-6. The fitted central peak1 and peak 2 frequencies of  $S_2$  and  $S_{1+2}$  very close with variable PSDs.

**Table 6-6.** Lorentz fitted frequency peaks parameters for the ASWs generated from the ration of  $S_1: S_2 = 1: 4$ .

Source	Peak1		Peak 2		Peak 3	
	Central frequency± FWHM	Height PSD × $10^{-6}$	Central frequency± FWHM	PSD	Central frequency± FWHM	Height PSD × $10^{-6}$
$S_1$	46.9±34.2	2.54	103.3±31.9	1.1	-	-
$S_2$	26.06±21.14	8.49	68.72±23.6	3.9	99.9±48.2	3.13
$S_{1+2}$	25.3±21.46	11.23	69.21±22.97	6.72	104.2±36.9	4.56

## 6.5 Summary

Time domain analysis of ASW from individual as well as counter propagating SWs generated from the ns LIB of air were presented. The resultant ASW pressures are a function of source separation distance. For single and dual plasma the acoustic spectral response is also presented. CCD and ICCD shadowgraphic images are also presented along with the acoustic data to get a correlation between plasma expansion and acoustic emissions. The acoustic parameters such as  $P_k$ ,  $A_t$  and  $E_s$  are observed to be incident laser energy dependent. The presence of two counter propagating LIB plasma generated SWs has resulted in stronger ASW signals.

Counter propagating dual plasma sources were formed by dividing the incident laser energy using two beam splitters of 50:50, 40:60 and 20: 80 leading to plasma sources of impedances 1:1, 1:1.5 and 1:4 respectively. Two plasmas with different densities resemble the two un-equal impedance fluids.

In all the three cases, the interaction of plasma sources has led to ASWs of higher peak pressures. The peak frequencies of the spectrum indicated presence of newer frequencies. The results confirmed the interaction of plasma/ SWs. The observed results have also shown that

the interaction varied with separation between the plasma sources and the incident laser energies. The results confirm that the acoustic emissions can be a diagnostic tool to understand atmospheric plasmas and their interactions.

## 6.6 References:

1. A. Tselev, A. Gorbunov, and W. Pompe, "Cross-beam pulsed laser deposition: General characteristic," *Review of Scientific Instruments* **72**, 2665-2672 (2001).
2. E. Irissou, F. Vidal, T. Johnston, M. Chaker, D. Guay, and A. N. Ryabinin, "Influence of an inert background gas on bimetallic cross-beam pulsed laser deposition," *Journal of Applied Physics* **99**, 034904 (2006).
3. P. K. Diwakar, S. S. Harilal, J. R. Freeman, and A. Hassanein, "Role of laser pre-pulse wavelength and inter-pulse delay on signal enhancement in collinear double-pulse laser-induced breakdown spectroscopy," *Spectrochimica Acta Part B: Atomic Spectroscopy* **87**, 65-73 (2013).
4. S. L. Ivanovski, A. Bonanno, S. Tudisco, N. Gambino, and D. Mascali, "Plasma astrophysics and laser experiments: hydrodynamical simulation of colliding plasmas," *Radiation Effects and Defects in Solids* **165**, 457-462 (2010).
5. S. L. Gupta, P. K. Pandey, and R. K. Thareja, "Dynamics of laser ablated colliding plumes," *Physics of Plasmas* **20**, 013511 (2013).
6. P. W. Rambo and J. Denavit, "Interpenetration and ion separation in colliding plasmas," *Physics of Plasmas* **1**, 4050-4060 (1994).
7. K. F. Al-Shboul, S. S. Harilal, S. M. Hassan, A. Hassanein, J. T. Costello, T. Yabuuchi, K. A. Tanaka, and Y. Hirooka, "Interpenetration and stagnation in colliding laser plasmas," *Physics of Plasmas* **21**, 013502 (2014).
8. D. Yuan, Y. Li, M. Liu, J. Zhong, B. Zhu, Y. Li, H. Wei, B. Han, X. Pei, J. Zhao, F. Li, Z. Zhang, G. Liang, F. Wang, S. Weng, Y. Li, S. Jiang, K. Du, Y. Ding, B. Zhu, J. Zhu, G. Zhao, and J. Zhang, "Formation and evolution of a pair of collisionless shocks in counter-streaming flows," *Scientific Reports* **7**, 42915 (2017).
9. C. Fallon, "Optical diagnostics of colliding laser produced plasmas: towards next generation plasma light sources," (Dublin City University, 2013).
10. C. Leela, S. Bagchi, V. R. Kumar, S. P. Tewari, and P. P. Kiran, "Dynamics of laser induced micro-shock waves and hot core plasma in quiescent air," *Laser and Particle Beams* **31**, 263-272 (2013).
11. L. C. Nagaraju Guthikonda, P. Prem Kiran, "Interaction of Two Counter-Propagating Laser Induced Shock Waves in Air," KIRAN, 2017.
12. E. Manikanta, L. Vinoth Kumar, P. Venkateshwarlu, C. Leela, and P. P. Kiran, "Effect of pulse duration on the acoustic frequency emissions during the laser-induced breakdown of atmospheric air," *Appl. Opt.* **55**, 548-555 (2016).

This page is intentionally left blank

## Chapter 7 : Conclusions and future scope

Investigations on evolution and propagation of ASW from LIB by focusing ns and ps laser pulses in atmospheric air is presented. The analysis of microphone signal levels was done and compared for both ns and ps lasers. Also the peak frequencies of both ns and ps acoustic pulses are observed to be distinct indicating the distinct plasma formation and oscillation mechanisms. Under same laser energies, the ns pulses have shown better conversion of optical energy to acoustic frequencies compared to that of ps pulses. With ns laser pulses the acoustic peaks localized over 65-35 kHz. While with ps pulses, that deliver two orders of magnitude higher peak intensities than the ns laser pulses, localization of acoustic spectrum towards higher frequencies (60-70 kHz) with less peak pressures is observed. This brings out the different decay mechanisms for the plasma generated using ns and ps pulses. The ASWs were found to be more intense and longer with increasing laser energy for both the cases. Evolution of ASWs from ns and ps LIB of air, as a function of laser intensities achieved via different focusing conditions were presented clearly. The role of breakdown mechanism for ns- and ps-LIB are observed to play a major role in the acoustic properties and the evolution of the central frequencies that followed the plasma profile due to the breakdown. The spatial distribution of the ASWs around the breakdown region is found to be almost spherical with similar central frequencies. Moreover, the observed broad band frequencies are widespread in comparison with traditional acoustic sources with a uniform spatial distribution. Conversion ratio of the laser energy to acoustic energy is presented. We can optimize the ASW frequencies, which varies from audible to ultra-sonic range by varying the laser pulse energies and pulse-width. These studies have established a relationship between the ASW parameters and laser pulse parameters in which the acoustic detection method can be used in real-time monitoring of laser matter interaction and can augment the traditional LIBS technique. Using ASW parameters, we can study the plasma properties from long distances. The capability of generating required ultrasonic frequencies at a standoff distance can also be used for Nondestructive evaluation studies of components at remote and hazardous locations.

ASW emissions from ns & ps-LIB of various target samples has been studied at various incident laser energies. Peak pressures, arrival times, area under the curve of both -ve and +ve peaks are plotted w.r.t incident laser energy. The increment in slopes of peak pressures w.r.t laser energy indicates the

conversion of optical energy into acoustic energy. With increasing laser energy decrement in arrival times were observed, indicating the rise in acoustic shock velocities with laser energy.

Of all the physical parameters like thermal conductivity, electrical conductivity, density, melting point and boiling point, the time domain acoustic parameters follow predominantly the order of melting point. For all the different category of materials studied the peak pressure and +ve peak width are increasing with increasing input laser energy. The peak frequencies obtained applying FFT to time domain signal of ns- & ps- LIB have given multiple peaks. The important peaks and their PSD values have shown material specific acoustic emissions. Repetitive ablation of Al using ns-LIB has shown that the peak pressures are reducing with number of laser shots. Though the peak pressure has reduced, the frequencies are observed to be remain unchanged. This is an essential setup makes acoustic emissions a useful tool to augment traditional LIBS. The ratio of +ve peak width to that of -ve peak height is higher value for 425 micron than the 2 micron particle size at all the densities of 60, 70, 80%. This same behaviour is observed for both ns and ps LIB.

The laser induced breakdown of 4-Nitro Imidazole, Lead nitrate ( $\text{Pb}(\text{NO}_3)_2$ ), Bismuth Nitrate ( $\text{Bi}(\text{NO}_3)_3$ ) samples in pellet form were done in background gases of Ar and ambient Air. We observed that, peak pressure and peak frequencies are enhanced in Argon background gas environment than the ambient Air. The lower thermal conductivity of Ar gas confines the plasma more than the remaining background gases, resulting in enhancement of acoustic parameters. Distinct spectral features were noticed from one gas environment to another one for a particular sample. Ns LIB of AN, DNT, TNT and NTO were presented at two laser energies of 25, 40 mJ. Ps-LIB of RDX, CL-20,  $\text{NaN}_3$  and TNT were presented at two laser energies of 6, 12mJ. The acoustic parameters were tabulated clearly. The peak frequencies of target samples are well separated at two laser energies. Ar gas environment is observed to generate higher acoustic pressures than  $\text{N}_2$  and Air.

Time domain analysis of ASW from individual as well as counter propagating plasma and SWs generated from the ns LIB of air were presented. The resultant ASW pressures are studied as function of two source separation distance. For single and dual plasma the acoustic spectral response is also presented. CCD and ICCD shadowgraphic images showing the extent of plasma and SW evolution are also presented along with acoustic data to get a correlation between plasma, SW expansion and acoustic emissions. Counter propagating dual plasma sources were formed by dividing the incident laser energy in the ratios of 1:1, 1:1.5 and 1:4. Two plasmas with different densities resemble the motion of counter propagating fluids of

the two un-equal impedance fluids. In all the three cases, the interaction of plasma sources has led to ASWs of higher Peak pressures (stronger acoustic signals). The peak frequencies of the spectrum indicated presence of newer frequencies. The results confirmed the interaction of plasmas/ SWs. The observed results have also shown that the interaction of shock waves varied with separation between the plasma sources and the incident laser energies. The results confirm that the acoustic emissions can be a diagnostic tool to understand atmospheric plasmas and their interactions.

## **7.1 Future plan:**

Measurements can be performed to study ablated layer thickness and depth of penetration material by using the ASW detection technique during the laser mater interaction. In the presence of high ‘Z’ inert gases, LIB experiments can be performed to optimize the desired frequencies. This technique can be further extended to study liquids layers (liquid layer on material target) to correlate the properties of liquids and liquid- solid interface. By generating the required laser generated ultrasonic frequencies at a remote location the ASWs from LIB can be useful tool for non-destructive testing/ evaluation. As these ASWs depends on the material properties, LIBS being a minimally invasive technique, material characteristics can be estimated remotely.



## List of publications

1. **E. Manikanta**, L. Vinoth Kumar, P. Venkateshwarlu, C. Leela, and P. P. Kiran, "Effect of pulse duration on the acoustic frequency emissions during the laser-induced breakdown of atmospheric air," *Appl. Opt.* 55, 548-555 (2016).
2. **E. Manikanta**, L. Vinoth Kumar, C. Leela, and P. Prem Kiran, "Effect of laser intensity on temporal and spectral features of laser generated acoustic shock waves: ns versus ps laser pulses," *Appl. Opt.* 56, 6902-6910 (2017).
3. **Manikanta Elle**, Vinoth Kumar L, Venkateshwarlu P, and P. K. P, "Acoustic shock wave emissions from ns and ps pulsed laser induced breakdown of air," *Technology Letters* 1, 16-19 (2014).
4. **E. Manikanta**, P. Venkateshwarlu, S. Sai Shiva, V. Rakesh Kumar, Ch. Leela, Surya P. Tewari, G. Manoj Kumar, P. Prem Kiran, "Dynamic response of metals and alloys to laser-induced shock waves", *Proc. SPIE 8433, Laser Sources and Applications*, 84331Z (11 May 2012); doi: 10.1117/12.922212.
5. L. Vinoth Kumar, **E. Manikanta**, C. Leela, and P. Prem Kiran, "Spectral selective radio frequency emissions from laser induced breakdown of target materials," *Applied Physics Letters* 105, - (2014).
6. L. Vinoth Kumar, **E. Manikanta**, C. Leela, and P. Prem Kiran, "Effect of laser intensity on radio frequency emissions from laser induced breakdown of atmospheric air," *J. Appl. Phys.* 119, 214904 (2016).
7. L. V. Kumar, **E. Manikanta**, C. Leela, and P. P. Kiran, "RF emissions from laser breakdown of target materials," in 2013 International Conference on Microwave and Photonics (ICMAP), (IEEE, 2013), 1-4.; doi: 10.1109/ICMAP.2013.6733512.
8. L. Vinoth Kumar, Ch. Leela, **E. Manikanta**, Surya P. Tewari, P. Prem Kiran, "Detection and analysis of low-frequency electromagnetic emissions from ns laser induced breakdown of air", *Proc. SPIE 8434, Nonlinear Optics and Applications VI*, 84340V (16 May 2012); doi: 10.1117/12.922179.

## Manuscripts under preparation

1. Enhancement of laser generated acoustic shock wave features in argon background gas.
2. Temporal and spectral measurements on acoustic shock waves from LIB of various materials: Effect of physical properties.
3. Interaction of two counter propagating shock waves: Acoustic diagnostics

## Oral presentations in conferences

1. **E. Manikanta**, L. Vinoth Kumar, P. Venkateshwarlu and P. Prem Kiran, "Acoustic shockwave emissions from ns and ps pulsed laser induced breakdown of air", *Optics'14, International conference on light*, NIT-Calicut, India (March 2014).
2. **E. Manikanta**, G. Nagaraju, L. Vinoth Kumar and P. Prem Kiran, "Acoustic diagnostics of interacting shock waves", 'Sensors 2016', *Advances in Sensors: Lab to Field*, 'Research Center Imarat (RCI), Hyderabad, India.

## Conference presentations- poster (National and International)

1. **E. Manikanta**, V. Kumar, L. Chelikani, P. Prem Kiran, "Detection of acoustic shockwave emissions from laser produced plasma in air", ISAMP-TC-2013, IPR, Gandhinagar, India (November 2013).
2. **E. Manikanta**, L. Vinoth Kumar, Ch. Leela, and P. P. Kiran, "Effect of Focal Geometry on the Acoustic Shock Wave Emissions from LIB of Medium," 29th National Symposium on Plasma Science & Technology (PLASMA 2014), Mahatma Gandhi University, Kottayam Kerala, India.
3. **E. Manikanta**, G. Nagaraju, L. Vinoth Kumar and P. Prem Kiran, "Acoustic diagnostics of interacting shock waves", RAOS 2016, University of Hyderabad, India.
4. Ch. Leela, **E. Manikanta**, P. Sai Shiva. S, Venkateshwarlu, V. Rakesh Kumar, G. Manoj, Kumar, S. P. Tewari, and P. P. Kiran, "Investigation of Laser Induced Acoustic Shock Waves and Vibrations from solids," 8th International High Energy Materials Conference & Exhibit (HEMCE-2011), TBRL, Chandigarh, India.
5. L. Vinoth Kumar, Ch. Leela, **E. Manikanta**, Surya P. Tewari, P. Prem Kiran, "Studies on the RF emissions from ns laser induced breakdown of air", ISAMP-2012, University of Hyderabad, India (January 2012).
6. L. Vinoth Kumar, **E. Manikanta**, Ch. Leela, Surya P. Tewari, P. Prem Kiran, "Investigation of RF and Acoustic emissions from ns laser induced breakdown of air", Frontiers in Physics (FIP)-2012, University of Hyderabad, India (September 2012).
7. L. Vinoth Kumar, Ch. Leela, **E. Manikanta**, Surya P. Tewari, P. Prem Kiran, "Investigation of low frequency emissions from ns laser induced breakdown of air", National Laser Symposium (NLS) -2013, Bhabha Atomic Research Centre (BARC), Mumbai, India (January 2013).
8. Vinoth Kumar L, **E. Manikanta**, Ch. Leela, G. Manoj Kumar, P. Prem Kiran, "Spectral analysis of RF emissions from laser produced plasma of atmospheric air and metals", SCIX -2013, Grand Sierra Resort, USA (September 2013).
9. L. Vinoth Kumar, **E. Manikanta**, Ch. Leela, P. Prem Kiran, "Analysis of RF emissions from laser induced breakdown of atmospheric air and metals", 55th Annual Meeting of the APS Division of Plasma Physics, Denver, USA (November 2013).
10. V. Kumar, **E. Manikanta**, L. Chelikani, P. Prem Kiran, "Analysis of RF emissions from laser produced plasma of target materials", ISAMP-TC-2013, IPR, Gandhinagar India (November 2013).

## Workshops

1. Workshop on Machine Drawing and Machining (WMDM- 2012), The Science Complex workshop, University of Hyderabad, Hyderabad – 500046.
2. CVSTA -2013, Course on Vacuum Science, Technology and Applications. GITAM University, Vishakhapatnam, INDIA.

# Acoustic Shock Wave Emissions from Laser Induced Breakdown of Materials

*by* Manikanta Elle

---

**Submission date:** 23-Jul-2018 11:28AM (UTC+0530)

**Submission ID:** 984557098

**File name:** Manikanta\_Thesis\_plagarism\_final.pdf (10.6M)

**Word count:** 42789

**Character count:** 204621

# Acoustic Shock Wave Emissions from Laser Induced Breakdown of Materials

## ORIGINALITY REPORT

14%

SIMILARITY INDEX

5%

INTERNET SOURCES

13%

PUBLICATIONS

1%

STUDENT PAPERS

## PRIMARY SOURCES

- 1** E. Manikanta, L. Vinoth Kumar, Ch. Leela, P. Prem Kiran. "Effect of laser intensity on temporal and spectral features of laser generated acoustic shock waves: ns versus ps laser pulses", Applied Optics, 2017  
Publication **8%**
- 2** [www.osapublishing.org](http://www.osapublishing.org)  
Internet Source **2%**
- 3** [ads.osa.org](http://ads.osa.org)  
Internet Source **1%**
- 4** Submitted to University of Hyderabad, Hyderabad  
Student Paper **1%**
- 5** Manikanta, E., P. Venkateshwarlu, S. Sai Shiva, V. Rakesh Kumar, Ch. Leela, Surya P. Tewari, G. Manoj Kumar, and P. Prem Kiran. "", Laser Sources and Applications, 2012.  
Publication **1%**